

UCL
Université
catholique
de Louvain



Centre de Recherche Public
Gabriel Lippmann

Evaporation of a small amount of gold onto polymers: Effects on surface morphology and signal enhancement in static SIMS

A dissertation submitted to the
École Polytechnique de Louvain

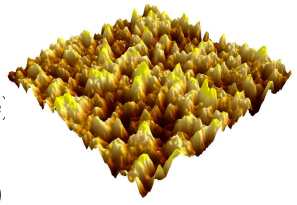
for the degree of
Docteur en Sciences de l'Ingénieur
by

Laurent Nittler

Promoteurs: Prof. P. Bertrand (IMCN - UCL, Louvain-la-Neuve)
Prof. H.-N. Migeon (SAM - CRPGL, G.-D. Luxembourg)

Président du jury:
Prof. Ch. Bailly (IMCN - UCL, Louvain-la-Neuve)

Membres du jury:
Prof. A. Delcorte (IMCN - UCL, Louvain-la-Neuve)
Prof. L. Houssiau (LISE - FUNDP, Namur)
Prof. B. Nysten (IMCN - UCL, Louvain-la-Neuve)
Dr. T. Wirtz (SAM - CRPGL, G.-D. Luxembourg)



05/2011

Copy for "Bibliothèque UCL"

Frustra fit per plura quod
potest fieri per pauciora

William of Occam
14th century

Copy for "Bibliothèque UCL"

Copy for "Bibliothèque UCL"

Acknowledgements

The thesis work described in this manuscript was realized within the Department *Science et Analyse des Matériaux (SAM)* at the *Centre de Recherche Public Gabriel Lippmann (CRPGL)* and within the Department *Physico-Chimie et de Physique des Matériaux (PCPM)** at the *Université Catholique de Louvain*. This thesis would not have come into existence without the support and inspiration of many people whose support I deeply appreciated and who I want to thank within these lines.

My words of gratitude go first to my supervisors *Prof. Henri-Noël Migeon* and *Prof. Patrick Bertrand* for allowing me to work on such an interesting and versatile scientific topic and for giving me the opportunity to do the research in their laboratories. I am very grateful that they gave me the freedom for my research and were always at disposal to discuss the results and resolve problems occurring during the work.

I want to thank *Prof. Patrick Bertrand* for giving me the opportunity to do this work in his research group *PCPM* at the *Université Catholique de Louvain* and the constant support during my stays at the UCL. I highly appreciate his enthusiasm and advices on the thesis subject, which have led to numerous comments in this manuscript.

I am also very grateful to *Prof. Henri-Noël Migeon* for proposing me this research topic, for welcoming me in his research group *SAM* and for providing excellent experimental facilities at the *Centre de Recherche Public Gabriel Lippmann*. I also want to thank him for the first corrections of the present manuscript.

Thanks also go to *Prof. Arnaud Delcorte*, who accepted to be in the accompaniment comity of this work. I appreciate the many fruitful discussions I had with him and which gave me valuable insights in this research topic.

I would like to thank all the other members of the jury of the thesis, namely *Prof. Laurent Houssiau*, *Prof. Bernard Nysten* and *Dr. Tom Wirtz* for their

*recently the denomination of the laboratory change into *Institute of Condensed Matter and Nanosciences (IMCN)*

Copy for "Bibliothèque UCL"

evaluation of this work. I also would like to thank *Prof. Christian Bailly* for taking the chair during the defense of my work.

I am very grateful to all the people from the *groups of the PCPM* and *SAM* who welcomed me in their group, introduced me to the different preparation and analytical techniques and always had the time to answer my questions in detail. I am very grateful for the nice working atmosphere and for the nice moments spend outside the work.

Special thanks go to *Marc Botreau* who acquainted me to the technique of secondary ion mass spectrometry and introduced me to the small secrets of the static SIMS and the ToF-III instrument.

I am very thankful to *Jérôme Guillot* who performed numerous XPS measurements on my samples, initiated me to the XPS evaluation methods and helped me to develop and to use the different evaluation models.

Furthermore I thank *Jean-Christophe Lambrechts* for the SEM and TEM measurements on my samples. These measurements were crucial for the results presented in this manuscript.

I want to thank *Taoufiq Mouhib* and *Nimer Wehbe* for the ellipsometry measurements and the evaluation of this data and the group of *Novelis Foil Innovation Center* located at the CRPGL for the measurements done on their Confocal Microscopy. With their measurements they allowed me to better characterize my pristine polymer samples.

I would like to express my gratitude to the *technical staff of the CRPGL*, and especially to *Arnaud Moschetta* for his useful advices and support during the conception and installation of the evaporation device and the encouragement in the moments when nothing seemed to be working.

Finally, and most importantly, I thank my *family* and all *my friends* for their support and patience. They gave me the strength to finalize this thesis.

I want to thank the *Ministère de la Culture de l'Enseignement Supérieur et de la Recherche* and the *Fond National de la Recherche du Luxembourg (FNR)* for the financial support, which led to this work and manuscript (BFR/03/080 and FNR/11/AM4/04).



Copy for "Bibliothèque UCL"

Contents

Contents **i**

1 General Introduction **1**

2 Literature Review **5**

2.1 ToF-SIMS 6

2.1.1 Introduction 6

2.1.2 Matrix-enhanced SIMS 6

2.1.3 Kinetic energy distribution and molecular dynamic simulation 9

2.1.4 Influence of electron guns 13

2.1.5 MetA-SIMS 14

2.1.6 Cluster sources 20

2.1.7 Originality of this work 21

2.2 Thin Film Deposition 22

2.2.1 Evaporation 23

2.2.2 Condensation Coefficient 24

2.2.3 Nucleation 26

2.2.4 Metal/polymer interaction 27

2.2.5 Surface diffusion 29

2.2.6 Structure of the metallic deposit 29

2.2.7 Diffusion into polymer bulk & Annealing 31

Copy for "Bibliothèque UCL"

3 Overview of the utilized Techniques 35
3.1 Introduction 35
3.2 Secondary Ion Mass Spectroscopy (SIMS) 37
3.2.1 Introduction 37
3.2.2 Energy deposition and secondary particle emission 38
3.2.3 Secondary Ion Formation 41
3.2.4 Dynamic and Static SIMS 46
3.2.5 Matrix-Effect 48
3.3 Atomic Force Microscope (AFM) 48
3.3.1 Introduction 48
3.3.2 Tip-Sample interactions 49
3.3.3 Image artifacts 53
3.4 X-Ray Photoelectron Spectroscopy (XPS) 54
3.4.1 Photoelectric effect 54
3.4.2 Chemical Shift 55
3.4.3 Charge Shift 56
3.4.4 Auger Electrons 56
3.4.5 Fine structure 56
3.4.6 Inelastic scattering of electrons 57
3.4.7 Other appearing peaks in XPS and AES 57
3.5 Electron Microscopy 57
3.5.1 Elastic Interactions 58
3.5.2 Inelastic Interactions 59
3.5.3 Emitted Electrons 59

4 Experimental Setup 61
4.1 Preparation of the Samples 62
4.1.1 Polymer Films 62
4.1.2 Spin-Coating 64

Copy for "Bibliothèque UCL"

4.2 Evaporation 75
4.2.1 Ex-situ metalization 75
4.2.2 In-situ evaporation 78
4.3 ToF-SIMS 91
4.3.1 Primary particles bombardment 91
4.3.2 Mass Analyzer 93
4.3.3 Experimental Setup 94
4.3.4 Data Evaluation 96
4.4 AFM-Instrumentation 96
4.4.1 Scanning elements 97
4.4.2 Detection System 97
4.4.3 Operating modes 98
4.4.4 Experimental Setup 99
4.4.5 Data Evaluation 100
4.5 XPS 101
4.5.1 X-Ray Source 101
4.5.2 Electron Kinetic Energy Analyzer 102
4.5.3 Experimental Setup 103
4.5.4 Data Evaluation - Thickness determination 103
4.6 Electron Microscopy - Instrument 105

5 Gold Quantity and Surface Morphology 109
5.1 Determination of the Sticking Coefficient 110
5.1.1 XPS Analysis 110
5.1.2 XPS Summary 127
5.2 Morphology of the deposited matter 130
5.2.1 AFM 130
5.2.2 Electron Microscopy 138
5.2.3 Morphology Summary 153

Copy for "Bibliothèque UCL"

6 Static SIMS **157**

6.1 Summary of the sample preparation and the metalization procedure 158

6.2 Influence of the substrate and polymer thickness 159

6.3 Evolution of TSIC and the atomic fragments 164

6.4 Evolution of characteristic and gold-adducted fragments . 173

6.4.1 Selection of the characteristic fragments 174

6.4.2 Evolution of characteristic fragments 175

6.4.3 Evolution of Au-adducted fragments 189

6.4.4 Conclusions of the characteristic and gold-adducted fragment evolutions 197

6.5 Evolution in Time and Storage 201

7 Summary and Conclusions **211**

Bibliography **240**

List of Figures **248**

List of Tables **251**

A **A-1**

A.1 Glossary A-1

A.2 Characteristic peaks A-4

A.2.1 Polycarbonate A-5

A.2.2 Polyethylene terephthalate - isophthalate A-10

A.2.3 Poly (methyl methacrylate) A-14

A.2.4 Polystyrene A-19

Copy for "Bibliothèque UCL"

Chapter 1

General Introduction

Nowadays the need of the industries to improve existing materials and to develop new materials with well defined properties becomes more and more important. Mainly the wanted properties are obtained by modifying the surface either in a chemical way or by changing its morphology. Thereby the obtained properties are increasingly due to modification on a micrometer or even nanometer scale, so that the resultant reduction of the available material volume for analysis constitutes a challenge for the detection limits of numerous analysis techniques. As a consequence the analysis techniques need to improve the qualitative and quantitative value of the provided information to keep up with the ongoing improvement of the materials.

With the static secondary ion mass spectrometer (S-SIMS), the elementary and molecular composition of the upper layers of the materials can be analyzed. The main requirements on the analysis of organic samples by S-SIMS are the maximization of the characteristic secondary ion intensities along with minimal sample degradation in order to maintain the molecular information of the sample high during the whole analysis. Therefore the desirable improvement in S-SIMS consists in the elaboration of a more efficient sputtering and ionization of the sample material to obtain a more intense and significant signal so that the spectral interpretation is simplified. This can be pursued by investigating either different primary ion beam bombardment conditions or sample preparation methods.

Copy for "Bibliothèque UCL"

A commonly used sample preparation method in organic static-SIMS is the so-called matrix-enhanced SIMS (ME-SIMS), which mainly consists in a thin layer deposition on a noble substrate. To this end it is essential to dissolve the sample and dilute it sufficiently to deposit a submonolayer of the analyte on a clean and flat noble metal substrate. For most studies of real-world or industrial samples additional constraints on the sample preparation are requested. So some analyses (e.g. imaging of an area of interest) require the preservation of the spatial information and often the quantity of sample material of interest is limited either due to a small concentration of material of interest inside the whole sample or, in case of imaging, due to its presence in a limited area. In these cases the creation of thin layers by dissolving and diluting the real-world or industrial samples and thus the use of the above-mentioned ME-SIMS method is not the adequate sample preparation method to amplify the secondary ion intensities.

A less sample-restricted approach, which was developed in the late 1990's and which sidesteps all the above-mentioned sample preparation problems of real-world and industrial samples, consists in coating the sample surface with a small amount of a noble metal prior to the SIMS analysis. The aim of this metal-assisted SIMS method (MetA-SIMS), on which this thesis is based, is to intensify the characteristic secondary ion intensities without further sample degradation or manipulation. Beside an intensity enhancement of the emitted ions by this metalization procedure, metal-adducted ions can also be created. These additional ions, which are also observable in the ME-SIMS, are characteristic of the sample and could allow an easier characterization of the sample surface. However, only a limited number of special organic samples have been studied with the MetA-SIMS method up to now, so that the aim of this thesis turned out to be two folded:

- From a pure analytical point of view, this work tries to find out the optimal conditions for the metalization procedure of various polymers that are widely used in the industries in order to maximize the characteristic secondary ion intensities in MetA-SIMS.
- A more theoretical aspect of this work is that with a combination of the exact determined quantity, the morphology of the deposited

Copy for "Bibliothèque UCL"

gold and the ToF-SIMS results, further fundamental insights of the secondary ion emission process can be made.

In order to achieve the above objectives, commonly used polymers with high molecular mass, which simulate real-world samples, are investigated. Furthermore the deposition of metal is performed in well-defined conditions *in-situ* in order to reduce unwanted and indefinite influences. In addition to numerous ToF-SIMS analyses, which allow observing the secondary ion intensity change due to the metalization of the polymer samples, XPS, AFM and electron microscopy analyses are performed too in order to characterize the exact amount and morphology of the gold overlayer.

This work is divided / partitioned in the following parts:

In the next chapter a review of the literature regarding the subject of this work is made. It handles all aspects of the MetA-SIMS (↪ *Chapter 2.1*) and reviews the main process of thin film deposition (↪ *Chapter 2.2*).

Chapter 3, which covers the fundamental principle of the utilized analytical techniques (ToF-SIMS, AFM, XPS, electron microscopy), may be overleaped by persons who are familiar with those techniques.

In the first section of the subsequent Chapter 4 the sample preparation is treated: First a brief description of a developed sample preparation method that allows the transfer of polymer films between the different analytical instruments with minimal distortion of polymer film, is described (↪ *Chapter 4.1.1*). Subsequently the sample preparation by spincoating and the characterization of the surface roughness and polymer thickness are presented in a more detailed way (↪ *Chapter 4.1.2*).

In the following Section 4.2, the different evaporation devices are described: It is shown that an *ex-situ* evaporation by sputtering leads to unserviceable results. Also the installed evaporation cell with quartz crystal microbalance (QCM), which allows an accurate *in-situ* metalization and reduces atmospheric contaminations and other influences to a minimum, is described there in detail. In the last

Copy for "Bibliothèque UCL"

sections 4.3-4.6 of this chapter, the different analytical instruments and their used parameters during this work are briefly described.

In Chapter 5, the results of the exact gold quantity determination on the polymer surface and its morphology are presented for the first time in MetA-SIMS: Two independent XPS evaluation methods reveal the exact deposited gold quantity on the polymer and disclose that the sticking coefficient of gold onto the polymer samples is far from unity (↪ *Chapter 5.1*). In the further section, the morphology of the deposited gold analyzed by AFM is presented (↪ *Chapter 5.2.1*) and by dint of electron microscopy an even more detailed morphology characterization of the gold deposit on the polymer samples is obtained (↪ *Chapter 5.2.2*).

Chapter 6 covers entirely the results obtained by ToF-SIMS analysis. In Section 6.2, the influence of the substrate and the polymer thickness are presented and compared to computer simulations. The following Section 6.3 shows the total secondary ion count evolution as a function of evaporated gold quantity and polymer thickness. Furthermore the intensity evolution of atomic ions and gold cluster ions as a function of evaporated gold is presented in this section. The subsequent Section 6.4 deals with the enhancement evolution of characteristic polymer fragments as well as their gold-adducted ions. In a further section the influence of different storage conditions and elapsed time between the metalization and the analysis is briefly investigated (↪ *Chapter 6.5*).

In the last Chapter 7, the results of the different experimental parts are summarized and the work ends with the obligatory conclusions and suggestions for future research.

Copy for "Bibliothèque UCL"

Chapter 2

Literature Review

In this bibliographic chapter the most important themes regarding the present work, namely the emission of organic fragments due to primary ion bombardment and the metalization process of organic samples, are overviewed. A general introduction to the secondary ion mass spectrometry and its fundamental underlying principles are described in Chapter 3.2.

In the first Section 2.1.2, former analyses of a organic (sub-)monolayer on a metallic substrate are presented and discussed. An actual ion emission model due to particle bombardment of molecules adsorbed on metallic substrate, which is elaborated from kinetic energy distribution experiments and molecular dynamic simulations, is described in the subsequent Section 2.1.3. The problems of analyzing insulating samples and the consequence of charge neutralization are briefly described in Section 2.1.4. The partially contradictory results of the secondary ion intensity enhancement in SIMS due to the metalization, are discussed in Section 2.1.5. And finally, to not deprive recent instrumental development, a brief overview of the use of cluster primary ion in SIMS analysis is done in Section 2.1.6.

In the second part of this chapter, the process of metal deposition is discussed in detail: First the evaporation event (↪ *Chapter 2.2.1*) and the metallic adsorption capability, reflected by the condensation coefficient (↪ *Chapter 2.2.2*), are discussed. Then the nucleation behavior of the adsorbed metal (↪ *Chapter 2.2.3*), the interactions between metal and polymer surfaces (↪ *Chapter 2.2.4*) and the diffusion

Copy for "Bibliothèque UCL"

of the metallic adsorbate over the surface (↪ *Chapter 2.2.5*) are treated, due to their important influence on the structure of the metallic deposit on a polymer surface (↪ *Chapter 2.2.6*). In the last Section 2.2.7 the diffusion of the deposited metal into the bulk polymer as well as the annealing of the metalized samples is overviewed.

2.1 ToF-SIMS

2.1.1 Introduction

Historically it was Benninghoven et al. who have surprisingly observed in 1976/1977 that characteristic parent-like ions and many characteristic fragment ions are emitted from the uppermost surface layer of amino acids and other organic molecules adsorbed on a metallic substrate [1, 2]. This observation leads to the development of the precursor model (↪ *Chapter 3.2.3.C*). Soon afterwards, Grade et al. made the observation of *cationized* ion emission from a mixture of aminobenzoic acid and an alkali-halogen salt. They also observed for the first time the emission of metal-cationized characteristic ions from organic molecules deposited on a metallic surface [3].

Besides instrumental developments (e.g. pulsed charge compensation by low-energy electrons [4]), several sample preparation strategies have been developed to favor the emission of high mass organic molecules. They involve the use of metallic or nitrocellulose substrates [5], the addition of 'ionizing' agents [6], the dissolution of the analyte in a low-molecular weight matrix inspired by the MALDI procedure [7] or the evaporation of an ultrathin metal layer on the sample [8, 9]. Over decades up to now, the most widespread sample preparation procedure for large molecule analysis in static SIMS consists of depositing a sub-monolayer of analyte on a metal substrate [3, 10–12] (↪ *Chapter 2.1.2*).

2.1.2 Matrix-enhanced SIMS

Metal-cationization denotes the complex process by which the molecule ($\mathbb{M}$) and the metal ($\mathcal{Me}$) combine and become ionized, so that the formed $(\mathcal{Me} + \mathbb{M})^+$ species can be detected by SIMS analyzers. In addition to the possible cationization of the whole molecule, also

Copy for "Bibliothèque UCL"

characteristic fragments of the molecule can combine with a metal atom. Furthermore, double charged cationization with two metal atoms has been observed. Besides the fact that the metal substrate acts as an external source for the analyte molecule ionization, it has the effect that the metallic substrate with a high atomic mass and a compact arrangement confines the projectile energy in the surface region and reflects this energy towards the vacuum, which favors the desorption of analyte molecules [13–15]. Blending the analyte with a low-molecular weight organic matrix (MALDI-type preparation procedure) or mixing alkali/noble metal salts with the analyte can lead to similar cationization effects [16, 17].

As long as the surface coverage is below a monolayer equivalent there is a linear relationship between surface coverage and the secondary ion intensity. It turns out that for most polymer sample, independent of its average molecular weight, the secondary ion yield is maximized for a deposition of about 1 $\mu g/cm^2$ polymer material. Due to the molecule entanglement, no cationized secondary ion can be detected from a closed polymer layers [18, 19].

The chemical interaction between substrate and adsorbate has a predominant role on the observed fragmentation pattern and also on the absolute as well as the relative yields of all the secondary ions [20]. Furthermore these yields are strongly influenced by the chemical surface composition of the metallic target and the surface coverage of the adsorbates molecules [18, 19, 21]. Silver and gold are very efficient substrates for cationization of molecular samples, followed by copper, palladium, indium and lead. Chromium has a significantly lower efficiency and aluminum does not cationize at all [22].

Concerning the emission process of metal-cationized molecules, there exists different hypotheses for the emission. In the case where the cationized ions are not sputtered as a preformed complex, the organometallic ion formation requires the concerted transfer of organic molecules and metal atoms from the solid phase to the vacuum in a single bombardment event.

One commonly accepted scenario for metal-cationization is that the ejected molecule recombines in the near surface region with a metal ion. This scenario has neither been demonstrated experimentally nor theoretically, so that still different uncertainties exist. For instance, there

Copy for "Bibliothèque UCL"

is no proof that the observed organometallic complexes are truly the result of a recombination or if their constituents have already formed a complex prior to their emission. Assuming that a recombination occurs, it is not known if this occurs in the force field of the surface where the sample can still act as an energy sink for the reaction, or out of the surface influence surface where the organometallic complex requires a specific route to evacuate the excess energy released by the exothermic association reaction. Due to the low encountering probability of the emitted particles at a distance of more than a few tens of nanometers from the surface, the low occurrence of emitted metal cations and other additional constraints in time, space and velocity vectors, the association of metal ions and neutral molecules above the surface should be a very low probability event and can not explain the high occurrence of cationized molecules [23].

Due to different experimental observations (e.g. the yield of the metal-cationized molecules $(\mathcal{M}e + \mathbb{M})^+$ and metal cations $\mathcal{M}e^+$ are generally not correlated [22, 24]) and theoretical considerations about the recombination process out of the influence of the surface, the above mentioned association of a metal ion with a neutral molecule presents major obstacles to be accepted as a reliable model.

As the calculated neutral yields are 10^2 (Ag, In) to 10^5 (Au) times larger than those measured for metal ions, Wojciechowski et al. proposed that neutral molecules recombine above the surface with metal *atoms* rather than metal *ions* and that the ionization of a nascent complex can occur via electron ejection during the association process [22, 25]. This process, called *associative ionization*, is a unique ionization process that occurs when an electronically excited atom $\mathcal{A}^*$ or a ground state one collides with a species $\mathcal{B}$, resulting in the formation of a charged association complex:

$$\mathcal{A}^{(*)} + \mathcal{B} - > \mathcal{A}\mathcal{B}^+ + \mathrm{e}^-$$

In the course of the recombination reaction, when $\mathcal{A}$ approaches $\mathcal{B}$, the energy difference between the potential energy curve of the molecular ion $\mathcal{A}\mathcal{B}^+$ and some of the curves describing the $\mathcal{A}^* - \mathcal{B}$ interaction may decrease. At certain distances, when the two constituents are closely enough, the energy curves cross and the complex becomes auto-ionizing, so that the ejection of an electron is favored. The electron emission, which locked the complex in the ionic state, constitutes also a way

Copy for "Bibliothèque UCL"

to dissipate the reaction energy. A slight alteration of the above model consists in the recombination of a vibrationally excited organic molecule and of a metal atom at its ground state. If both scenarios are energetically equivalent, the second scenario should be favored because the number of ground state atoms is at least one order of magnitude larger than the number of excited atoms.

2.1.3 Kinetic energy distribution and molecular dynamic simulation

Experimentally, different emission process hypotheses can only be verified by the observation of the absolute and relative yield of all the secondary ions as well as by measuring their kinetic energy distribution (KED).

Contrarily to the kinetic energy distribution of atomic ions, which follows the Sigmund-Thompson law, the KED of the molecular ions have a much more intriguing structure, whereas the KED of molecular ions sputtered from organic and polymer targets is narrower than that of atomic ions [26, 27]. The peak energy value and the high energy tails observed in the energy distributions of fragment ions provide support to collisionally-induced emission mechanisms [15]. Furthermore it has been shown that larger characteristic ions are emitted with a low kinetic energy, reflecting a soft emission process, whereas fragmented molecular ions exhibit a higher mean kinetic indicating a more violent ejection mechanism [26–31]. In general, the shape of kinetic energy distribution of fragment ions is found to be almost independent upon the primary ion and energy [31].

During numerous KED experiments [13, 15, 26, 30, 32], different effects have been observed, which are based on the assumption that the total energy that is transferred to the fragment during its emission is distributed as kinetic and internal energy. So the KED of C_xH_y shifts and broadens when the number y of hydrogen atoms decreases (unsaturation effect). This unsaturation broadening is observed in both polarities, suggesting that the energy transfer mechanism may be similar and little affected by the ionization processes. The more saturated ions, which have a structure close to that of the original molecule, have a narrower energy distribution and are only slightly dependent on the fragment

Copy for "Bibliothèque UCL"

mass. For a given impact energy, the greater the emitted fragment, the lower will be its kinetic energy (size effect). For a given emitted fragment, the greater the total energy, the greater will be the kinetic and internal energies. The internal energy (vibration and rotation), whose fraction is increasing with the fragment size, is considered as excess energy. If the internal energy is superior to the corresponding potential barrier for reorganization, the fragment undergoes either a rearrangement or dissociation.

In any case, to give an interpretation to these results and to understand the collision cascades, the atomic motions after bombardment of keV projectiles, the chain scissions and the successive particle emission, only molecular dynamic (MD) simulations can help to obtain a macroscopic view of the occurring processes [33–36].

Thereby the sample is approximated by a finite micro-crystal model and the Hamilton's equation of motion is integrated to yield the positions and momenta of all particles as a function of time. From the final positions and velocities of all the ejected species, various properties are determined, such as mass spectra and kinetic energy distributions. In addition the sputtering mechanism can be analyzed by visualizing the individual particle trajectories.

The molecular dynamic simulation approach needs as input a force field or interaction potential among the atoms. In the beginning of the calculation, when the computer power was not high and the interaction potential was not developed, only small and simple model have been simulated. In these simulations a pairwise interaction potential among all atoms is used and only a sample model with a small number of atoms was bombarded by a low energy primary ion. In the past decade, the increasing computer power as well as the development of many-body potentials was an improvement for the simulations, so that more realistic sample models with larger molecules on a larger crystal bombarded by particles with higher energy, can be simulated. With special potentials even bond breaking, bond formation and hybridization can be simulated [37].

With the simulation, not only the above mentioned effects in the KED experiments can be explained [38], but also the appearance of up to 3 peaks in the KED [27, 29, 39] can be clarified. The main peak of the KED correspond to the fast rearrangement and ionization of the

Copy for "Bibliothèque UCL"

molecule within the time of the collision cascade (10^{-12} s) resulting in the direct formation and ion emission at the surface. In contrast to the simulation, unimolecular dissociation happening before 10^{-9} s cannot be distinguished from direct emission fragment in the KED experiments. If the emitted fragment has an excess of internal energy it will reorganize mainly by hydrogen elimination. Thereby the fragment releases its excess of internal energy, keeping its kinetic energy nearly unchanged. An additional peak in the negative energy tail of the KED appears if the lost of H and H_2 occurs in the drift section of the spectrometer. Metastable decay of the ions in the acceleration section of the spectrometer (after $10 - 100$ ns after emission) leads to the regular intensity decrease in the negative energy tail. In any case, numerous KED experiments show that an important fraction of the secondary ions is detected with an energy deficit due to the dissociation of their metastable parents in the linear part of the spectrometer [15, 39].

Overall the simulations point out that the sample preparation and the bonding geometry of the molecule on the surface strongly influence the ejection process and thus the mass spectrum [40]. Although the number of molecule and fraction ejection increase with the primary ion energy, their ratio is relatively constant. The entity of the observations made by the simulations and the KED measurements lead to the development of a ejection mechanism model, which is described in the following paragraphs.

The direct collision between the incoming primary ion and a carbon atom of the molecules is the most efficient way to produce fragments and atoms. Numerous of these fragments and atoms move in the $1 - 5$ Å region above the substrate. Because these moving particles have sufficient kinetic energies, they can fragment other molecules, induce chemical reactions to form new molecules, or eject molecules and molecular fragments. For an intact ejection of a chemisorbed molecular species, the decisive step is in any case a collision near the molecule attachment point to the surface as well as the escape route for the molecule [41–47]. The simulations reveal that the fragmentation degree is rather insensitive to surface binding energy, because the energies required to fragmentation the molecular are usually significantly larger than the surface binding energies. On the other side, soft collisions, which lead to molecular desorption, are more sensitive to the value of the binding energy of the adsorbate particle.

Copy for "Bibliothèque UCL"

In the simulations, the angular distribution of ejected molecules shows a normal and a off-normal component. Analysis of individual trajectories reveal that the off-normal ejection has higher kinetic energies and arises from single collisions between substrate atoms and the molecule, while multiple collisions with the substrate atoms (cooperative uplifting mechanism) result in low-energy ejection along the surface normal [48, 49].

On the time scale of the emission process, the molecular dynamic simulation shows that the energy transfer from the impinging particle to the sample is from tens of femtoseconds to several picoseconds depending on the material [50]. During the first 1 ps after impact many free H atoms and hydrocarbon radicals are created due to a direct interaction between the primary particle and a close neighbor atom of the nascent fragment. These fingerprint fragments in the range $0 - 150$ Da, which are mainly created by bond-scissions, have a high velocity (> 1 km/s).

Larger particles, which are emitted with velocities lower than 1 km/s, are sputtered at times larger than 1 ps, so that the energy of the impinging particle has dissipated considerably by multiple collisions in the solid. The molecular dynamic simulation reveals that the amount of time before a large molecule can escape increases with its mass. The ejection of these large fragments can be induced either by a single energetic collision, where large amount of vibrational motion is transfered to the molecule or by a cooperative uplifting of several substrate atoms resulting in a desorption of molecules with low internal energy and high kinetic energy [14, 41, 48, 51, 52]. Simulations also reveal that fragments with very little kinetic energy can drift free over the sample for many picoseconds and can either recombine to produce more stable molecules or fragment other molecules.

As in the experiments, the simulated kinetic energy spectrum of the ejected molecules is significantly narrower for the bulk sample than the overlayer on metal, which gives an indication of different emission processes on these two kind of samples [53, 54]. In the bulk organic sample, where the trajectory of the projectile is only slightly deflected by the interactions in the sample [50], the sputtering process is slow (10 ps) and the energy remains localized in the molecules (excited vibrations). This results in a comparatively low kinetic energy of the desorbed molecules, which suggests that exothermic chemical reactions in the film

Copy for "Bibliothèque UCL"

may play a role in producing a thermal-like desorption event. Excited molecules arise mainly from the surface layer since molecules originating from below the surface tend to be cooled by multiple collisions with other molecules in the interfacial region [53]. In the case of molecules adsorbed on a metal substrate, the sputtering process is characterized by the quick dissipation of the projectile energy in the metal substrate and an efficient upward reflection of the projectile momentum due to the heavy metal substrates [43, 48]. The cooperative motions in the metal substrates induce the molecule ejection with a larger average kinetic and a limited amount of internal energy, so that only low subsequent fragmentation of these emitted particles occurs [13, 55, 56].

The recombination of a metal atom with a molecule can be explained by a hybrid mechanism: The molecule is ejected intact by a soft collision and combined with an ejecting metal atom from a neighboring site to form the cluster slightly above the surface [48, 57]. Thereby it is not necessarily that the metal atom is the closest atom to the molecule on the surface.

Despite the increase of the computer power and optimized models, the molecular dynamic simulations have still some restrictions. Up to now, the ionization process of the emitted fragment is not incorporated in the simulations, so that a direct comparison of the molecular dynamic simulation with the SIMS experiments is not possible. A low ionization efficiency of a frequently emitted fragment results in a detection lack in the experiment [38, 48]. However, studies showed that the simulations are able to describe the properties of secondary ions when they are emitted via collisional processes [13, 15]. The short time scale of the simulation and the absence of long-range intermolecular interactions deprive the dissociation of metastable fragments and highly excited molecules, which decompose unimolecularly before reaching the detector. An internal energy threshold, which depends on the fragment size, can be used to determine the fragments that can reach the detector [38, 41, 48].

2.1.4 Influence of electron guns

The analysis of (sub-)monolayer on a substrate, necessitate dissolving of the analyte. Besides that this can often be time-consuming or very difficult (e.g. in cross-linked polymers), it prohibits the surface

Copy for "Bibliothèque UCL"

characterization of intact polymer films or the analysis of real-world samples. Nowadays, the electrostatic charging of the samples, which arise during the SIMS studies of thick and insulating samples, is compensated by flooding the surface with electrons. If the neutralization is insufficient, the surface starts to charge. This causes the beam to move across the surface and deform as well as a degradation of the mass resolution. In ToF-SIMS system a pulsed electron gun is used, which emit low-energy electrons and have a current up to 10 μA, to ensure that even the most challenging samples (e.g. rough, bulk insulators) are always fully neutralized [4]. Spectra of insulators obtained by using a electron flood gun are restricted to the low mass range because frequently the electrons cause fragmentation in addition to that induced by the ion beam.

Gilmore et al. showed that the damage caused by low energy electrons (between 10 and 20 eV) from a flood gun used for charge neutralization in static SIMS can be significant [58, 59]. In a typical ToF-SIMS analyze of an insulator, where the delivered electron fluence by an electron flood gun may typically be $1.9 \cdot 10^{20} electrons/m^2$, the appropriate electron beam fluence for damage-free analysis is exceeded by a factor of 10^2 !

For completeness, the methodology of polymer analysis by static SIMS developed by the same group of Gilmore et al. should be mentioned. This method, called G-SIMS, consists in extrapolation the fragmentation behavior of different analysis conditions (variation of energy or nature of the primary ions) to a virtual low fragmentation "plasma temperature" [60, 61].

2.1.5 MetA-SIMS

Another method for analyzing organic samples by ToF-SIMS is called metal-assisted SIMS (MetA-SIMS). The method, which was developed by Karen et al. [62] and Yanashima et al. [63], consists in the deposition of a small amount of metal onto the analyte prior to the static SIMS analyze. In later experiments, Delcorte et al. observed also cationized molecules emitted from metalized polymers [9]. As this method, on which this work is based, requires no further sample manipulation, this method suits for all kind of samples, including insulating, insoluble and bulk samples.

Copy for "Bibliothèque UCL"

In fact the origin of the idea of a metallic overlayer dates back to the experiments of Bletsos et al. in which a conducting Ni grid was placed onto the polymer surface to overcome the difficulties arising from charging of the polymer [64]. In these experiments, cationization of polymer fragments with atoms emitted from the metallic grid was observed.

The subsequent important milestone in the development of this method is the publication of Belu et al. [65]. In their article a patterned silver overlayer was deposited on polymer films. The coverage variation was obtained by the variation of mesh size of the TEM grids. They suggested that the detection of Ag cationized polymer fragment through the thick overlayer (> 500 nm) is due to defects in the Ag overlayer and to the diffusion of the sample constituents. As diffusion rates depend on the size or molecular weight of a species, they concluded that the smaller oligomers diffuse more readily through the Ag overlayer.

A linear increase of the positive metal ion emission and a drastic decrease in the emission of characteristic polymer fragment ions at metal coverage above 10% of a monolayer (not calibrated) has been pointed out by Karen et al. for oxygen containing polymers [62]. Yanashima et al. observed an increase of the secondary ion counts with Au deposition, but no detection of cationized ions (e.g. $[M^+ + Au]^+$). The negative characteristic ions emitted from Au covered surfaces remarkably increase their intensity whereas small positive clusters (e.g. $C_2H_3^+$) remained constant. They observed also difference in the coverage dependence between the Ag/PET and Au/PET system. In general, they found that the dependence of the metal coverage on the secondary ion signal varies widely between the different metal/polymer systems. However, for all Au/polymer systems, the coverage dependence of positive ions was relatively similar: The characteristic ions of polymers increased with Au evaporation. They suggest that due to the metal evaporation, the surface conductivity could affect the secondary ion intensities and that the deposited metal ions could stabilize polymer characteristic ions [63].

The first observation of cationized molecules on metalized polymers was delivered by Delcorte et al., who showed that the metalization enhances the fingerprint fragment intensities of polystyrene samples [9]. Although the intensity enhancement is observed for all recorded ions, it appears to be very dependent on the ion species,

Copy for "Bibliothèque UCL"

whereas the (protonated) molecular ions undergo the largest intensity improvement [66–69]. In general the metalization procedure does not affect the fine spectral features of the polymers that are traditionally used for characterization, but the ion intensities can be different [9, 66, 70]. Furthermore the group of Bertrand showed that the dynamics of yield enhancement by metal deposition is also strongly dependent on the choice of the projectile [70, 71]. The enhancement is nearly the same for Xe^+ and Bi^+, more pronounced for Ar^+ and with up to one order of magnitude highest for Ga^+ ion bombardment. For monoatomic primary ions, the increase in energy results in only slight yield changes.

Contrarily to Adriansen et al., which state that the metalized samples hardly give rise to Ag and Au adduct ions under primary ion bombardment [66], Delcorte et al. observed in their experiments a new series of peaks in the mass range $200 - 600$ Da [9]. These new peaks are cationized fragments which directly mirror the molecular structure of the polymer. These Au-cationized molecules are only present in the spectrum for light-weighted polystyrene molecules and not for the polystyrene with a molecular weight of 3000 Da or above [9]. Delcorte et al. presume that the structure of the sample surface is not stable and that, in order to minimize the surface free energy, either a diffusion of the gold clusters toward the polymer bulk or a migration of small polystyrene oligomers over the gold clusters occurs. In any case, Delcorte et al. assume that within a few minutes after metalization, the gold clusters are located right underneath the top surface layer.

Numerous experiments conclude that gold followed by silver, are good cationizing agents and give the strongest secondary ion yield enhancement [9, 22, 56, 66, 72]. Furthermore, gold, which is more noble than silver, has a single isotope so that no disturbance due to interference of the isotopic pattern occurs. Experiments with Pt overlayer, where no significant increase of secondary ion yield was observed, show that the stronger enhancement of gold in comparison with silver can not be led back to the difference in atomic mass [66]. Prabhakaran et al. suggest that low yield of Pt-cationized fragments is due to the low yield of Pt^+ and not due to the low recombination probability [73]. Comparably to the submonolayers cast on metallic substrate, the measured yields for metalized films are more than 2 times lower and the shape of the oligomer distribution changes significantly [56, 66]. However, with the metalization procedure, the efficiencies seem to be much less dependent

Copy for "Bibliothèque UCL"

on the molecule nature (less sensitive to the matrix effect) [9, 56]. And although gold coverage reduces the area of emitting organic fragment ions, ion images can be observed without restriction in lateral resolution and without interference of the deposited metal [74].

Concerning the metal deposition method, the group of Inoue et al. found that the sample had to be cooled down for the silver deposition by the diode sputtering method to prevent prevent damage of the sample surface due to thermal oxidation. For the vacuum evaporation method they found that no damage at all occurs to the sample surface at room temperature [74]. In some SIMS articles, different statements are made on the size of the deposited metal clusters on organic samples. Some groups found that the Ag particles are larger than that of the other metals (Au, Pd, Cu) [63] and other groups argue the converse (Au islands larger that Ag) [66].

For the sake of completeness, the deposition method of metal on polymer for SIMS analysis that was developed by Marcus et al. should also be mentioned here. Their method consists in a deposition of a submonolayer coverage of metal nanoparticles on the polymer surface by exposing the sample surface to a solution of citrate-capped metal nanoparticles [75]. The nanoparticle coverage is dependent upon the type of metal nanoparticles and the polymer to be examined as well as the exposure time to the nanoparticles. The signal intensities are comparable to those found using conventional metal deposition.

The behavior of the secondary ion intensity as a function of the amount of evaporated metal, depend on the ion fragment [9, 66]. The gold monocation signal increases almost linearly with gold coverage up to 20 $nmol/cm^2$ and continues to increase with a softer slope afterward [9]. Silver monocation has a similar behavior [66]. Characteristic fragment ions of molecules, cationized fragments and molecules reach a maximum intensity and decreases significantly for larger gold doses [9, 66]. But also an almost linear increase with the deposited gold quantity was reported for cationized polypropylene fragments [70].

In the negative mode too, there are contradictory statements about the secondary ion enhancements due to the metalization of the samples. No enhancement and even a intensity decrease of the negative ions have been observed by the Adriansen group [66, 68]. On the other hand,

Copy for "Bibliothèque UCL"

Delcorte et al. report a gradual increase of the negative ion yields, which they assign to the change of sample band structure induced by the present of metal at the surface [9, 70, 76]. The behavior of the yield in the negative polarity seems to depend on the type of molecules too.

Adriaensen et al. observed that the time elapsed between metal deposition on the sample surface and the measurement of the sample with Tof-SIMS appears to have an important influence on the enhancement of the secondary ion intensities. Depending on the sample and the deposited metal, the secondary ion signals reach their maximum at different times. This behavior not only makes it difficult to know when the best time is to analyze the samples but also poses problems regarding the reproducibility of the results [66, 68, 72]. The period after that maximum enhancement occurs is shortened by sample storage at elevated temperatures [72], which suggest surface rearrangements to occur with time for metal evaporated samples. Here too, the occurrence of diffusion processes can explain observed the time effect: When samples are measured too soon after metalization (before sufficient diffusion has taken place), no enhancement effect is recorded. In addition, the sample analyses in that the organic molecules have diffused too much also give no yield enhancement.

Overall, studies about the mechanism of the ejection process in combination with surface metalization as a sample preparation route for SIMS analysis are relatively scarce in the literature. However, the kinetic energy distribution can give some insights into the emission processes of quasimolecular ions from metalized surfaces.

As in ME-SIMS, the kinetic energy distributions of MetA-SIMS samples show the same features: a broad and asymmetric shape, with a maximum between 2 and 4 eV and in the high-energy part of the distributions a slowly decaying and extending beyond 8 eV. The apparent negative energies in the KED distribution indicate the presence of metastable ions. Differences in the absolute intensities of the ions measured for the two samples is probably due to an overall change of the ionization or the ion survival probability rather than a drastic change of the emission mechanism. Beside these similarities, there exist also contradictory results.

On the one side, Luxembourg et al. state that the KEDs obtained for the gold-coated sample are much wider than for the precursor ion in the

Copy for "Bibliothèque UCL"

ME-SIMS [77, 78]. This distribution broadening, which predominantly takes place at the high kinetic energy side, results from the high stopping power of the deposited gold. On the other side, Delcorte et al. found that the KED of cationized molecular ions sputtered from Au-covered heavy weighted polystyrene are narrower than those emitted from the PS submonolayer on gold. But they found also that KEDs of PS fragments as well as Au-cationized Irganox molecules, emitted from both type of samples, match each other. This behavior indicates that the emission process is not significantly influenced by the different sample preparation [56]. Delcorte et al. assume that the difference rises from the different diffusion behavior of the molecules. In the case where the molecules diffuse over the gold island the analyzing MetA-SIMS sample results in a system similar to the molecule cast on a metal substrate. In the case of large molecules, where the diffusion are comparatively low, the covering of the gold island can be neglected so that, on a microscopic level, the metalized sample can not be compared to the submonolayer on a metal [9, 76]. Other hypotheses for the limited detection of large cationized molecules are the relative inefficiency of keV projectiles to desorb several kDa molecules from a thick organic sample and the chain entanglement in the polymer layer. All these phenomena can be disregarded in the in submonolayer sample preparation.

Contrarily to ME-SIMS, there are up to now only very few molecular simulation performed for MetA-SIMS. First simulations are presented by Restrepo et al. in the year 2009 [79, 80]. Their results show for instance that the projectile type and the position of the impact point on the metal-covered surface critically influences the calculated yields. So is the yield with Ga bombardment on the polymer surface significantly lower than with the C_{60} bombardment. In contrast, the yield with C_{60} is larger on the gold clusters than with Ga. Furthermore, on the interface between the gold cluster and the polymer, the yields of both projectiles are similar.

This limited availability of theoretical calculations makes it difficult to verify the established ejection mechanisms in MetA-SIMS. One of the several hypothetical models is that the secondary ion intensity enhancement is based on specific desorption/ionization enhancement provided by the metalization, which creates conducting paths at the surface by the gold pattern so that the sample charging is suppressed. Thereby the metalization changes the work function of the surface,

Copy for "Bibliothèque UCL"

lowers the ionization potential of the organic molecules by the proximity of the metal and/or provides an external source of ionizing particles [9, 67, 70, 81]. Another interpretation for the MetA-SIMS effect assumes that the molecules are diffused on the metallic clusters, which then lead to a similar situation where the metal islands act in a way similar to metal substrates. In that case, the heavy metal substrate facilitates molecular desorption via an efficient upward reflection of the projectile momentum [56, 66, 70]. A further explanation of the observed enhancement in MetA-SIMS is that the gold islets, due to the higher scattering cross section of gold, may deflect the primary ions into surface-near trajectories. Thereby the near-surface energy deposition increases and enhances the molecule and fragment ejection [70, 71, 82]. Heile et al. state that combining different yield enhancing techniques such as polyatomic primary ion bombardment with MetA-SIMS, lead to a combined yield enhancement which is in most case smaller than the sum of the yield enhancements obtainable with each technique taken by itself [82].

Finally, one should restate that the metalization procedure still provides a drastic qualitative improvement for thick organic samples in comparison with the direct analysis of pristine (non-metalized) samples, in which no molecular ions are detected at all.

2.1.6 Cluster sources

The recent developments of ion sources can not be ruled out. The bombardment of organic materials by cluster ions (e.g. C_{60}^+, Au_n^+, Bi_n^+) results in a yield enhancement of at least 30-100-fold as compared to yields observed under Ga^+ bombardment with the same energy. Thereby the mass spectrum delivers no other molecular fragmentation than any other primary projectile used in SIMS, but the levels of fragmentation and dehydrogenation of the sputtered ions are larger with C_{60}^+ than Ga^+ [70]. Furthermore the beam induced damage on some organic materials is substantially reduced under cluster bombardment, so that molecular depth profiling on selected polymer films become possible and biological samples imaging is enhanced [83–88].

Molecular dynamic simulations reveal differences in the desorption process between monoatomic and polyatomic projectiles. While for

Copy for "Bibliothèque UCL"

monoatomic projectiles the development of a linear collision cascade is the predominant mechanism responsible for the particle ejection, cluster projectiles liberate their energy in the topmost layers of the sample in a correlated manner (pressure wave followed by a fast expansion of the superheated interaction volume in the gas-phase) [55, 89–91]. Consequences of the changed sputtering and ionization process by the use of polyatomic clusters are the formation of nanoscopic crater and the non linear increase in secondary yield [71, 92]. Because the damage cross section increase less than the corresponding yield, the use of cluster sources will increase in future

The positive effect of metalization on the secondary ion yields of organic ions is rather limited with C_{60}^{+} cluster projectiles [70, 71, 76, 93, 94] and even a decrease of the secondary ion yield with increasing gold deposition was reported [71]. Although the deposited gold may also promote the secondary ion emission, the resulting yield enhancement is so small that it cannot compensate for the yield decrease due to the reduction of uncovered organic sample area [71, 82]. However, it has to be noted that the secondary ion yields obtained with polyatomic ion bombardment on pristine samples are higher than the yields obtained with monoatomic ion bombardment, regardless of whether the samples were pristine or gold-covered [66, 71].

2.1.7 Originality of this work

After reviewing the state of the art in S-SIMS on the previous pages, this section points out the new aspects, which this work brings to the MetA-SIMS domain.

- For the first time, the sample metalization is performed ***in-situ***. This has the advantage that the metalization process can be better controlled and the contamination added to the surface between the metalization process and the sample analysis is minimized. Furthermore this *in-situ* sample metalization and subsequent analysis also allows an enhanced controlling of the storage conditions, which has demonstrably an influence on the intensity enhancement in S-SIMS.

Copy for "Bibliothèque UCL"

- Up to now MetA-SIMS studies on real-world samples, such as high molecular mass polymers used in the industries are scarcely, so that the samples studied in this work complete these results.
- For the first time a detailed study shows the intensity evolution of the characteristic secondary ions as well as the atomic ions in both polarities as a function of the evaporated gold quantity.
- The determination of the exact amount of gold on the polymer samples as well as a detailed and quantitative morphology study of the Au deposit in combination with a MetA-SIMS study was also performed for the first time in such an elaborated way as in this work.

All the above mentioned improvements not only permit to test the use of MetA-SIMS for real-world samples but also allow further insights in the secondary ion emission process in MetA-SIMS. Concerning the part of the sample preparation and thin film deposition, no process improvements have been intended nor performed in this work. However a study about the morphology evolution of gold-islands as a function of the deposited gold quantity is, to my knowledge, not yet published.

2.2 Thin Film Deposition

The noble metal deposition plays a significant role in this work, so that in the following sections the main phenomena of the metal/polymer interface formation are reviewed. There are many different metalization techniques (electrochemical deposition, sputtering, chemical vapor deposition or evaporation) available to prepare metal/polymer interfaces. Each of them produce interfaces with different physical and chemical properties, which also depends on the polymer pretreatment and the particular metal deposition process [95–97]. Here, principally the metal/polymer interfaces prepared by noble metal evaporation onto pristine polymer surface will be discussed.

In Figure 2.1 a summary of the basic processes occurring during the initial stages of deposition of low interacting metal on a polymer is sketched. For very reactive metals like Cr or chemically modified

Copy for "Bibliothèque UCL"

polymer surfaces, the metal atom diffusion process over the polymer surface or into the polymer can be suppressed by direct chemisorption. This leads to a different nucleation and growth behavior of the reactive metal on polymer surfaces. In this bibliography principally low metal-polymer interaction, which is the case of gold deposition onto untreated polymer, is reviewed.

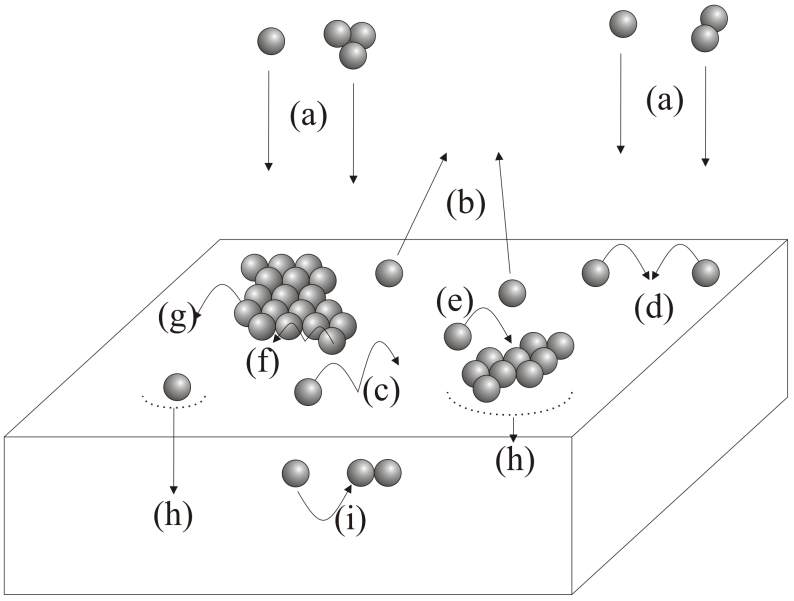


Figure 2.1: *Schematic diagram of the basic processes occurring in the initial stages of metal/polymer interface formation by physical vapor deposition (modified from [98]). Sketched are: (a) adsorption of atoms and clusters, (b) desorption, (c) surface diffusion, (d) nucleation of critical clusters, (e) aggregation, (f) edge diffusion, (g) dissociation, (h) diffusion into the bulk, (i) aggregation in the bulk.*

2.2.1 Evaporation

Overall, growth of thin films deposited from the gas phase is intrinsically a non-equilibrium phenomenon governed by a competition between

Copy for "Bibliothèque UCL"

various processes (adsorption, surface diffusion, metal reemission into vacuum, nucleation, coalescence of smaller structure into larger ones, etc) [99]. Although one can presume that under normal evaporation conditions, the metal vapor consists of single metal atoms, Barnes et al. suggest that the clusters observed by TEM in their experiment did not nucleate on the substrate but are already formed in the gas phase. They state that the major flux for film deposition is composed of positively charged and amorphous clusters [100].

In any case, to become absorbed on the polymer surface, the metal atom/cluster must loose some of its transitional energy that it has gained during the thermal evaporation. In the opposite case the metal atom/cluster is desorbed again to the vacuum. Thran et al. observed that the angular distribution of re-emitted atoms does not depend on the angle of incidence, so that there is no indication of a direct reflection of the impinging metal atoms/clusters. Therefore it seems to be justified to assume that all the metal atoms/clusters become initially adsorbed onto the polymer surface before they eventually desorb again [101].

2.2.2 Condensation Coefficient

The ratio of the metal amount (number of atoms/clusters) that become trapped on the surface to the total amount of metal hitting the surface defines the condensation coefficient C (sometimes also called the sticking coefficient).

Zaporojtchenko et al. investigate the condensation coefficients C of different noble metals on various polymer surfaces (untreated as well as Ar^+ beam-treated polymer surfaces) in the initial stages of growth [101, 102]. By comparison of the metal quantity determined by XPS measurements with the nominal thicknesses measured by a quartz microbalance during deposition, they found that C depends strongly on the chemical composition of the polymer surface and can vary by more than three orders of magnitude at room temperature. The large differences in the condensation coefficient may be due to differences in the chemical interaction (i.e. favorable interaction with the polymer functional groups) [103]. But also other variables have influence on the sticking coefficient:

Copy for "Bibliothèque UCL"

- The condensation coefficient C decreases with increasing *substrate temperature*. Approaching the glass-transition temperature, the decrease of C is especially steep and above the glass-transistion temperature the condensation coefficient has a very low value. This decrease of C with the substrate temperature was related to morphological changes occurring at the metal-polymer interface [103].

- The polymer *surface energy* seems to play an important role: Smithson et al. found a relation between the surface energy and growth parameters for gold on different polymers. A low surface energy, which impedes macroscopic wetting of the surface, also impedes metal condensation onto the surface [104].

- The condensation coefficient was found to depend on the *deposition rate* of the metal [102, 105]. As the deposition rate increase, the number of diffusing metal adatoms on the polymer surface increase, which has an influence on the critical nucleus formation probability. In addition, a high evaporation rate impedes the embedding of isolated metal atoms into the polymer, which may affect the condensation coefficient.
  By contrast, Jones et al. have found that a slow evaporation is a more effective way to deposit gold onto a polymer than a faster evaporation. They argue that higher evaporation rate produces atom with higher kinetic energy, which then do not stick on the polymer surface [106].

- The *nucleation site density*, which can be considerably increased by ion beam treatment of the pristine surface, has also an influence on the condensation coefficient because the absorbed metal atoms can be trapped by a nucleation site before they desorb again [98].

- Furthermore the condensation coefficient depends exponentially on the *activation energy for adsorption and surface diffusion* [102, 107]. Because adsorption/desorption and surface diffusion are thermally activated processes, they depend strongly on the substrate temperature. However, metal atoms trapped at defects or at stable clusters are bound much more tightly and will need a much higher energy to leave the polymer surface. As a consequence, during metal growth on a polymer surface, metal

Copy for "Bibliothèque UCL"

atoms can only desorb as long as they diffuse on the free polymer surface and are not trapped at defect sites or in existing clusters.

- The *diffusion of metal atoms into the bulk* can falsify the determination of the condensation coefficient, because the metal quantity that is diffused into the bulk is maybe not detected by the analytical technique used for condensation coefficient determination [98].

2.2.3 Nucleation

There are two extreme cases for metal nucleation and cluster growth on a polymer surface. In the so-called *preferred* or *heterogeneous nucleation* the metal atoms are trapped at preferred sites. The nature of these sites is not yet known exactly: it may be impurities, terminal groups or attractive local arrangements of the polymer chains [108]. In *random nucleation*, also called *homogeneous nucleation*, metal clusters follow from critical clusters, which are formed by association of metal atoms encountering each other on their diffusion path. The critical cluster is defined as the number at which for the first time the cluster becomes more stable with the addition of just one more atom. For a given system, the critical cluster depends on temperature and supersaturation [99, 107]. In any case, all the metal atoms on the polymer surface that do not become trapped at defect sites or at critical clusters will eventually desorb from the polymer surface.

At the beginning of the deposition process, the cluster density increases steeply because new nucleation sites are formed and only little cluster growth occurs. The increasing cluster density enhances the chance that the diffusing atoms will be captured by an existing cluster before they can form a new nucleation site. At a certain point, the cluster density reaches a maximum before it decreases again, because growing clusters become close enough for coalescence [98, 106].

Analysis of the nucleation and growth behavior of metals on polyimide, on which the condensation coefficient is close to unity, revealed that the metal cluster density depends on the evaporation rate. A high deposition rate leads to a high stationary concentration of metal atoms diffusing on the sample surface and thus the probability for the formation of critical cluster increases. An increase in the deposition

Copy for "Bibliothèque UCL"

rate by a factor of 10 results in an increase in the cluster density by a factor of two at the same nominal metal-layer coverage [108]. So the dependence of the evaporation rate on the nucleation behavior indicates that the metal clusters on polyimide are formed by random nucleation [101, 102, 105].

In contrast to polyimide, the cluster density for other polymers (polycarbonate, polystyrene, Teflon), on which the noble metals/polymer interaction is even weaker, is significantly lower and independent on the deposition rate. This indicates that on these polymers, preferred nucleation at defect sites becomes the dominant mechanism for cluster formation. Furthermore Zaporojtchenko et al. found indications that preferred nucleation is often accompanied by a very low condensation coefficient [98].

The cluster density not only depends on the specific metal-polymer combination [105], but it can also be influenced in the initial stage of metal–polymer interface formation by the substrate temperature, by the number of diffusing adatoms on the polymer surface, by the surface diffusion coefficient and by the number of defects created on the polymer surface prior to metal deposition (e.g. ion bombardment) [102, 105, 109].

2.2.4 Metal/polymer interaction

The interface growth is governed by the competition between ad-atom/ad-atom and ad-atom/substrate interactions. In Figure 2.2, the three principal growth mode are shown: In the case where the adatom-adatom interactions are stronger than those of the adatom with the surface, three-dimensional adatom clusters or islands are formed on the surface, which finally coalesce at high metal coverages (*Volmer-Weber* growth). In the case where adatoms attach preferentially to the surface rather than on the already deposited atoms, atomically smooth and fully formed two-dimensional layers are created (*Frank-van der Merwe* growth). *Stranski-Krastanov* growth is an intermediary process characterized by both 2D layer and 3D island growth.

The interaction between moderately reactive metals (e.g. Cu, Ag, Au) and polymers is generally very weak in comparison to the strong metal-metal binding forces. As a consequence of the high cohesive energy

Copy for "Bibliothèque UCL"

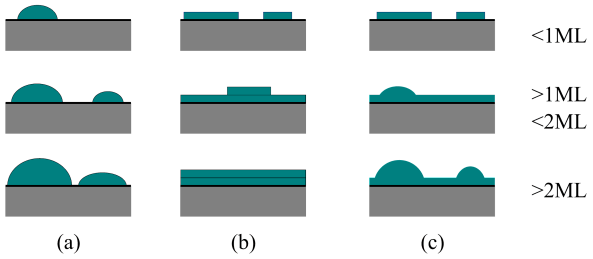


Figure 2.2: *Schematic cross-section views of the three primary modes of thin film growth: (a) Volmer-Weber (island formation), (b) Frank-van der Merwe (layer-by-layer), and (c) Stranski-Krastanov (layer-plus-island). For each growth mode different amounts of surface coverage (expressed in monolayer (ML)) are shown.*

of metals, which is typically 2 orders of magnitude higher than that of polymers [110, 111], the metals of low reactivity do not wet untreated polymer surfaces and exhibit a Volmer-Weber growth mode.

By dint of angle resolved XPS measurements on in-situ thermally evaporated Au onto polycarbonate film, Patnaik et al. have observed a new $C1s$ feature at a binding energy of 282.6 eV. This observation of the negative shift of the $C1s$ level at 85° electron take-off angle is interpreted as a weak Au $\longrightarrow$ C=O charge transfer type interaction by a π back bond [112]. Due to the facts that this new $C1s$ feature is not observed at 0° electron take-off angle and that at this angle also no changes on the $O1s$ signal have been observed, it indicates that the metal interacts predominantly with the carbonyl carbon. These angle-resolved XPS analysis of in-situ Au-metalized PC substrate did not provide an indication for a direct bonding of the metal on the polymer chain, so that no strong metal interaction with the polymeric backbone, which would lead to an organometallic complex formation, occurs.

The same group reveals by XPS depth profiling with 3 keV Ar^+ ions that the interface between the Au film and the PC substrate is sharp covering a few monolayers [102]. By the means of these sputtering experiments, Patnaik et al. argue that the growth of Au on PC, in contrast to the Volmer-Weber growth, proceeds by metal monolayer

Copy for "Bibliothèque UCL"

deposition followed by cluster growth on the Au, which is already weakly bonded to the C=O carbon of the polymeric backbone.

Depending on the surface treatment (low pressure air plasma or presputtering by argon ions) prior to the metal deposition, different bonding mechanisms were found, resulting in very different sticking probabilities [113].

2.2.5 Surface diffusion

The adatom diffusion on a flat surface or terrace, which never has been observed directly [99], is by far the most important kinetic process in film growth. The adatoms and the small metal clusters are mobile until they reach a certain size [114, 115]. The surface diffusion, which is usually treated as a random walk process, is a thermally activated process and therefore depends strongly on the substrate temperature. At elevated substrate temperature, the mobility of the smaller clusters on the polymer surface increases, so that the smaller clusters agglomerate to larger clusters [103, 105].

Calculations showed that the nucleation rate due to the random movement of absorbed atoms on the substrate surface is at least 10^2 to 10^3 times greater than the nucleation rate due to the direct addition of atoms to the critical nucleus from the vapor phase [116].

By comparing the cluster density of different metal at the same deposition rate, Zaporojtchenko et al. have estimated relative surface diffusion coefficient D_s at room temperature [98]:

$$D_s(Ag) : D_s(Cu) : D_s(Au) = 100 : 1 : 2$$

2.2.6 Structure of the metallic deposit

The bonding between metal atoms and the surface determines the structure of the metal film. In real growth, atoms are randomly and continuously deposited on the surface, and an adatom reaching an island will attempt to relax locally in order to find an energetically more favorable configuration. The 'Hit-and-stick' growth mechanism, where no local relaxation and therefore fractal growth occurs, can be ruled out for the noble metal deposition on polymer substrate [99]. As the

Copy for "Bibliothèque UCL"

cohesion forces between metal atoms are generally stronger than the adhesion forces between metal atoms and the polymer surface, the metal will form clusters on polymer surfaces.

Zaporojtchenko et al. showed by TEM and AFM measurements that the evaporated metals (Au, Ag and Cu) initially form discontinuous layers consisting of three-dimensional spherical clusters on different polymer substrates. In other numerous articles the formation of small metallic clusters were confirmed by different analytical techniques [100, 104–106, 115, 117–122]. The rate of metal evaporation was found not to affect the structure of the metal film on polymer surfaces [106]

In the initial stages of metal deposition, the cluster density increases rather than the individual clusters size. In a second stage, when the diffusing atoms (or small individual clusters) at the surface will be captured by an existing cluster before they form a nucleation site, the clusters can grow in size. The cluster growth occurs either by the trapping of metal atoms diffusing on the polymer surface or by direct deposition from the vapor phase [102]. The high cohesive energy between the metal atoms inhibits the cluster from dissociation [99].

At higher metal coverage, the clusters can touch each other, so that they coalesce into larger islands. Due to the liquid-like coalescence, the islands have an asymmetric and irregular form [98, 100, 104, 106, 115]. The evolution of the cluster size distribution, which is well approximated by an asymmetric distribution, is consistent with a coalescence mechanism of clusters [115]. Charton et al. observed that the surface coverage grows very rapidly with increasing film thickness. As the surface coverage reaches a value around 0.9, this growth is appreciably reduced until a closed film is formed [123].

At further metal deposition times, when a continuous coverage is already formed, the presence of regions with lower gold thickness were observed. These regions, gradually disappear at larger deposition times. Furthermore these thin metallic layer copies the substrate surface relief [121, 122].

Although some publications mention a spherical nature of the metallic clusters on all polymer substrate at the beginning of the deposition [98, 115, 117, 124–126], it seems more realistic to consider a more ellipsoid cluster shape with the symmetry axes parallel with the substrate plane [106, 127]. This ellipsoid shape is generated by

Copy for "Bibliothèque UCL"

cluster surface tension where metal-metal interaction between atoms dominates the metal-substrate interaction [110]. Another group makes the assumption, that the clusters become flat due to high momentum of the cluster impact on the substrate and the liquid-like properties of the clusters [100]. In contrast to these flat metal islands, the results of Smithson et al. pointed out that the islands have a higher vertical aspect than for hemispherical-type clusters [104]. In any case, from the top view, all ellipsoid shaped clusters are round, which indicates that the equilibration time for the shape of gold particle is less than the mean time between coalescence events [115].

In contrast to the surface coverage, which increases at a similar rate on different polymer substrates, the density of particles and average size showed markedly different values. Smithson et al. correlated these differences to the surface energy of the polymer substrates [104]. They found out that the higher surface energy polymers began with more and smaller particles which then increased in size and coalesced into larger more intricately shaped particles as growth proceeded. Although the surface tension of the polymer depends on the molecular weight M_w, no significant dependence on cluster density and size on the molecular weight has been observed [126, 128]. Furthermore, differences in the surface structure of plastics, which cause variations in the adhesion force between metal atoms and the substrate, lead also to differences in the density and size of the metal clusters [106]. In addition, the cluster density and size can be attributed also to the deposition parameters, the particular metal-polymer combination [105], molecular structure of the surface [129] and the substrate temperature [108, 115].

2.2.7 Diffusion into polymer bulk & Annealing

Especially at low deposition rates (less than one monolayer per minute) and at the early stages of the nucleation process, a large fraction of isolated metal atoms is able to diffuse into the polymer [97, 98, 105]. Later arriving atoms become more and more trapped when the cluster density on the surface increases. At higher deposition rate, the diffusion into the bulk usually plays only a minor role, because the pronounced aggregation tendency of metals and their high mobility on polymer surface result in cluster formation that impedes the embedding of the metal. Furthermore, the diffusing metal atoms in the polymer bulk can

Copy for "Bibliothèque UCL"

agglomerate into clusters when they meet, so that further embedding in the bulk is stopped. Also a predeposition of a small amount of reactive metals (e.g. chromium), a predeposition of noble metal clusters or an increase of the number of nucleation sites also impede the diffusion of metal atoms into the polymer bulk [97, 130, 131].

In contrast to the metal deposition onto polymer, no diffusion of gold or polymer at all occurs and an abrupt interface is formed when an oligomer is stepwise deposited on a clean Au polycrystalline foil. Here too, the weak interaction between the Au atoms and polymer as well as the high cohesive energy of the gold inhibit the diffusion of the metal atoms into the polymer film [132].

It has been realized that the physical properties (e.g. viscosity, glass-transition temperature) of polymers near the surface or at interfaces are different from those in the bulk; this is the so-called surface or interface effect. It results from the surface forces that alternate the chain packing and segmental motion [126, 133]. The glass-transition temperature T_g is known to be one of the most fundamental properties of a polymer. Exceeding this temperature T_g, a glassy polymer undergoes a phase transition from a more rigid state (the glass state) to a softer state (the rubbery state).

Results from molecular simulation and theoretical calculations predict that the polymer surface becomes either softer [134, 135], or harder [136] than the bulk. Experimental determined glass-transition temperature on the polymer surfaces shows also controversial behavior: Either T_g increases [137], decreases [133, 137, 138] or does not change at all [139] at the surface in comparison with the bulk glass-transition temperature. At a first view, these contradictory behavior of the glass-transition temperature may be surprising, but such differences may be due to differences in the depth resolution of the applied method, in the applied heating rate, in the kind of analyzed interface (polymer/vacuum or polymer/air), and in the molecular weight and its distribution [126].

If one makes the intuitive assumption that the polymer segments near the free surface have a higher mobility due to the release of steric constraints, then the glass-transition temperature T_g is lowered at this near-surface layer. This assumption is supported by results, which give direct evidence that the glass-transition temperature is significantly lowered on the surface of different polymers (polycarbonate,

Copy for "Bibliothèque UCL"

polyimide and Teflon) [98]. On polystyrene surfaces, the glass-transition temperature was found be be substantially lowered until a depth of ≈ 500 Å [133]. Furthermore, measurements on polystyrene pointed out that the glass-transition temperature depends on the film thickness for very thin films [137, 140, 141], on the interfacial energy [137] and on the molecular weight [126, 131, 142].

For embedding of metal clusters in polymers, the reduction in Gibbs free energy and thus the lowering of the surface energy is the driving force [131, 143]. Due to the high cohesive energy of metal, the surface Gibbs free energy of these metal particles is also high. By embedding, the Gibbs free energy of a metal particle inside the polymer is reduced. This happens when the surface tension γ_M of the metal particles exceeds the sum of the interfacial tension γ_{MP} and the polymer surface tension γ_P [144, 145]:

$$\gamma_M > \gamma_{MP} + \gamma_P$$

Although the cohesive energy of polymers is much lower than that of metals, the γ_P is very small in comparison to γ_M, so that embedding is only possible when the mobility of the polymer chains is sufficiently high [126]. At temperature far below the bulk glass-transition temperature $T_g(bulk)$, where the polymer surface has a such high viscosity surface, no embedding of clusters occurs in a typical experimental time scale. When substrate temperature of a glassy polymer approaches the glass-transition temperature, the viscosity starts to decrease, long distance chain mobility becomes possible and the clusters embedding becomes faster. Large clusters will embed only at temperatures close to or higher than the glass transition temperature T_g of the polymer, which is not the case in this work [126, 143].

If the particles (atoms or clusters) are completely embedded, they stay in a region close to the surface, because there is no more driving force for further embedding [98, 126]. They keep diffusing through the bulk by Brownian motion and they can agglomerate to larger clusters even below the polymer surface [124, 131]. The diffusion into the bulk can be enhanced substantially by ion bombardment, deposition at elevated substrate temperatures and by using low deposition rates. Furthermore, atoms deposited by sputtering or evaporation diffuse faster than those prepared by CVD technique and the diffusion coefficient is larger for smaller atom sizes [112, 131, 146].

Copy for "Bibliothèque UCL"

During an annealing treatment, the average size of the discrete gold particles significantly increases [115]. Furthermore, the formation of clusters and the embedding process can occur simultaneously [130]. It should be mentioned that, the apparent diffusion of metal inside PET under annealing conditions is partly due to the diffusion of oligomeric species upon the metallic clusters, where the metallic clusters may play the role of nucleation agent for oligomer crystallization [147, 148]. However, with small amounts of deposited metal on polymer without annealing treatment, it is impossible to distinguish between the embedding processes of the metallic clusters and the diffusion of polymer chains over the metal.

Copy for "Bibliothèque UCL"

Chapter 3

Overview of the utilized Techniques

3.1 Introduction

Nowadays the industries not only develop new materials in order to satisfy the claims of the society but also change and optimize the properties of existing materials. Particularly the surface properties (adsorption, moistening, hydrophilic/hydrophobic behavior, adhesion, biocompatibility, ...) define the application in the industries (microelectronics, metalworking, packing, aerospace, sanitary industries, ...).

In addition to the new production methods for those new materials, also the different analysis techniques must be improved or new characterizing techniques must be developed. To understand and subsequent to control, to optimize and to forecast the surface properties of the material it is inescapable to characterize the surface not only in the macroscopic range but also down to the atomic scale. For an exhaustive characterization of the properties of newly developed material, supplemental to the chemical composition, the molecular structure, mechanical and thermodynamic properties, also the high spatial resolution of these properties should be considered. Because no analytical techniques can fulfill all the requirements, a combination of

Copy for "Bibliothèque UCL"

different analysis techniques is involved to characterize the sample and make a relation between microscopic and macroscopic properties.

Analytical Technique	Detected Signal	Detected Information	Detection Limit	Depth Resolution	Lateral Resolution
D-SIMS	Secondary ions	$H-U$ Small clusters	max. ppm-ppb	$1-30$ nm	>50 nm
S-SIMS	Secondary ions	$H-U$ Molecular species	max. ppm	<5 nm	>100 nm
Auger	Auger electrons	$Li-U$	0.3-1at%	$2-6$ nm	<20 nm
XPS	Photoelectrons	$Li-U$ Chemical bonding	0.3-1at%	≈ 10 nm	$0.01-2mm$
SEM & EDX	Secondary e^- & backscattered e^-	-	-	-	1nm
	X-Rays	$B-U$	0.1%	$0.3-5$ µm	0.5 µm
TEM & EDX	Transmitted e^- & secondary e^-	-	-	-	<1 nm
	X-Rays	$B-U$	0.5%	-	10 nm
AFM	Topography	-	-	0.01 nm	$1.5-5$ nm

Table 3.1: *Overview of the capabilities and limitations of surface-analytical techniques available at the CRP-Gabriel Lippmann.*

In Table 3.1 an overview of different analytical techniques, which are available in the Centre de Recherche Public Gabriel Lippmann, are listed. In this work, where the surface properties of the samples are of interest, mainly the following analysis techniques are utilized:

- Static Secondary Ion Mass Spectrometer (S-SIMS) permits to observe the emission of secondary ions as a function of the evaporated metal quantity (↪ *Chapter 3.2*).
- Atomic Force Microscopy (AFM) allows to characterize the microscopic morphology of the metal, which is evaporated onto the polymer surface (↪ *Chapter 3.3*).
- X-ray Photoelectron Spectroscopy (XPS) is used to determine the exact amount of deposited metal as well as to find out the macroscopic coverage of the evaporated metal (↪ *Chapter 3.4*).

Copy for "Bibliothèque UCL"

- Secondary electron microscopy (SEM) and transmission electron microscopy (TEM) allows to image the structure of the evaporated metal (↪ *Chapter 3.5*).

In this chapter, the theoretical and physical basics of the utilized analysis techniques for this work are briefly described.

3.2 Secondary Ion Mass Spectroscopy (SIMS)

3.2.1 Introduction

The sputtering of neutrals and charged particles as a results of a primary particle bombardment has been reported by J.J. Thomson at the beginning of the 20th century [149]. It last until the 1960's that the groups of Castaing and Slodzian had independently developed the first complete and commercially exploited SIMS instrument. In 1969 the static SIMS was introduced as a surface analysis technique by Benninghoven et al. [150, 151][152, p.672].

The technique of secondary ion mass spectrometry is able to measure trace levels of nearly all elements in the periodic table. Lateral and depth distributions (microanalysis) of elements and organic molecules within a sample can also be provided by a SIMS analysis [153–156]. Beside the electronic materials industries [157] and the geological community [158, 159], the interest in the SIMS analysis increases also in the biological field in the last years [160–166]. The major domain of static SIMS is still the characterization of polymers and their additives [11, 36, 69, 167–173], the efficiency of surface treatments [174–177] and the determination of (surface) contamination [178–181].

Common point to all analysis with a secondary ion mass spectrometer is that the sample, situated in an ultra high vacuum chamber, is bombarded with an energetic beam of ions (↪ *Figure 3.1*). When these primary ions penetrate into the sample, they interact with the atoms and molecules within the sample (↪ *Chapter 3.2.2*). Thereby the primary ions lose their energy and the target atoms are set in motion. If the transmitted energy to an atom of the sample is sufficient, a displacement of the atom in the solid or an ejection into the vacuum of particles could occur. Some of these sputtered secondary particles are either directly

Copy for "Bibliothèque UCL"

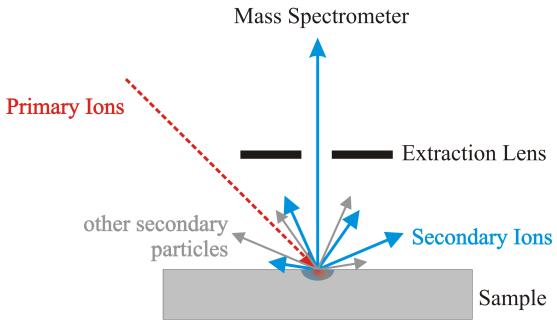


Figure 3.1: *Principle of the SIMS technique: Impinging primary ions interact with the atoms in the sample and the hereby created secondary ions are analyzed in a mass spectrometer.*

ionized or are ionized above the sample surface (↪ *Chapter 3.2.3*). These secondary ions are separated by mass in the spectrometer and finally are counted by a detection system. If the internal energy of the emitted clusters is to large, they can be dissociated into smaller fragments before they reach the detector.

In the following sections an overview of the processes occurring in the target during ion bombardment and the related theoretical models are briefly presented. Thereafter, in Section 3.2.4, the distinction between dynamic and static SIMS is explained with the primary ion fluence and the damage cross-section. In the subsequent Section 3.2.5 the cause of non-quantitative analysis in secondary ion mass spectrometry is outlined. In a later chapter, the instrumental setup is discussed (↪ *Chapter 4.3*).

3.2.2 Energy deposition and secondary particle emission

Primary ions approaching the sample surface may first be neutralized by surface-particle electron transfer. Particles penetrating into a sample interact with the atoms of the sample and transfer their energy in a great number of collisions to the target atoms [182]. These numerous interactions with atoms and electrons provoke a zigzagging trajectory of the primary ions through the solid. Hereby the ions loose quasi-continuous their kinetic energy by elastic collisions with the atoms

Copy for "Bibliothèque UCL"

and inelastic collisions with the electrons within the target. These energy depositions induce changes in the atom structure of the target and thus damage the sample (↪ *Chapter 3.2.4*). The energy lost dE along the distance dx is called "Stopping Power" and depends mainly on the mass, charge and velocity of the impinging ion as well as on the mass, binding energy and density of target. In SIMS analysis, where the energy of the primary ions normally do not exceed $30\,keV$, the primary ions predominantly interact with the nucleus of the target atoms, so that the interaction can be treated as elastic collisions between two heavy particles.

Numerous models describe this energy deposition and the relating processes which lead to the emission of secondary particles from near-surface layers. Beside the models briefly described hereafter, there exist other more or less complex theories of emission of secondary particles, which play a major role at higher primary particle energy (Coulomb explosion) [183] or in cluster primary ions bombardment [184–186].

A. von Hippel and C.H. Townes postulated that the entire energy of the primary impinging particle is dissipated as heat in the solid, and thus a small hemispherical volume around the impact point is brought to elevated temperature for a short time [187, 188]. From this hot spot, thermal evaporation of the target material can occur.

By contrast, M. Thompson and R. Nelson developed a thermal model where only a very small quantity of energy is transfered to the crystal lattice [189]. Thereby the energy is dissipated in thermal vibrations of the lattice, which brings a small target volume to temperature at which thermal evaporation could take place.

Based on Boltzmann's transport theory, P. Sigmund introduced the concept of collision cascade [191–193]. If the transfered energy and momentum between the primary bombarding ion to the target is large enough, the target atom will recoil and could provoke other secondary recoils by binary collisions, so that a collision cascade is formed (↪ *Figure 3.2a*). A part of the recoiled particles, which reached the samples surfaces, can be emitted to the vacuum, when the energy of these particles exceed the surface binding energy.

P. Sigmund also reintroduced the concept of the thermal spike [192]. In his concept, a spike is a collision cascade of such high density that the

Copy for "Bibliothèque UCL"

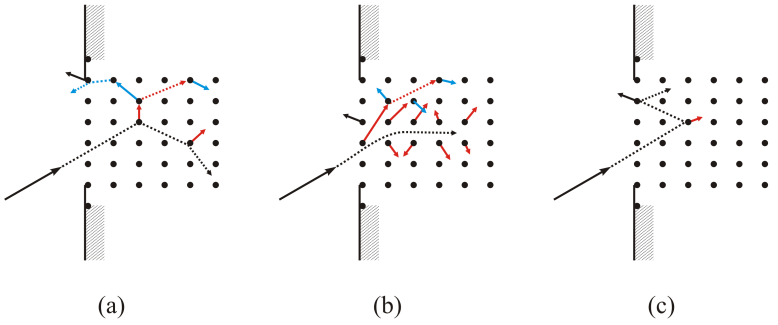


Figure 3.2: *Different Models of energy deposition: a) Collision Cascade - b) Hot Spot - c) Single-knock out. For more details refer to Section 3.2.2 (adapted from [190] ([191]).*

individual linear collision cascades spatially overlap, so that every atom in a certain volume is set into motion. This excited volume behaves like a dense gas at high temperature (↪ *Figure 3.2b*).

Another model, called "single knock out" also assumes binary collisions between the impinging ion and the target atom [191]. In this model, the transfer of energy and momentum of the primary particle leads to a direct emission of the struck target atom (↪ *Figure 3.2c*).

Qualitatively these three models can be ordered as follow: The single knock-out model describes the particle emission in the low and middle eV range. The linear collision cascade and the thermal spike model explain the sputtering behavior in the keV range. The difference between these last two models only consists in the deposited energy density and of the number of participating target atoms.

To characterize the erosion in the so-called sputtering process, one defines the sputter yield Y as the number of sputtered particles per impinging primary ion:

$$Y = \frac{\text{number of the emitted particles}}{\text{number of impinging ions}} \tag{3.1}$$

Copy for "Bibliothèque UCL"

3.2.3 Secondary Ion Formation

Beside secondary electrons, the major part of the sputtered particles are neutrals ($\approx 98\,\%$). Accordingly only a minor part of the emitted secondary particles are elementary positively or negatively charged. Because only this minor part of the emitted particle can be detected in SIMS, an important factor is the ionization probability:

$$\epsilon^{\pm} = \frac{\text{number of pos. or neg. charged particles}}{\text{number of emitted particles}} \tag{3.2}$$

Although several models describe qualitatively the ionization of the emitted particles exist, none of them can explain quantitatively the molecular spectra. In the following paragraphs the most common ionization models are briefly described.

3.2.3.A Bond Breaking Model

This model, proposed by Slodzian [194], is based on the assumptions that a molecule $\mathcal{AB}$ exists in the solid as $\mathcal{A}^+\mathcal{B}^-$ (ionic bonding) and that the molecule leaves the sample surface in an excited autoionizing state. Depending on the particle-surface distance, at which the neutral and the ion potential curves cross each other, the extraction of $\mathcal{A}^+$ and $\mathcal{B}^-$ may be energetically more favorable than the ionization of $\mathcal{AB}$. This bond-breaking model describes the ionization behavior for ionic samples (e.g. salts) and partially ionic materials (e.g. metal oxides) [182, 195].

3.2.3.B Nascent Ion-Molecule Model

Another ionization model, based on the energy level-crossing processes, is the *nascent ion-molecule model* [196, 197]. Due to the high efficiency of the neutralization processes (deexcitation occurs within $10^{-13}\,s$), only a few particles can leave the solid in the ionic state, so that the ionization must occur above the surface ($\hookrightarrow$ *Figure 3.3*). In this nascent ion-molecule model, which explains the ion yield enhancement for metal oxides samples, the ions are formed whenever nascent ions pairs have sufficient energy to get ionized by minimal fragmentation or by breaking up into smaller ionized fragments above the surface.

Copy for "Bibliothèque UCL"

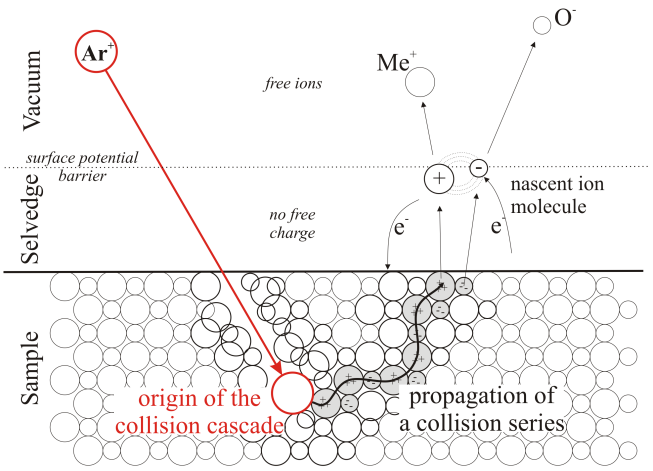


Figure 3.3: *Nascent Ion Model for metal oxides. As a result of the collision cascade, a neutral molecule leaves the surface and dissociates at some distance, producing a metal cation and an oxygen anion.*

3.2.3.C The Precursor-Model

Analysis of aminoacid layers on metal surfaces has led Benninghoven et al. to develop a model, that can explain the relatively high yield for molecules. The model is based on the following assumptions [21, 198, 199]:

- A preformed ion exists at the surface before the primary ion impinges on the surface.
- As a result of the rapid primary ion energy transfer into the solid (within 10^{-12} s), which limits the probability of thermal degradation and fragmentation, the precursor ion can be entirely ejected.
- The probability of retaining the initial charge of the original precursor ion is high.

The recoiling component of the cascade mechanism is assumed to generate an energy gradient at the surface around the point of

Copy for "Bibliothèque UCL"

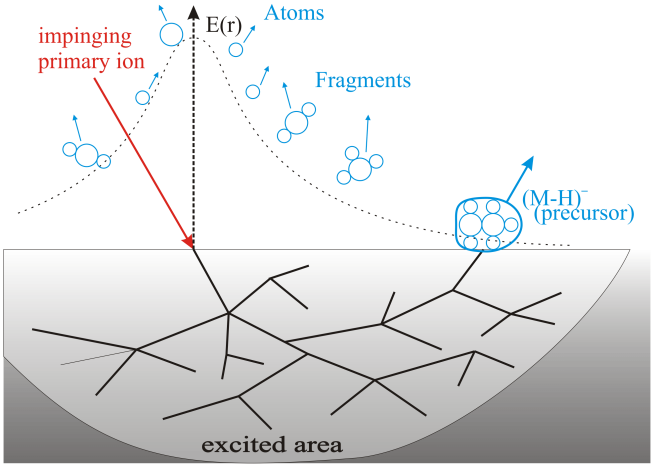


Figure 3.4: *Precursor model: The energy transfer to preformed ion (precursor) and the subsequent emission of parentlike secondary ions (adapted from [152]).*

impact (↪ *Figure 3.4*). In that central area, the energy transfered back to the surface species is sufficiently high to break inter- and intramolecular bonds. The molecules herein will be destroyed and/or emitted as atomic species or low mass fragments. At the boundaries of the excited area, the recoil energy is insufficient to break the intermolecular forces within the surface layer so that no emission occurs. Between these two extremes there is a zone where sufficient energy is transfered to eject the surface molecules.

3.2.3.D Desorption-Ionization Model

Based on the isomerization (loss of identity) of the input energy, Cooks et al. proposed a desorption-ionization model [200, 201]. They suppose that, in an early stage, fast thermal processes provoke atomic and molecular emission from the bulk solid. In a second step, fragments would be emitted by early collision cascade processes and through late thermal relaxation processes (↪ *Figure 3.5*).

Another important hypothesis of this model is the separation of the desorption and ionization steps, except for the preformed ions. Contrarily to the precursor model, it is supposed that the ionization of

Copy for "Bibliothèque UCL"

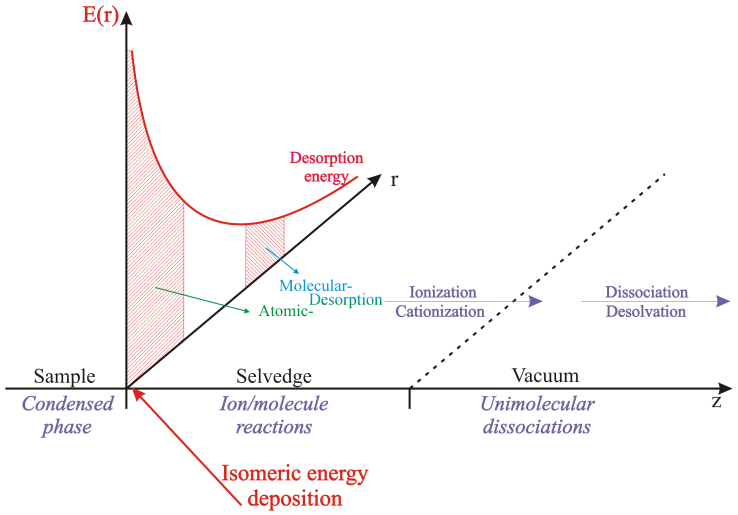


Figure 3.5: *Summary of the processes thought to occur in the Desorption-Ionization Model (adapted from [200]).*

most organic molecules take place in the selvedge either by ion-molecule interactions or by the ionization of the released neutrals in combination with secondary electron emissions. The major part of the detected fragments may result from the unimolecular decay of metastable ions in the vacuum.

3.2.3.E Ion Formation from Polymers

Due to the absence of a well-defined crystal orientation on polymer surfaces, the energy transfer mechanism between atoms and molecules during sputtering is not obvious. Therefore Vickerman et al. distinct in their model three different regions in which fragmentation and emission occur [33]:

- Close to the primary particle impact site and by analogy with the degradation due to radiation and pyrolysis, the primary ion interaction leads to polymer chain scissions and to the creation of radical sites (↪ *Figure 3.6a*).

Copy for "Bibliothèque UCL"

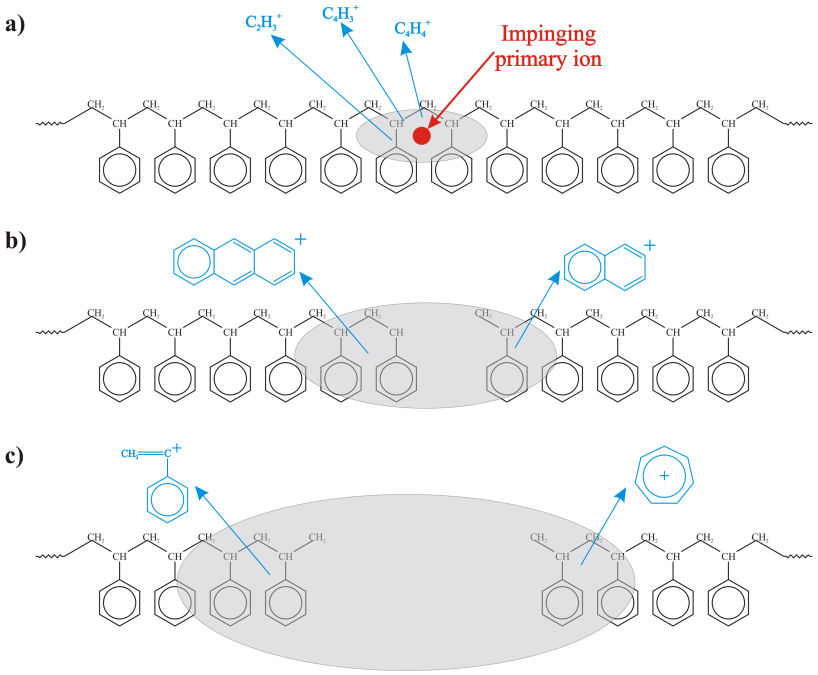


Figure 3.6: *Model for the formation of secondary ions observed in a polymer sample in SIMS (adapted from [33]).*

- Surrounding the impact area, in the zone with decreased energy density, structural rearrangements take place. The excess of deposited energy produces unzipping-type processes resulting in essentially neutral species emission. Some of these particles are ionized above the surface (↪ *Figure 3.6b*).

- Further away from the impact point, in the monomer region, where only a minimal energy for rearrangements is available, the ejection of monomers or minimally rearranged species prevails. This gives rise to larger and structurally most informative fragments (↪ *Figure 3.6c*).

Copy for "Bibliothèque UCL"

3.2.3.F Dissociation above the surface

Due to the nature of the emission process, the ejected molecular fragments often have en excess of internal energy. If this internal energy excess is sufficient, these fragments may dissociate in the vacuum before they could reach the detector. Such metastable reactions are described by the unimolecular reactions theory [202].

3.2.4 Dynamic and Static SIMS

Due to the interaction of the impinging primary ion with the target atoms (↪ *Chapter 3.2.2*), a damage of the sample occurs along the primary ion trajectories. The size of this damage depends on the energy which is deposited into the target by the ion. The surface area corresponding to that perturbation region of the sample, created by an individual primary ion, is called damage cross-section σ (↪ *Figure 3.7*).

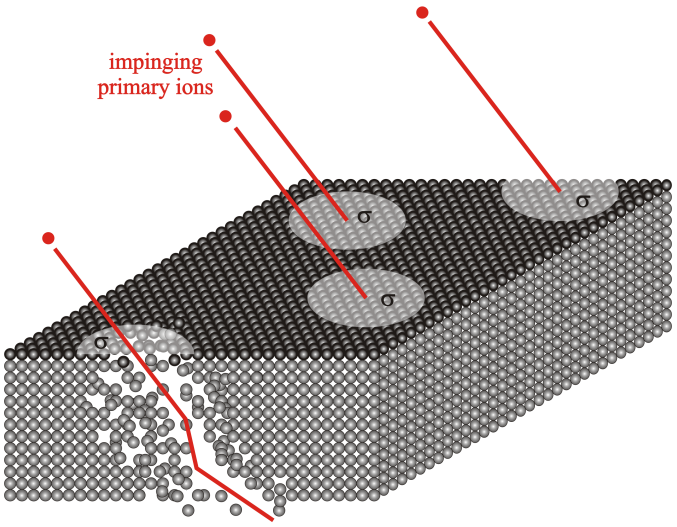


Figure 3.7: *The impact of a primary ion on a surface results in the emission of secondary particles and the damage of the surface molecules in an area σ around the impact point (adapted from [152]).*

Copy for "Bibliothèque UCL"

One parameter which is related to the total deposited energy and thus the damage of the sample surface is the primary ion fluence:

$$\text{primary ion fluence } D_p = \frac{\text{number of impinging ions}}{\text{bombarded surface}} \tag{3.3}$$

The primary ion fluence D_p (unit: $\frac{ions}{cm^2}$) can be calculated by the current of the primary ions I_p hitting the sample:

$$D_p(t) = \frac{I_p \cdot t}{e \cdot A} \tag{3.4}$$

with e the elemental charge, A the bombarded surface and t the time of the ion bombardment.

Depending on the degree of the sample surface damage, two different analysis modes can be distinct in SIMS: static SIMS and dynamic SIMS. The assumption for static SIMS is that the damage cross-sections of the primary ions do not overlap and thus every primary ion hits a pristine area of the sample [152, p.671]. This means that the coverage $\theta(t) = \theta(t_0)e^{-\sigma \cdot D_p(t)}$ of the intact surface monolayer only slightly vary, so that the limit for static SIMS analysis can by expressed by the following equation:

$$D_p(t) \cdot \sigma \ll 1 \tag{3.5}$$

Considering a typical value for the damage cross-section of an individual ion ($\sigma \approx 100\,nm^2$), the primary ion fluence should not exceed $10^{13}\,\frac{ions}{cm^2}$ in order to leave the surface damage low during the whole analysis. For typical static SIMS analysis conditions an analysis time of $100 - 1000$ s is used in order to minimize the damage of the sample surface so that the analysis of organic samples become possible.

By exceeding this static SIMS limit (↪ *Equation 3.5*), the detected signal will contain less and less molecular information of the original sample. Because the molecules are all damaged by the previous primary ion impacts, only elemental information of the analyzed sample volume can be determined in the dynamic SIMS mode.

Beside the damage of the surface due to the impinging ions, damage induced by the electron flood gun, used for charge compensation during SIMS analysis, can occur. Gilmore et al. show that the damage by those electrons can not be negligible during SIMS analysis of insulating samples [58, 59].

Copy for "Bibliothèque UCL"

3.2.5 Matrix-Effect

The major drawback of the SIMS analysis technique is that the quantitative interpretation of the results is difficult and not always possible. Due to the fact that the ionization efficiencies of atoms an molecules can variate, depending on their chemical environment within the analyzed material, by several order of magnitude, an eventual proportionality factor between the detected ion intensity and the element concentration in the sample strongly depends on the given matrix [203]. However, with standardized sample, i.e. using a standard sample with known concentrations and a composition (matrix) similar to the unknown sample, a quantification is still possible (semi-quantitative analysis). Also the use of the analysis mode known as MCs^+, either by use of a Cs^+ primary ion gun or by evaporated neutral cesium on the sample prior the analysis, will reduce considerably the matrix effect, but it still persists [204, 205]. In the project "Storing Matter", another method for getting rid of this matrix effect is under examination at the CRP-Gabriel Lippmann [206–208].

3.3 Atomic Force Microscope (AFM)

3.3.1 Introduction

The atomic force microscopy, which belongs to the category of Scanning Probe Microscopes (SPM), was developed in 1986 by G. Binnig et al. [209].

The acquisition of the surface topography or the mapping of other physico-chemical properties is done by detecting all forces leading to a deflection of an elastic cantilever during scanning the sample surface with it (↪ *Chapter 3.3.2*). Contrarily to the Scanning Tunneling Microscope (STM), the AFM has the advantage that it is not restricted to the analysis of conducting materials, but it is able to characterize the surface of semi-conductors and non-conducting samples. Beside AFM and STM, it exists other scanning probe microscopes; each of them could detect specific physico-chemical property: Lateral Force Microscope, Electrostatic Force Microscope, Magnetic Force Microscope, etc..

Copy for "Bibliothèque UCL"

The ability of determining the spatial distribution of physico-chemical properties (topography, adhesion, friction, elasticity, electrochemistry, ...) results in an increasing interest of SPM analyses in different scientific fields (physics, chemistry, biology, material science) [210–213]. Another advantage of the AFM is that it can be used in different environments (atmosphere, vacuum, liquid) [214, 215] and so biological and chemical process can be observed in real time [216]. In addition to its imaging capabilities, the AFM can be used as a tool for nanolithography. This can be done mechanical or thermal scribing with the tip the sample surface [217–220]. Even nanometric structures can be deposited electrochemically with the tip in an aqueous solution [221, 222]. In a later Chapter 4.4 the instrumental setup is discussed.

3.3.2 Tip-Sample interactions

When the SPM tip is brought into proximity of a sample surface, forces between the tip and the sample lead to a cantilever deflection according to Hook's law. With an AFM, forces down to $10^{-9}\,N - 10^{-12}\,N$ could be detected. The acting forces, which are divided in repulsive and attractive forces, can be described by using an empirical potential (↪ *Figure 3.8*).

Attractive Forces - Van der Waals: The Van der Waals force is a long-range force which relies on interactions between induced dipoles. In the range up to ~ 150 Å the Van der Waals interaction show a r^{-6} behavior. Due to the long interaction range of the Van der Waals force and the finite size of the tip, the forces between all interacting atoms must be summed up to get the complete attractive force.

Repulsive Forces: At very small distance (few Å) between tip and sample surface the Coulomb repulsion of the overlapping orbits of two atoms, leads to a repulsive force. Contrary to the attractive forces, these repulsive forces have a small interacting range (< 3 Å), hence only a small volume of the tip interacts in that way with the sample surface. This is the main reason why the AFM is capable to image the topography of a surface in a subnanometer scale.

Copy for "Bibliothèque UCL"

Other Forces: Depending on the sample, the utilized tip and the measuring mode, additional forces appear and can be measured. Hereafter, a selection of those forces are listed:

- Due to the scanning of the tip over the sample surface, lateral forces occur, which twist the cantilever. This friction force appears mainly in the contact mode (↪ *Chapter 4.4.3*).
- If a voltage $U(t)$ is applied between the tip and the sample, local dielectric properties of the samples could be measured by using a cantilever and tip with a conducting coating. This is called Electric Force Microscope (EFM).
- By using a tip with a ferromagnetic coating, the tip mainly interacts with the magnetic field of the sample. As in EFM, in the magnetic force microscope (MFM) the measurements are also done in the two pass mode.

Capillarity: Under normal atmosphere conditions a thin film of water is present at every surface. The thickness of this film can reach some nanometer and depends on the humidity and on sample surface properties. If the tip approaches the surface a meniscus between the tip and the surface is created. In order to minimize the surface tension of the meniscus, an additional attractive force appears (see inset 4 in Figure 3.9). This force can reach important values and can be avoided if the AFM analysis is done in ultra high vacuum or in liquid environment.

The numerous attractive and repulsive interactions rule out the formulation of a global interaction potential. Consequently, an empirical potential is used for mathematical description and for simulation of the tip-surface interaction. The most known formulation of the interaction potential is the Lennard-Jones potential (↪ *Figure 3.8*), which is described by the formula:

$$U(r) = 4\epsilon \left(\left(\frac{\zeta}{r} \right)^6 - \left(\frac{\zeta}{r} \right)^{12} \right) \tag{3.6}$$

The first term of Equation 3.6 describes the long-distance attraction caused basically by a dipole-dipole interaction, and the second term

Copy for "Bibliothèque UCL"

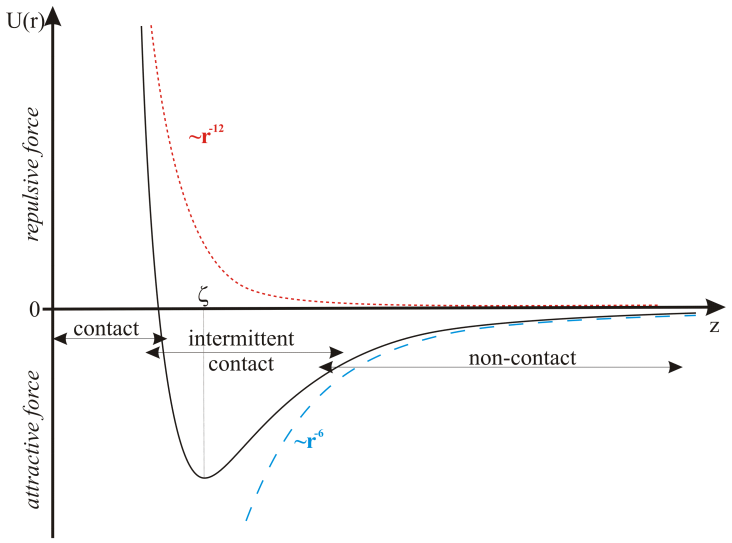


Figure 3.8: *The Lennard-Jones potential (black line) is the sum of the attractive potential (blue) and the repulsive potential (red). Furthermore the regions for the different type of AFM measurements, which are described in Chapter 4.4.3, are indicated in the graph.*

takes into account the short range repulsion due to the Pauli exclusion principle. The parameter ζ is the equilibrium distance between atoms at which the potential value is minimal ($\hookrightarrow$ *Figure 3.8*).

The plot of the cantilever bending ΔZ due to the interaction forces as a function of the tip-sample distance z is called force-distance curve ($\hookrightarrow$ *Figure 3.9*). Far away from the sample surface, the tip is not submitted to any forces, so that the cantilever is not bended ($\hookrightarrow$ *Figure 3.9(pt 1)*). During the approach to the surface the tip gets in the reach of attractive forces, which bend the cantilever toward the surface. If the probe further approaches, the tip experiences a repulsive force and the cantilever bends in the opposite direction ($\hookrightarrow$ *Figure 3.9(pt 2)*). The slop of the force-distance curve is determined by the elastic properties of the cantilever and the sample.

Copy for "Bibliothèque UCL"

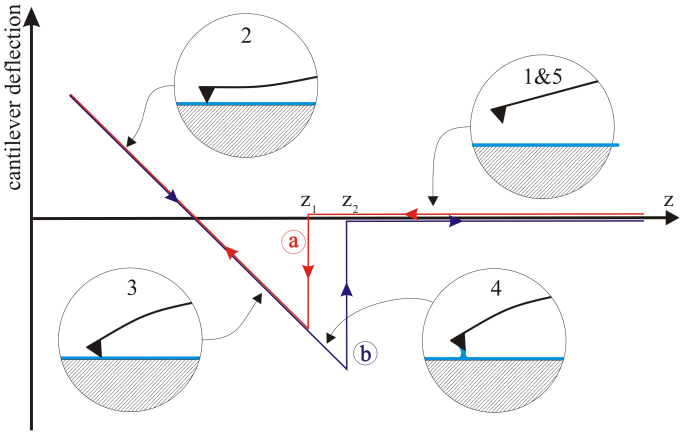


Figure 3.9: *A typical force-distance curve $\Delta Z = f(z)$. The red line shows the approach of the tip to the sample and the blue line indicates the acting forces on the tip when it is retracting from the surface. The inlets show the bending of the cantilever at different points of the curve. For a more detailed description see the text in Chapter 3.3.2.*

When the tip is then retracted the tip rests sticked onto the sample surface until the "snap-off" distance z_2 due to the long range interaction of the attractive forces ($\hookrightarrow$ *Figure 3.9(pt 3)*). If the interactions are perfectly elastic, the force-distance curves of the forward and the reverse motion of the tip coincide. The formation of a meniscus between the tip and the sample leads to an additional attractive force ($\hookrightarrow$ *Figure 3.9(pt 4)*), which results in a larger snap-off distance $z_2 > z_1$ ($\hookrightarrow$ *Figure 3.9(pt b)*).

By the shape of the force-distance curve it is possible to obtain information on the tip-surface interaction and to study the local sample stiffness as well as the spatial distribution of the adhesion forces [223].

Copy for "Bibliothèque UCL"

3.3.3 Image artifacts

The finite size of the tip apex is one of the drawbacks of all STM. Cavities smaller than the tip apex cannot be imaged correctly and heightenings are measured wider (↪ *Figure 3.10*).

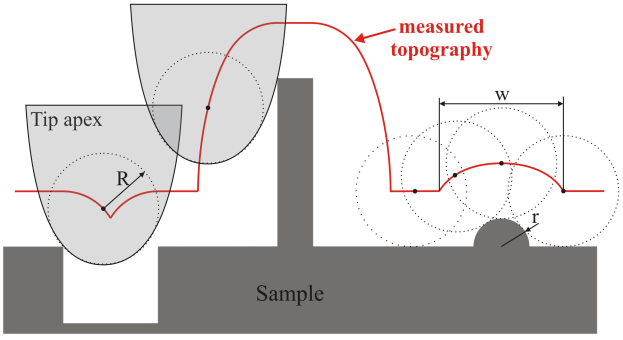


Figure 3.10: *Formation of artifacts in an AFM measurements due to the tip apex dimension and size of the surface structures. The measured topography of the sketched sample is drawn in a thick solid line. The measured elevation is broader than the real structure. The depth of too small cavities are not measured accurately.*

A rough estimation of the width broadening of an object is done with the assumption of spherical tip and a hemispherical structure. The observed width w of the structure could be calculated with the formula [224]:

$$w = 2\sqrt{2rR + r^2} \tag{3.7}$$

where R and r are the radii of the tip apex and sample structure respectively.

Furthermore the imaged structure of the sample surface depends on the irregular tip form, which wears off with progressing measurement. The size and form of the tip apex leads to essential deterioration of the spatial resolution and to significant distortions in SPM images.

Other image artifacts are related to the piezoceramics, which are required for the tip scanning over the sample. Nonlinearity of

Copy for "Bibliothèque UCL"

the piezoelectric properties and the presence of hysteresis during the distortion of piezoceramics leads also to image distortions.

External vibrations constitute also unwanted influences on SPM images. Therefore a protection against vibration is necessitated. External mechanical vibrations with frequencies coinciding with the resonant frequencies of the SPM instrument results in fluctuations of the tip relatively to the sample. This can be perceived as a parasitic periodic noise deforming and dithering the SPM images of samples surface. To reduce the influence of external vibrations the measuring heads are made of massive metal. Another, additional measure to reduce external vibration influences on the SPM image is to put the measuring head of the SPM in a vibration-insulating system.

3.4 X-Ray Photoelectron Spectroscopy (XPS)

The photoelectron spectroscopy, based on the photoelectric effect (↪ *Chapter 3.4.1*), is a method to determine the elemental composition as well as the type of chemical binding in the sample surface.

3.4.1 Photoelectric effect

Photons with energies higher than the work function Φ and up to $10\,keV$ interact with the atomic electrons primarily via the photon absorption process (↪ *Figure 3.11(a)*). Thereby all the energy $h\nu$ of the photon is transfered to a bonded electron. This energy transfer arises the electron to a free state and, near the surface, the electron can be ejected (↪ *Figure 3.11(b)*). The kinetic energy E_{kin} of the ejected photoelectron is

$$E_{kin} = h\nu - E_B - \Phi \tag{3.8}$$

where E_B is the binding energy of the electron in the atom and Φ is the work function of the spectrometer. The binding energy of electrons is well known and depends on a number of factors, including:

- the element from which the electron is emitted,
- the orbital of the atom from which the electron is ejected,

Copy for "Bibliothèque UCL"

- the chemical environment of the atom from which the electron is emitted (↪ *Chapter 3.4.2*).

By measuring the kinetic energy E_{kin} of the collected electrons, it is possible to calculate the binding energy of the emitted electron and thus to identify the different elements and their chemical state at the sample surface.

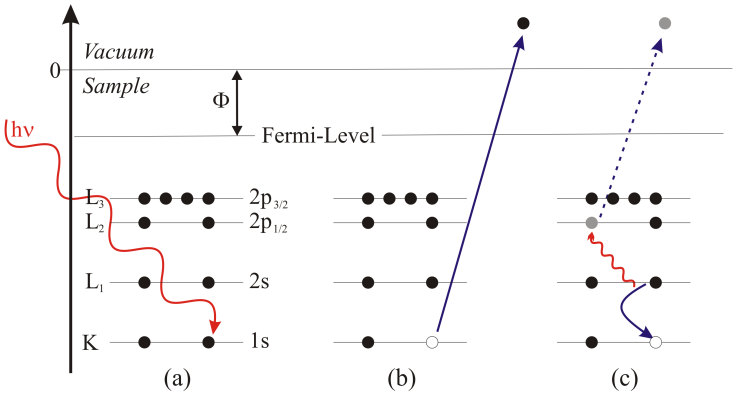


Figure 3.11: *Principle of XPS and Auger: a) Excitation of an inner shell electron by a radiation of energy hν - b) Ejection of a photoelectron which leaves a hole in the inner 1s shell - c) Ejection of an Auger electron KL_1L_2.*

3.4.2 Chemical Shift

The exact binding energy for an electron in a given atom depends on the chemical environment of that atom. Any change in the chemical environment of the atom will involve a spatial redistribution of the valence electron charges of this atom. When atoms with different electronegativity are bonded together, the electrons are displaced into the direction of the more electronegative atom. This redistribution affects the potential of the core electrons and results in a change of their binding energies. These electrons will leave the sample with a different kinetic energy.

Copy for "Bibliothèque UCL"

3.4.3 Charge Shift

During the XPS analyze, photons impinge on the sample surface and electrons are ejected from the sample, which create a local lack of electrons on the surface. Insulating sample or phase can not compensate this electron deficiency and thus the work function Φ of the sample increases. As a consequence the whole spectrum is shifted toward higher binding energies.

3.4.4 Auger Electrons

When an electron is removed from a core level of an atom due to a previous interaction (e.g. ↪ *Chapter 3.4.1*), an electron from a higher energy level may fill this vacancy. The energy, which is released in this relaxation process, can be either emitted by a photon or transferred to another electron, the Auger electron, which is then ejected from the atom (↪ *Figure 3.11(c)*).

The kinetic energy of the Auger electron is independent on the excitation energy (of the X-ray), but depends only on the different orbitals energy involved in the process.

3.4.5 Fine structure

Due to the spin-orbit interaction, the emission lines of the p, d and f orbitals will split up. The exact energy could be calculated by means of the angular momentum $j = l + s$. With increasing principal quantum number n, the size of the fine structure splitting becomes larger, but diminish with increasing azimuthal quantum number l.

For some materials, two intrinsic energy loss processes, which gives rise to an reorganization of the valance electrons, are a further source for structure in an XPS spectrum. During this relaxation process, the photoelectron can give a part of its energy to another electron of the same atom, which is then excited from a valence level to a bound state (shake-up) or a free unbounded state (shake-off). The energy required for this transition is not available to the photoelectron and therefore the emitted photoelectron is shifted to discrete higher energy on the binding energy scale.

Copy for "Bibliothèque UCL"

3.4.6 Inelastic scattering of electrons

When photoelectrons are leaving the sample, they could scatter on the atoms. By these inelastic collisions, the photoelectrons loose an undefined amount of energy so that an allocation of the electrons to a defined energy level is not possible any more. For a quantitative evaluation (↪ *Chapter 4.5.4*) the scattered electrons, which form a continuous background, must be subtracted from the whole acquired spectra.

3.4.7 Other appearing peaks in XPS and AES

These additional peaks could appear on the one hand due to energy loss of the electron during its escape from the sample (Plasmon) or on the other hand due to the X-ray source (Satellite-Peak for a non-monochromate X-ray source).

3.5 Electron Microscopy

In this section a short overview of the impinging electrons interactions with matter, and the resulting emitted electrons is given. In a later chapter the corresponding analytical instruments (SEM and TEM) are briefly described (↪ *Chapter 4.6*).

When an electron hits a material, different interactions, which are summarized in Figure 3.12, can occur. The chance that an electron interacts with the matter can be described either by the probability of a scattering event and expressed by the interaction cross-section σ_i, or by the average distance an electron travels between two interactions, the mean free path λ. The penetration of the primary electrons into the matter come along with an broadening of the beam diameter and a progressive diminution of the electron energy. The size of the pear-like shape interaction volume (↪ *Figure 3.12b*) and the penetration depth of the electrons increase with increasing electron energy and decrease with atomic number Z_A of the material. One can classify the electron-matter interactions into two different types, namely elastic and inelastic interactions.

Copy for "Bibliothèque UCL"

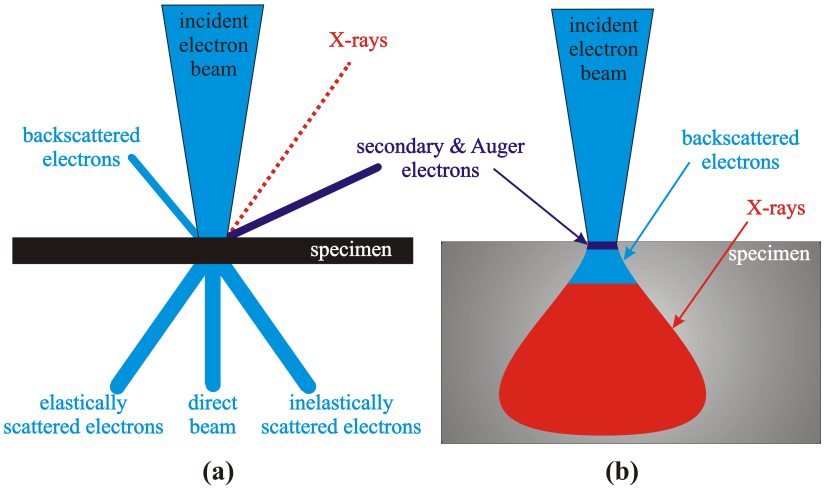


Figure 3.12: *Scheme of electron-matter interactions arising from the impact of an electron beam onto a specimen. a) A signal below the specimen is only observable if the thickness is thin enough to allow some electrons to pass through. b) In thick samples the interaction volume has a pear-like shape.*

3.5.1 Elastic Interactions

In this case, no energy is transferred from the electron to the sample. As a result, the electron leaving the sample has still its original energy. This is the case when an electron is penetrating into the electron cloud of an atom without further interaction with them. Then the electron is attracted by the positive potential of the nucleus (Coulombic interaction), and its path is deflected toward the core, and in rare cases, even a complete backscattering of that electron can occur. Due to the large mass difference between the impinging electron and the atom nucleus only a negligible amount of energy is lost during the elastic interaction.

The Coulomb force increases with increasing atomic number Z_A of the respective element, so that the deviation is more important for heavy elements than for light elements. Furthermore the deviation increases with decreasing primary electron energy. In the case where the electron

Copy for "Bibliothèque UCL"

passes through the sample without any interaction at all (e.g. TEM analysis), the electron keeps logically all its energy.

3.5.2 Inelastic Interactions

If the incident electron travels through the electron cloud of an atom, it might interact with an electron localized in any of the atom's electron shells. Because the participating particles have the same mass, the energy transfer between the electrons is important. Beside other appearing mechanisms (Bremsstrahlung, Phonons, Plasmons, X-rays, ...), several mechanisms of inelastic electron-matter can lead to the ejection of a secondary electron:

- Electrons located in the valence or conduction band need only the transfer of a small energy amount to gain the necessary energy to overcome the work function and to be ejected into the vacuum. Their energy is typically below 50 eV and thus they are designated as "slow SEs".
- Electrons that are located in the inner shell are stronger bound and less readily ejected. This process leads to an ionization of the atom and subsequently to the generation of characteristic X-rays or Auger electrons. These electrons from inner shells can carry a rather large energy and are therefore called "fast SEs".

3.5.3 Emitted Electrons

The secondary electrons (SE), the backscattered electrons (BSE) and the X-rays are the most important signals in the electron microscopy. The different signals originate from distinct volume inside the sample (↪ *Figure 3.12*).

- Secondary electrons and Auger electrons with rather small energy are readily absorbed in a material and thus only such generated close to the surface can leave the sample (typical depth: < 10 nm). The lateral resolution depends on the primary beam diameter and can reach about 3.5 nm.

Copy for "Bibliothèque UCL"

- Back-scattered electrons have (nearly) the same energy as the incoming beam and thus penetrate the sample more easily. The depth depends on their energy and the atomic number Z_A of the material (typical depth: $100 - 200$ nm). Because the backscattered electrons are usually produced by multiple scattering events, they travel considerable distances within the specimen, so that the lateral resolution is much larger (≈ 100 nm) than the diameter of the primary electron beam.

- The emission of X-rays can occur in the whole interaction volume.

3.5.3.A Secondary electrons

The secondary electrons are created by inelastic interaction between the impinging electron and the electrons of the sample within the sample. On their way out of the sample they can interact again with the matter. They can only leave the surface if their energy overcome the work function of the sample.

Due to the small energy (< 50 eV) of these slow secondary electrons, their trajectories are curved, which permits to detect signal from cavities and behind reliefs. The emission of secondary electrons varies only slightly with the atomic number Z_A, so that the contrast in the images obtained by secondary electrons are mainly due to the sample topography. On homogeneous sample, inclined surface, steep surfaces and edges tend to be brighter than flat surfaces.

3.5.3.B Backscattered electrons

Even if the backscattered electrons are reflected from the sample by elastic scattering, they can loose a part of their energy by inelastic scattering on their trajectories. In general they leave the sample at energies > 50 eV.

The number of backscattered electrons depends on the inclination of the sample, the energy of the primary electron beam and the atomic number Z_A of the sample, so that by BSE either a contrast of the sample topography or a contrast of atomic number can be imaged.

Copy for "Bibliothèque UCL"

Chapter 4

Experimental Setup

The following sections cover the experimental part of this work: First the development of a sample preparation method, which allows the transfer of polymer films between the different analytical instruments (ToF-SIMS, XPS, AFM, NanoSIMS50, ...) with minimal manipulation/distortion of polymer film samples, is presented (↪ *Chapter 4.1.1*). However it turned out that the determination of morphology as well as the occurring charging effects on these samples complicate or even inhibit a correct and adequate sample analysis. As a way out, thick polymer samples are prepared by spincoating (↪ *Chapter 4.1.2*). The characterization of those pristine sample prepared by spincoating (surface roughness and film thickness) are presented in this chapter too.

In the subsequent Section 4.2.1, the results obtained by an *ex-situ* polymer metalization by sputtering clearly show that clean and well determined conditions during metal deposition is an absolute necessarily prerequisite for the metalization of organic samples in MetA-SIMS. So a further section covers the installed evaporation system with integrated quartz crystal microbalance, which allows for the first time a controlled *in-situ* metalization (↪ *Chapter 4.2.2*). Furthermore the characterization of the used evaporation cell is presented in this section. At the end of this chapter the used analytical instruments (ToF-SIMS, XPS, AFM) are presented and their experimental parameters are denoted (↪ *Chapters 4.3-4.6*).

Copy for "Bibliothèque UCL"

4.1 Preparation of the Samples

A major goal in secondary ion mass spectrometry consists in improving the qualitative and quantitative value of the information provided by the mass spectrum. The standard method utilized since several decades for secondary ion mass spectroscopy on organic sample is to deposit a (sub) monolayer of the organic sample onto a metallic substrate [152]. A significant drawback of this sample preparation procedure is that only (sub)monolayer films, which are carefully prepared from very dilute solutions, can be analyzed. Therefore this method is useless for samples that cannot be prepared as ultrathin films as well as for real world surfaces that must be analyzed as such. In the beginning of the 90's, an other method for sample preparation, which is applicable to all kind of samples, was developed. These preparation method consists in metallizing the organic sample prior to the static secondary ion mass spectroscopy [8, 9, 63, 65, 225].

In this work, where the enhancement of the static SIMS analysis due to the deposited metal morphology is of interest, different polymeric substrates, with different molecular structures and intermolecular bonds, are chosen.

First investigations are done on commercial polymers (↪ *Chapter 4.1.1*), but the AFM results of the deposited metal morphology on the polymer films are dubious (↪ *Figure 4.4*) due to the high roughness of the pristine polymer bulk. Therefore the polymer samples are prepared in the second step by spincoating which provides more flat sample surfaces (↪ *Chapter 4.1.2*).

In the subsequent Section 4.2 the different sample preparation procedures as well as the design of the evaporation cell are described.

4.1.1 Polymer Films

Based on different composition, elemental ratios and chemical bonds, different polymer films have been selected to study. These polymer films, which were purchased at Goodfellow™ are listed in Table 4.1.

Since the samples are characterized with different techniques (ToF-SIMS, AFM, XPS), the thin film samples must be transfered to the different analytical instruments. Due to the fact

Copy for "Bibliothèque UCL"

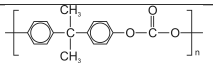
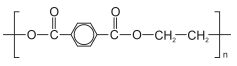
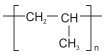
#	Polymer (Abbreviation)	Thickness	Formula
A	Polycarbonate (PC)	125 μm	
B	Polyethylene terephthalate (PET)	50 μm	
C	Polypropylene (PP)	50 μm	
D	Polytetrafluoroethylene (PTFE)	50 μm	

Table 4.1: *List of the used polymer in form of thin films.*

that the influence of sample bending on the surface structure is not known, the films must be distorted as little as possible during the transfer. Therefore the thin films are fixed on a hard and flat metallic disc (diameter: 10 mm, thickness 1 mm).

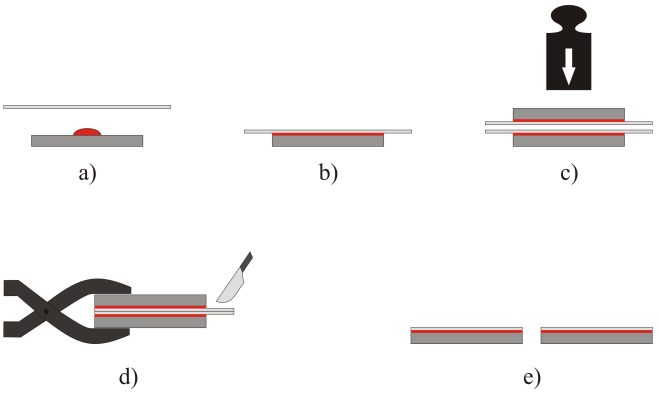


Figure 4.1: *Preparation of the polymer film samples. See text for a detailed description of the preparation method.*

In Figure 4.1 the different preparation steps for the bulk polymer films are illustrated and this whole preparation procedure is described hereafter. After rinsing a large piece of the polymer in n-hexane & ethanol in order to remove eventual contamination on the surface, it is fixed with a drop of conducting silver. In order to avoid surface contamination and to obtain a good adhesion between the polymer and the metallic support a second sample is laid upside down on the

Copy for "Bibliothèque UCL"

first. This pill is weighted down and is dried at room temperature for several hours. Before using the sample, the overlapping polymer is cut off with a scalpel and the pill is carefully disassembled. These samples can be mounted on the samples holder of different analysis instruments (ToF-SIMS, AFM, XPS, Nano-SIMS, ...) without further modification.

4.1.2 Spin-Coating

Imaging of the small metallic clusters on the polymer bulk samples turned out to be very difficult due to the high roughness of the pristine polymer films (↪ *Figure 4.3a and 4.4*). After some preliminary test of sample preparation by spincoating at the institute of Physical Chemistry and Physics of Material (PCPM), this method, promising flat surfaces, is retained. The samples described in this manuscript are prepared with a new-acquired spincoater at the department of Science and Analysis of Material (SAM) of the Centre de Recherche Public Gabriel Lippmann (CRPGL). In the following paragraph an overview of the spin-coating technique and the sample preparation method is given.

Modeling of the spin coating process is complex due to the many involved mechanisms. The first authors who described the spin coating procedure, assumed a Newtonian behavior of the fluid [226]. Later even more complicated models appeared, which described the experimental data better by using a non-Newtonian behavior of the fluid and taking into account the evaporation process during the spin coating procedure [227, 228]. Here, for a better understanding of the spin coating procedure, only the main four process phases will be described.

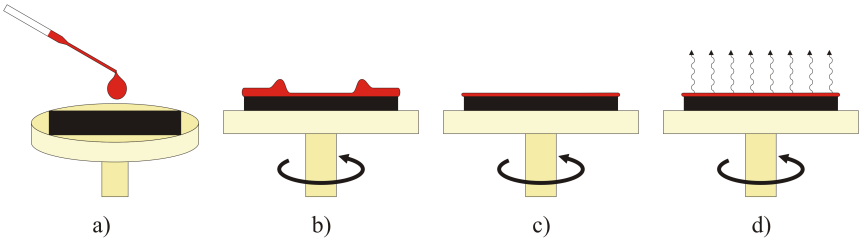


Figure 4.2: *The four process phases in spin-coating. See text for a detailed description of the spincoating process.*

Copy for "Bibliothèque UCL"

a) Deposition: In the first phase, the polymer solution is deposited onto the wafer or substrate by using a nozzle (↪ *Figure 4.2a*). In order to prevent an incomplete sample coverage, it is important at this stage, to provide the necessary amount of solution onto the sample.

b) Acceleration: After the deposition phase, the next step is to accelerate the substrate up to its final, desired, rotational speed. During this phase a large amount of the solution will be removed from the substrate by lack of the centripetal force (↪ *Figure 4.2b*).

c) Spinning at a constant rate (flow controlled): In this stage, which last from few seconds to several minutes, relatively high speeds ($1000 - 10000\,\text{rpm}$) can be used to thin the fluid to the final thickness (↪ *Figure 4.2c*). The combination of the rotation speed and time will define the final film thickness. In general, higher rotation speeds and longer spinning time lead to the formation of a thinner film. Edge effects are often seen because the fluid flows uniformly outward, but must form droplets at the edge to be flung off.

d) Spinning at a constant rate (evaporation controlled): In this phase the main influence is the the solvent evaporation and the change of the film thickness due to the substrate spinning is negligible (↪ *Figure 4.2d*). Due to the evaporation of the solvent, the viscosity of the fluid increases and so the rotation speed is not strong enough to remove the fluid from the surface and to thinner the film in this way. Therefore all further changes of the film thickness are only the effect of the evaporation process. Stages 3 and 4 occur simultaneously during all the spincoating procedures, but at an engineering level the viscous flow effects dominate early while the evaporation processes dominate later.

Because not all the polymers, which were studied under the form of a film (↪ *Table 4.1*) can be easily dissolved, the indissoluble polymers have to be replaced. The different polymers studied in this work, which were selected according to their different compositions, elemental ratios and chemical bonds, are mentioned in Table 4.2. In Table 4.3 the suitable solvent of the polymers as well as their origin and their weight average molecular weight are noted.

Copy for "Bibliothèque UCL"

It has to be noted that samples, prepared with the same parameters, have a different appearance in the both laboratories. No further investigation has been done on this surface difference. Hereafter only the sample, which are prepared with the spincoater (Single Wafer Spinner SPIN150 from APT (D)) at the department SAM at the CRP-Gabriel Lippmann, will be discussed. The parameter for the spincoating procedure are noted in Table 4.4.

Because a silicon wafer is flatter than the metallic discs, which were used for the preparation of the polymer films (↪ *Chapter 4.1.1*), a silicon wafer is cleaved with special developed tools in pieces of $\approx 1 \times 1\,cm^2$ surface. These square pieces are cleaned consecutively in an ultrasonic bath of absolute acetone and ethanol. Afterward they were dried with a flow of pure nitrogen.

A depression, which is created by a primary rotary pump, fixes the silicon sample in the center of the spincoater rotation plate. Immediately before the deposition of the polymer solution, the dust eventually present on the sample is blown off with a pure nitrogen blast.

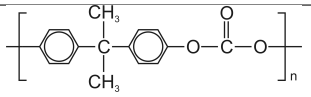
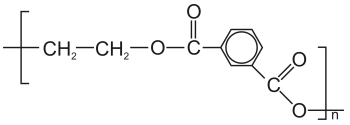
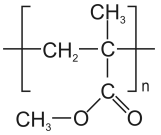
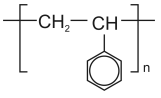
#	Polymer (Abbreviation)	Molecular Structure
K	Polycarbonate (PC)	
L	PET-co-isophthalate (PET-I)	
M	Polymethylmethacrylat (PMMA)	
N	Polystyrene (PS)	

Table 4.2: *List of the spincoated polymers which were studied in this work. Also mentioned are the internal reference # and the structure of the monomer.*

Copy for "Bibliothèque UCL"

Polymer	Supplier	Solvent	Molecular Weight	Glass transition T_G	Surface energy
PC	Fluka	Chloroform	30600 u	423 K	$46\frac{mN}{m}$
PET-I	ICI/PCPM	Chloroform	unknown	348 K	$42\frac{mN}{m}$
PMMA	Fluka	Toluene	20000 u	378 K	$41\frac{mN}{m}$
PS	Fluka	Toluene	30000 u	368 K	$38\frac{mN}{m}$

Table 4.3: *The different polymers under study with their supplier, their suitable solvent, their weight average molecular weight, their glass transition temperature T_G and their typical surface energy.*

Parameter	Value
Concentration of the solution	variable
Acceleration	$20000\,\frac{rpm}{s}$
Rotation velocity	$5000\,rpm$
Time	$60\,s$

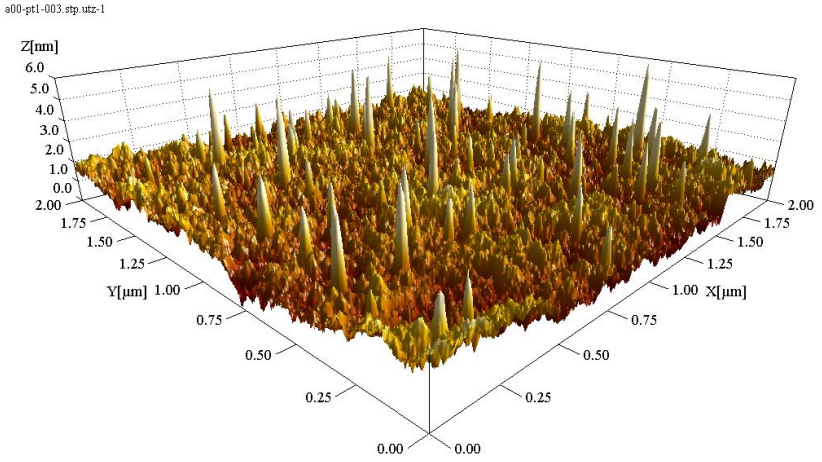
Table 4.4: *Parameters for the spincoater used for the sample preparation in this work.*

A small amount of the polymer is weighted with a balance of milligram accuracy. With a pipette an amount of the adequate ultra-pure ($> 99\%$) solvent is added in order to reach the desired concentration of the polymer solution. The concentration of the used solution is expressed in this work either by $\frac{\text{mass of polymer}}{\text{volume of solvent}}\ \left[\frac{mg}{ml}\right]$ or by $\frac{\text{mass of the polymer}}{\text{mass of the solution}}\ [\%]$. For the $\approx 1cm^2$ large silicon samples at least $40\,\mu l$ of this polymer solution is deposited by a nozzle in the middle of the sample. This excess of solution on the sample as well as the good wettability of the used solvent on the clean silicon result in a complete coverage of the sample.

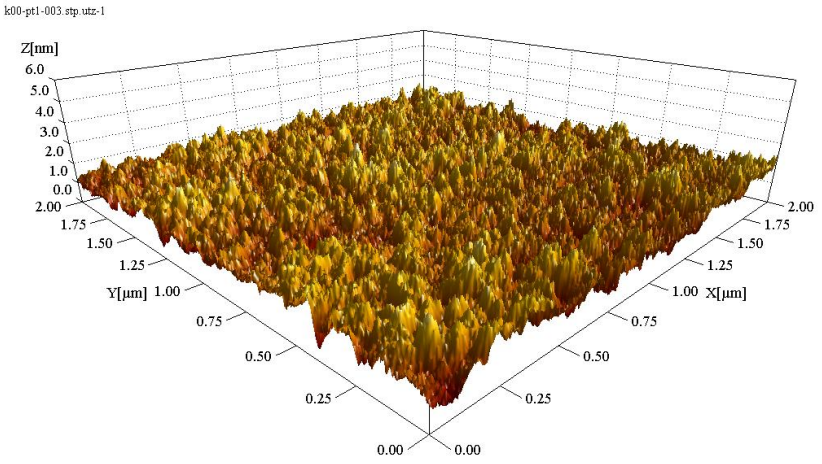
In order to verify that the roughness of the spincoated samples is smaller than the bulk samples, AFM measurements have been performed on the different pristine polymers. Figure 4.3 presents the topography of the different pristine polycarbonate samples. These intermittent contact AFM images illustrate the roughness difference between a bulk polymer sample (↪ *Chapter 4.1.1*) and a sample prepared by

Copy for "Bibliothèque UCL"

spincoating (↪ *Chapter 4.1.2*). One can note that the surface of the polymer sample prepared by spincoating does not possess large peaks contrarily to the bulk polymer.



(a) *PC - bulk*



(b) *PC - spincoated*

Figure 4.3: *AC-AFM topography (fov:* $2 \times 2\mu m^2 \times 6\text{nm}$*): Different pristine polycarbonate samples*

Copy for "Bibliothèque UCL"

A more complete and detailed roughness evaluation of the different samples is performed by calculating the most commonly used roughness amplitude parameters (Roughness Average S_a, Root Mean Square S_q, Surface Skewness S_{sk} and Surface Kurtosis S_{ku}) for the different samples. These surface roughness parameters are described by the following equations:

$$\begin{aligned} S_a &= \frac{1}{M \cdot N} \sum_{k=0}^{M-1} \sum_{l=0}^{N-1} |z(x_k, y_l) - \mu| \\ S_q &= \sqrt{\frac{1}{M \cdot N} \sum_{k=0}^{M-1} \sum_{l=0}^{N-1} [z(x_k, y_l) - \mu]^2} \\ S_{sk} &= \frac{1}{M \cdot N \cdot S_q^3} \sum_{k=0}^{M-1} \sum_{l=0}^{N-1} [z(x_k, y_l) - \mu]^3 \\ S_{ku} &= \frac{1}{M \cdot N \cdot S_q^4} \sum_{k=0}^{M-1} \sum_{l=0}^{N-1} [z(x_k, y_l) - \mu]^4 \end{aligned} \tag{4.1}$$

where M and N the number of datapoints in x and y direction and $\mu = \frac{1}{M \cdot N} \sum_{k=0}^{M-1} \sum_{l=0}^{N-1} z(x_k, y_l)$ is the mean height of the sample [229]. These roughness parameters for the different samples are shown in Figure 4.4. For a better comparison the average roughness values of the spincoated polymer are indicated by horizontal lines.

As can been noted in Figure 4.4, the roughness values of the spincoated films are well below those of the bulk polymers, so that the spincoated films constitute an extremely flat and featureless surfaces, which are suitable for studying nucleation and growth process [104]. High values for the surface kurtosis S_{ku} for the bulk samples confirm the observation of peaks on the bulk polymer sample (↪ *Figure 4.3a*). In addition there is less variation across the polymer samples prepared by spin coating than across the bulk samples.

In order to verify the complete and sufficient coverage of the silicon substrate with the polymer, the thickness of the polymer layer is determined. In a first time, the reduction of the SIMS silicon substrate signal by two orders of magnitude in comparison with a clean silicon surface indicates that the polymer covers completely the substrate (↪ *Figure 4.5*) and that the average polymer layer thickness

Copy for "Bibliothèque UCL"

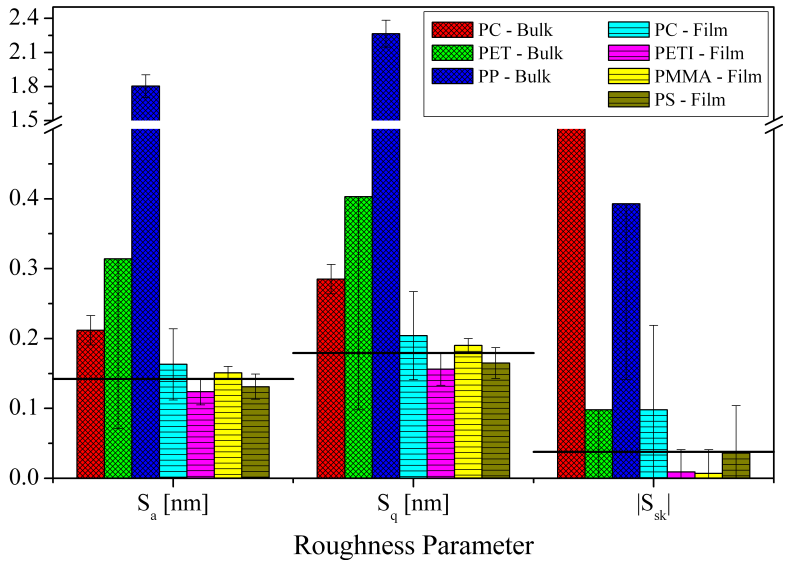


Figure 4.4: *Most commonly used roughness parameter (S_a, S_q and S_{sk}) for the pristine samples prepared either as bulk or by spin-coating.*

is at least 50 Å [230]. This is confirmed by the absence of the Si_{2p} signal in the XPS spectra. Knowing the inelastic mean free path of an photoelectron originating from the silicon substrate and propagating through a polymer matrix ($<$ 42 Å [231]), the average polymer thickness is at least 10 nm.

To determine the exact thickness of the spincaoted polymer films, ellipsometry measurements of various samples have been performed at the PCPM laboratory. This non-destructive and contactless surface analysis method consists in the investigation of thin film dielectric properties (complex refractive index). Thereby the change of polarization of linearly polarized light, which is reflected from a sample, is analyzed with a second polarizer (analyzer) (↪ *Figure 4.6*). Different sample properties (thickness, refractive index) determine the the polarization change. By ellipsometry, the amplitude ratio of the perpendicular and parallel light components ($\tan\Psi$) as well as the phase shift Δ after reflection are measured [232].

Copy for "Bibliothèque UCL"

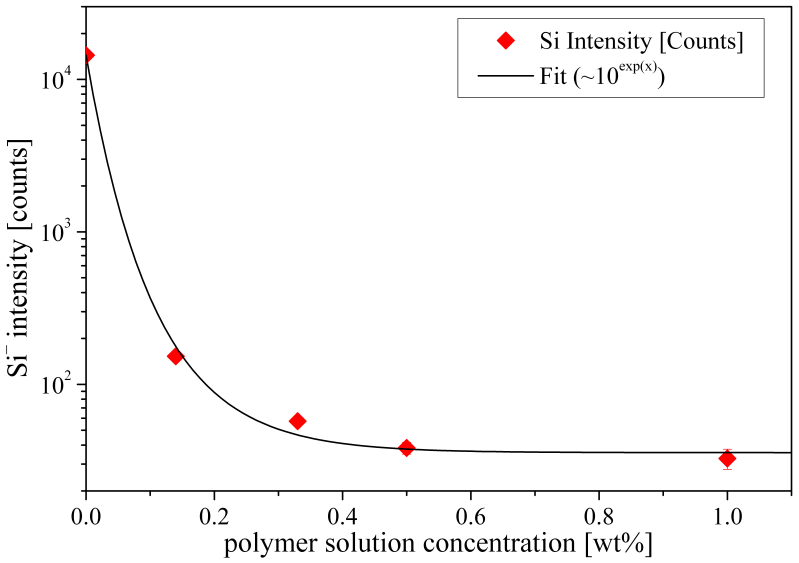


Figure 4.5: *Evolution of the silicon substrate signal in ToF-SIMS as a function of the PC polymer concentration of the solution used for spincoated sample preparation.*

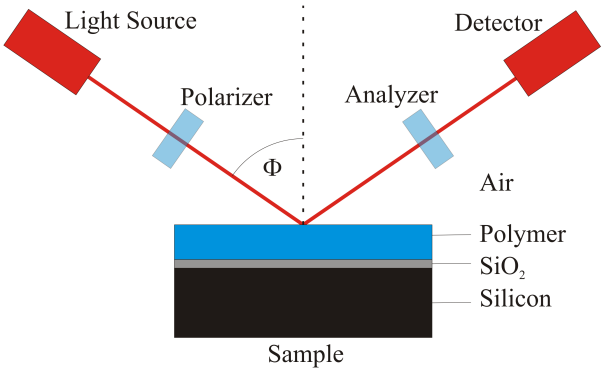


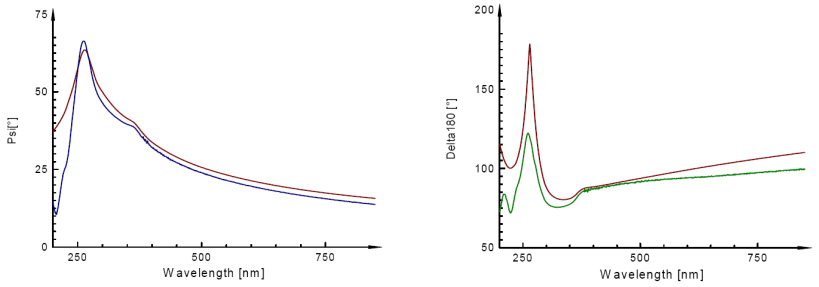
Figure 4.6: *Schematic setup of the ellipsometry experiment*

In the majority of cases the ellipsometry is an indirect method, so that normally a model analysis must be performed. Therefore the sample must be composed of a small number of discrete, well-defined, optically

Copy for "Bibliothèque UCL"

Layer	Thickness	$\tilde{n}$
Air	-	1.000
Polymer	fit	↪ *Table 4.6*
SiO_2 (therm)	$0.5nm$	1.461
Silicon (Hertziger)	∞	$3.874 + 0.015i$

Table 4.5: *Optical constants (thickness and refracting index $\tilde{n}$) for the components of the ellipsometric model (↪ Figure 4.6).*



(a) *amplitude ration* Ψ **(b)** *phase shift* Δ

Figure 4.7: *(a) and (b) show the fitting plots for a polycarbonate film. The red lines indicate the expected signal from the model, whereas the other lines represent the measurement.*

homogeneous and isotropic layers. Based on a model, which considers the optical constants and thickness parameters of all layers of the sample, an iterative procedure allows to determine unknown optical constants or the thickness of the individual layers.

In the case of the spincoated polymers studied in this work a model containing a silicon, a native silicon oxide and a polymer layer is assumed (↪ *Figure 4.6*). In Table 4.5 the thickness and the refracting indexes of the different layers of the ellipsometric model, which are used to determine the thickness of the polymer layer, are noted. The figures 4.7a and 4.7b show the fits for the amplitude ratio of the perpendicular and parallel light components as well as for the phase shift after reflection for the 0.5% polycarbonate sample.

All the thicknesses of the four polymers determined by the ellipsometry are plotted in Figure 4.8. Because the samples are always

Copy for "Bibliothèque UCL"

prepared under the same acceleration and final velocity (↪ *Table 4.4*), the polymer thickness d_s obtained by the ellipsometric measurements can be fitted by the function

$$d_s = k \cdot c^{\alpha} \tag{4.2}$$

where c is the concentration of the polymer solution, k and α are fitting parameters [233]. The fitting parameters for the different polymers are noted in Table 4.6 and the fitting curves (↪ *Equation 4.2*) are plotted in Figure 4.8.

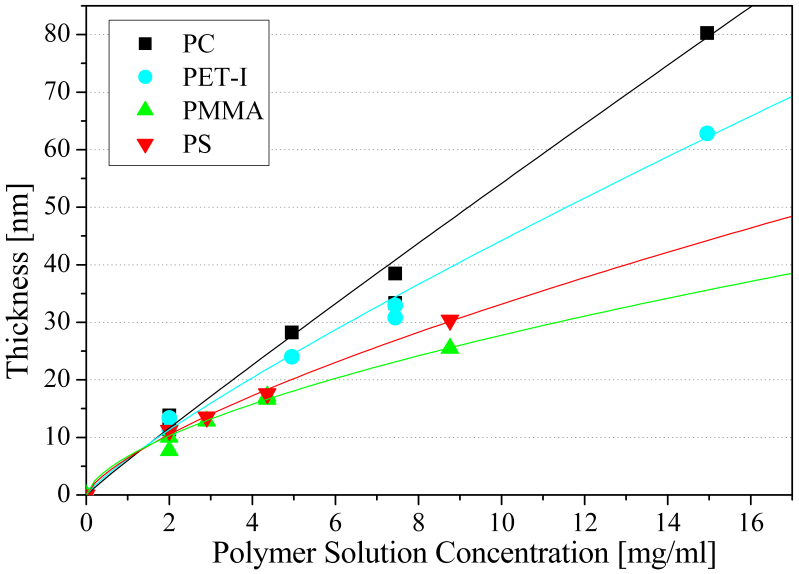


Figure 4.8: *Evolution of the polymer thickness as a function of the solution concentration for the different spincoated polymers. The data points are fitted by the equation* $d_s = k \cdot c^{\alpha}$ *using the parameters denoted in Table 4.6.*

In order to check a clean preparation of the spincoated samples, a ToF-SIMS analysis is performed before every further sample treatment. Furthermore the intensities of the characteristic acquired ToF-SIMS spectra are compared with reference spectra found in the Münster High Mass Resolution Static SIMS Library [234].

Representatively for all the polymer samples, Figure 4.9 compares the relatively intensities of characteristic peaks between the acquired

Copy for "Bibliothèque UCL"

Polymer	ñ	k	α
PC	1.582	6.01 ± 0.69	0.96 ± 0.05
PET-I	$1.575 + 0.052i$	6.31 ± 0.65	0.85 ± 0.04
PMMA	1.486	6.71 ± 0.23	0.62 ± 0.02
PS	1.586	6.41 ± 0.37	0.71 ± 0.03

Table 4.6: *Thickness fitting parameters for the different polymers*

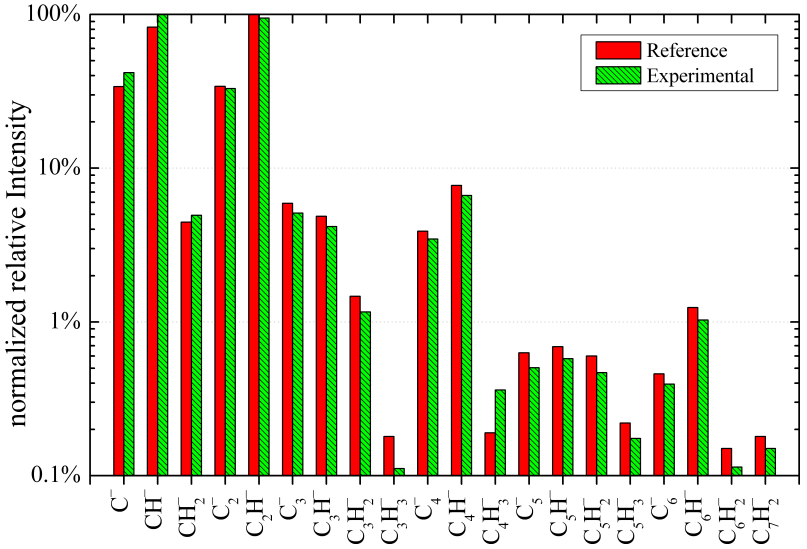


Figure 4.9: *Comparison of the relative intensities of the characteristic negative secondary ions of polystyrene between the samples prepared by spin-coating and the data in the Münster High Mass Resolution Static SIMS Library [234].*

spectra and the reference spectra of the database. As can be seen in the plot, a good agreement of the relative intensities between the reference spectra and the samples prepared by spin-coating in the laboratory is obtained.

Copy for "Bibliothèque UCL"

4.2 Evaporation

To achieve the aim of this work, the polymer samples have to be metalized. A general aim in surface analysis is to prevent an unwanted pollution of the samples by adding contamination during metalization, especially organic contamination on a polymer sample. The sample metalization is performed by different methods. At the beginning, tests by *ex-situ* sputtering deposition are performed (↪ *Chapter 4.2.1*). Due to indeterminable contamination problem during the sputtering, the deposition of gold was thereafter performed *in-situ* by thermal evaporation method (↪ *Chapter 4.2.2*).

4.2.1 Ex-situ metalization

In a first time, and until the assembly of the in-situ-evaporation cell, the sample metalization is performed *ex-situ* by using the Bal-Tec MED020 coating system, which is based on high vacuum sputtering.

After introducing the samples into the metalization chamber, undesired residual gas components are eliminated from the vacuum chamber by a high vacuum pump until a pressure of ($\approx 10^{-5}$ mbar) is reached. The working pressure inside the chamber, required for sputtering ($\approx 5 \cdot 10^{-2}$mbar) is then reestablished with the admission of argon gas. To start the sputtering process a high voltage field is applied between the target and the specimen table (anode). Thereby the argon atoms are ionized. The positively charged argon ions are accelerated to the cathode (target) where they impinge and knock off metal atoms toward the chamber. Because the metal atoms scatter widely, they form a diffuse cloud, impinge on the specimen from all directions and condense evenly on it.

The Bal-Tec MED020 coating system of the Lab is not equipped with a disposition which allows to measure the deposited amount of evaporated metal. The desired thickness is obtained by changing the sputter time and the current on the basis of a calibration plot.

The results of these experiments are quite unfruitful, because the appearance of inexplicable peaks in subsequent ToF-SIMS analysis. Figure 4.10 shows a juxtaposition of ToF-SIMS of the four examined spincoated polymer samples with a ≈ 2 nm gold evaporation.

Copy for "Bibliothèque UCL"

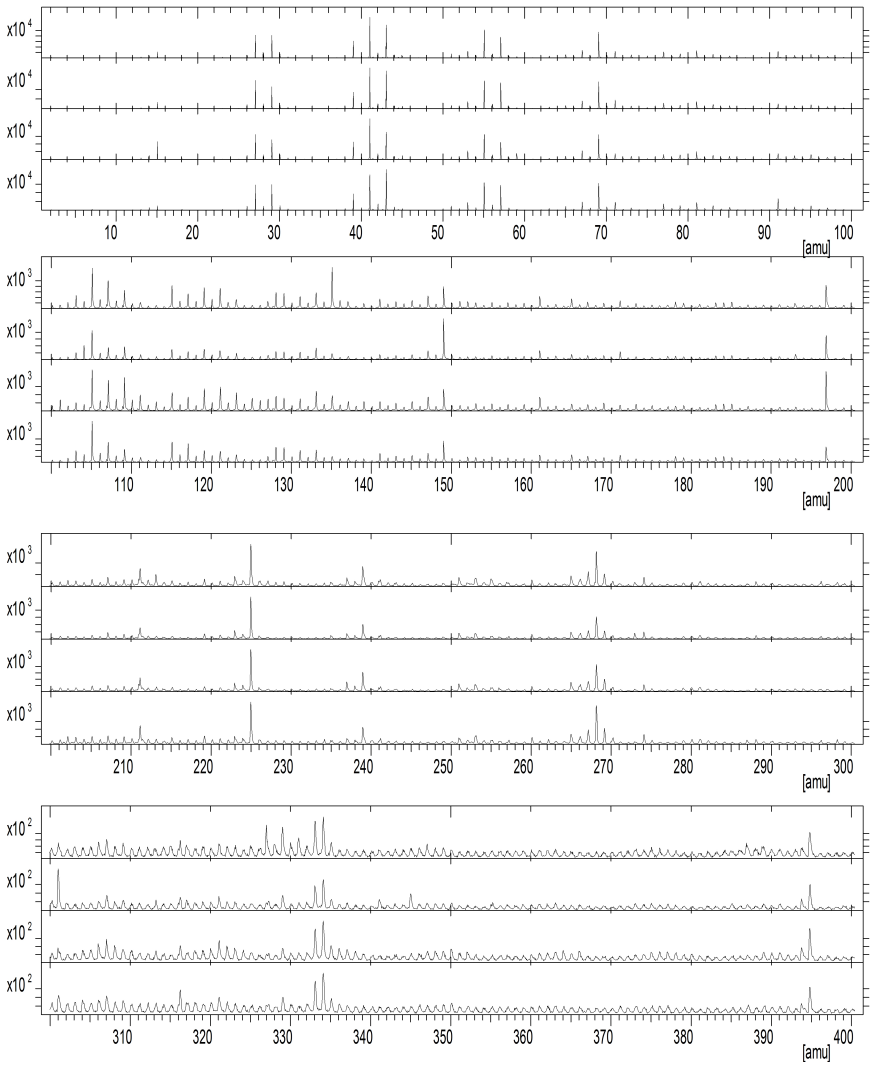


Figure 4.10: *ToF-SIMS spectra in positive polarity of the 4 polymers (in each graph from top to bottom: PC, PET-I, PMMA, PS) with a* ≈ 1 nm *nominal thickness deposition of gold by sputtering. The mass of the peaks as well as their probable Label are noted in Table 4.7.*

Subsequent XPS analysis reveals that only a nominal gold thickness of ≈ 1 nm was deposited on the sample. Assuming that the calibration

Copy for "Bibliothèque UCL"

graphs of the Bal-Tec MED020 coating system are correct, the sticking coefficient of gold by the sputtering process is about 0.5. Similar sticking coefficients have been figured out by a much more detailed evaluation for the *in-situ* evaporation process (↪ *Chapter 5.1*).

Although the initial polymer spectra are different and the thickness of the gold deposit is small, the spectra are quite similar. Different sources of contamination have been examined and eliminated, but the contamination still remains. The most significant peaks in positive polarity of this contamination, which is present on the four samples, are noted in Table 4.7.

negative polarity		positive polarity	
Mass	Label	Mass	Label
26.02	$C_2H_2^-$	27.02	$C_2H_3^+$
34.97	$^{35}Cl^-$	29.04	$C_2H_5^+$
36.97	$^{37}Cl^-$	39.02	$C_3H_3^+$
108.0		41.04	$C_3H_5^+$
109.0		43.05	$C_3H_7^+$
149.0		55.06	$C_4H_7^+$
153.0		57.08	$C_4H_9^+$
183.1		69.07	$C_5H_9^+$
223.0	$AuC_2H_2^-$	91.06	$C_7H_7^+$
231.9	$Au^{35}Cl^-$	105.1	$C_8H_9^+$
233.9	$Au^{37}Cl^-$	107.1	$C_8H_{11}^+$
248.9		109.1	$C_8H_{13}^+$
253.2		149.0	
255.2		224.9	$AuC_2H_4^+$
257.9		239.0	$AuC_3H_6^+$
		268.2	

Table 4.7: *List of intense peaks observed on all polymers after the gold deposition by sputtering (↪ Figure 4.10). In the case where an indisputable association to an ion is possible, the label of this ion is noted.*

A brief evaluation of these spectra turns out that the origin of these peaks is probably due to presence of nitrogen, oxygen and

Copy for "Bibliothèque UCL"

fatty acids. Also cationisation of small unspecified organic fragments are detected. Because the same peaks appear on all four polymers, reasonable explications are either an unremovable contamination of the entire instrument or a degradation of the polymer surface during the plasma deposition [74]. Although an exact determination of these peaks is ambiguous, the spectra clearly show that an differentiation between the polymer is no longer possible after this metalization procedure.

4.2.2 In-situ evaporation

To prevent surface degradation of the sample surface by plasma interaction and preclude the samples from unwanted contamination during metalization and during the subsequent transfer to the analysis instrument (↪ *Chapter 4.2.1*), another coating technique has been chosen. Especially to exclude organic contamination during the metalization, and in order to minimize the manipulation and the modification of the samples, the metalization is performed *in-situ* by thermal evaporation of the metal onto the samples.

Therefore an evaporation cell is installed in a ultra high vacuum chamber next to the ToF-SIMS analysis chamber, so that a transfer between these two chambers can be made without any atmosphere contact. The evaporation cell consists in two rods out of steel between which a tungsten evaporation boat is fixed. A small amount of the metal (gold), which one wants to evaporate is put inside the evaporation boat. By applying a tension between the two ends of the evaporation boat, a transformer induces a high current through the boat and thus the evaporation boat heats up. The tension applied on the transformer, is measured by a voltmeter, which ensures the exactness and the reproducibility of the deposition condition. The usual pressure inside the preparation chamber during metalization is between $5 \cdot 10^{-7}$ mbar and $5 \cdot 10^{-9}$ mbar.

By the Equation 4.3, the vapor pressure of an element at a given temperature can be calculated. The coefficients $A = 9.152$, $B = -19343$, $C = -0.7479$ and $D = 0$ are used for gold [235, 236]. Although the system is permanently pumped, a steady state should be reached around the evaporation cell after a short time. As the pressure around the evaporation cell can not be determined, the evaporation temperature for gold in the vapor pressure chart may only be used as an approximation.

Copy for "Bibliothèque UCL"

$$\log(p/Pa) = 5.006 + A + BT^{-1} + C\log(T) + DT^{-3} \tag{4.3}$$

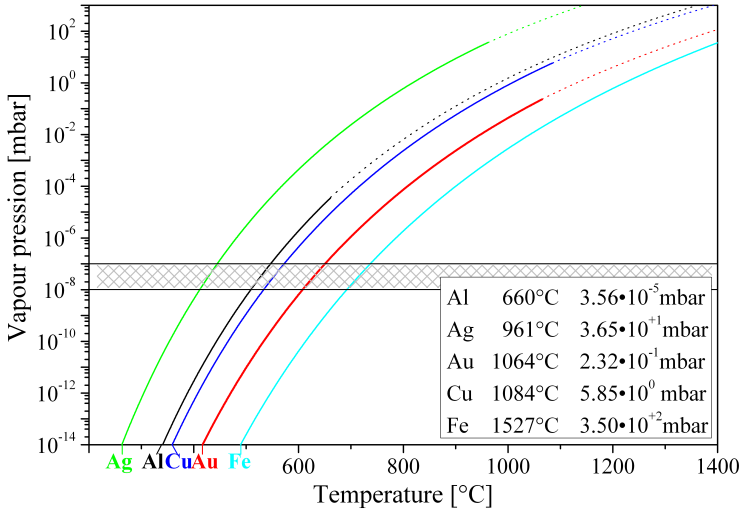


Figure 4.11: *Vapor pressure of different metals. The solid line represents the vapor pressure of solids. The dotted line correspond to the vapor pressure of the liquid metal. The melting temperature of the elements as well as the corresponding vapor pressure are noted in the inset.*

The Figure 4.11 shows the vapor pressure for different metals depending on the temperature. The equilibrium between vapor pressure for gold and the environment in the preparation chamber is reached by a temperature of approximately 630 °C. Due to the fact that the pressure gauge is dislodged from the evaporation system, the pressure and thus the evaporation temperature is underestimated. For an effective evaporation of gold a much higher temperature is needed, which is supported by the annealing color of the evaporation boat during the metalization.

The flux r of the evaporated metal is measured with a quartz crystal microbalance (QCM) (electronic: Bal-Tec QSG060 - physic: Balzers

Copy for "Bibliothèque UCL"

QSK135), which is placed on the opposite side of the evaporation source. Due to a water circuit, the QCM is cooled all the time. Regardless of the use of a manipulator, the position of the QCM during the flux measurement is not the same as the sample position during metal deposition. Thus the measured flux value, that is detected by the QCM must be corrected in order to obtain and display the flux which reaches the samples in reality. The needed correction of the evaporation flux, which is due to the geometrical arrangement of the evaporation boat, samples and QCM, is described by the tooling factor F_T:

$$F_T = \frac{\sin \alpha_s}{\cos \alpha_q} \cdot \frac{L_q^2}{L_s^2} \tag{4.4}$$

where L_s is the distance between the evaporation source and the sample, L_q the distance between the evaporation source and the QCM, α_s the evaporation angle and α_q the angle between the evaporation source and the normal of the QCM [237]. Because the evaporation source, the samples and the QCM are in line ($\alpha_s = 90°$ and $\alpha_q = 0$), the tooling factor is reduced to $F_T = \frac{L_q^2}{L_s^2}$.

The thickness d of the evaporated metal could be calculated with the formula

$$d(t) = f \cdot t \tag{4.5}$$

with f the measured evaporation flux and t the time of sample exposition.

The manually stopped evaporation time t and the stability of the evaporation rate f provides an error $\Delta d = \Delta f \cdot t + f \cdot \Delta t$ on the determined thickness d. With $\Delta f = 0.2 \frac{\text{Å}}{s}$ and $\Delta t = 1\,s$ reasonable errors for the system are chosen. Another error in the thickness measurement is the exactness of the tooling factor. In the case where the exact geometry of the evaporation cell could not be measured, the tooling factor is determined experimentally by measuring the thickness of some coatings by other techniques (profilometry and XPS).

In Figure 4.12 the side view of the first assembly can be seen. The evaporation source was installed at approximately $25\,cm$ from the sample surface. On the opposite side the QCM was installed on a manipulator, which permits the move the QCM to the same distance from the evaporation source as the sample, so that the tooling factor

Copy for "Bibliothèque UCL"

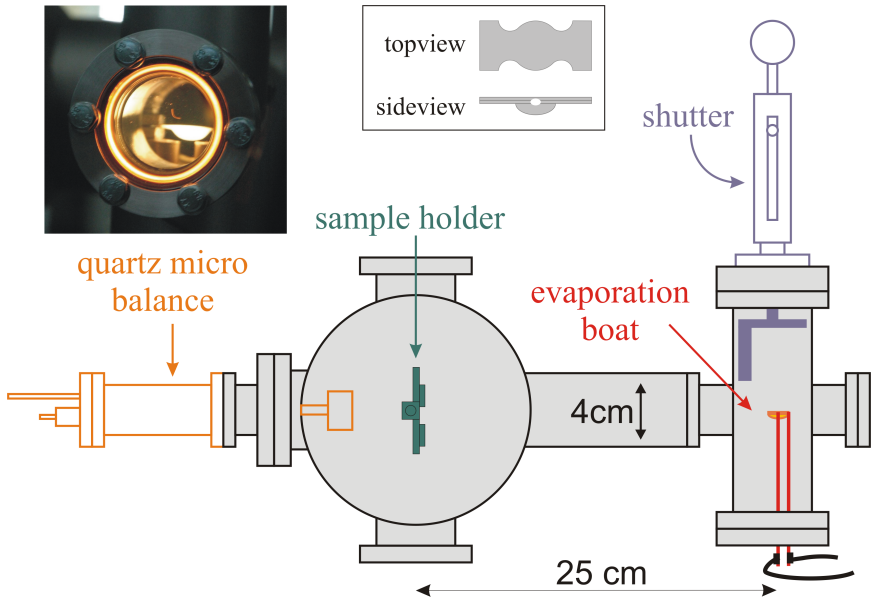


Figure 4.12: *Side view of the first geometry of the evaporation system.*

is unity for that geometry. Also a shutter was installed in order to interrupt the flux abruptly. This horizontal design of the evaporation cell necessitates an evaporation boat which is capable of evaporating the metal sideward. Therefore a commercial available tungsten evaporation boat was covered with a tungsten plate. A hole ($\varnothing 2\,mm$) that was milled out at one side of the evaporation boat permits the metal vapor to escape sidewise toward the sample.

The large distance between evaporation source and sample and thus a small solid angle of the evaporation flux results in an homogeneous covering of the whole sample holder. The homogeneity of the evaporation flux was tested by distributing five InP pieces onto the sample holder ($\varnothing 5\,cm$). During $50\,s$, an evaporation flux of $0.4\frac{\text{Å}}{s}$ of gold was performed. These five samples were subsequent analyzed by XPS. The measured thickness (by XPS) was $0.95 \pm 0,07\,nm$, indicating an homogeneous covering over the whole sample holder [238].

The presented evaporation cell geometry has some disadvantages. First metal evaporation flux is near the QCM detection limit, which considerably limits the range of evaporation conditions. Furthermore

Copy for "Bibliothèque UCL"

the evaporation chamber becomes too hot even with a cooling system made out of flexible metallic tube. As a consequence either an irregular evaporation flux is observed or even other inorganic material such as iron and copper, originating from the fixation of the evaporation boats are evaporated and thus subsequently detected on the samples by ToF-SIMS and XPS analysis [238].

4.2.2.A Final evaporation setup

In the order to sidestep the problem of overheating and low evaporation rate, the evaporation source is approached toward the sample (↪ *Figure 4.13*). Due to the design of the preparation chamber, the evaporation source is finally installed on a flange closer to the sample. The quartz crystal microbalance, which stays installed on a manipulator, was fixed on the opposite flange of the evaporation system. The distance between the evaporation boat and the sample is ≈ 5 cm and between the evaporation boat and the lowest possible position of the QCM is ≈ 10 cm. Furthermore, due to the vertical assembly, no special designed evaporation boat is required. Into the evaporation boat, which is made out of tungsten, a small part of a gold foil (Goodfellow, purity: 99.95 %, thickness: $0.05\,mm$) is put.

The design of the preparation chamber does not allow installing a shutter. Therefore, while stabilizing the flux of the evaporation source, the sample holder is hidden in a part of the preparation chamber where it is not exposed to the evaporation flux. For metalizing, the sample holder is moved to a position just above the evaporation source. After the desired evaporation time is passed, the sample-holder is moved forward to a third position, where the sample also is not exposed to the evaporation flux.

In order to characterize the evaporation source as well as the sample degradation due to the evaporation, the following performed experiments are described in the subsequent paragraphs:

- Verification of the tooling factor and the homogeneity of the deposit
- Verification of the chemical composition of the deposit

Copy for "Bibliothèque UCL"

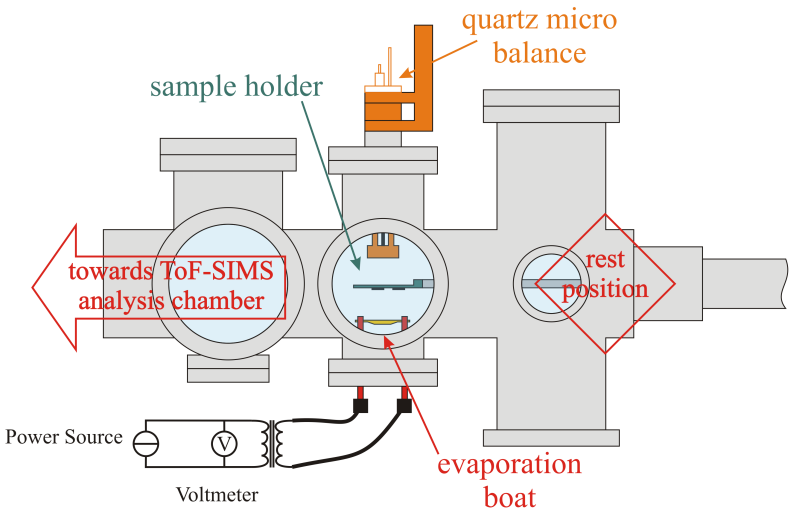


Figure 4.13: *Final position of the evaporation cell*

- Verification of the insensitivity of the polymer to the heating of the evaporation boat

4.2.2.B Tooling factor and homogeneity

Four silicon samples ($\approx 1.4\ \mathrm{cm}^2$), on which a corner was masked with a smaller ($\approx 0.25\ \mathrm{cm}^2$) silicon piece, are placed homogeneously over the sample holder. After being exposed during 130 ± 1 s to an evaporation flux of $3 \pm 0.2\ \frac{\text{Å}}{s}$ the four samples are covered, assuming an unity sticking coefficient of gold on Si, with a thickness 39 ± 2.9 nm of gold. Afterward the small silicon parts are removed and the appearing steps are measured with a surface profiler (Tencor P10).

The average of six measured step heights on each sample is noted in Table 4.8. It can be noted that the thickness of the evaporated metal is homogeneous over the four samples. Assuming a unity sticking coefficient of gold on silicon, the value of thickness of the deposited metal measured by the surface profiler are consistent with the value determined by the QCM, so that the tuned and utilized tooling factor of $F_T = 2.6$ is admissible. In addition, the thick gold

Copy for "Bibliothèque UCL"

# sample	thickness $[nm]$
1	34.7 ± 2.8
2	34.7 ± 3.0
3	36.0 ± 3.2
4	34.8 ± 2.0
Average	35.0 ± 2.7

Table 4.8: *Distribution of the gold thickness on Si samples to check the homogeneity of the evaporation. The thickness was determined by profilometry by averaging six points of measurements on each sample*

coverage obtained in this experiment served later for standards in XPS measurements (↪ *Chapter 4.5.4 and 5.1.1.B*).

Another experiment, shows the homogeneity of the deposition for lower thicknesses. Therefore five pieces of InP, homogeneous distributed on the ToF-SIMS sample holder, were metalized in the preparation chamber of the ToF-SIMS. The stabilized evaporation flux was 1.6 $\frac{\text{Å}}{s}$ and the evaporation time was 10 s, so that the evaporated gold thickness can be calculated to 1.6 ± 0.4 nm. ToF-SIMS analyses show the presence of gold without other significant organic or inorganic contaminations, which could be have added during the metalization. Afterward the thickness of the coverage were determined by XPS. Table 4.9 shows the average gold thickness on the InP determined by XPS with the two layer model (↪ *Chapter 5.1.1.A*) for the different samples of this experiment.

sample	thickness [nm]
1	1.83 ± 0.06
2	1.71 ± 0.21
3	1.73 ± 0.02
4	1.80 ± 0.19
5	2.03 ± 0.02

Table 4.9: *Distribution of the gold thickness on InP samples to check the homogeneity of the evaporation for small evaporated gold quantity. The thickness was determined by XPS analysis by averaging three points of measurements*

Copy for "Bibliothèque UCL"

Assuming that the sticking coefficient of gold onto InP is unity, the determined thickness by XPS is within the thickness range measured by the QCM, so that the tooling factor of $F_T = 2.6$ is also admissible for lower gold deposition quantity. It can be seen that the samples 1 and 4 as well sample 2 and 3 have approximately the same thickness. The thickness of sample 5, which was situated in the middle of the holder, is the highest. Knowing the repartition of the samples on the sample holder, this asymmetrical distribution of the thickness could be explained by an asymmetric geometry of the evaporation source.

In the following, it will be assumed that the thickness distribution is homogeneous. This assumption will be satisfied if the different samples are close to each other. Furthermore, as most metalization and subsequent ToF-SIMS analysis are performed only one by one, it is paid attention that the sample is fixed on a same position on the sample holder each time, so that a comparison of different deposition series is possible.

During this work it turned out that the sticking coefficient of metal onto the polymer samples is not unity, so that the values measured with the QCM are overestimate, and so have only an indicating character. The exact thickness determination is done by subsequent XPS measurements (↪ *Chapter 5.1.1*).

4.2.2.C Chemical composition of the deposit

The external evaporation of gold on the polymers showed that the metalization procedure can completely mask the polymer fingerprint (↪ *Chapter 4.2.1*). To verify qualitatively the amount of contamination and to identify the material composition added to the sample surface by the gold evaporation, spectra of a thick (≈ 13 nm) gold layer on silicon are investigated. As one can see on the figures 4.14 and 4.15, only very little contamination is observed. The most significant peaks of the spectra, probably fragments of fatty acids, are noted in Table 4.10.

Copy for "Bibliothèque UCL"

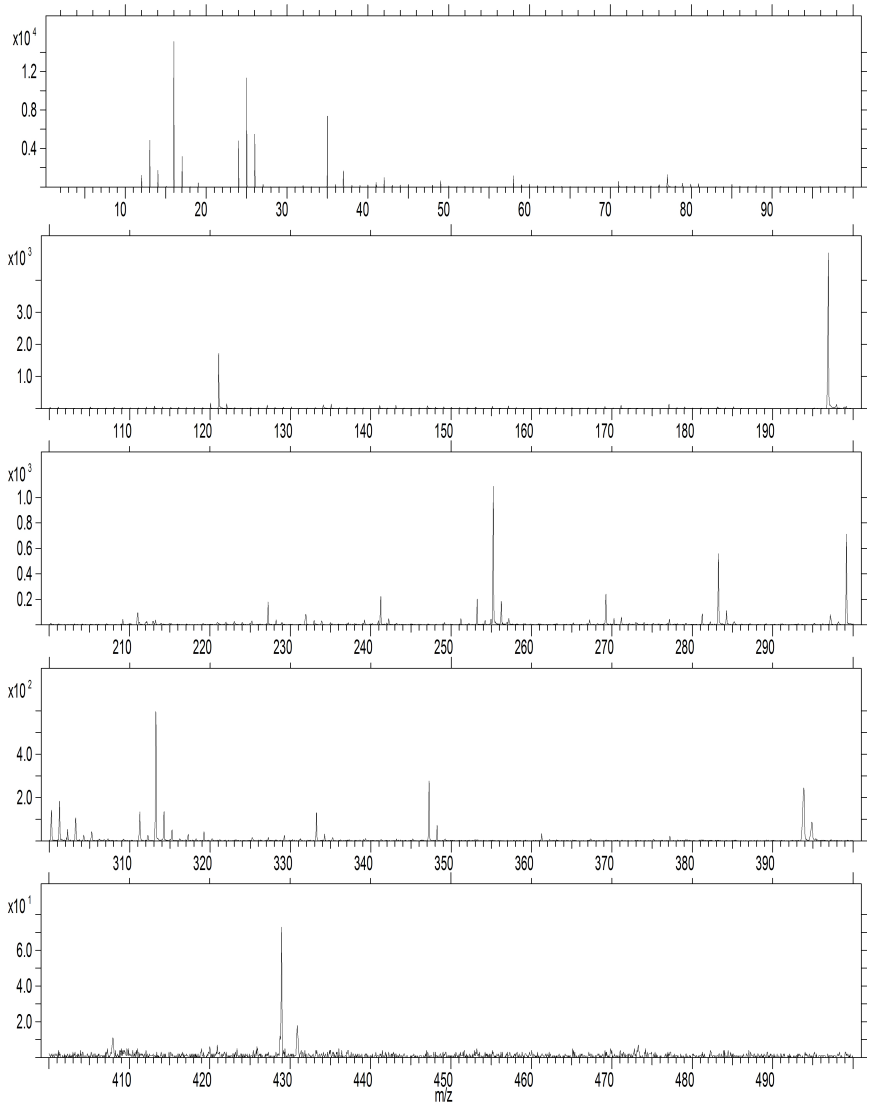


Figure 4.14: *ToF-SIMS spectrum in the negative polarity of a thick (≈ 13 nm) gold deposit on native silicon. The mass of the peaks as well as their probable label are noted in Table 4.10.*

Copy for "Bibliothèque UCL"

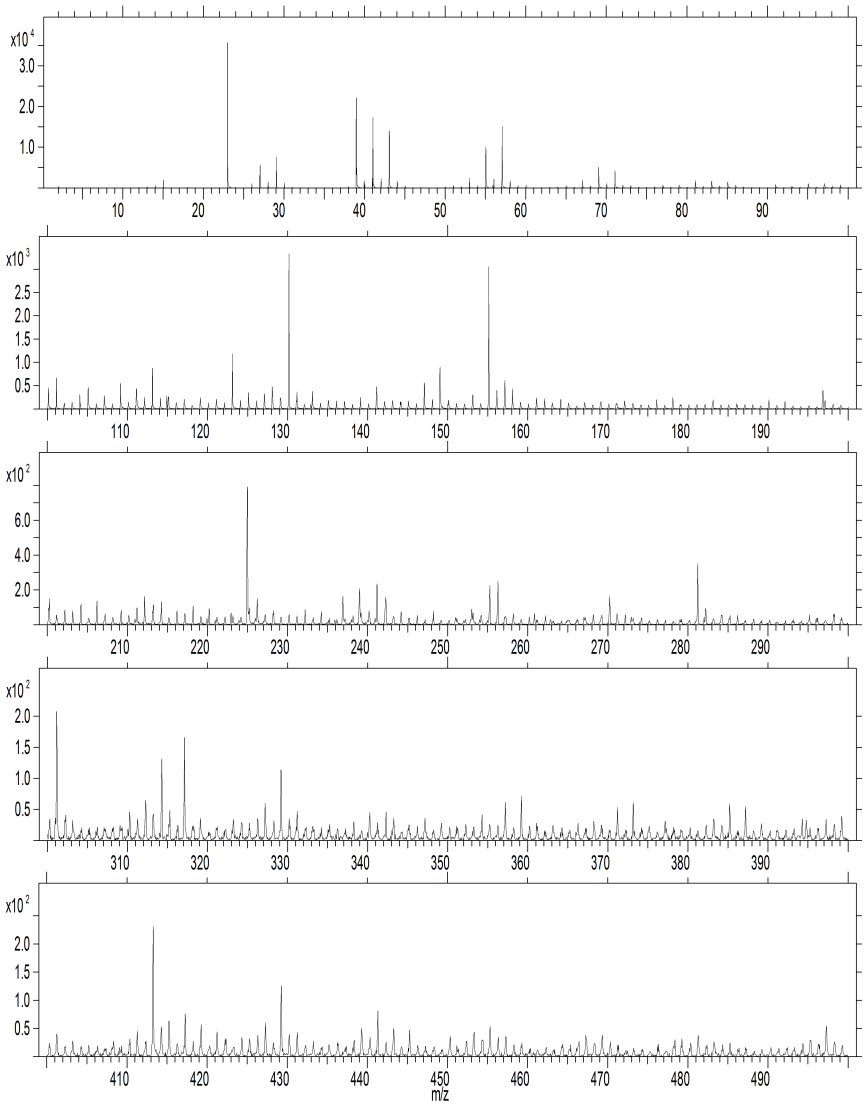


Figure 4.15: *ToF-SIMS spectrum in the positive polarity of a thick (≈ 13 nm) gold deposit on native silicon. The mass of the peaks as well as their probable label are noted in Table 4.10.*

Copy for "Bibliothèque UCL"

negative polarity		positive polarity	
Mass	Label	Mass	Label
15.99	O^-	22.99	Na^+
25.01	C_2H^-	38.95	K^+
34.97	$^{35}Cl^-$	41.03	$C_3H_5^+$
58.01	$C_2H_2O_2^-$	43.05	$C_3H_7^+$
77.04	$C_6H_5^-$	55.04	$C_4H_7^+$
121.0	$C_7H_5O_2^-$	57.06	$C_4H_9^+$
197.0	Au^-	69.06	$C_5H_9^+$
231.9	$Au\,^{35}Cl^-$	71.08	$C_5H_{11}^+$
241.2	$C_{15}H_{29}O_2^-$	130.1	$C_8H_{18}O^+$
255.2	$C_{16}H_{31}O_2^-$	149.0	
269.2	$C_{17}H_{33}O_2^-$	155.1	$C_{10}H_{19}O^+$
283.3	$C_{18}H_{35}O_2^-$	224.9	$AuCO^+$
299.2	$C_{17}O_{31}O_4^-$	281.2	$C_{18}H_{33}O_2^+$
313.2	$C_{18}O_{33}O_4^-$	301.1	
347.0		314.2	
393.9	Au_2^-	413.2	
428.9	$Au_2\,^{35}Cl^-$		

Table 4.10: *List of intense peaks observed on a thick (≈ 13 nm) gold deposit on naitive silicon. In the case where an indisputable association to an ion is possible the label of this ion is noted.*

4.2.2.D Sample degradation due to the thermal evaporation

To inhibit the diffusion of the evaporated metal into the polymer sample, the sample temperature must be below its glass transition temperature (↪ *Table 4.3*). In order to verify the insensitivity of sample degradation due to the close evaporation source distance, the temperature rise and the surface change has been examined.

To determine the temperature rise due to the heating of the evaporation boat, a thermocouple (type K - Chromel-Alumel) has been installed on a retractable manipulator at the same distance from the evaporation source as the samples. This allows measuring the temperature increase under the same conditions as the samples are

Copy for "Bibliothèque UCL"

metalized. In order to expose a greater area to the heating, the thermocouple has been winded in a spiral way.

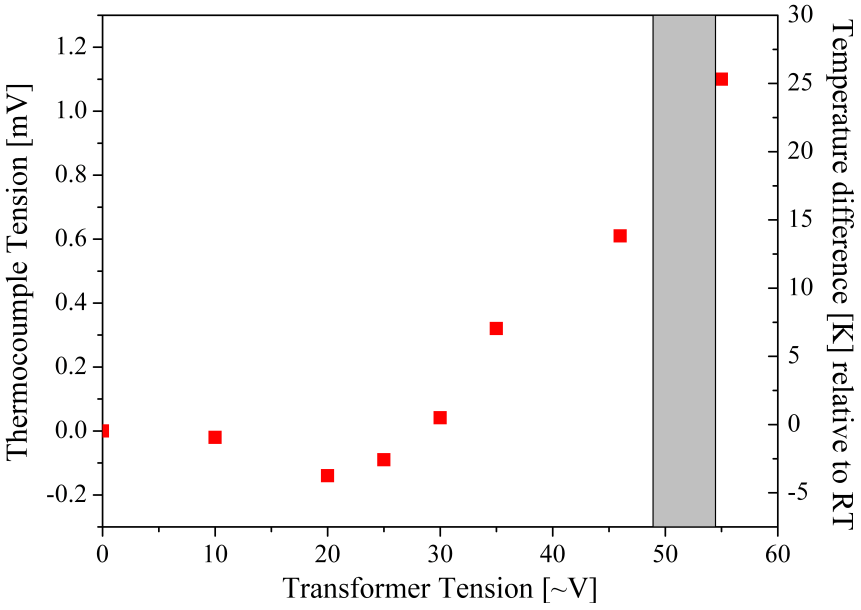


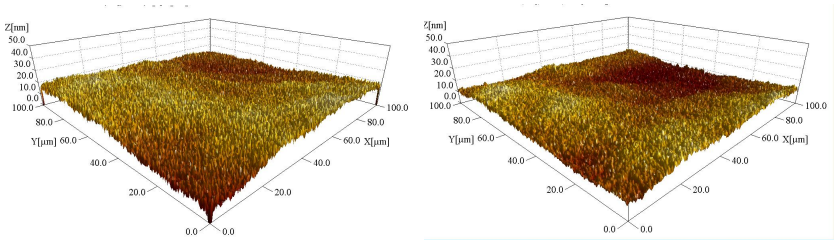
Figure 4.16: *Temperature rise as a function of the power of the evaporation source. The gray area marks the power during evaporation of gold.*

The increase of temperature for different working powers is measured after equilibrium conditions are reached. At the typical gold evaporation working power, a temperature rise of ≈ 25 K above the room temperature is observed ($\hookrightarrow$ *Figure 4.16*). As the mass inertia of the sample and the sample-holder is not considered in this experiment, the temperature increase on a sample will be lower. Thus the temperature of the sample during metalization is well below the glass transition temperature of the polymer samples, so that a diffusion of the evaporated metal can be excluded.

Furthermore to exclude any surface modification a blank evaporation was performed. Therefore a new evaporation boat was installed into the evaporation cell and the evaporation system was outgased for a while. Then polymer samples are exposed ≈ 30 s to typical evaporation conditions. With gold inside the evaporation boat a deposition of

Copy for "Bibliothèque UCL"

several nanometers of gold would have been evaporated onto the polymer samples. Afterward the ToF-SIMS spectra and the topography were compared with those of pristine/untreated samples.



(a) *pristine* **(b)** *after heat treatment*

Figure 4.17: *Confoval Microcopy (fov:* $100 \times 100\mu m^2 \times \approx 50\text{nm}$*): Topography of pristine and heat-treated spincoated polystyrene - measurements kindly provided by Novelis Luxembourg S.A.*

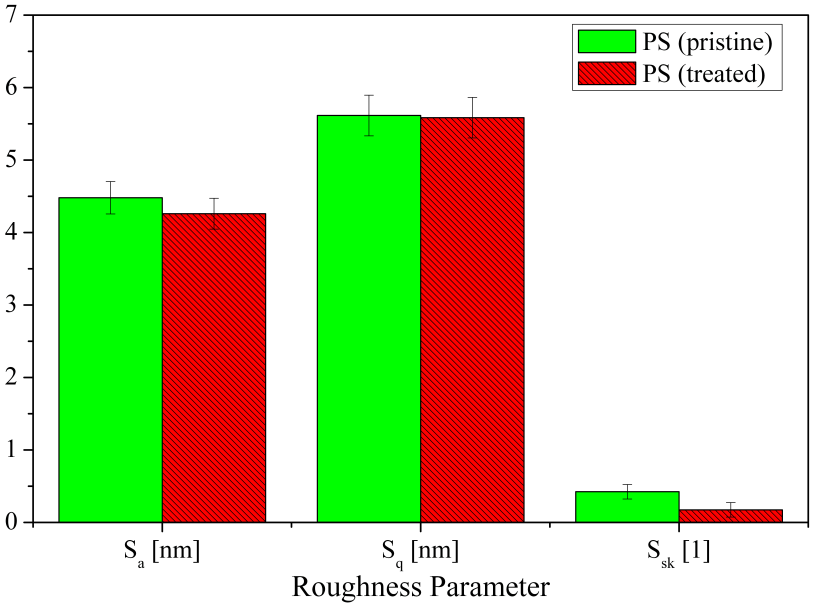


Figure 4.18: *Roughness parameter for the pristine polymer (PS) and the heat-treated pristine polymer.*

Copy for "Bibliothèque UCL"

No difference between the ToF-SIMS spectra of the pristine sample and the heat-exposed sample is observed, so it can be admitted that the evaporation cell does not spread any organic or inorganic material itself. Additional to AFM measurement, the topography of the samples have been determined by a confocal microscope, which was kindly provided by *Novelis Luxembourg S.A.* (↪ *Figure 4.17*). Here also no difference between the samples can be observed, so that the roughness parameters show similar values for both samples (↪ *Figure 4.18*). It can be concluded that no unwanted modification of the sample surface is induced by the evaporation method.

4.3 ToF-SIMS

A secondary ions mass spectrometer (SIMS) setup must be capable to perform different kind of analysis, e.g. acquisition of survey mass spectra, depth profiles and images. In order to make SIMS analysis of organic samples possible, the sputtered matter must not exceed 1 % of a monolayer (↪ *Chapter 3.2.4*). As only a minor part of the ejected particle are charged and therefore could be analyzed, a good detection sensitivity and high analyzer transmission of the secondary ions are necessary, in order to detect sufficient secondary ions from the sample over a large m/z range within the static limit. Nowadays, mainly time-of-flight (ToF) analyzers are used in S-SIMS. Time-of-flight spectrometers allow detecting a quasi-unlimited mass range and contrarily to magnetic field or quadrupole spectrometers, a quasi-parallel detection of all emitted secondary ions of one polarity occurs. In the following paragraphs a short overview of a ToF-SIMS instrument is given.

4.3.1 Primary particles bombardment

To increase the mean free path of the primary and secondary ions and to prevent sparkover in the ion optics components, ultra high vacuum (UHV) is required. The UHV ($< 1 \cdot 10^{-8}$mbar) is reached by the use of a system of primary rotary pump and turbomolecular pumps. In order to allow a fast introduction of the sample without venting the whole analysis system and consequently introduce uncontrolled

Copy for "Bibliothèque UCL"

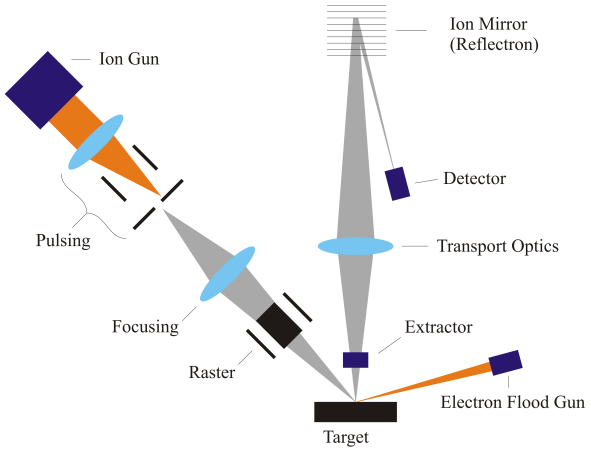


Figure 4.19: *Draft of the main components of a SIMS.*

contamination, the samples are locked into the analysis chamber through the introduction chamber, which is pumped by an independent system of primary rotary and turbomolecular pumps.

To adjust the position of the sample under the primary ion beam, the sample holder is attached inside the analysis chamber on a 5-axis manipulator, which permits a movement of the sample in all three spacial directions as well as tilting and rotating of the whole sample. The position of the sample can be observed by a stereo microscope.

In this work argon primary ions, which are produced by electron impact, are used to obtain secondary ion mass spectra of high mass resolution. The continuous beam of argon ions, which is extracted from the source, is sectioned with a 90°-deflection unit into $100 - 150$ ns long ion packages. These are reduced even more to a typical ≈ 2.5 ns pulse length by an electrodynamic bunching system. The ion beam is then focused so that the beam can be used as microprobe. Thereby the focused beam is rastering over the sample, so that a surface of several hundred square micrometers can be homogeneously bombarded and a full mass spectrum is acquired from each point.

The particle bombardment of non-conducting materials leads to a more or less drastic change of the surface potential, which causes disturbance in the SIMS analysis. The most used method for charge

Copy for "Bibliothèque UCL"

neutralization in SIMS is the bombardment of the sample surface with low energy electrons, which are created by an electron flood gun. In order to prevent damaging the detector, the electrons should be hindered to enter into the analyzer. Hagenhoff et al. have elaborated a technique based on the low duty-cycle ToF system: after each primary pulse the extraction voltage is removed and $20\,eV$ electrons from a pulsed flood gun impinge on the sample [4].

4.3.2 Mass Analyzer

All types of ToF-SIMS instruments are based on the same principle: The secondary ions, created by the ion bombardment, are accelerated to a constant kinetic energy by the extractor voltage. Thereafter the secondary ions pass a certain distance in a field free environment, where they conserve their velocity, before they are collected on a single-count detector. Basically the secondary ion velocity at the entry of the field-free region depends on the mass to charge ratio m/q of the secondary ion, and therefore the time of flight t of the ions in the field free region of the analyzer can be related to the mass to charge ratio of the detected ion:

$$t \propto \sqrt{\frac{m}{q}} \tag{4.6}$$

In reality, the sputtered particles have an initial velocity ($v_0 \neq 0$), so that ions with the same mass enter the analyzer with different velocities. In order to get a better mass resolution, the distribution of the secondary ion velocities is corrected by an electrostatic mirror, which is composed by a assembly of electrostatic equidistant rings. This type of analyzer is called two stage-reflectron.

The detection of the different secondary ions, which are separated by their flight time (and hence by mass), is performed by a arrangement of a microchannel plate, a scintillator and a photomultiplier. To improve the detection of high mass secondary ions, a post-acceleration of $5 - 10\,kV$ is applied to all secondary ions before their impact on the channelplate. In the end, the signal is normalized by a constant fraction discriminator and further processed in a time-to-digital converter (TDC) before the signal is treated by a personal computer in order to display the acquired spectrum.

Copy for "Bibliothèque UCL"

The separation power of secondary ions of the same nominal mass to charge ratio is expressed in the mass resolution R, which is defined as the ratio of the mass m and the mass difference Δm. For a ToF analyzer, the resolution is traditionally calculated from one peak, where Δm is defined as FWHM (full width at half maximum) of the peak. For a linear drift tube, with an identical time-mass relation as in Equation 4.6 the mass resolution can also be expressed with time.

$$R = \frac{m}{\Delta m} = \frac{t}{2 \cdot \Delta t} \tag{4.7}$$

where Δt is influenced by the variation of primary pulse length, the dead time of the detection system and the aberration of the time flight analyzer optics.

4.3.3 Experimental Setup

The ToF-SIMS III instrument (1992, ION-TOF GmbH, Münster, Germany) at the CRP-Gabriel Lippmann is a reflector-based instrument (↪ *Figure 4.20*). It is equipped with three primary ion sources (an electron impact ion gun with argon primary ions, a gallium liquid metal ion gun and a cesium sputter gun). All ion beams reach the sample, which is kept at ground potential, with an angle of 45° and the secondary ions are extracted perpendicular to the sample surface by an extraction potential of 2 keV. After the reflection, the secondary ions are post-accelerated to an energy of 10 keV before they reach the detector. A pulsed low-energy (≈ 20 eV) electron source can be used for charge compensation. The achievable mass resolution of the ToF-SIMS III used in this work about $3000 - 4000$ at mass 41 u for organic ions.

In each polarity, mass spectra on three different areas ($\approx 100 \times 100$ µm^2) are acquired. The analysis are performed with primary argon ions. The pulse width was tuned to $2 - 2.5$ ns. The time resolution of the TDC is set to 472 ps. A cycle time of 150 µs permits a detection of secondary ions up to a mass of ≈ 2000 u. The primary ion current was ≈ 0.7 pA and the acquisition time was 180 s, so that the total primary ion fluence ($\approx 8 \cdot 10^{12}$ cm^{-2}) is below the static limit.

Since the polymer films, which are analyzed in this work, are thin (↪ *Figure 4.8*), a good electrical conductivity of the samples is ensured. Hence no electron flood gun is used and surface damage

Copy for "Bibliothèque UCL"

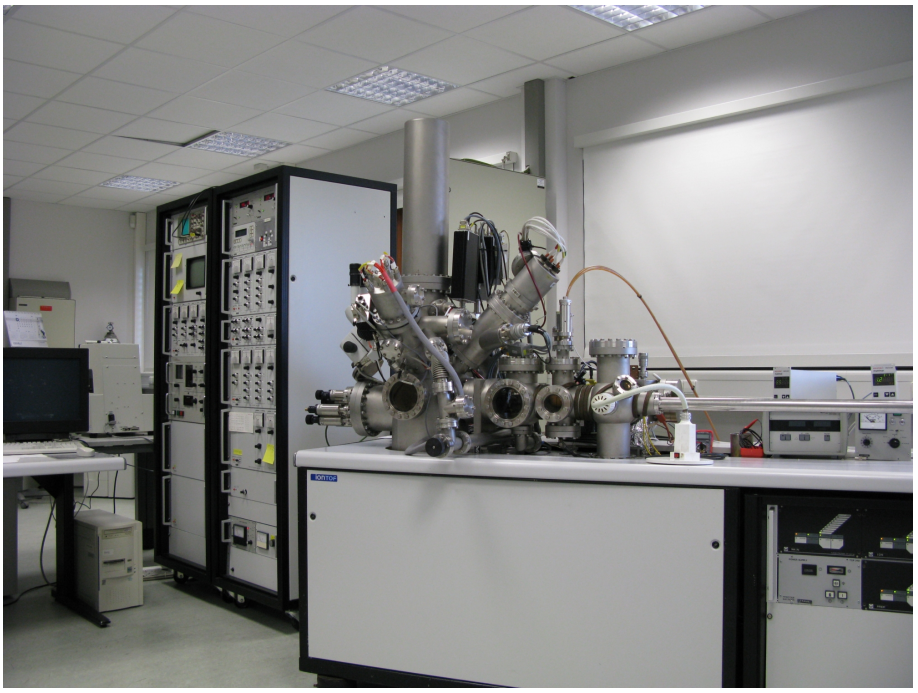


Figure 4.20: *Photo of the ToF-SIMS III instrument at the SAM department of the CRP-Gabriel Lippmann.*

caused by electrons can be excluded [59]. The small shift in the initial kinetic energy of the emitted secondary ions, which occurs inter alia due to minor electrostatic charges during the ion bombardment [239], is compensated by the means of an electrostatic mirror in the analyzer.

Before further sample manipulation/analysis are performed, it is checked that the polymer sample shows the characteristic fragments and intensities as well as that no significant contamination is present. The spectrum of all pristine polymers in the mass* $30 - 300$ u can be found in the annex A.2. They clearly show the characteristic fragments in the predicted intensity found in the literature [234, 240, 241]. For the completeness, the structural information of the most characteristic fragments can also be found in the annex A.2.

*As multiple-charged fragments are very rare, and for alleviating the reading, the measured mass-to-charge ration m/z is designated in this work as mass m. The unit is atomic mass unit (u) or Dalton (Da).

Copy for "Bibliothèque UCL"

Between the analysis chamber and the air-lock, the used ToF-SIMS III instrument has a third chamber. In this preparation chamber the evaporation cell, which is used in this work, is installed (↪ *Chapter 4.2.2*). Furthermore to minimize the disturbance in the analysis chamber during the maintenance of the evaporation system, substantial modification of the vacuum system have been carried out.

4.3.4 Data Evaluation

Due to the principle of the ToF-analyzer, where the detection time is registered, the mass scale must be calibrated. This is done by assigning multiple characteristic peaks to their exact mass. To assure the same evaluation on every spectra, it is essential to superpose all the spectra, so that eventually manual adjustments in the mass calibration must be performed.

Even with a reflectron mass analyzer, not all the secondary ions of the same mass reach the detector at the same time, which results in a broadening of the peaks in the mass spectrum. In order to consider all the detected ions, not the peak height is used as ion intensity, but the integrated peak signal in a mass range. This ion peak area is called hereafter intensity, which is exported to MS Excel for further data treatments (average, ratio, principle components analysis, ...). The exact data treatment depends on the problem and is described in the corresponding result chapter.

4.4 AFM-Instrumentation

The AFM consists in a sharp tip that is scanned by means of piezoelectric ceramics over the specimen surface (↪ *Chapter 4.4.1*). The tip is mounted on a microscale cantilever, which bends when the tip is brought into proximity of a sample surface. This deflection, due to the forces interacting between surface and tip (↪ *Chapter 3.3*), is evaluated by a detection system (↪ *Chapter 4.4.2*).

Because of the high sensibility of a SPM, a protection against external influences is necessary. External vibrations, which disturb the SPM measurements, are minimized by placing the measuring head of

Copy for "Bibliothèque UCL"

the microscope on a vibration-insulating platform. Protection against acoustic noise, which also lets oscillate the tip, is done by placing the SPM head in an enclosure.

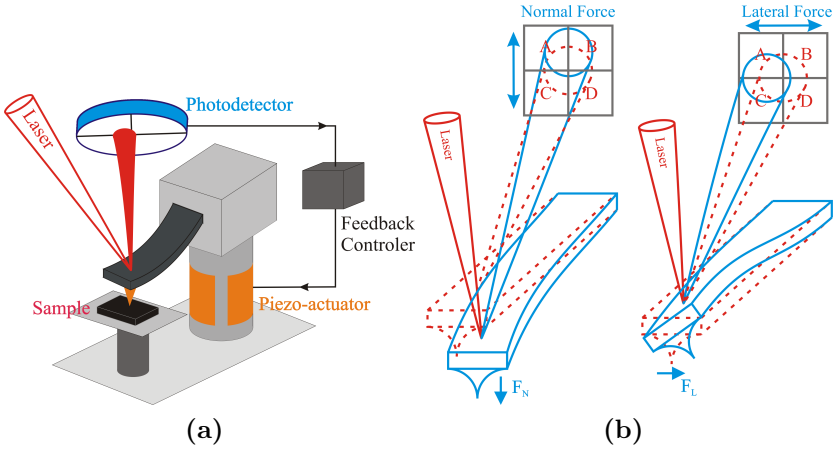


Figure 4.21: *a) Main AFM components and b) Laser spot deviation due to cantilever deformation (adapted from [242]).*

4.4.1 Scanning elements

In order to scan the sample surface with high accuracy, it is necessary to control the tip-position in each space direction. Today the SPM scanning devices are made of piezoelectric materials, which have the property of changing their sizes in an external electric field [243]. The most used design for them is a hollow thin-walled piezoelectric cylinder (tubular piezoelement) with electrodes on the external and internal tube surfaces, which allow movements in each three directions (x,y,z) by using control voltages.

4.4.2 Detection System

The deflection of the cantilever, due to the interacting forces, is mostly measured by a beam bounce detection system. Thereby a laser beam, which is produced by a diode, is focused by an optical system onto the cantilever and its reflection is detected at a four-section

Copy for "Bibliothèque UCL"

photodetector (↪ *Figure 4.21a*). The four-section photodetector detection system permits to distinguish between the bending of the cantilever due to the attractive and/or repulsive force F_N and the torsion of the cantilever due to lateral forces F_L (↪ *Figure 4.21b*).

4.4.3 Operating modes

The deformation of the cantilever due to the forces between the sample and the tip is common to all SPM measuring modes. In dependency of the tip-sample distance, three main modes of an AFM can be distinguished (↪ *Figure 3.8*):

Contact mode: In this mode the topography of the sample surface is determined by measuring the sum of attractive and repulsive forces between the surface and the sample surface. During the scanning of the tip over the sample, the tip is in contact with the sample and the variation of the intensity of the laser beam reflection is recorded in each quadrant of the photodetector. Thereby not only the cantilever deflection is recorded but also its torsion due to the friction force. Beside the constant height mode, mainly the constant force mode is used in contact AFM. Thereby the electric voltage of the piezoceramic is controlled by a feedback loop during the scanning in order to keep the sum of the interacting forces between surface and tip constant, so that the cantilever deflection is kept constant.

Tapping mode: In this so-called intermittent-contact mode, a piezo-vibrator lets oscillate the cantilever near its resonant frequency (typically $100 - 400$ kHz). Thereby the tip approaches perpendicular toward the sample until the tip barely touches the sample surface. As opposite to the contact mode, the tip is not dragged along the surface, so that no lateral forces, which could damage the sample, occur.

Because the cantilever oscillation amplitude changes in response to tip-to-sample spacing, the topography of the sample can be acquired. In order to detect even small changes in the amplitude and in the phase of cantilever oscillations in non-contact mode, the amplitude is kept constant by dint of a feedback loop. The

Copy for "Bibliothèque UCL"

phase shift between the piezoceramic frequency generator of the cantilever and the cantilever oscillation provides also some data of the sample surface properties. This so-called phase imaging responds sensitive to, inter alia, adhesion and viscoelasticity of the sample surface.

Non-contact mode: In this mode the cantilever vibrates near the surface of a sample. The spacing between the tip and the sample is in the order of tens to hundreds of angstroms. This mode, in combination with another mode, is especially used in electric force microscopy (EFM) and magnetic force microscopy (MFM).

4.4.4 Experimental Setup

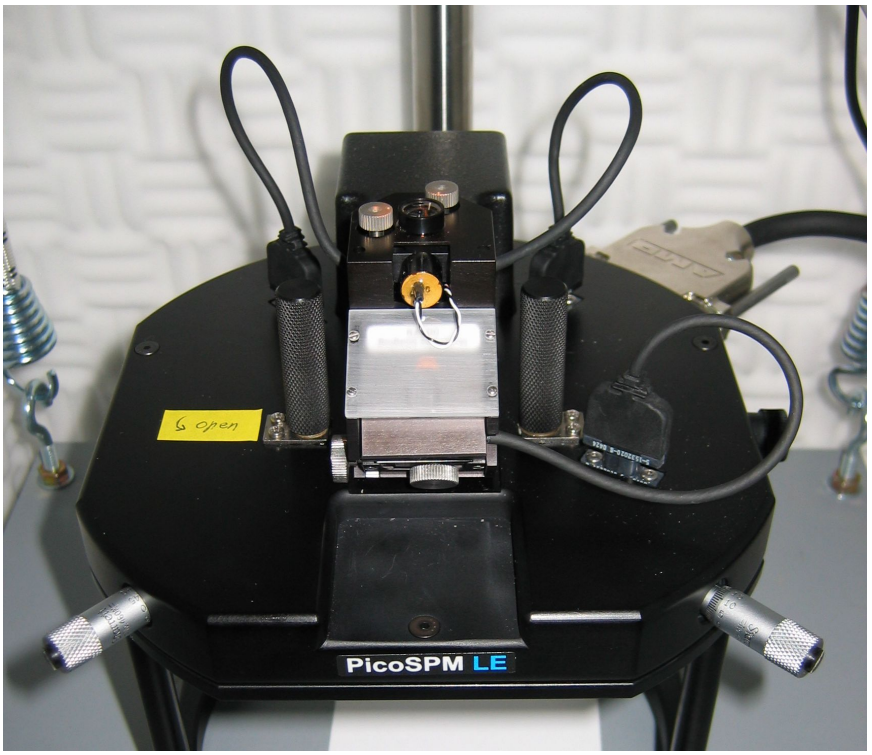


Figure 4.22: *Photography of the AFM instrument in the CRP-GL*

Copy for "Bibliothèque UCL"

The AFM measurements were performed on a PicoLE™ from Molecular Imaging (now Agilent Technologies, Inc.) (↪ *Figure 4.22*) using the acoustic mode (tapping mode) which minimize the sample damage. On different random sample points, topography and phase images of different scan sizes are acquired using the small piezoceramic scanner (max scan area: $9\mu m \times 9\mu m \times 2nm$). Regularly the Pointprobe® cantilever from NanoWorld AG was replaced. The main characteristics of the utilized points are noted in Table 4.11. The integral and the proportional gain were adjusted so that the amplitude signal shows least texture. A scan speed of $1\frac{line}{s}$ was not exceeded.

Tip radius	< 10 nm
Thickness	4 µm
Mean Width	30 µm
Length	125 µm
Force Constant	42 N/m
Resonance frequency	≈ 320 kHz

Table 4.11: *Main characteristic parameters of the Pointprobe® cantilever from NanoWorld AG (from Datasheet).*

4.4.5 Data Evaluation

The physical meaning of SPM images depend on the parameters used in the feedback loop and on the properties that are measured. Mainly the topography images are evaluated in this work.

The SPM surface images normally show inclination, which is mainly due to a tilted installation of the sample onto the scanner or due to non-flatness of the sample. Inclined images take a large portion of Z-axis, so that the small image details does not become visible. To eliminate this inconvenience, a subtraction of the constant inclination is usually performed by software tools.

Due to small movements in the elements of the head structure or due to changes on the tip form (e.a. capture of a micro particle from the surface by the tip) the tip-sample distance changes frequently during scanning. This produces steps parallel to the direction of scanning and

Copy for "Bibliothèque UCL"

these defects in SPM images can be corrected by using a line-by-line average procedure in the software tool.

SPM images can also be affected by hardware noises, instabilities of the tip-sample contact during scanning, external vibration, etc. Theses SPM image noises can be removed using software tools with help of different filters. High high-frequency random noise in SPM images can be removed by using the median filter. Applying filters to images should be done with care. It is important not to remove any information from the images. This is checked by watching for some unexpected texture on the difference image between the original and the processed images.

In summary, first a leveling of the SPM images is performed. Then, depending on the information one wants to obtain, different filters are applied to the images. For roughness calculations the use of filters are minimized, for grain detection a combination of different filters is applied to the images. SPIP™ (Scanning Probe Image Processor) version 4.5 is used as software tool.

4.5 XPS

An XPS spectrometer consists in a X-rays source and an electron energy analyzer. The X-ray, which is generated in the source (↪ *Chapter 4.5.1*), impinges on the sample from where photoelectrons and Auger electrons are emitted in a wide angular range. These electrons are collected by the transfer lens and focused into the entrance of the analyzer. In the analyzer (↪ *Chapter 4.5.2*) the electrons are separated according to their kinetic energy and are finally registered in the detector.

4.5.1 X-Ray Source

In commercial XPS instruments, the X-rays are generated by the bombardment of a metallic target (anode) with a high-energy ($10 - 15\,keV$) electron beam. The energy of the emitted X-rays depends on the anode material and the intensity of the X-ray beam depends on the number of electrons striking the anode and their energy. Less than 0.1% of the electron energy is converted into X-rays. The major part is converted into heat by absorption so that the source must be

Copy for "Bibliothèque UCL"

cooled down by water. The generated X-ray pass a thin aluminum windows (thickness: $< 2\mu m$, transmission: 93%), which shields the sample chamber from the field generated in the source region and prevents sample contamination (desorption from filament). A welcome side effect of this non-monochromatic X-ray gun and thus of the thin aluminum window is, that low energy electrons are emitted from the aluminum foil, so that the occuring charges on insulating samples can be partly compensated.

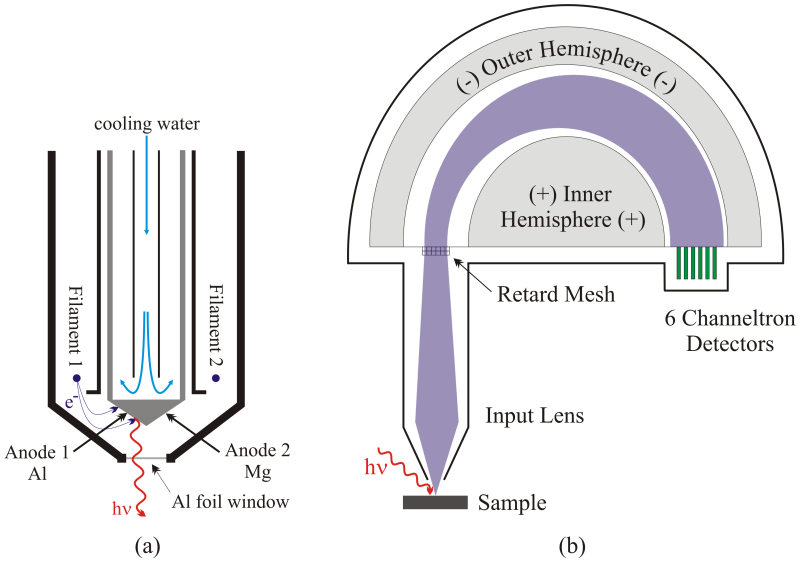


Figure 4.23: *Typical components of an XPS instrument: Schematics of a) a twin anode X-ray source - b) Hemispherical electron energy analyzer used in the Thermo VG Microlab 350.*

4.5.2 Electron Kinetic Energy Analyzer

The purpose of the analyzer is to separate the electrons by their kinetic energy. The Thermo VG Microlab 350, which is used in this work, is equipped with a hemispherical sector analyzer (HSA) (↪ *Figure 4.23(b)*). Because the kinetic energy of the electrons ejected from the sample is usually too great for the analyzer

Copy for "Bibliothèque UCL"

to obtain a sufficiently high resolution, the electrons are decelerated by passing a retard mesh before they enter the analyzer.

Due to a potential difference, which is applied across the two hemispheres, the electrons, injected tangentially at the input to the analyzer, will only reach one of the six channeltron detectors if their kinetic energy E_{kin} is equal to:

$$E_{kin} = k \cdot e \cdot \Delta V \tag{4.8}$$

where e is the electron charge, ΔV is the potential difference between the hemispheres and k is known as the spectrometer constant. In XPS, the instrument is used in the constant analyzer energy mode, where the electrons are retarded to a preselected kinetic energy and therefore the absolute energy resolution (ΔE) is constant throughout the whole spectrum.

4.5.3 Experimental Setup

The XPS measurements were performed on a Thermo VG Microlab 350 instrument, which is equipped with a twin anode X-ray source and an hemispherical sector analyzer. In this thesis the aluminum anode, which produces $K_{\alpha 1,2}$ X-rays at an energy of $1486.6\,eV$ is utilized as X-ray source. The power of the source was tuned at $100\,W$ which provide a good signal/noise ratio and minimize the irradiation defects on the polymer samples.

The samples were analyzed with a take-off angle of $\beta = 0\,^\circ$ (the analyzer axis is perpendicular to the sample surface) and, on each sample, spectra were recorded on three different points. On each analysis point, different kind of spectra, depending on their later utilization, are recorded. Thereby the pass energy, which has an influence on the analyzer resolution, has varied. Table 4.12 indicates the pass energy as well as the purpose for the different kind of spectra. Afterwards the spectra were calibrated with the help of the $C-C/C-H$ component of the $C1s$ peak, which was defined at a binding energy of $285.0\,eV$.

4.5.4 Data Evaluation - Thickness determination

In this work, the XPS technique is mainly used to determine the deposited amount of gold on the polymer sample. Within XPS, the

Copy for "Bibliothèque UCL"

type of spectra	pass energy	purpose
survey: overall view of the spectra	100	elemental identification
high energy resolution	20	quantification and chemical identification
Tougaard method	50	study of background

Table 4.12: *Pass energy for the different type of acquired spectra.*

current of the collected photoelectrons of a specific element A in a homogeneous sample can be described as:

$$I_A = J \cdot k \cdot \sigma_A \cdot \lambda_A \tag{4.9}$$

where J (in $\frac{photons}{cm^2 \cdot s}$) is the X-ray flux density of the source at the analysis position, k the instrumental factor, σ_A the specific sensitivity factor of the element and λ_A the inelastic mean free path of the photoelectrons.

One approach to determine the thickness of an homogeneous overlayer is based on the assumption that an increasing overlayer thickness causes an exponential attenuation of the photoelectron signal.

The sample storage at the atmosphere between the gold evaporation and the XPS characterization, leads to an additional thin layer of organic contamination onto the metalized polymer samples. This additional layer requires that the previous two layer model is modified, so that, by reconstructing the experimental spectrum with two reference spectra, the contamination layer can be considered.

Because no spatial distribution of the deposited gold is taken into account with the homogeneous layers models, the assumption of an homogeneous overlayer of gold is in conflict with the observed structure of the overlayer in AFM, SEM and TEM (↪ *Chapter 5.2*). Therefore another method developed by S. Tougaard et al. is used to determine the deposited gold quantity including the spatial information of the deposit. This method relies on the phenomenon that the spectrum shape nearby at lower kinetic energy of all XPS peaks carries depth information of the emitted electrons and thus information on spatial repartition of the detected element [244, 245].

A detailed description of the different utilized evaluation methods of the XPS spectra is presented in Chapter 5.1.1.

Copy for "Bibliothèque UCL"

4.6 Electron Microscopy - Instrument

Electron propagation necessitates that the whole instrument is operated at a pressure of $< 10^{-5}$ mbar. The electrons, which are emitting from the electron gun (cathode), are accelerated by a tension of $1 - 200$ keV toward the anode. With a system of 2-3 electromagnetic lenses and apertures, the electron beam is focalized onto the sample. Furthermore the apertures reduce the aberrations and the intensity of the electron beam. Deflector plates, situated before the last lens, permit to scan the electron beam over the sample.

Normally a TEM is used, contrarily to a SEM, as a microscope so that no deflection plates are needed. In that case the lenses and apertures allow the beam of the primary electron to homogeneous irradiate the sample.

In Table 4.13 a comparison between different electron gun is shown. In general the electron guns can be classified into two categories:

Thermoelectric emission: the energy that is needed to emit electrons is obtained by heating a filament (tungsten or LaB_6)

Field emission: the electrons are emitted due to a high electric field between the cathode and anode.

Cathode	curvature radius $[\mu m]$	working temperature [K]	life time [h]	Brightness $\left[\frac{A}{cm^2 \cdot sr}\right]$	lateral resolution [nm]
Tungsten	100	2700	10−100	$\approx 5 \cdot 10^4$	10
LaB_6	$1 - 10$	2000	$\gg 100$	$\approx 5 \cdot 10^6$	
Field emission	0.1	300-1200	$\gg 1000$	$10^7 - 10^9$	1

Table 4.13: *Comparison of theoretic characteristics of different electron guns.*

The emitted signal from the sample (secondary electrons, back-scattered electrons, transmitted electrons, X-rays) due to the primary electron bombardment, is collected by the corresponding detector. Thereby the scanning of the electron beam over the surface

Copy for "Bibliothèque UCL"

is synchronized with the detectors, which permits to form an image of the sample. The brightness of each image point is directly associated to the intensity of the detected signal. Depending on the signal and the kind of electron microscope, the corresponding image contains different information (↪ *Chapter 3.5.3*).

- The secondary electron based images, which are mainly used in SEM, give rather a information about the topography of the sample.
- The probability that an electron is deflected from its direct path by an interaction with an atom increases with the atomic number Z_A. Therefore, heavier elements represent more powerful scattering centers than light elements, so that the contrast of areas in which heavy atoms are localized will appear in back-scattered electron mode brighter than of such comprising light atoms.
- Contrarily to SEM, the scattered electrons cause darker areas in TEM. Furthermore, the number of actually occurring scattering events depends on the numbers of atoms that are lying in the path of the electron. As the result, there are more electrons scattered in thick samples than in thin ones, so that, in TEM, thick areas appear darker than thin areas of the same material. However, for scattering events in the TEM, the sample thickness does not exceed the typical mean free path of electron, which is in the range of some tens of nm.

The scanning electron microscope (StereoScan 430i - Leica, Germany, 1994) available in the CRP-Gabriell Lippmann is equipped with a secondary electrons, back-scattered electrons and X-ray detector. Because this instrument uses a tungsten filament as electron gun, the achievable lateral resolution is not sufficient to image the gold grains on the polymer samples.

In the frame of the acquisition of a new generation SEM, also polymer samples with different amount of gold deposition were tested in different SEM from various companies with a field emission gun. These images are shown in this work.

The TEM images where acquired on a LEO 922 Omega (Leo, Germany, 1994) with a LaB_6 tip (from Denka). The acceleration voltage

Copy for "Bibliothèque UCL"

was 160 kV and the observations were performed in bright field mode with zero loss energy filtering (EF-TEM). The pictures were obtained on a Proscan CCD camera, with the maximal resolution of 1 MP. The samples were observed at two different magnifications (g:500 000X, 1 000 000X).

For data evaluation, first the field of view was exactly determined by dint of the scale bar, which is incorporated in the electron microscope images. For a further image evaluation the scale bar as well as the whole caption of the images are cropped. This image is opened with SPIP™, where the determined size of the image is also entered. To reduce the noise in the image, a median filter is applied to the image. Subsequently the detection of the grains is performed by applying a threshold (automatic value). The obtained distribution of the grain parameters are fitted , if possible, by a non-symmetrical distribution using the solver-function of the MS Excel.

Copy for "Bibliothèque UCL"

Copy for "Bibliothèque UCL"

Chapter 5

Gold Quantity and Surface Morphology

This chapter deals with a detailed characterization of the gold overlayer.

In the first Section 5.1 the exact amount of gold is determined by XPS. Therefore different models for the evaluation of XPS spectra are presented. It turns out that it is necessary to consider a contamination layer on the top of the deposited gold. At the end, similar sticking coefficients of gold on the different polymer layer are found by two independent evaluation methods.

After the determination of the exact amount of deposited gold, in the Section 5.2, the morphology of the gold layer is determined by different imaging techniques. Although the AFM analyses provide 3-dimensional data of the surface, an evaluation of these images turned out to be difficult (↪ *Chapter 5.2.1*). Only the images acquired by electron microscope allow a reliable interpretation of the surface structure, so that a detailed characterization of the deposited gold morphology is presented here (↪ *Chapter 5.2.2*).

In the subsequent Chapter 6, the results obtained in this chapter are used to explain the influence of the gold deposit on the secondary ion emission.

The samples in this chapter were prepared exactly as for ToF-SIMS analysis: A 1% polymer solution was spincoated on a clean silicon substrate (↪ *Chapter 4.1.2*). Then the samples were individuallly

Copy for "Bibliothèque UCL"

metalized inside the preparation chamber of the ToF-SIMS with different gold amounts by using similar evaporation rate ($\approx 0.08\frac{nm}{s}$) and various exposure time.

5.1 Determination of the Sticking Coefficient

5.1.1 XPS Analysis

In order to assure a correct measurement of the deposited metal quantity, the settings of the quartz crystal microbalance (QCM) should be adjusted. This is done by setting the correct density for gold, and by adjusting the tooling factor F_T, which corrects the measured flux due to the geometric arrangement of the evaporation cell. The tooling factor, which is an internal parameter of the QCM electronics, causes that the displayed value corresponds to the amount of matter, which strikes on the sample*. Assuming a unity sticking coefficient of gold on silicon or InP, the thickness values of the deposited metal measured by the surface profiler or by XPS fit in the error range of the value determined by the QCM, so that the utilized tooling factor of $F_T = 2.6$ is admissible. Chapter 4.2.2.B gives more details about calculation and determination of the tooling factor.

To determine the exact amount of deposited gold on polymers, XPS analysis are performed on a couple of polymer samples subsequently to the ToF-SIMS analysis. The concentration of an element inside a sample is proportional to its corrected peak area in the XPS spectra. Because the created photoelectrons may collide in an inelastic way with the atoms inside the sample, which create a kind of unwanted background intensity (↪ *Chapter 3.4.6*), it is necessary to remove mathematically this background signal from the spectrum before quantifying the spectrum. In this work a linear background is used for determining the peak area between the limits noted in the Table 5.1.

*In all the displayed thicknesses and evaporation rates in this work, the tooling factor has already been considered.

Copy for "Bibliothèque UCL"

	Binding energy $[eV]$	
	lower limit	upper limit
$C1s$	280.1	294.5
$Au4f$	80.1	94.0

Table 5.1: *Limits of the $C1s$ and $Au4f$ peaks used for the reconstruction and thickness evaluation.*

5.1.1.A 2 Layer Model

In the simplest model used in this work, the thickness of an homoegeneous overlayer ($\hookrightarrow$ *Figure 5.1(a)*) assumes that an increasing overlayer thickness causes an exponential attenuation of the photoelectron signal. For a flat and homogeneous substrate S with an homogeneous overlayer O of thickness d the intensities of the overlayer and the substrate signals are:

$$\begin{aligned} I_o &= J \cdot k \cdot \sigma_o \cdot \left[1 - \exp\left(\frac{-d}{\lambda_o \cdot \cos(\beta)}\right)\right] \\ I_s &= J \cdot k \cdot \sigma_s \cdot \exp\left(\frac{-d}{\lambda_s \cdot \cos(\beta)}\right) \end{aligned} \tag{5.1}$$

where σ_o and σ_s are the sensitivity factors, λ_o and λ_s are the inelastic mean free path of the photoelectrons in the respective layer, k the instrumental factor and β is the take off angle (with respect to the surface normal) of the emitted photoelectrons.

In order to get rid of the unknown instrumental factor k and the X-ray flux J, the analysis are performed in the same conditions and the ratio $\frac{I_o}{I_s}$ of the two equations 5.1 is calculated:

$$\ln\left(\frac{\frac{I_o}{\sigma_o}}{\frac{I_s}{\sigma_s}}\right) = \ln\left(1 - e^{\frac{-d}{\lambda_o \cdot \cos(\beta)}}\right) + \frac{d}{\lambda_s \cdot \cos(\beta)} \tag{5.2}$$

In Table 5.2, the values for the different factors in the Equation 5.2 are indicated. To determine the thickness d, this expression is solved numerically with the aid of the *Solver* function in Microsoft© Excel. Thereby the divergence of the Equation 5.2 is minimized by adjusting the thickness d in the equation with a simplex method.

Copy for "Bibliothèque UCL"

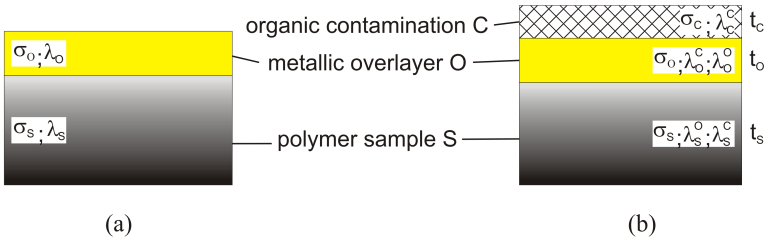


Figure 5.1: *Sections through samples: (a) polymer sample with an overlayer - (b) polymer sample with an overlayer and a contamination layer. The values for the sensitivity factors σ_i and the inelastic mean free path lengths λ_i^j are noted in Table 5.2.*

$\sigma_c = 0.25$	$\lambda_c^c = 3.303$
$\sigma_o = 4.95$	$\lambda_o^o = 1.574 = \lambda_o$
$\sigma_s = 0.25$	$\lambda_o^c = 3.732$
$\beta = 0$	$\lambda_s^o = 1.408 = \lambda_s$
	$\lambda_s^c = 3.303$

Table 5.2: *Values for the sensitivity factor of Au (σ_o) and of C (σ_c, σ_s). λ_i^j is the inelastic mean free path in layer j for electrons emitted from the layer i. The values for the inelastic mean free path are calculated by the TPP2M formula [231].*

The thickness determined by the two layer model is represented in Figure 5.2, in which one can see a linear relation between the amount of gold measured by the QCM and the amount determined by the XPS calculations. It can be seen that the gold amount on the polymer, determined by XPS, is lower than the amount measured by the QCM. This observation suggests that not all gold atom, which impinges on the polymer surface, remains on that surface. The ratio of the number of adsorbate atoms (or molecules) that do adsorb, or "stick", on a surface to the total number of atoms that impinge upon that surface during the same period of time is called *sticking coefficient*. The sticking coefficient of gold on the examined polymers, which correspond to the slope of the linear fit of the data in Figure 5.2 are given in Table 5.3.

Copy for "Bibliothèque UCL"

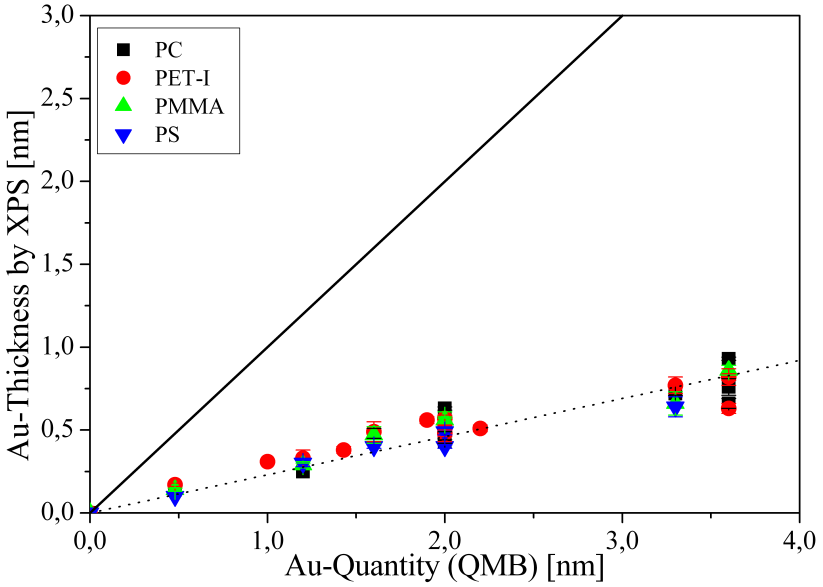


Figure 5.2: *Au-Thickness determined by XPS with the 2 layers model without reconstruction. The bold diagonal line represent the unit sticking coefficient.*

Polymer	PC	PET-I	PMMA	PS
Sticking Coefficient	0.23 ± 0.01	0.23 ± 0.01	0.24 ± 0.02	0.21 ± 0.01

Table 5.3: *Sticking coefficients for gold on different polymers determined by the two layer model.*

5.1.1.B Reconstruction and Three Layer Model

Because the transfer to the XPS instrument could not occur under vacuum, the sample were exposed to the lab atmosphere for a more or less long time. Thereby an unknown amount of atmospheric contamination (mainly H, C, O and C_xH_y) was able to deposit onto the sample surface (↪ *Figure 5.1(b)*). This contamination leads to a change in $C1s$ line shape.

In order to separate the signal originating from the contamination from the signal of the polymer a reconstruction of the $C1s$ peak of a

Copy for "Bibliothèque UCL"

metalized sample by dint of a combination of the fresh polymer $C1s$ shape and the $C1s$ shape of the thick gold layer sample, is done by using a *Non Linear Least Square Fit* in the XPS program *Avantage®* .

The characteristic $C1s$ fingerprint of the polymers is acquired on fresh polymer samples and the fingerprint of the $C1s$ contamination peak is obtained by acquiring spectra of a thick (35 nm) gold layer onto a Si substrate, which was stored for several weeks in the lab atmosphere. In Table 5.4 the theoretical and the experimental percentage of the $C1s$ peak contribution for the different polymers as well for the contamination are marked. The difference between the theoretical and the experimental composition percentage of the polymers becomes minimal if one assumes a shake-up contribution due to the presence of aromatic rings in the polymer to about $\approx 3-4$ %. This shake-up contribution must be added to the C−C contribution on the PC, PET-I and PS polymers. The $C1s$ peak shape of the contamination is close to the shape belonging to the polymers PET-I and PMMA, so that eventually a larger error can occur during their following reconstruction.

	PC		PET-I		PMMA		PS		Cont-
Contribution	theo	exp	theo	exp	theo	exp	theo	exp	amination
C−C / C−H	81	75	60	55	60	66	100	93	67
C−O	13	16	20	21	20	17	0	3	16
C=O / O-C-O	0	0	0	2	0	4	0	0	7
O−C=O	0	0	20	19	20	12	0	0	7
CO_3 / $\pi \rightarrow \pi^*$	6	9	0	3	0	1	0	4	3
max. deviation		±1		±1		±4		±1	±2

Table 5.4: *Theoretical and experimental percentage of the different $C1s$ peak contribution of the different polymers and the contamination on a thick Au layer. $C1s$ peak contribution graphs of the different polymers are shown in Annexe A.2.*

By using the *Non Linear Least Square Fit*-function, which is incorporated in the XPS program *Avantage®* , the intensity scale and the binding energy scale of the two reference spectra (fresh polymer and thick evaporated gold layer) are displaced and adjusted in the way that the sum of these two references matches best with the experimental spectrum.

Figure 5.3 shows reconstructions of the experimental data of the $C1s$ peak of the different metalized polymers using the corresponding pristine

Copy for "Bibliothèque UCL"

polymer $C1s$ peak and the contamination signal obtained from a thick gold layer. It should be noted that the experimental $C1s$ line shape could only be rebuilt in an adequate way by using a combination of these two references. This gives a strong indication that the assumption of a second overlayer on the polymer, representing a surface contamination, is true. With these assumptions, the data evaluation using Equation 5.2, which is based on a two layer model is not correct and the values of the sticking coefficient are underestimated. Therefore the equations 5.1 are expanded to the following equations, which indicate the intensities of the contamination layer I_c, the evaporated metallic layer I_o and the substrate signals I_s:

$$\begin{aligned} I_c &= J \cdot k \cdot \sigma_c \cdot \left(1 - e^{\frac{-d_c}{\lambda_c^c \cos\beta}}\right) \\ I_o &= J \cdot k \cdot \sigma_o \cdot \left(1 - e^{\frac{-d_o}{\lambda_o^o \cos\beta}}\right) \cdot e^{\frac{-t_c}{\lambda_o^c \cos\beta}} \\ I_s &= J \cdot k \cdot \sigma_s \cdot e^{\frac{-d_o}{\lambda_s^o \cos\beta}} \cdot e^{\frac{-d_c}{\lambda_s^c \cos\beta}} \end{aligned} \tag{5.3}$$

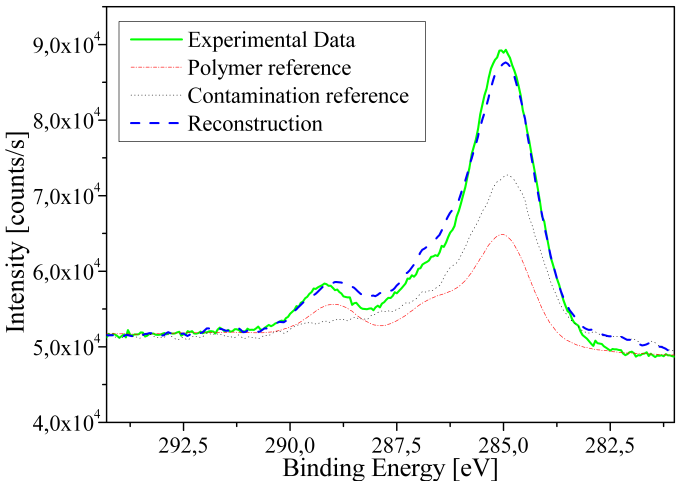
where k the instrumental factor, σ_i is the sensitivity factors and λ_i^j the inelastic mean free path in layer j of an electron emitted from an atom in layer i. The utilized values are noted in Table 5.2.

To get rid of the unknown instrumental factor k and the X-ray flux J, the ratios $\frac{I_c}{I_o}$ and $\frac{I_o}{I_s}$ are calculated:

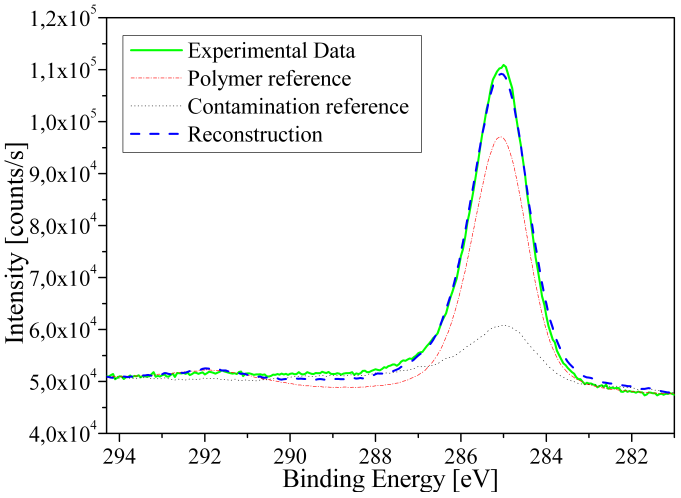
$$\begin{aligned} \ln\left(\frac{\frac{I_c}{\sigma_c}}{\frac{I_o}{\sigma_o}}\right) &= \ln\left(1 - e^{\frac{-d_c}{\lambda_c^c \cdot \cos\beta}}\right) - \ln\left(1 - e^{\frac{-d_o}{\lambda_o^o \cdot \cos\beta}}\right) - \left(\frac{-d_c}{\lambda_o^c \cdot \cos\beta}\right) \\ \ln\left(\frac{\frac{I_o}{\sigma_o}}{\frac{I_s}{\sigma_s}}\right) &= \ln\left(1 - e^{\frac{-d_o}{\lambda_o^o \cdot \cos\beta}}\right) + \left(\frac{-d_c}{\lambda_o^c \cos\beta}\right) - \left(\frac{-d_o}{\lambda_s^o \cos\beta}\right) - \left(\frac{-d_c}{\lambda_s^c \cos\beta}\right) \end{aligned} \tag{5.4}$$

In order to determine the thickness d_o of the evaporated metallic layer as well as the thickness d_c of the organic contamination layer, the sum of the absolute divergences of the two equations 5.4 is minimized by adjusting the two thicknesses d_o and d_c with the aid of a simplex method.

Copy for "Bibliothèque UCL"



(a) *PET-I*



(b) *PS*

Figure 5.3: *Examples of the C1s reconstruction for the different metalized polymers (PET-I and PS) by dint of a pristine polymer and a contamination samples. The nominal thickness of the evaporated gold layer is* ≈ 0.9 nm. *Between the elaboration and the XPS characterization, the metalized sample was stored several weeks in the lab atmosphere.*

Copy for "Bibliothèque UCL"

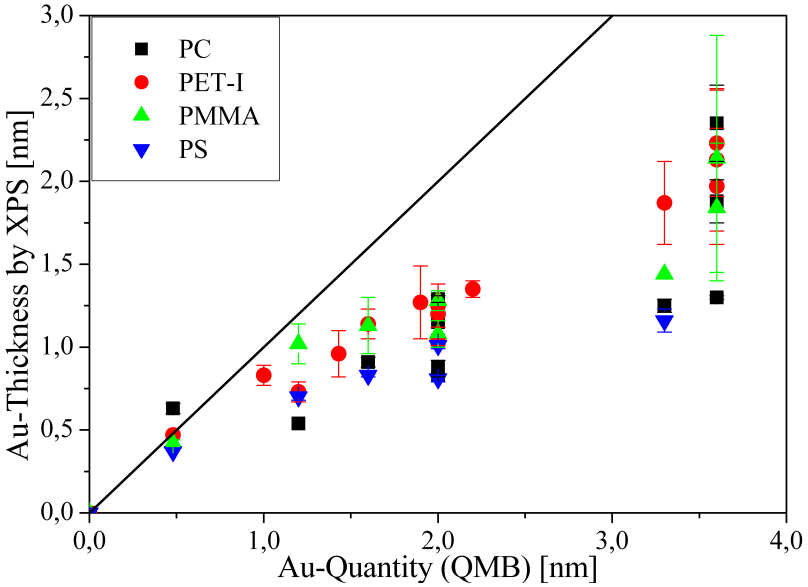


Figure 5.4: *Au-Thickness determined by XPS with the 3 layers model with the reconstruction of the C1s peak. The bold diagonal line represents the unit sticking coefficient.*

Polymer	PC	PET-I	PMMA	PS
Sticking coefficient	0.44 ± 0.07	0.54 ± 0.03	0.47 ± 0.06	0.34 ± 0.05

Table 5.5: *Sticking coefficients for gold on different polymers determined by the three layer model.*

In Figure 5.4, the thickness of the gold deposition onto the different polymer samples, which was determined by the three layer model, is represented. Here too a correlation between the amount of gold measured by the QCM and the amount determined by the XPS calculations can be observed. A linear fit through the data points intercept the y-axis at 0.17 ± 0.12. This y-axis interception > 0 is an indication that in the beginning of the evaporation process the sticking coefficient is higher and probably close to unity. This high sticking coefficient in the first stage of the evaporation process can be explained by the assumption that on the pristine polymer samples a high number of

Copy for "Bibliothèque UCL"

nucleation sites are present, so that at the beginning of the evaporation, the impinging gold atoms mainly stick on these sites (↪ *Chapter 2.2.3*). With ongoing metalization, these sites vanish, so that the gold atoms need to diffuse longer on the surface to find an adequate adsorption site. As a consequence the probability of their desorption increases and thus the sticking coefficient decreases. The slop of the linear fit, which indicated the sticking coefficient is indicated in Table 5.5. As expected, the sticking coefficient obtained by this model is higher than in the two layer model (↪ *Table 5.3*).

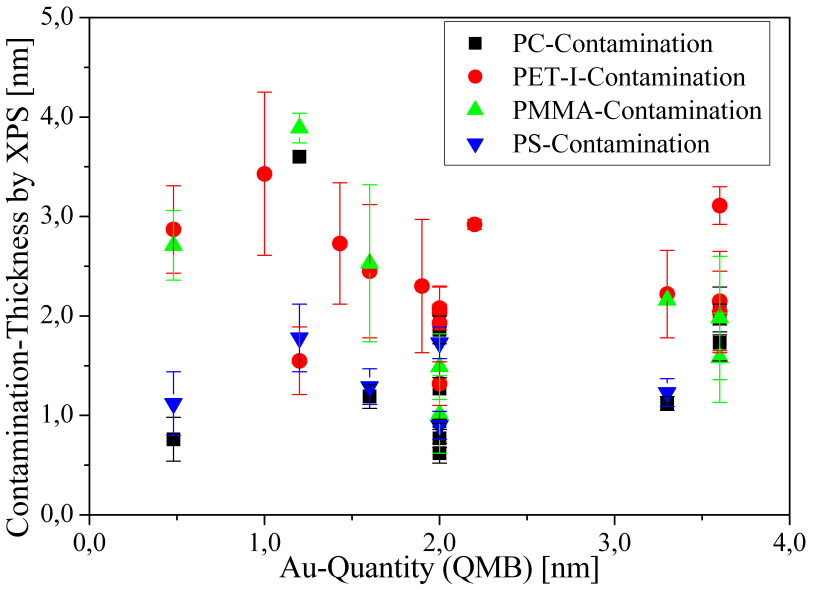


Figure 5.5: *Thickness of the contamination layer determined by the three layer model.*

The absence of any recognizable relation between the amount of the QCM and the thickness of the contamination layer (↪ *Figure 5.5*) proves that this contamination stands in no relation to the evaporation procedure, but has certainly an external origin. The determination of the deposited gold quantities by both models, results in different sticking-coefficients. The reconstruction of the $C1s$ peak by two reference spectra clearly indicates that a consideration of the contamination layer is absolutely necessary for the sticking-coefficient determination. In the following section, an additional method which

Copy for "Bibliothèque UCL"

is independent on the intensity and shape of the $C1s$ peak is used to evaluate and confirm the sticking coefficient.

5.1.1.C Evaluation on background shape using QUASES™

The two and three layer models, which are described in the previous section, give no information about the spatial distribution of the gold deposit on the polymer sample. Furthermore these models assume an homogeneous and flat sample, which is in contradiction with the observation in AFM, SEM and TEM (↪ *Chapter 5.2*). These images show that islands are formed at the surface during the gold evaporation onto the polymer and thus the assumption of flat sample, on which the layer models are based, is not correct. Nevertheless the previous equations 5.2 or 5.4 can be used to determined the total amount of deposited gold (called nominal or equivalent thickness).

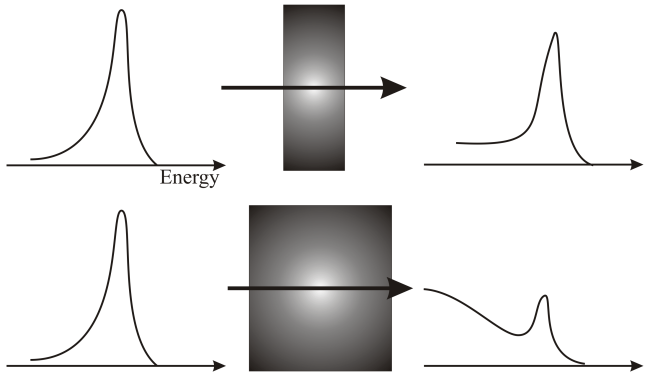


Figure 5.6: *Distortion of the energy spectrum depending on the distance the electrons travel on their way out of the solid.*

Another method to determine the thickness and spatial information of an overlayer was developed by S.Tougaard et al. [244, 246–250]. This method is based on the fact that the photoelectrons may lose a part of their kinetic energy on the way out of the sample, so that they are detected at higher binding energy in the XPS spectrum. For electrons that pass only a short distance in the solid, the chances that they will lose energy is small and thus the change in energy distribution is

Copy for "Bibliothèque UCL"

small. The longer the electrons travel through the solid, the larger is the fraction of electrons that have lost energy (↪ *Figure 5.6*). Hence the shape of the spectrum below the peak not only depends on the in-depth distribution of the element in the solid but also carries information on spatial repartition of the detected element. The evaluations based on this method are done with the program *QUASES*™ †.

For this kind of evaluation, the inelastic mean free path of the analyzed electrons as well as the inelastic cross section for those electrons must be known. For calculating the background intensity, the universal inelastic cross section is used. The inelastic mean free path is calculated using the *QUASES-IMFP-TPP2M*© program, which is based on the Tanuma, Powell and Penn formula [231]. For the examined $Au4f$ electrons, which were emitted perpendicular to the sample surface, the inelastic mean free path is 15.7 Å.

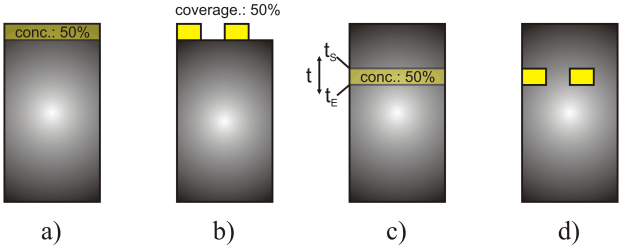


Figure 5.7: QUASES™ *-Models: a) Top layer (buried layer with d_S = 0) - b) Island (Passive Substrate) - c&d)* buried layer.

The utilized model for this kind of evaluations is named *buried layer* in the *QUASES*™ program. This model corresponds to a homogeneous layer in or on a substrate (↪ *Figures 5.7a* and *5.7c*). The evaluation is accomplished by adjusting the starting depth d_S and the end depth d_E of the layer until a best visual overlapping of the experimental peak with the reference spectra is obtained, by minimizing the root mean square deviation between the calculated spectrum and the scaled reference one. The reference spectrum is obtained from a thick pure gold layer (> 30 nm) which was evaporated with the evaporation system installed in the ToF-SIMS preparation chamber. In Figure 5.8 an example of a metalized polycarbonate film fitted by the *QUASES*™

† **Qu**antitative **A**nalysis of **S**urfaces by **E**lectron **S**pectroscopy

Copy for "Bibliothèque UCL"

program is shown. No obvious difference between the experimental peak an the reference peak can be remarked. The results obtained for the different models (↪ *Figure 5.7*) are shown in the insets of Figure 5.8.

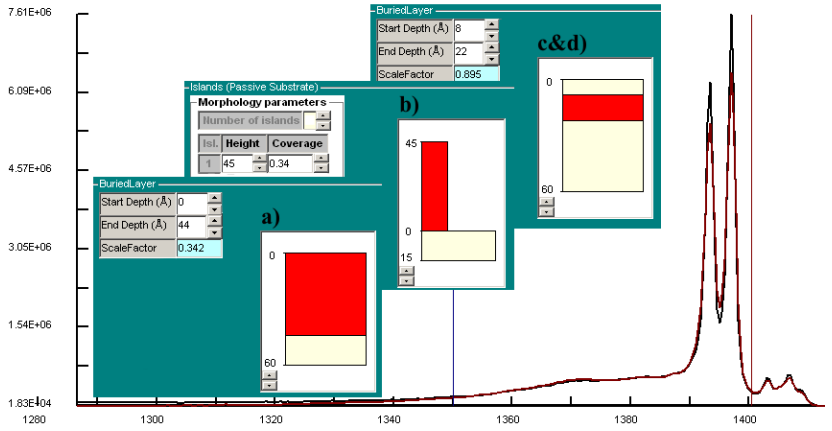


Figure 5.8: *Example of fitting a Au4f XPS spectrum of a metalized (≈ 3.3 nm polycarbonate film with the* QUASES™ *program. The insets show the results obtained from the different models (↪ Figure 5.7).*

Top layer (without contamination consideration) In a first step, the starting depth d_S of the *buried layer* model is set to zero and only the end depth d_E of the layer is varied until a best superposition between the experimental and the reference spectrum is obtained. As a result, the average thickness $d = d_E - d_S$ of the overlayer and the so-called scale factor s_f is obtained. The scale factor s_f indicates the proportion of the reference $Au4f$-spectrum which corresponds to the experimental $Au4f$-spectrum. The values can be interpreted in two ways:

- the layer is an alloy with a s_f percentage atomic concentration in gold and has an average thickness of d,
- the layer covers s_f percent of the surface and the average height of these islands is d.

Due to the observed structure on the electron images (↪ *Figures 5.21 and 5.22*) an homogeneous alloy layer can be excluded. In the *QUASES*™

Copy for "Bibliothèque UCL"

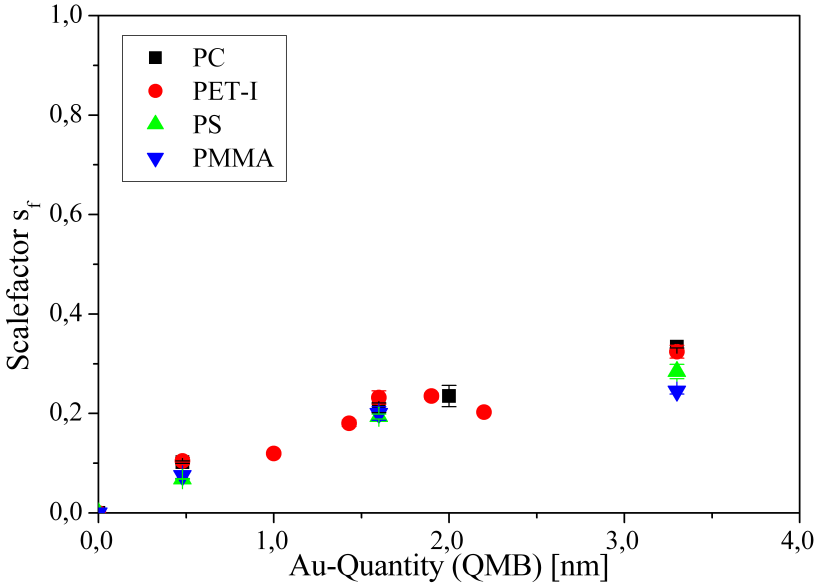


Figure 5.9: *Scale factor s_f determined by* QUASES™ *with the* buried layer *with $d_S = 0$. The scalefactor can be interpreted as coverage percentage.*

program, the *Island (Passive Substrate)* model, which is specialized on the evaluation of island-like structure onto a substrate, is also included. Although, both models are based on different structure-assumptions, the results obtained by both models are in this case identical [↪ *QUASES*™ program Manual]. Since the *buried layer* model provides additional evaluation possibilities (e.g. consideration of a contamination layer onto the gold island: see paragraph on page 123), this model is selected for the evaluation in this section/work.

In Figure 5.9 the scale factor s_f, which should correspond to the gold coverage of polymer surface is plotted as a function of the evaporated amount of gold measured by the QCM. One can see that even at an evaporated amount of over 3 nm the coverage of the surface with gold is far to be completed (max: $\approx$ 30%). This stands in contradiction with the results obtained by electron microscopy, where a nearly complete coverage is already obtained for an evaporated amount below 3 nm (↪ *Chapter 5.2*).

Copy for "Bibliothèque UCL"

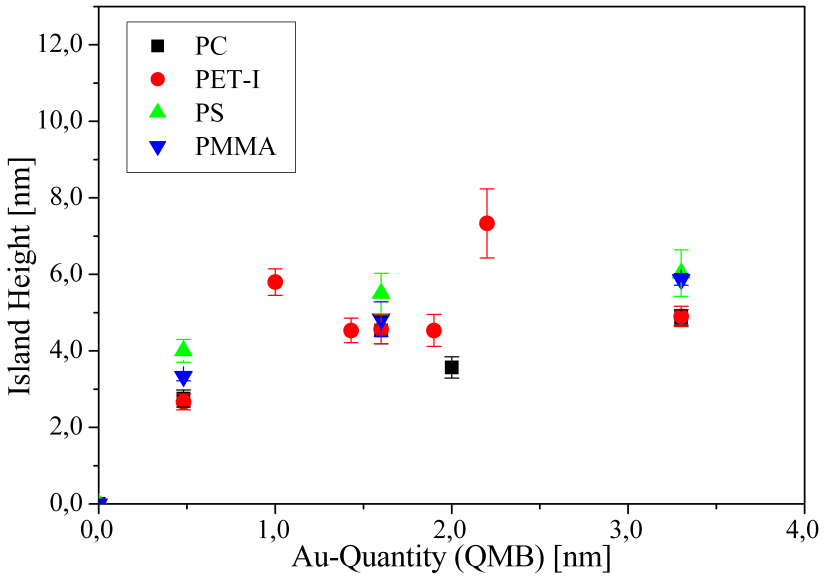


Figure 5.10: *Height of the gold islands determined by* QUASES™ *with the* buried layer *with* $d_S = 0$.

The height evolution of the gold islands as a function of the amount of evaporated gold can be seen in Figure 5.10. The minimum observed height for the gold islands is ≈ 3 nm. But because the evolution of the gold island height as a function of the evaporated gold quantity is ambiguous and the scalefactor do not corresponds to the values found by electron microscopy, further evaluation statements were hazardous. For this reason, the calculated amount of deposited gold on the sample as well as the sticking coefficients are not determined. Finally no reliable information at all can be extracted from this surface model (*buried layer* with $d_S = 0$).

Buried islands (with contamination consideration) As seen in the previous section, the results obtained on the surface coverage by using the top layer model (*buried layer* with $d_S = 0$) does not correspond with the surface coverage determined by the electron microscopy (↪ *Figure 5.23*).

Copy for "Bibliothèque UCL"

A way out was found by setting the scale factor s_f to the coverage value found by electron microscopy, and adjusting the starting depth d_S and the end depth d_E of the layer in the *buried layer* model inside the *QUASES*™ program until the experimental and reference spectrum superpose themselves. In this model too, the scalefactor can be interpreted as a presence of gold islands. This kind of data evaluation, where a structure below the surface are examined, can not be performed by using the *Island (Passive Substrate)* model.

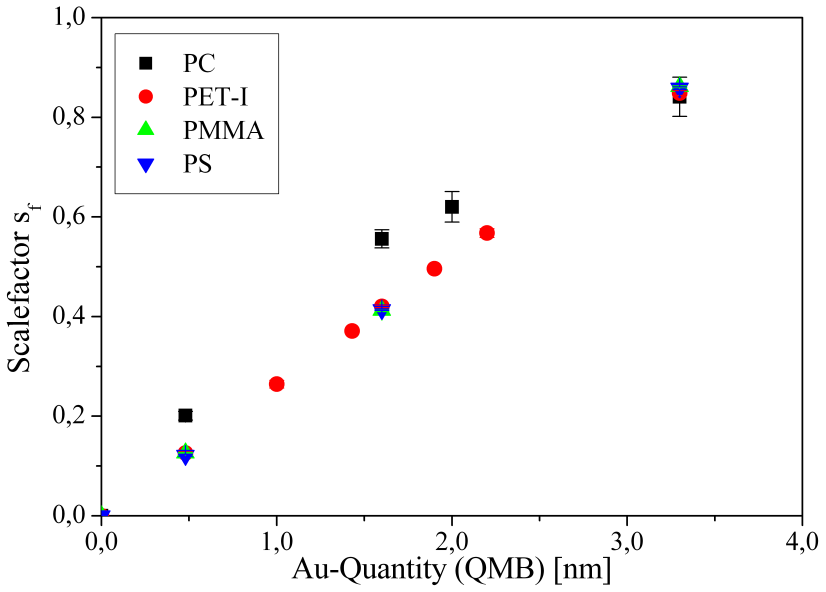


Figure 5.11: *Scalefactor $s_f \hat{=}$ surface coverage θ.*

Because the behavior of the starting depth and the end depth onto scale factor is opposite, an unique solution can be found where the spectra overlap and the scale factor corresponds to the preset surface coverage value of the electron images.

As mentioned above, the coverage evolution in this evaluation (↪ *Figure 5.11*) corresponds to the coverage determined by the electron microscopy (↪ *Figure 5.23*): The surface coverage continuously increase with the deposited gold quantity and a nearly complete coverage ($\approx 90\%$) is obtained for an evaporated gold amount above 3.5 nm.

Copy for "Bibliothèque UCL"

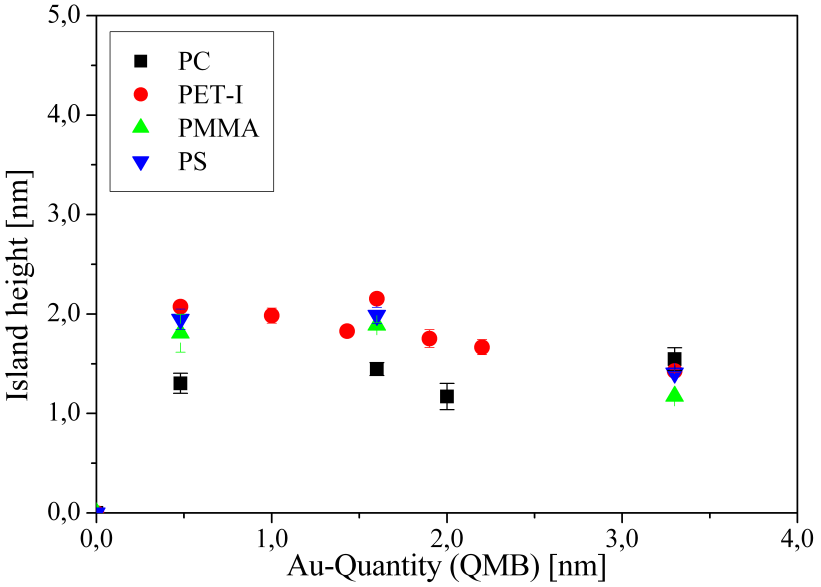


Figure 5.12: *Average height of the gold islands, which are determined by evaluating with the* buried layer *model in the* QUASES™ *program.*

The height of gold islands is determined by the subtraction of the end depth d_E from the starting depth d_S. As one can seen in Figure 5.12, the height of the islands rises abruptly to a value of ≈ 2 nm and then stays constant or even slightly decreases. For the depth of the gold island below the surface, which is equal to the average thickness of the contamination layer, no clear tendency as a function of the evaporated amount of gold can be seen in Figure 5.13. The islands are embedded between 0.5 nm and 1 nm below the surface. These values are underestimated, because the inelastic mean free path (IMFP) of the contamination layer is by a factor of 2 lower than the IMFP of the gold. This variation in the IMFP is not taken into account in the *QUASES*™ program. However, although the islands are not at the surface, the information depth limit of the XPS technique is not reached, so that the obtained results are accurate.

The multiplication of the scale factor s_f with the average island height d gives the total deposited amount of gold. This evaluation as a function of the evaporated amount of gold is shown in Figure 5.14.

Copy for "Bibliothèque UCL"

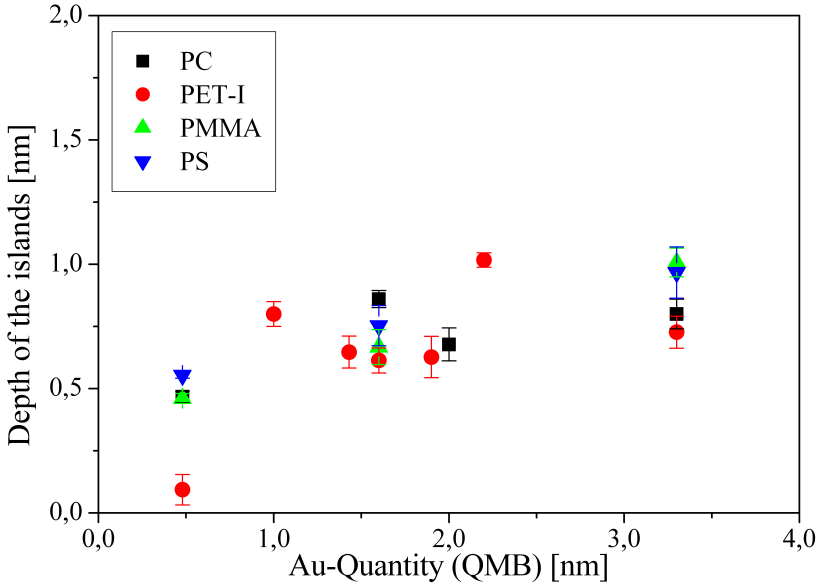


Figure 5.13: *Average depth below the surface of the gold structure (corresponds to the contamination thickness). The data was evaluated by using the* buried layer *model in the* QUASES™ *program.*

A correlation between the evaporated amount of gold measured by the QCM and the amount determined by the *buried layer* algorithm can be observed. A linear fit of the data intercepts the y-axis at 0.09 ± 0.09, which indicates that the sticking coefficient in the beginning of the metalization is larger than in the subsequent metalization process. The sticking coefficient of gold on polymer, which is calculated here by the slope of the linear regression, can be seen in Table 5.6.

Comparing the deposited amount determined by the 3 layers model and by the *QUASES*™ method, a strong correlation can be remarked. This observation is also reflected by the similarity of the sticking coefficient determined by both methods. The mean sticking coefficient is 0.40 ± 0.08.

Copy for "Bibliothèque UCL"

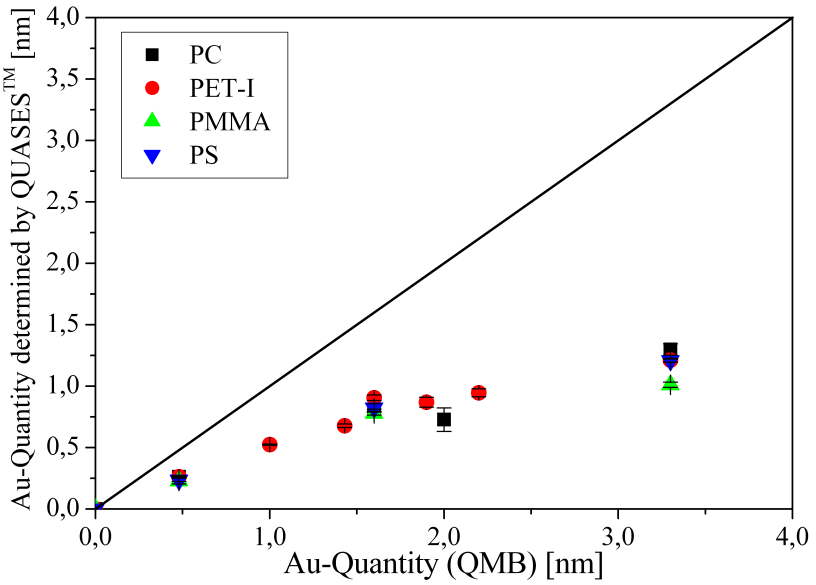


Figure 5.14: *Deposited gold quantity as a function of the evaporated gold quantity, which is measured by the QCM. The deposited quantity is determined by multiplying the average height of the islands with the surface coverage obtained from the* QUASES™ *program. The bold diagonal line represents the unit sticking coefficient.*

Polymer	PC	PET-I	PMMA	PS
Sticking coefficient	0.38 ± 0.04	0.38 ± 0.03	0.31 ± 0.07	0.37 ± 0.05

Table 5.6: *Sticking coefficients for gold on different polymers determined by the* buried layer *model.*

5.1.2 XPS Summary

The determination of the deposited gold quantity on the polymer samples is an important information for this work. In a first step, the correct calibration of the the quartz crystal microbalance (QCM) was checked on different samples, where a unity sticking coefficient can be assumed (↪ *Chapter 4.2.2.B*). In a second step, the gold

Copy for "Bibliothèque UCL"

quantity, which is evaporated on polymer samples and analyzed in XPS is determined with two independent methods. The two-three layer models and the *QUASES*™ algorithm are completely different evaluation methods because:

- The two-three layer model is based on the Beer-Lambert absorption law and on the intensity attenuation study of the "zero loss peaks" ($C1s$ and $Au4f$). In order to determine the deposited amount of gold onto the polymer both peaks must be considered.
- The *QUASES*™ method is based on the intensity study of the photoelectrons peak and on the corresponding background lineshape, which is characteristic on the emission depth of the photoelectrons. For this kind of evaluation only the $Au4f$ and the shape of its background at lower (kinetic) energy must be considered.

One has seen that the simple assumption of a gold overlayer on the polymer surface (↪ *Chapter 5.1.1.A*) is not correct because the reconstruction of the experimental spectrum is only acceptable by assuming the presence of an organic contamination layer (↪ *Chapter 5.1.1.B*). This contamination presence is taken into account in the development of the three layer model.

In contrast to the two-three layer models, the *QUASES*™ also provides structural information about the deposited gold. But here too, the simple model of a gold overlayer gives wrong results, because the determined surface coverage, which corresponds to the scale factor, is not in agreement with the values determined by the electron microscopy analysis (↪ *Chapter 5.2.2*).

An evaluation with the *QUASES*™ program, where the correct gold coverage was considered, was only possible when one allows that the gold was embedded below the surface. In this case, the obtained sticking coefficient matches quite well the sticking coefficient obtained by the three layer model.

The determined amount of deposited gold by these both independent methods gives similar values. Comparing to the value on the QCM, which indicates the evaporated amount of gold, the deposited gold quantity on the polymer sample is by a factor of $\approx 0.40 \pm 0.08$ lower.

Copy for "Bibliothèque UCL"

Furthermore, no significant difference on the evolution of the gold quantity has been observed between the different polymers.

On the figures 5.4 and 5.14 one has seen that the sticking coefficient is higher in the first stage of the evaporation than in the subsequent metalization process. This difference of the sticking coefficient can be explained by the assumption that on the pristine polymer a high number of nucleation sites are present. These nucleation sites, which may be defect sites or impurities of the surface but the exact nature of these sites are not yet known, cause that the impinging gold atoms directly keep sticking on these sites (↪ *Chapter 2.2.3*). With ongoing metalization, the number of these nucleation sites diminishes and the gold atoms need to diffuse longer on the surface to find an adsorption site. Hence the probability of their desorption increases and, as consequence, the sticking coefficient decreases. For larger evaporated gold quantities, which are not investigated here, it can not be excluded that the sticking coefficient varies again.

Concerning the describing function of the relation between the evaporated and the deposited gold quantity, here a linear fit is used, where the y-axe interception respects the fact that in the first stage of the evaporation process a different sticking coefficient occurs. Although the errors of the measurements inhibit the exact determination of the function, the linear fit used here gives sufficient precision in the studied range of the evaporation process. However it can not be excluded that the sticking coefficient can be described more accurately by an other, more complex function, which respects the various behavior of the sticking coefficient in the different deposition steps.

Hereafter some deliberations about the observation that the gold is covered by an organic layer are made. One can suspect that small oligomers, which are present on the polymer samples, can diffuse over the gold clusters so that after some time the gold is completely covered by a thin polymer layer. However, the here used analytical gel permeation chromatography standards (GPC) for the polymer sample preparation have a low polydispersity index so that one can assume that only very little amount of small diffusing oligomers are present on the sample.

One can also imagine that the deposited gold diffuse into the polymer sample. But as the used evaporation rate is high (compared to a monolayer per minute), the diffusion into the bulk can be neglected

Copy for "Bibliothèque UCL"

because the pronounced aggregation tendency of metals results in cluster formation that impedes the embedding of Au into the polymer sample (↪ *Chapter 2.2.7*).

Because no temperature rise is observed on the sample distance during the evaporation process (↪ *Chapter 4.2.2*) and no relation between the thickness of the contamination layer and the evaporated amount of gold is observed (↪ *Figures 5.5 and 5.13*), the origin of this organic component is not related to the evaporation process but rather has an external source. The necessity of the reconstruction of the C1s peak by means of a polymer reference and the contamination of a *thick* gold layer spectra is a further indication that the organic layer has is due to an external source.

As for XPS, AFM, SEM and TEM analysis the sample is transferred through the atmosphere and because gold and especially gold islands are also known to adsorb organic molecules on its surface [251], such an organic contamination layer can be formed on the metalized samples on contact with the atmosphere. But for ToF-SIMS analyses, where the metalization is done *in-situ*, the adsorption of residual molecules left in the UHV is very small, so that formation of a contamination layer on the metalized polymer samples can be neglected.

5.2 Morphology of the deposited matter

5.2.1 AFM

To characterize the morphology of the gold deposit, the sample surface is analyzed by AFM, which was the technique with the best lateral resolution available at CRP-Gabriel Lippmann during my experimental work.

The AFM analyses were done in ambient atmosphere on a PicoLE™ from Molecular Imaging (now Agilent Technologies, Inc.) (↪ *Figure 4.22*). Sample preparation and its metalization are described in the chapters 4.1.2 and 4.2.2, respectively. The instrument was used in the acoustic mode (also called tapping mode). Topography and phase images were acquired simultaneously. Images were taken at different random points on the sample. The images are acquired with the small scanner, permitting a maximum scan area of $9\mu m \times 9\mu m$ and

Copy for "Bibliothèque UCL"

a maximal cantilever deflection of 2 µm. Regularly the Pointprobe® cantilever from NanoWorld AG was replaced with a new one, in order to prevent image degradation due to deformed tip-shape (e.g enlarged point radius). The integral and the proportional gain of the feed-back loop of the AFM were adjusted in the way that the amplitude signal (error signal) is low and shows least texture. In Table 5.7 the main parameters for the AFM analysis and the characteristics parameters of the utilized tips are summarized.

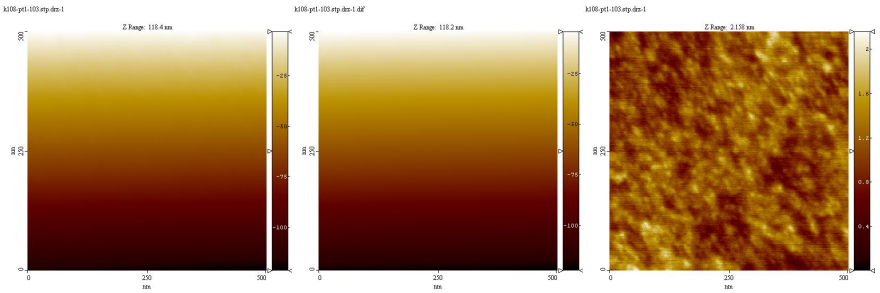
Acquisition mode	acoustic (tapping)
Scanning size	500×500 nm^2
Number of pixel	512×512
Scan speed	max. $1\,line/second$
Name of Cantilever	Pointprobe®
Radius of curvature	< 10 nm
Force constant	42 N/m
Resonance frequency	≈ 320 kHz

Table 5.7: *Main characteristic parameters for the AFM analysis and the utilized Pointprobe® cantilever from NanoWorld AG.*

Due to the fact that a skew fixation of the sample onto the AFM sample holder is hardly avoidable, the AFM raw data must be post-treated in order to emphasize the texture of the sample surface. By performing any image treatment, one must assure that no significant information, which would not be considered in the subsequent evaluation, are removed from the initial image. This is checked by watching for some unexpected texture on the difference between the original image and the processed image. In order to compare the images acquired on the different samples, the same image transformations are performed on all the images. The image processing is done with the software SPIP™ (Scanning Probe Image Processor) version 4.5. In the figures 5.15, 5.16 and 5.17 the data treatments from the raw data to the final evaluated image are illustrated on a polycarbonate sample with 3.3 nm of evaporated gold.

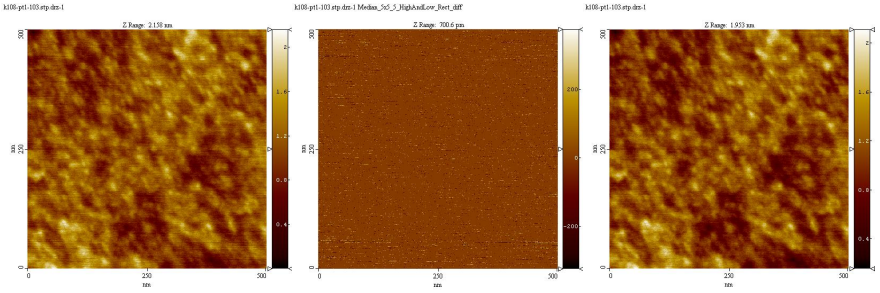
First, the sample inclination is corrected (↪ *Figure 5.15*). This is done by subtracting an averaged plane, which is calculated from the average profiles (↪ *Figure 5.15b*), from the raw AFM-data (↪ *Figure 5.15a*).

Copy for "Bibliothèque UCL"



(a) *Raw data* **(b)** *Correction plan* **(c)** *Leveled image*

Figure 5.15: *AC-AFM topography (field of view (fov):* $500{\times}500nm^2$*): Image transformations - plane correction: a) raw data - b) correction plane - c) leveled image.*



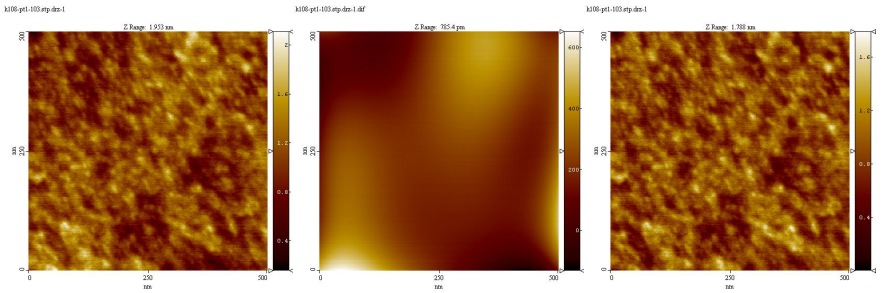
(a) *Leveled Image* **(b)** *Image noise image* **(c)** *Median filtered image*

Figure 5.16: *AC-AFM topography (fov:* $500 \times 500nm^2$*): Image transformations - noise reduction: a) leveled image - b) median filter - c) noise-free image.*

Subsequent, in order to reduce high-frequency random noise and horizontal scanning artifacts, a median filter is applied to the image (↪ *Figure 5.16*). Figure 5.16b shows these artifacts, which are subtracted from the leveled image (↪ *Figure 5.16a*).

Finally (↪ *Figure 5.17*), the long-range waves, which are even present at the surface of pristine polymers, are reduced by subtracting a polynomial surface of the fifth order (↪ *Figure 5.17b*), which is calculated using the least-squares method, from the filtered

Copy for "Bibliothèque UCL"



(a) *Median filtered image* **(b)** *Polynomial plane* **(c)** *Final image*

Figure 5.17: *AC-AFM topography (fov: $500 \times 500 nm^2$): Image transformations - polynomial subtraction: a) median filtered image - b) polynomial plane - c) final image.*

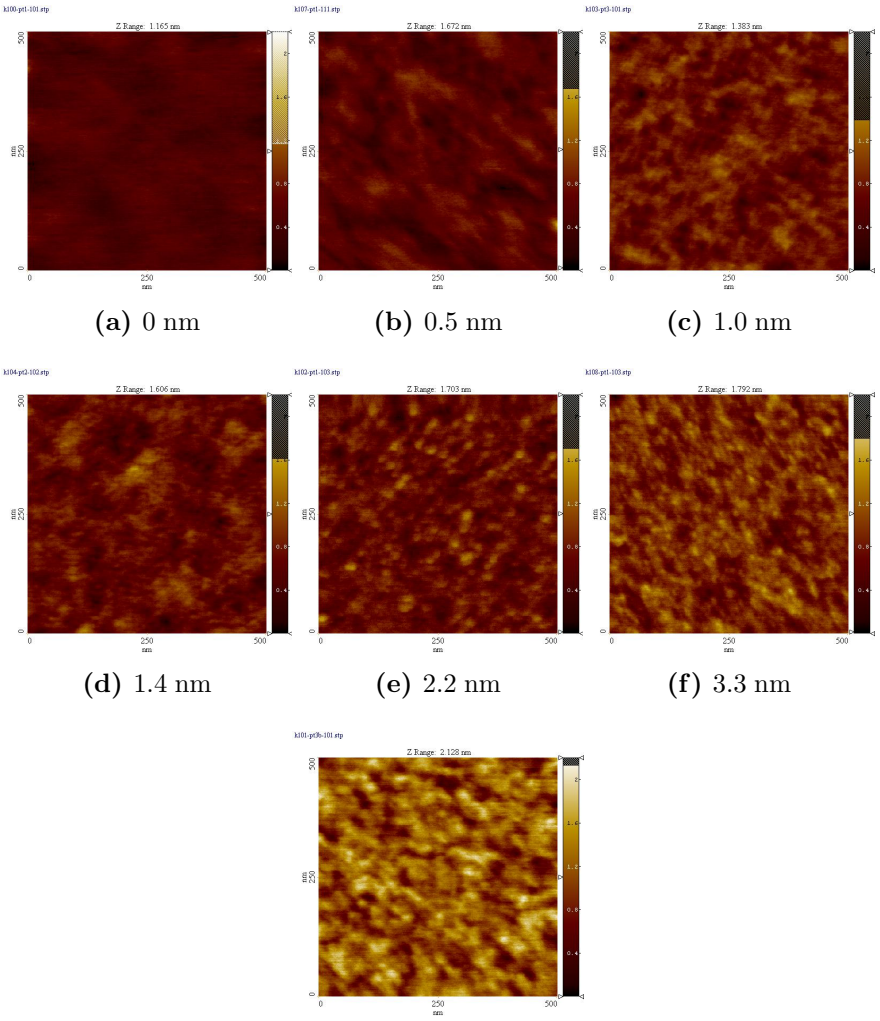
image (5.17a). This last step emphasizes the small structure present at the surface. Although no obvious difference can be observed between the figures 5.15c and 5.17c, the image treatments between those images are needed in order to apply later the threshold grain detection algorithm (see next paragraph).

In Figure 5.18 some AFM images of polycarbonate samples with different evaporated gold amounts are shown. As mentioned before, in each image processing step it is controlled that no information disappears by the image operation. The topography of some metalized PS sample, which were also used for SEM analyses (↪ *Chapter 5.2.2*), can be seen in the figures 5.19a-5.19c.

The observations are similar for all metalized polymers: On the sample with 0.8 nm of evaporated gold (↪ *Figure 5.19a*) one can notice small structure, which gets larger on the sample with 1.6 nm of evaporated gold (↪ *Figure 5.19b*). At even higher amount of evaporated gold (2.4 nm) an even larger texture can be seen (↪ *Figure 5.19c*). Unfortunately, no additional information can be found on the phase images of the samples (↪ *Figures 5.19d-5.19f*).

Although the differences are obvious for the human eyes (↪ *Figures 5.19a-5.19c* or ↪ *Figures 5.19g-5.19i*), a quantitative evaluation of the grains' characteristics can not be performed due to

Copy for "Bibliothèque UCL"



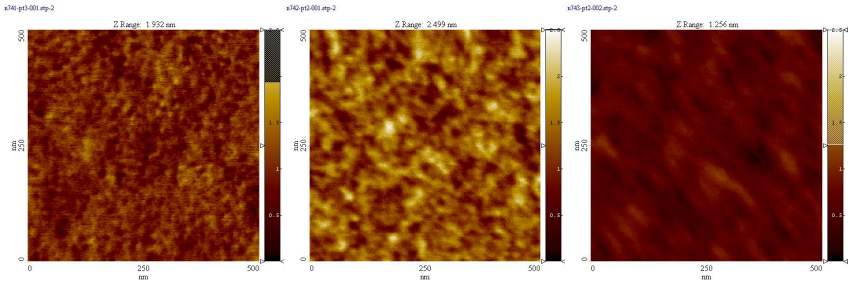
(a) 0 nm **(b)** 0.5 nm **(c)** 1.0 nm

(d) 1.4 nm **(e)** 2.2 nm **(f)** 3.3 nm

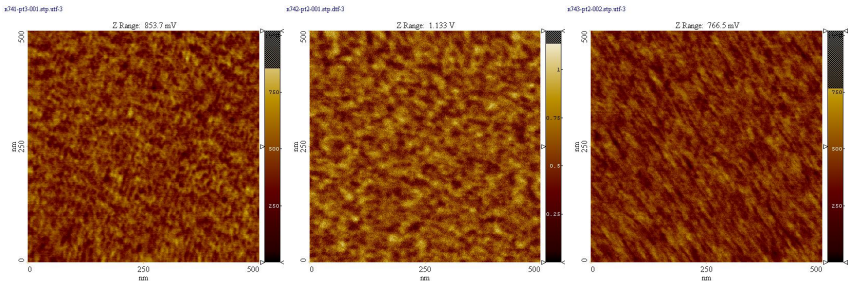
(g) 4.4 nm

Figure 5.18: *AC-AFM topography (fov:* $500 \times 500nm^2$*) of PC with different amount of deposited gold (from a) pristine sample to g)* 4.4 nm *of gold. The color scale on these AFM topography images is from 0 to* 2.2 nm*.*

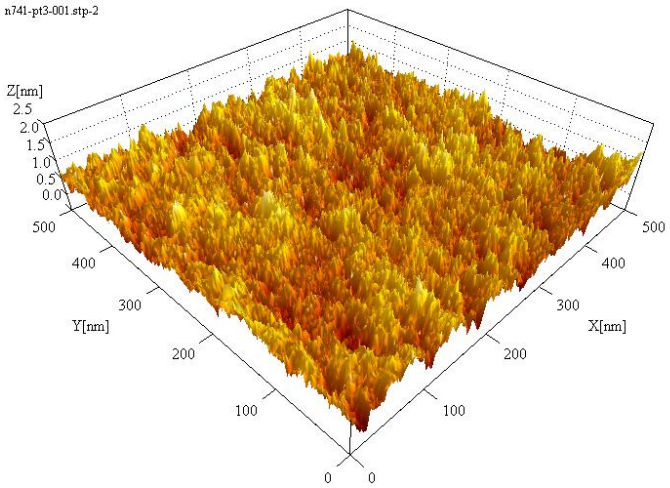
Copy for "Bibliothèque UCL"



(a) *0.8nm* **(b)** *1.6nm* **(c)** *2.4nm*

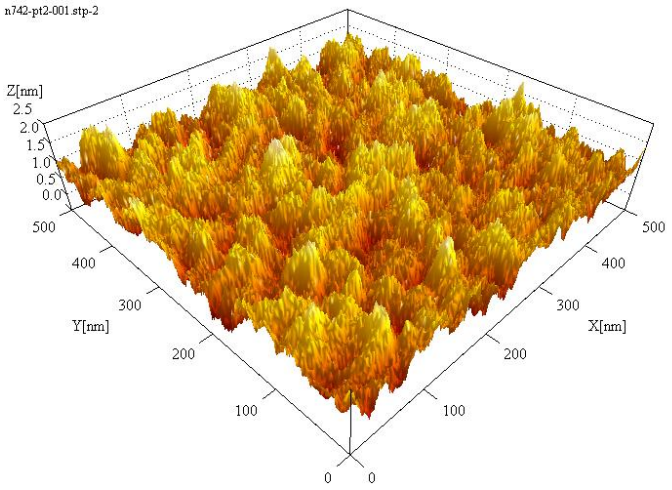


(d) *0.8nm* **(e)** *1.6nm* **(f)** *2.4nm*

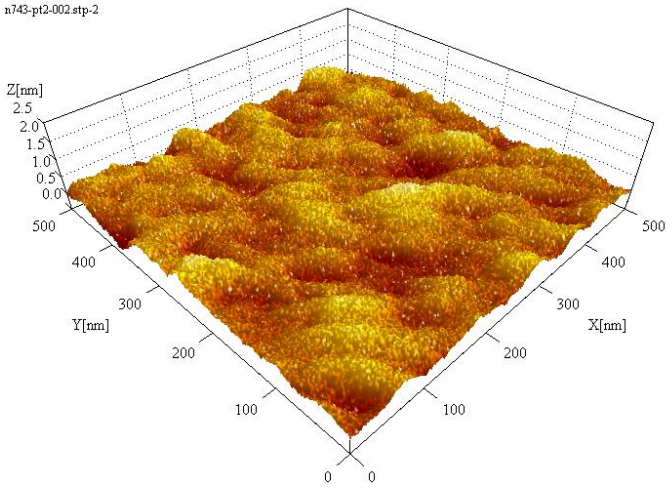


(g) *0.8nm*

Copy for "Bibliothèque UCL"



(h) *1.6nm*



(i) *2.4nm*

Figure 5.19: *AC-AFM topography and phase (fov:* $500 \times 500nm^2$*) of metalized PS: a)-c) topography (color range:* $0 - 2.5$ nm*) - d)-f) phase images (color range:* $0 - 1.2$ V*). The amount of evaporated gold is noted below the images. g)-i)For an enhanced perception of the topography of the samples, a 3D representation of the same AFM data is shown (color range: adapted on the individual maximal z-range).*

Copy for "Bibliothèque UCL"

a large wavy background morphology of the polymer samples. Even after the polynomial plane subtraction one can see some small residual structure on the pristine polymer samples (e.g. ↪ *Figure 5.18a*). This kind of observed residual long waves on the polymer samples inhibits the particle detection with the threshold grain detection algorithm of SPIP™. With this threshold algorithm the particles are detected on the basis of their pixel intensity. Thereby the scale of the pixel intensity is divided by the means of a threshold value and the pixels on either sides of the threshold value are allocated to grains or pores respectively. A depiction of this algorithm is that grains are the 'islands' left when the image landscape is flooded to the threshold level [229]. For a clear detection of nm-sized grains, an atomic flat surface should be required. Although the polymer sample surface prepared by spincoating on silicon is flatter than the bulk polymer samples (↪ *Figure 4.4*), the polymer surface is unfortunately not flat enough to allow an univocal detection of the nm-sized structures by AFM. In the phase image too (e.g. ↪ *Figure 5.19*), no clear distinction between gold and polymer can be made, so that the phase images can not be used for grain detection too.

Although a quantitative evaluation of the deposited gold grains on the basis of the AFM analysis is not possible, some remarks about the surface texture of the metalized polymer can be made: On the different polymers, a similar morphology can be observed and with increasing amount of deposited gold, one gets the impression that the structure became denser and the surface rougher. To confirm this impression the roughness of the samples is calculated.

In Figure 5.20 the average roughness S_a of the different polymers are plotted versus the evaporated gold amount. On can see that the variation of the average roughness S_a is similar for the different polymers. The average roughness S_a of the pristine polymers is around 0.10 nm. With increasing amount of evaporated gold, the average roughness increased to 0.15 nm before it decreases nearly to its initial value. A local maximum of the average roughness $S_a \cong 0.15\,\text{nm}$ is reached for an evaporated gold amount of ≈ 1 nm. At larger gold amount, the average roughness increases again. For comparison, the average roughness S_a determined on a ≈ 100 nm thick gold layer deposited by MBE on silicon is about 1 nm.

Copy for "Bibliothèque UCL"

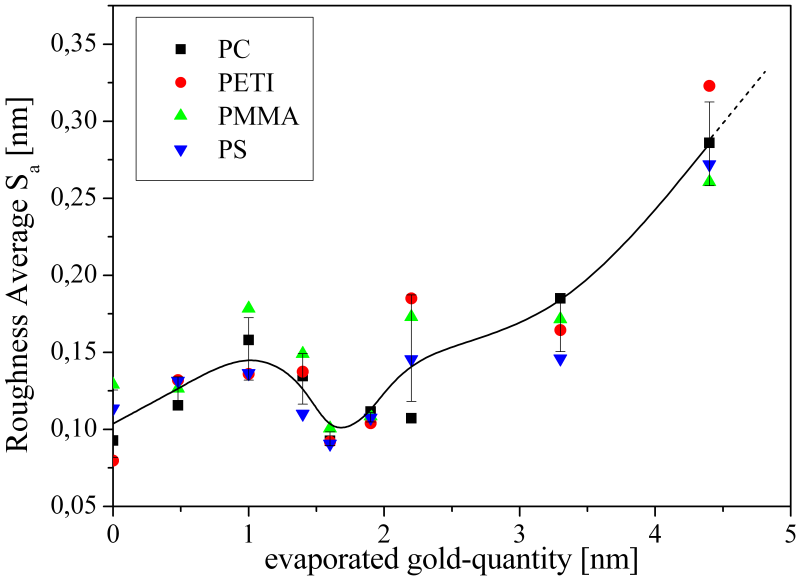


Figure 5.20: *Average roughness S_a of the different polymers as a function of the evaporated amount of gold. The position and the size of the error bars are calculated on the basis of all the data.*

Based on the AFM images and the variation of the roughness parameter only an ambiguous interpretation of the evaluation of the deposited gold structure is possible. Therefore some additional analyses, which clarify the deposit texture, are necessary.

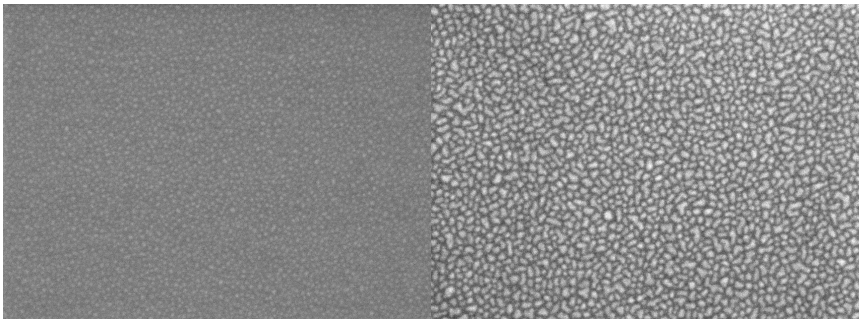
5.2.2 Electron Microscopy

Preliminary tests on metalized polymer samples with the scanning secondary electron microscopy present at the CRP-Gabriel Lippmann (StereoScan 430i, Leica, Germany, 1994) do not point any texture on the surface of metalized polymer samples. This is certainly due to the low lateral resolution capabilities of the tungsten filament as electron source. Within the frame of the acquisition of a latest generation SEM in 2008/2009, I had the possibility to verify the results obtained by AFM with secondary electron images. Therefore some samples have been analyzed on different SEM instruments of overall four different

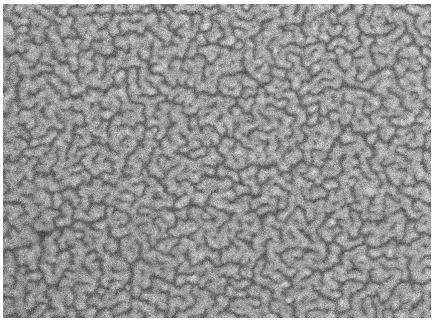
Copy for "Bibliothèque UCL"

manufacturers. The sources of those new generation SEM are principally based on field emission guns, so that the lateral resolution of these instruments is significantly enhanced (↪ *Table 4.13*).

Before sending the polystyrene samples to the manufacturer for test analysis of their new generation secondary electron microscopes, some AFM analyses on these samples are performed in order to compare the results obtained by AFM (↪ *Figure 5.19*) and SEM (↪ *Figure 5.21*). Contrarily to the AFM images, small independent grains of gold can clearly be observed on the secondary electron image (↪ *Figure 5.21a*). The size of the grains is increasing with the evaporated gold amount (↪ *Figure 5.21b*) before the individual grains finally coalesce to a larger irregular structure (↪ *Figure 5.21c*).



(a) 0.8 nm **(b)** 1.6 nm



(c) 2.4 nm

Figure 5.21: *SEM images (fov: $\approx 600 \times 440 nm^2$): spincoated PS with different gold amounts. These images were acquired with the JSM-7500F from Jeol Ltd..*

Copy for "Bibliothèque UCL"

In parallel to the SEM analyses I had also the possibility to do some TEM analyses. For this purpose, a drop of the 1% polystyrene solution was put on a vertical clipped 400 mesh TEM copper grid. After some time the solvent has evaporated and a thin polystyrene film remains between some mesh of the grid. This kind of samples was also metallized with different gold amounts inside the ToF-SIMS preparation chamber. The analysis condition of the TEM are noted in Chapter 4.6. During the TEM analysis no sample degradation has been noticed and contrarily to the SEM analysis, the TEM analyses were done within a much shorter time after the metalization.

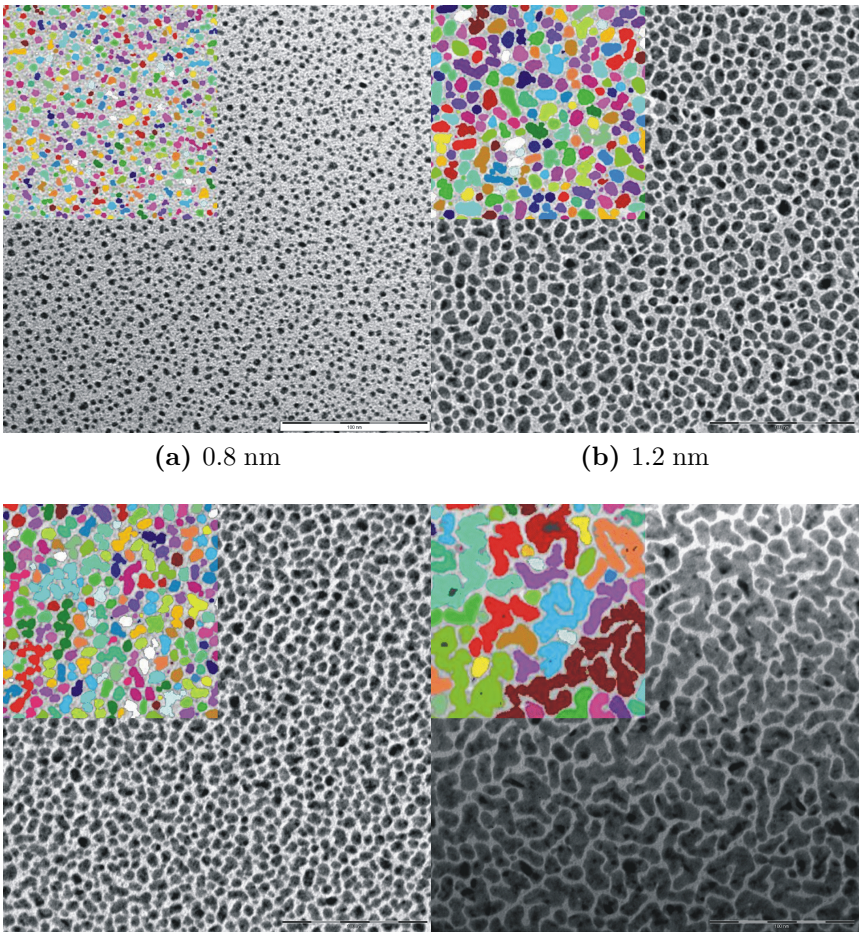
In Figure 5.22 transmitted electron images of polystyrene with different amounts of evaporated gold are shown. Contrarily to the SEM images and due to the higher electronic density of gold, the gold grains appear as dark islands in TEM images. As on the SEM images (↪ *Figure 5.21*) the initial small grains of gold coalesced to larger irregular structures when a higher gold amount is evaporated.

Because of the different analysis conditions used on the different electron microscopy instruments, the quality and contrast of the images vary, so that the images for grain evaluation must be chosen carefully. For the evaluation of the electron images, the exact size of the field of view (fov) of every SEM and TEM picture has been determined by counting the number of pixel on the scale bar and on the entire image. After opening the image with the program SPIP™, the correct size and unit are entered. It goes without saying that, contrarily to the AFM images, the color scale in images acquired with electron microscopes contains no practical physical information and is therefore arbitrary. Before applying a median filter on these images to remove some image noise, the legend of the image has been cropped because it perturbs the different image operations as well as the grain detection algorithm performed by SPIP™. The evaluation of the observed grains is performed by applying the automatic‡ threshold level to the image. In the insets of Figure 5.22, each detected grains are dyed by an individual color.

It should be mentioned that for large gold amount that causes a nearly complete surface coverage the automatic threshold algorithm misidentifies the grains so that in these cases the threshold value for

‡The automatic threshold level sets the threshold value to the dominating height plus 20% of the difference between the highest height value and this dominating plane.

Copy for "Bibliothèque UCL"



(a) 0.8 nm **(b)** 1.2 nm

(c) 1.6 nm **(d)** 2.8 nm

Figure 5.22: *TEM images (fov: $\approx 300 \times 300 nm^2$): dried PS with different gold amount. These images were acquired with the LEO 922 Omega from LEO. In the upper left corner of each image, each detected grain by SPIP™ is indicated by an individual color.*

the grain detection is adjusted manually. For small gold amount, the main error in the image evaluation is due to the lateral resolution limit and image noise. Therefore a grain must exceed a certain size or must be composed of more than a few image pixel to be identified

Copy for "Bibliothèque UCL"

explicitly as a gold cluster. Due to the lateral resolution limitation of the techniques, detected structure diameters of less than 1 nm are doubtful. Furthermore detected structures that have a length up to $2-3$ pixels can be attributed to noise during the image acquisition and is therefore not considered in the further evaluation.

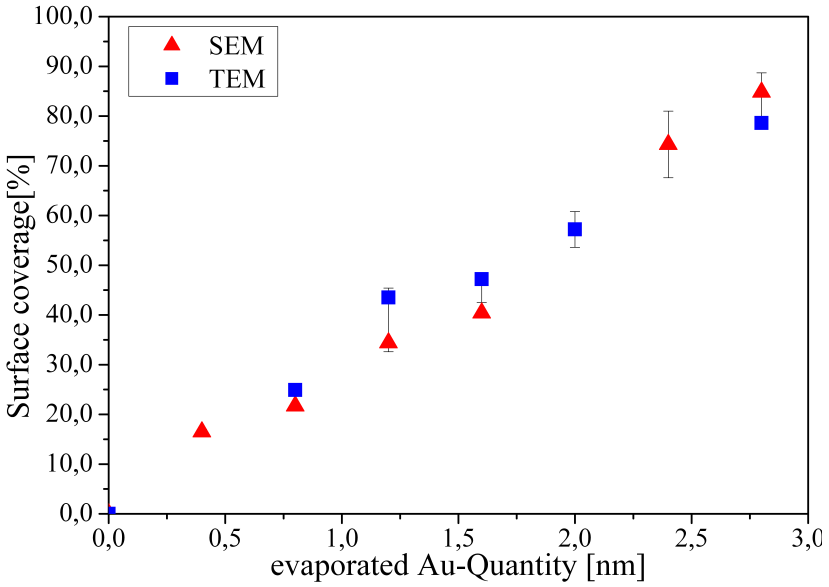


Figure 5.23: *Gold coverage percentage of PS samples as a function of the deposited gold amount. The different symbols correspond to the different analysis technique (▲: SEM and ■: TEM). The error bars are calculated on the basis of all the data.*

With the grain detection algorithm of SPIP™, the percentage of the surface that is covered by gold and the number of detected grains per square micrometer are determined on the different images. The gold coverage on the polystyrene sample as a function of the evaporated gold amount is displayed in Figure 5.23. The values of the surface coverage obtained by means of the different analysis techniques (SEM and TEM) are represented with different symbols. The position and size of the error bar are obtained from all the data of both analysis techniques. It can be seen that the determined surface coverage values are similar for both analysis techniques. A linear relation between the gold coverage

Copy for "Bibliothèque UCL"

and the evaporated amount of gold can be noticed in this interval of initial gold deposition. The proportionality constant is 0.30 ± 0.01. The fact that the value of the proportionality constant is below the sticking coefficient (↪ *Table 5.6*) can be explained by the development of 3-dimensional gold clusters and confirms the deposition of gold onto polymers by the Volmer-Weber growth mechanism (↪ *Chapter 2.2.4*).

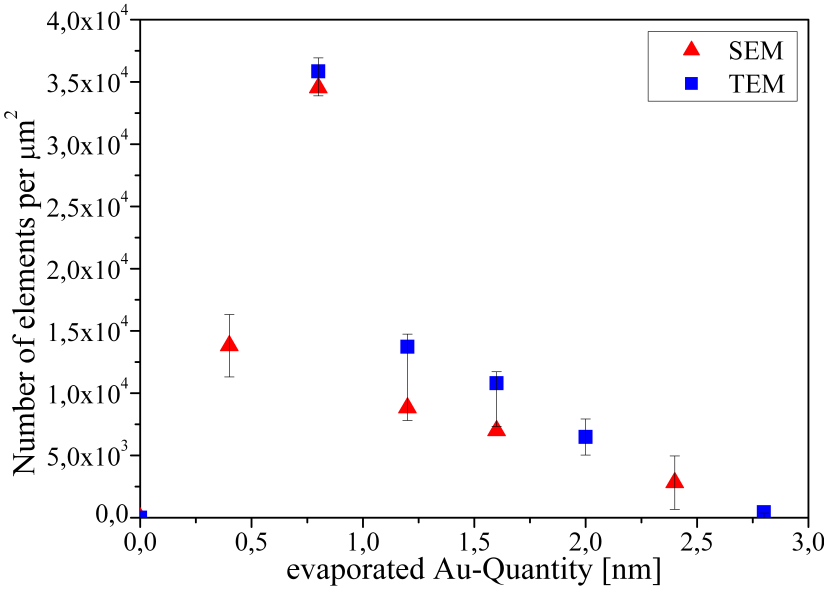


Figure 5.24: *Density of detected gold grains as a function of the evaporated amount of gold. The different symbols correspond to the different analysis technique (▲: SEM and ■: TEM). The error bars are calculated on the basis of all the data.*

In Figure 5.24, the number of grains per square micrometer is represented. Here too, the two different symbols of the points stand for the different analysis techniques. One can notice that the number of grains per square micrometer, first strongly increases, before it decreases towards zero. This can be interpreted that in the initial stage of deposition new isolated islands are formed. Around ≈ 0.8 nm of evaporated gold, the cluster density reaches a maximum. With further gold evaporation, the present islands grow in size so that they coalescence and thus the number of gold islands per square micrometer decreases.

Copy for "Bibliothèque UCL"

Beside the surface coverage and the density of detected elements the program SPIP™ provides also other grain characteristics (e.g. area, size, diameter, perimeter, etc.). These additional parameters are determined for each detected grain, and the obtained values from SPIP™ are saved into a text file. For further treatment, these thousands of individual grain data are imported into a self-written Matlab® program, where the distributions of these data are plotted. Considering the asymmetric shape of these histograms, which is an indication of coalescence mechanism for particle growth (↪ *Chapter 2.2.6*), the distributions are fitted by the gamma-distribution ($f(x) = a \cdot x^{p-1} \cdot e^{-b \cdot x}$), where a, b and p are the fitting parameters.

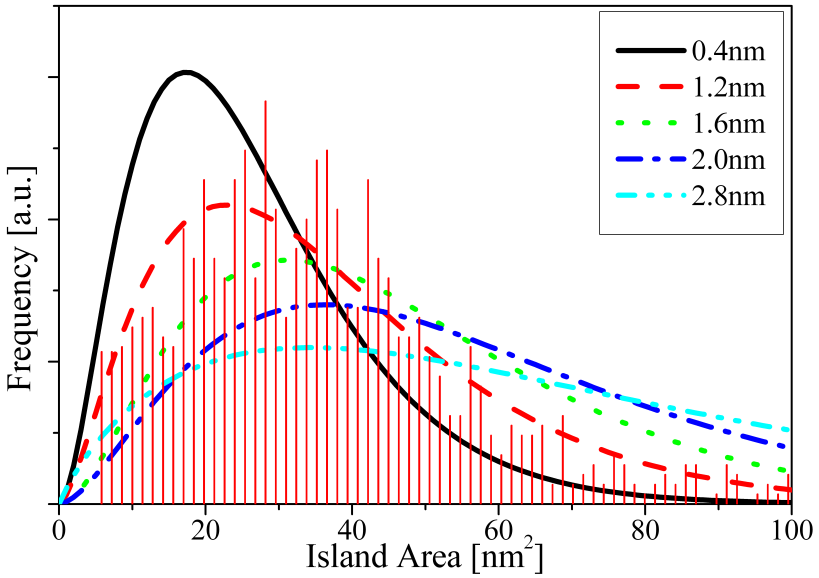


Figure 5.25: *Evolution of the normalized distributions of the detected grain area as a function of the evaporated gold amount (Normalized to the total number of detected grains). The histogram represents the grain area distribution for a* 1.2 nm *amount of gold. The associated fit with a gamma function* ($f(x) = a \cdot x^{p-1} \cdot e^{-b \cdot x}$) *is better than* $r^2 = 0.90$.

In Figure 5.25, the distribution of the grain areas for different amounts of evaporated gold is represented. The frequency counts

Copy for "Bibliothèque UCL"

are normalized to the total number of detected grains. For a better survey only the histogram for 1.2 nm of evaporated gold is plotted in Figure 5.25. For the other amount of gold, only their fit is shown in the figure. One observes that the distributions become more and more broad and the expectation value ($x_M = \frac{p}{b}$)[§], which corresponds to the mean value of the distribution, increases with increasing amount of deposited gold.

It should be mentioned that for large evaporated gold amounts (> 2 nm), the small number of detected grains is insufficient to perform a statistical evaluation. The detected structures, which are related to the image noise, occur only at small values. They are neither shown in the histogram nor their contribution is considered for the fit.

The other above-mentioned grain parameters (e.g. perimeter, diameter) show analogous distributions as a function of the evaporated gold amount. The expectation value of these distribution fits are plotted in separate graphs (↪ *Figures 5.26, 5.27 and 5.28*). For these expectation values a good agreement between both analysis techniques can be found too.

Figure 5.26 shows the evolution of the expected area of the gold grains as a function of the evaporated gold amount. For small amounts of evaporated gold, the mean grain area seems to be constant ($\approx 13 \pm 1$ nm^2). Between 0.8 nm and 1.2 nm of evaporated gold an change of the mean grain area occurs: the mean grain area continuously increases. Due to the coalescence of more and more islands, the distribution of the island area becomes broader and thus also the error bar in Figure 5.26. The values for the grain area above 2 nm of evaporated gold are consciously not shown because a significant number of grains touches the image border, so that the grain area depends on the field of view of the examined image.

The evolution of the grain area is coherent with the evolution of the number of grains per square micrometer and the surface coverage: Firstly the increase of surface coverage is mainly achieved by increasing the number of grains rather than increasing the area of the individual grains. In a second step, from ≈ 1 nm of evaporated gold, the surface covering

[§]Contrarily to "mean value" for discrete data, for distribution function the term "expected value" is used. It must not be confused with the "most probable value".

Copy for "Bibliothèque UCL"

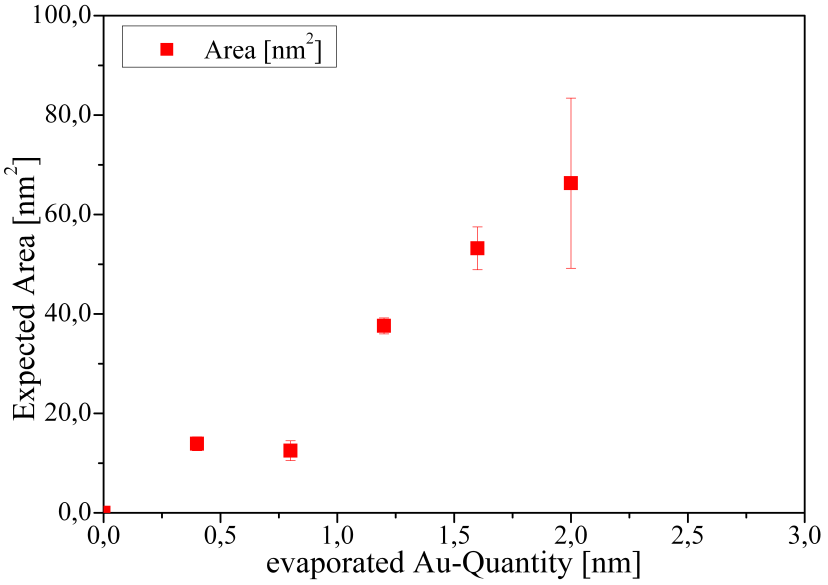


Figure 5.26: *Expectation values of the grain* area *as a function of the evaporated gold amount on PS.*

with gold mainly occurs by growing and coalescence of the individual gold islands.

The evaluation of the mean diameter of the gold grains (↪ *Figure 5.27*) shows a similar behavior than the mean area. This fact is due to the way the diameter is determined: SPIP™ do not determine the grain diameter from the image but the diameter is calculated from the area parameter. Because the observed structure for values above 2 nm can not be characterized with a diameter, these values are consciously not indicated in Figure 5.27.

Figure 5.28 shows the mean perimeter of the individual gold grains as a function of the evaporated amount of gold. For large gold quantity this parameter corresponds rather to the perimeter of the polymer holes in the gold structure than the perimeter of the gold islands. As no clear delimitation between both observations (gold islands on polymer or polymer holes in large gold structure) can be made, the

Copy for "Bibliothèque UCL"

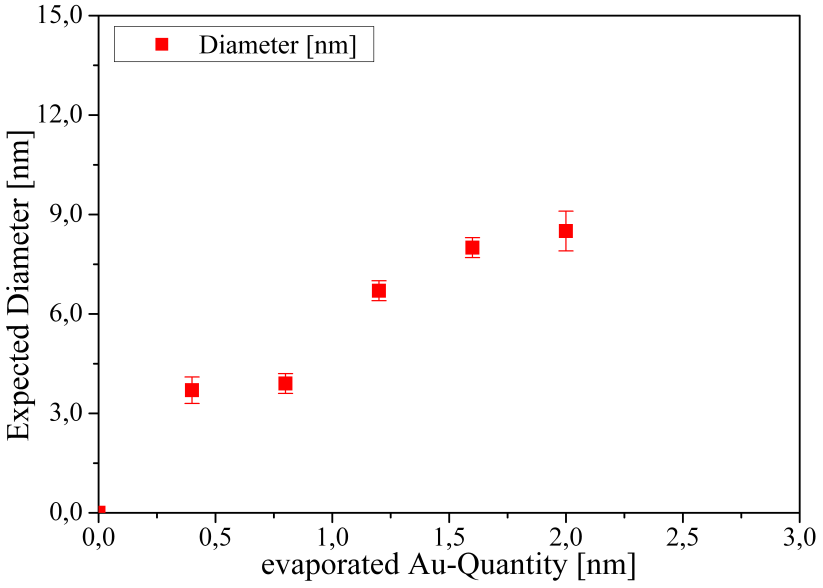


Figure 5.27: *Expectation values of the grain* diameter *as a function of the evaporated gold amount on PS.*

determined perimeter is named hereafter as "interface perimeter" for both states. As in the previous plots, one sees that for small amount of evaporated gold (< 1 nm), the interface perimeter does not vary a lot. Contrarily to the area plot, the mean interface perimeter does not increase continuously but reaches a maximum between 1.6 nm and 2.0 nm. Due to the proceeding coalescence of the islands to a bigger structure occupying nearly the whole surface, the interface perimeter decreases again for large amount of evaporated gold.

The grain evaluation of the electron images by SPIP™ also provides for each grain the distance to its nearest neighbor. The mean distance between the grains is well below 10 nm and so this distance is smaller than the used AFM tip radius! This is another explanation why a clear distinction of the individual gold grains is not feasible by AFM.

Unfortunately, it is impossible to determine the height of the islands from electron microscopy images. But with the simple assumption that

Copy for "Bibliothèque UCL"

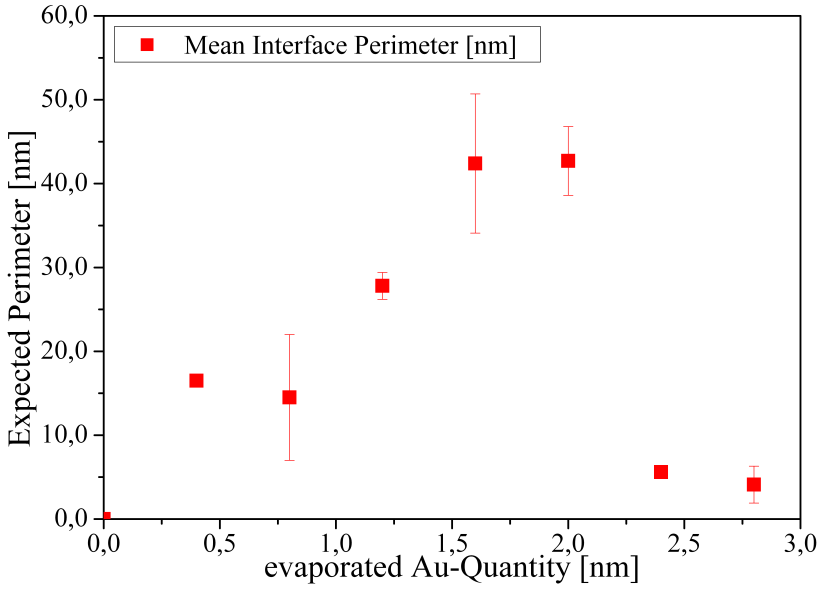


Figure 5.28: *Expectation values of the grain* interface perimeter *as a function of the evaporated gold amount on PS.*

the islands have the form of half-ellipsoids, it is possible to estimate the averaged height h_a of the gold islands. The round shapes of the Au islands observed on the SEM and TEM images justify this assumption.

The total volume of the deposited gold V_d can be calculated by the multiplication of the nominal equivalent thickness d of the gold (e.g. measured by XPS (↪ *Chapter 5.1.1*)) with the sample surface A:

$$V_d = d \cdot A \tag{5.5}$$

Assuming that the islands are all identical, this volume V_d is equivalent to the product of the average volume of an individual island V_a in form of an half-ellipsoid and the total number of islands n present on the sample surface:

$$V_d = n \cdot V_a = n \cdot \frac{2}{3}\pi r_a^2 h \tag{5.6}$$

where r_a and h are the average radius and the height of a gold island, respectively.

Copy for "Bibliothèque UCL"

The total area A_c of the sample covered by gold islands can be determined by the multiplication of the surface coverage of gold θ with the sample surface A:

$$A_c = \theta \cdot A \tag{5.7}$$

This Au-covered area A_c is the sum of the individual gold island area, and can be expressed by the product of the number of gold islands n and the averaged surface of an gold island A_a

$$A_c = n \cdot A_a = n \cdot \pi r_a^2 \tag{5.8}$$

Combining equations 5.5, 5.6 and 5.8 leads to an expression which allows, by dint of the deposited amount of gold and the surface coverage, the height calculation of the half-ellipsoid:

$$d\frac{n \cdot \pi r_a^2}{\theta} = n\frac{2}{3}\pi r_a^2 h \tag{5.9}$$

In order to compare this model with the values obtained by XPS measurements, one need to average the height of the ellipsoid formed islands by multiplication the height of the half-ellipsoid h with the factor 3/5, so that the averaged height h_a of an gold island can expressed as:

$$h_a = \frac{3}{5} \cdot \frac{3}{2}\frac{d}{\theta} = \frac{9}{10}\frac{d}{\theta} \tag{5.10}$$

Equation 5.10 is only valid for round shaped islands, which is the case for nominal gold thickness below ≈ 2 nm. At higher gold thicknesses this model is not valid anymore due to the irregular structure of the gold islands (e.g. ↪ *Figures 5.21c and 5.22d*). In Figure 5.29, the average height h_a of the gold islands calculated by this model is shown as a function of the evaporated gold quantity. For a direct comparison also the height values obtained by the XPS model (↪ *Figure 5.12*) are shown in Figure 5.29 too. One can see that for both independent calculation methods the height evolution is similar: The height of the islands rises abruptly and stays constant around a value of $\approx 1.5 - 2.0$ nm.

Copy for "Bibliothèque UCL"

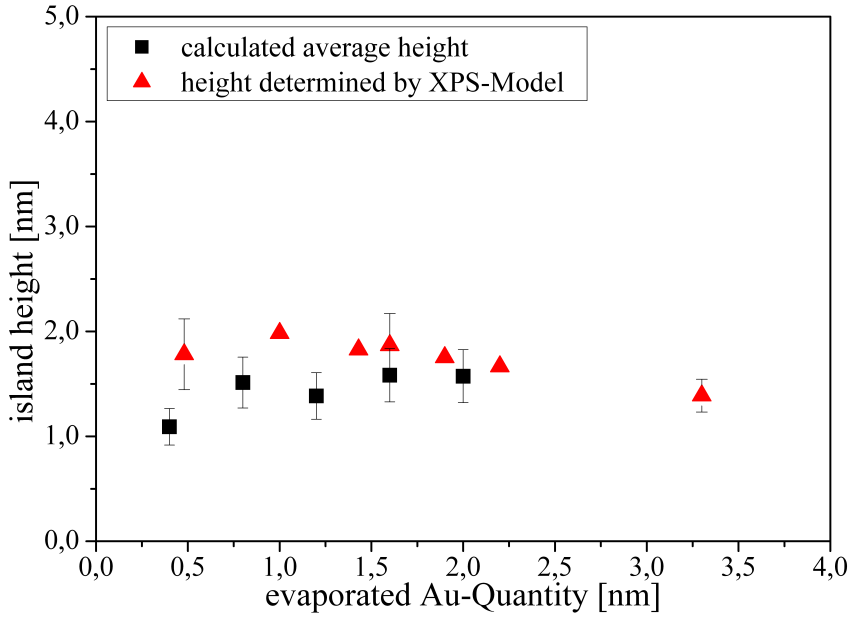


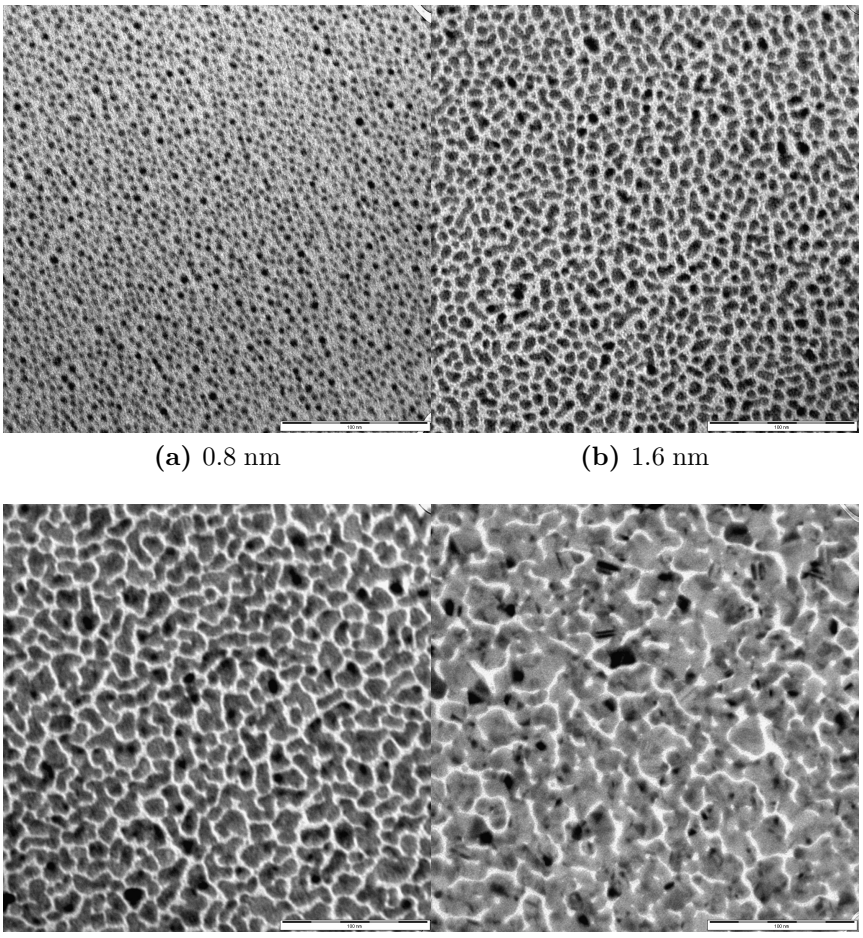
Figure 5.29: *Averaged height calculated with the assumption of ellipsoid-formed Au islands as a function of evaporated gold quantity (↪ Equation 5.10). For comparison, the height of the Au islands determined by XPS measurements (↪ Chapter 5.1.1) are shown too.*

Polycarbonate Samples

Beside the polystyrene samples, also some metalized polycarbonate samples have been examined with the TEM. The polycarbonate samples are prepared by sectioning industrial manufactured pellets of polycarbonate with an ultra-microtome (Leica, Ultracut UCT) into around ≈ 80 nm thick slices. These slides are laid on 400 mesh square copper grids and the TEM grid with the polycarbonate slices are fixed onto the ToF-SIMS sample holder. Different samples are exposed different times to a similar evaporation flux ($0.08\frac{nm}{s}$) in order to metallize the sample with different amount of gold.

The analysis conditions for TEM analysis, as well as the evaluation procedure are the same as for the polystyrene samples (↪ *page* 140). The most representative grain structure of the polycarbonate samples

Copy for "Bibliothèque UCL"



(a) 0.8 nm **(b)** 1.6 nm

(c) 2.0 nm **(d)** 2.8 nm

Figure 5.30: *TEM images (fov: $\approx 300 \times 300 nm^2$): sliced PC with different amount of evaporated gold. The images were acquired with the LEO 922 Omega from LEO.*

with different amount of gold are shown in Figure 5.30. By analyzing different areas on the sample, one has observed that the structure of the deposited gold is not so homogeneous than on the polystyrene sample. However, the evaluation results are quite similar to those obtained on the polystyrene sample: the initial small gold grains coalesced to larger irregular structure when a higher amount of gold is evaporated. Not only

Copy for "Bibliothèque UCL"

the behavior for surface coverage, number of elements per micrometer square, grain area and grain perimeter is similar, but also their values are similar to the values found on the polystyrene samples.

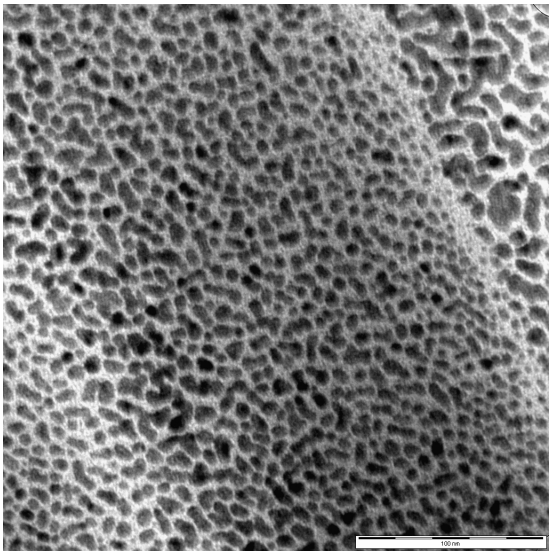


Figure 5.31: *TEM images (fov:* $\approx 300 \times 300nm^2$*) of metalized PC slices prepared by microtome. The amount of evaporated gold was* ≈ 2.0 nm.

In Figure 5.31, an extreme example of the inhomogeneous deposition of ≈ 2.0 nm evaporated gold on the polycarbonate sample is shown. One can see the different structures (small and large individual islands as well as already coalesced islands) on the same sample. Remarkably is the fact that these different structures can be observed simultaneously even at this small field of view ($\approx 300 \times 300nm^2$).

Because the PC samples have been metalized simultaneously with the PS samples, the origin of this inhomogeneous gold deposition can not be the evaporation condition. Even that an heterogeneity of the industrial sample can not totally be excluded a more probable explanation is the sample preparation technique. Due to the microtome slicing, an inhomogeneous roughness is induced on surface so that different concentration of nucleation sites are present over the surface, which lead to the observed difference in the structure of the deposited gold.

Copy for "Bibliothèque UCL"

5.2.3 Morphology Summary

In order to correlate the ToF-SIMS results with the structure of the deposited gold, a detailed evaluation of the morphology of the gold deposit is necessary.

In a first attempt, the morphology was analyzed by AFM. Thereby it was especially paid attention to the subsequent image treatments, in order to avoid information lost. On the different polymers a similar evolution of the deposit morphology has been observed: The structure seems to become denser with increasing amount of deposited gold (↪ *Figure 5.18*). Although an obvious evolution of the surface texture has been observed and the obtained AFM image quality was similar to those found in the literature [98, 105, 122, 123]¶, a detailed evaluation of the AFM data was not possible.

A quantitative evaluation failed due to the wavy structure of the polymer surface. But also an organic layer on the metalized samples (↪ *Chapter 5.1*) can inhibit the correct imaging of the gold islands by AFM. As this small organic layer is nearly transparent to an electron beam, this contamination layer does not influence the SEM and TEM analysis. These electron microscopy images point out that the distance between the grains is smaller than the radius of the utilized AFM tip, so that an accurate measurement of the surface topography cannot be guaranteed (↪ *Chapter 3.3.3*). It is most probable that this circumstance implies that bleary AFM images are acquired and that minor differences between the polymer samples might not be observed.

Knowing the exact structure of the deposit from the electron images, it is possible to interpret the roughness evolution of the samples obtained by AFM (↪ *Figure 5.32-lower frame*). In the initial stage of deposition, where the number of grains increases, the roughness increases too. When the individual islands begin to coalesce into larger structure, the roughness decreases because the tip can not follow the surface profile due to its large radius. With further evaporation, the deposition mainly occurs on the existing gold islands rather than sparse remaining polymer surface, so that the existing islands grow in height and the roughness increases again. Although the absolute values of the roughness

¶In the literature only the AFM images are shown and no further evaluation is performed or presented for these data.

Copy for "Bibliothèque UCL"

parameter are doubtful because an optimal contact between the AFM tip and the sample surface can not be controlled and ensured, the overall tendency of the roughness can be justified.

The "real" structure of the gold morphology has been revealed by the electron microscope images. For the lowest amount of evaporated gold the grains seem to be spherical (↪ *Figure 5.21a* and ↪ *Figure 5.22a*). With increasing amount of evaporated gold, the cluster shape gets more and more asymmetrical, indicating that the individual spherical islands coalesce into large and irregular structures (↪ *Figure 5.21c* and ↪ *Figure 5.22d*).

With these images, the gold surface coverage, the number of gold particles per square micrometer and the particle area/diameter/perimeter distributions are determined as a function of the evaporated gold amount. For all these grain characteristics similar values are found by TEM and SEM analyses. As SEM and TEM analyses were done within different time-scales after the sample metalization, the similarity of the results obtained from both techniques indicates that the morphology of the gold overlayer is stable within that time period. Furthermore, on electron images no significant differences have been observed between different polymers. In Figure 5.32 a summary of the obtained results for the different island characteristics is sketched.

For the surface coverage, one observes a strong linearity between the gold surface coverage and the evaporated gold amount, with a proportionality constant of 0.30 ± 0.01.

By comparing this proportionality constant to the sticking coefficients (around 0.40 ± 0.08 ↪ *Table 5.5 and 5.6*), a further statement about the gold deposition can be made. The fact that the surface coverage increase slower with the amount of evaporated gold than the deposited gold amount, indicates that a significant part of the evaporated gold is deposited onto already adsorbed gold. As consequence 3-dimensional gold clusters, with a high vertical aspect, grow on the polymer surface. This growth behavior is characteristic for the Volmer-Weber growth mechanism.

In the initial stage of gold deposition, new isolated islands (critical clusters) are formed, so that the density of gold clusters first strongly increases with the deposited gold amount. Around ≈ 0.8 nm, the cluster

Copy for "Bibliothèque UCL"

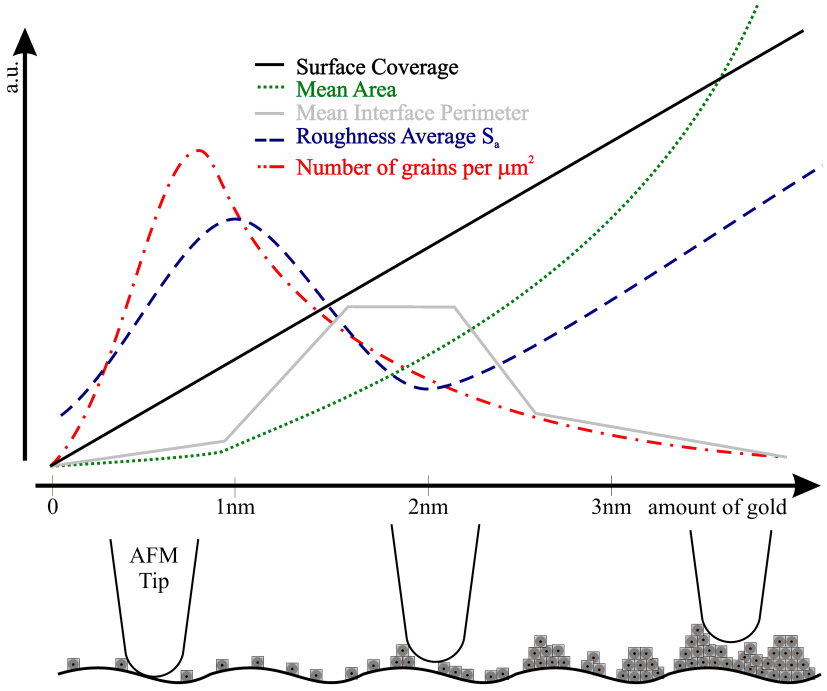


Figure 5.32: *Schematic evolution of different morphology results. The lower frame shows that under certain circumstances, the AFM tip can not follow the surface profile.*

density reaches a maximum before it decreases towards zero, because the growing islands become close enough for coalescence.

By the means of asymmetric fits of the area and interface perimeter distributions, the expected area of the gold grains and interface perimeter between the gold and the polymer as a function of the evaporated amount of gold are determined. In the initial stage of gold deposition, the grain area does not vary. This is certainly due to the fact that the new arriving gold atoms find new nucleation site (see the increasing cluster density) rather than sticking to existing gold islands. In a second step, the grain area increases either by island growing or by coalescence of existing gold islands.

Copy for "Bibliothèque UCL"

For the same reason as the gold island area, the interface perimeter does not vary significantly in the initial stage of gold deposition. Then the interface perimeter of the individual grains does increase and reaches a maximum value at ≈ 1.8 nm of evaporated gold. With further gold deposition, the island coalescence to bigger structures proceeds, so that the interface perimeter between the gold and the polymer decreases again towards zero. The evolution of all the determined morphology parameters is sketched in Figure 5.32.

Unfortunately it is not possible to determine the height of the islands, neither by AFM (due to inter alia the large tip apex) nor by electron microscopy (due to the physical limitation of the electron microscopes). But with a simple assumption based on half-ellipsoid formed gold islands, one can calculate the average height of the islands. So two independent calculation methods (↪ *Chapter 5.1.1 and 5.2.2*) shows that the islands height steeply increases in the beginning of the evaporation process and levels for higher amount of evaporated gold.

TEM analysis on microtomed polycarbonate samples point out that the sample preparation may have a significant influence on the morphology of the gold deposit. Which implication this observation entails for MetA-SIMS analysis remains open [‖].

[‖] It may be conceivable, that an unidentified irregularity in the morphology of the metallic deposition, which implicates a dissimilar secondary ions enhancement across the sample, results in a misinterpretation of the obtained results by S-SIMS.

Copy for "Bibliothèque UCL"

Chapter 6

Static SIMS

This second result chapter regroups the results from numerous ToF-SIMS analyses and is therefore subdivided into different sections.

In a first section a short summary of the sample preparation, the ToF-SIMS analysis conditions and the metalization procedure is given (↪ *Chapter 6.1*). A more detailed description of the sample preparation/metalization and analysis condition can be found in Chapter 4.

The subsequent Section 6.2 handles the influences of the substrate nature and polymer thickness on the characteristic peak intensities of the different polymers in order to study the influence of the polymer thickness on the ToF-SIMS signal enhancement. At the end these results are compared with binary collision simulations.

From the third section, the influence of a gold deposition on the polymer is discussed in detail. Firstly (↪ *Chapter 6.3*), the evolutions of the total secondary ion count (TSIC), the atomic species and the $Au_n^{\pm}$-clusters are presented as these results give a first insight into the emission process. Further sections handle the evolutions of characteristic polymer fragments and gold-adducted fragments as a function of deposited gold quantity (↪ *Chapter 6.4*) and as a function of time and storage between treatments and analyses (↪ *Chapter 6.5*).

In each section, it is tried to describe first the findings of the analyses and then to discuss them in an overall context. In order to not overload

Copy for "Bibliothèque UCL"

the work, only a limited number of graphs are shown in this work. Unless noted otherwise, the results of the other polymers are similar.

6.1 Summary of the sample preparation and the metalization procedure

The samples in this chapter were prepared as thin films spin-cast on silicon substrates with their native oxide layer. The secondary ion mass analyses are performed on an IONTOF Time-of-Flight SIMS (TOFSIMS III) using the $^{40}Ar^{+}$ primary ion gun. Detailed description of the sample preparation method and the ToF-SIMS analysis conditions can be found in chapter 4.1.2 and 4.3.3, respectively.

The *in-situ* metalization is performed in a preparation chamber, which is installed between the analysis chamber of the ToF-SIMS instrument and the air-lock. Sample metalization is carried out by thermal evaporation from a tungsten evaporation boat, in which a small amount of a gold foil (Goodfellow, $99,9\%$ purity) is loaded. The flux of evaporated metal is measured with a calibrated quartz crystal microbalance (QCM), which is placed on the opposite side of the evaporation source. A more detailed description of the evaporation device can be found in Chapter 4.2.2. In Section 4.2.2.C it is shown that the metalization procedure add only very small amount of contamination.

The mean sticking coefficient of gold on the polymers was determined by XPS analysis to be around 0.40 ± 0.08 ($\hookrightarrow$ *Chapter 5.1*). As seen in Chapter 5.2, the local gold quantity can radically change from point to point, so that the nominal evaporated gold-thickness, which is referred hereafter as "gold-quantity", indicates only the mean gold thickness which was evaporated onto the samples. On the graphs representing the SIMS signal evolution as a function of the gold-quantity, the QCM measured value of the evaporated gold quantity is used and not value of the deposited gold amount, determined by various XPS models.

To eliminate the daily instrument-based variation of the signal-detection sensibility, which complicated the comparison of measurements made on different days/weeks/months, all the measurements of one sample series are, if possible, performed within a

Copy for "Bibliothèque UCL"

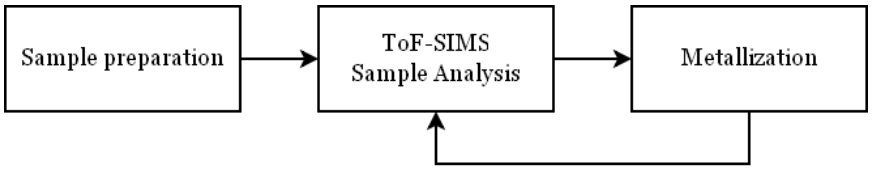


Figure 6.1: *Flow diagramm of the analysis procedure.*

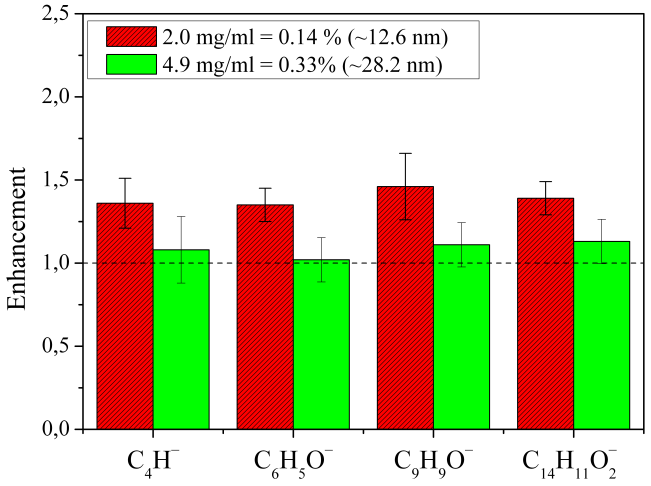
day. Within that day, the electronic settings are not altered, and the Ar pressure is manually stabilized, so that analysis conditions (primary ion current and detection sensibility) are assumed to be unchanged during the whole day. Figure 6.1 shows the analysis procedure that is used for all the studies where the influence of the evaporated gold quantity is examined. It should be mentioned that the sample size is sufficiently large to secure the analysis of a pristine sample surface during one analysis sequence without exceeding the static-SIMS limit. In order to minimize the cumulated error of the QCM measurements the evaporation flux was about 0.08 nm/s and each evaporation step lasted 5 s.

6.2 Influence of the substrate and polymer thickness

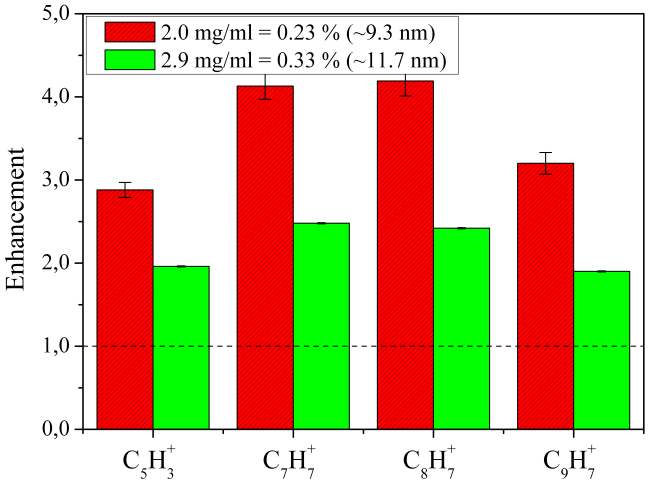
As already mentioned in the literature review (↪ *Chapter 2.1.2*), besides an external ionization source, the substrate under a thin analyte layer can significantly influence the sputter and ionization processes [13–15]. This "substrate" effect has a predominant role on the observed fragmentation pattern for a thin overlayer over the substrate. A maximum exaltation is observed for a monolayer on a noble metal.

Although the polymer thicknesses utilized in this work are not comparable to a monolayer (↪ *Chapter 4.1.2*), the aim of this section is to figure out if the substrates have any influence on the intensity exaltation of these polymers. For this investigation, two concentrations of the polymer solution were spincoated under the same conditions on two different substrates (on a native silicon wafer and a on thick gold layer which was evaporated prior on a silicon wafer by MBE).

Copy for "Bibliothèque UCL"



(a) *PC - neg*



(b) *PS - pos*

Figure 6.2: *Enhancement* $\frac{I_{Frag}(Au)}{I_{Frag}(Si)}$ *of some characteristic fragments of the PC and PS polymers as a function of the concentration of the polymer solution used for spincoating. The measured thickness of the polymer layers is noted in brackets.*

Copy for "Bibliothèque UCL"

The intensity exaltation of characteristic polymer fragments was calculated by dividing the intensity of a fragment on the gold substrate by the intensity of the same fragment on the silicon substrate $\left(\frac{I_{Frag}(Au)}{I_{Frag}(Si)}\right)$. Figure 6.2 shows the exaltation of characteristic peaks of PC and PS. Similar results can be found on PET-I and PMMA samples.

An obvious observation on both polymer is that the exaltation for the polymer spincoated from the 2 mg/ml solution concentration is larger than that of the $4.9\frac{mg}{ml} = 0.33\%$ concentration (PC, PET-I) and $2.9\frac{mg}{ml} = 0.33\%$ concentration (PMMA, PS), respectively. However, a difference between both polymers can be observed: On the PC sample, the exaltation for the $4.9\frac{mg}{ml}$ polymer is closer to unity than for the PS sample. The same observation can be observed also between PET-I and PMMA. This exaltation difference indicates that the $4.9\frac{mg}{ml} = 0.33\%$-PC (and PET-I) is less substrate-sensitive than the $2.9\frac{mg}{ml} = 0.33\%$-PS (and PMMA) sample.

Bearing in mind the used solvent (↪ *Table 4.3*) or the measured thickness of the different polymer by ellipsometry (↪ *Figure 4.8*), this difference can be easily explained: The used solvent of PC and PET-I (Chloroform - 1.48 g/cm^3) is denser than the solvent for PMMA and PS (Toluene - 0.87 g/cm^3). Due to this difference, not only the polymer concentration inside the solution is lower, but also the resulting polymer thickness after spincoating.

As a consequence the collision cascade permeates the polymer layer and reaches the underlying substrate if the polymer thickness is too low. Due to higher gold atomic mass, the gold substrate reflects better the energy. Hence a greater amount of the energy deposited by the ion bombardment reaches the sample surface, and thus more fragments can be emitted from the sample. Noteworthy is that the influence of the substrate can also be observed here on, compared to a monolayer, large polymer thicknesses.

As in this work the influence of a gold deposition on a *bulk* polymer sample is investigated, the substrate should not have any impact on the sputtered particles. To ensure this prerequisite, the polymer thickness should be thick enough that the collision cascade fully develops inside the polymer layer and does not interact with the underlying substrate.

Copy for "Bibliothèque UCL"

To figure out the theoretical influence of the substrate as well as the depth of collision cascade induced by the impinging ion for various polymer-substrate combinations, some simulations with SRIM have been performed.

SRIM/TRIM is a software package, based on Monte-Carlo calculation, which allows to simulate elemental* sputtering yields of numerous materials and to investigate the development of the collision cascade inside these materials [252]. The different parameters (surface binding energy, lattice binding energy, displacement energy, density) for the substrates and the polymers were selected from the internal database of SRIM. The primary ion settings for the SRIM simulations are chosen as close as possible to the experimental setup. Overall 20000 trajectories of 10 keV ^{40}Ar atoms impinging under an angle of incidence of 45° on various samples are investigated. The samples are polymer overlayers of different nature and thicknesses on a SiO_2/Si or Au substrate, which allow to check the influence of the substrate on the emitted ions as a function of the polymer thickness. Above a polymer thickness of ≈ 10 nm, neither a gold nor a silicon atom is sputtered from the sample. However, for atomic species of the polymers there is still a difference in the sputter yield.

Figure 6.3 shows the enhancement of the sputter yield of C-atoms on a gold substrate as a function of the polymer thickness. The enhancement was determined by the ratio of the sputter yield on both substrate $\left(\frac{Y_C(Au)}{Y_C(Si)}\right)$. The different atomic species of the polymers (H, C, O) show a similar evolution. Furthermore no significant difference of the sputter yield can be observed between the different polymers, due to their comparable densities ($1.06 - 1.40$ g/cm^3). For polymer thicknesses below ≈ 13 nm the sputter yield enhancement shows the expected and observed yield enhancement for the gold substrate. With increasing polymer thickness the substrate influence diminishes and the ratio converges to unity. For thin polymer thicknesses, the impinging energy is better confined and back-reflected in the case of gold than for silicon substrates, which leads to a higher sputtering yields of fragments and molecules.

*As no long range interactions are considered, this simulation software is not suitable for determining molecular sputter yields and so the determined sputter yield should only be seen as an approximation.

Copy for "Bibliothèque UCL"

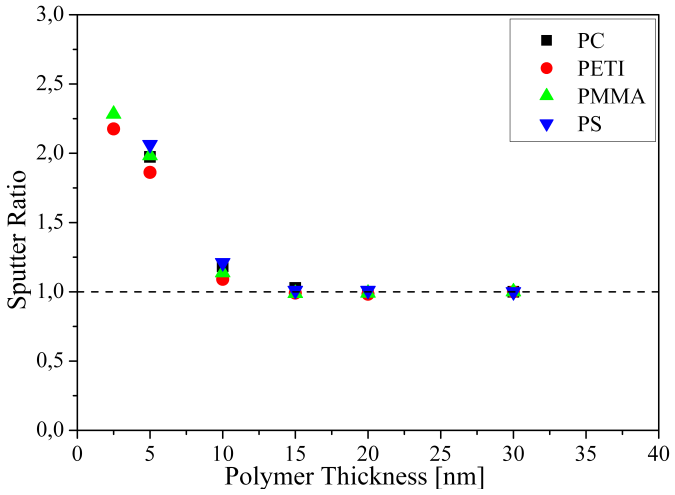


Figure 6.3: *SRIM/TRIM Ratio* $\frac{Y_C(Au)}{Y_C(Si)}$ *of the sputtered C-Atoms on the different polymers as a function of polymer thickness. H and O atoms show a similar evolution. Simulation-Parameter:* 10 keV ^{40}Ar - 45° *incidence.*

These theoretical findings confirm the results in the previous paragraphs, where samples with low polymer concentration/thickness show a higher secondary ion intensity on a gold substrate than on a native silicon substrate (↪ *Figure 6.2*).

Despite the independence of the atomic sputter yield from the substrate nature in these simple simulations at polymer thickness above ≈ 13 nm, the longitudinal ranges, which corresponds to the penetration depths of the collision cascade, differ significantly on both substrates at these polymer thicknesses. For different polymer-substrate combinations, the evolution of the longitudinal range is shown in Figure 6.4. One observes that for thin polymer layers, the longitudinal range tends to the value of the substrate. For polymer thickness above ≈ 25 nm the longitudinal range does not depend anymore on the nature of the substrate but mainly on the polymer density. This indicates that the stopping power of the primary ion is significant lower in the polymer layer than in the substrate.

One should keep in mind that these simulations are based on a perfect homogeneous and flat polymer layer and on individual

Copy for "Bibliothèque UCL"

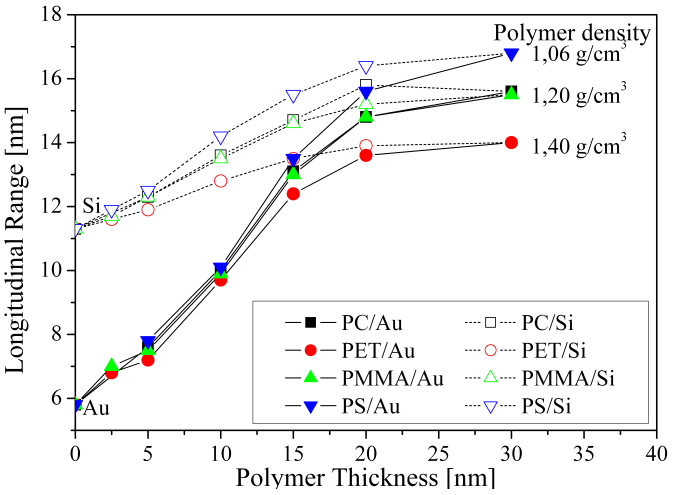


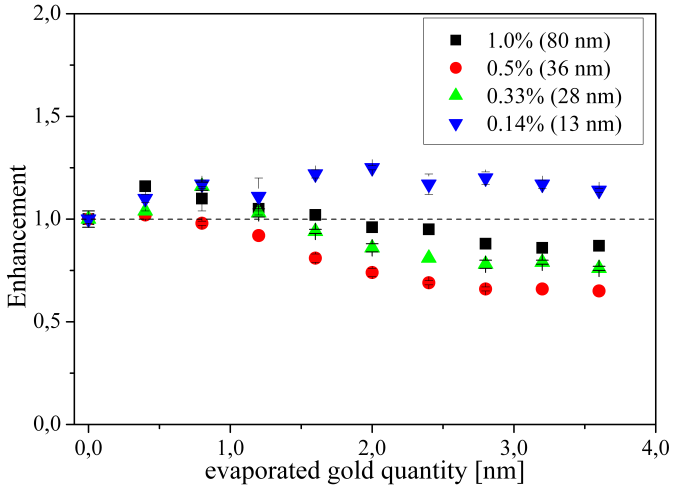
Figure 6.4: *SRIM/TRIM evolution of the longitudinal ion-range on different substrates/polymer combinations as a function of the polymer thickness. Simulation-Parameter:* 10 keV ^{40}Ar - 45° *incidence.*

ion bombardments on a pristine sample. Hence no roughness and inhomogeneity effects, which are induced by the sample preparation as well as no simultaneous lift-up of molecules due to overlapping collision cascades, are considered in these simulations. Therefore it seems reasonable to choose a polymer thickness above 25 nm to ensure the development of the collision cascade fully inside the polymer layer.

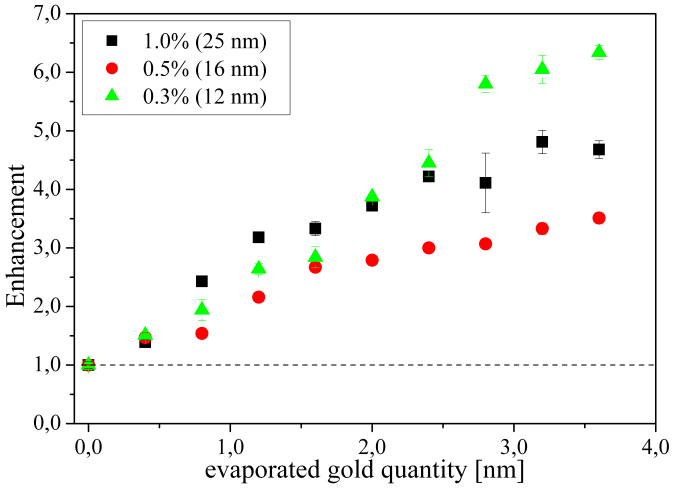
6.3 Evolution of the total secondary ion count and the atomic fragments

The total secondary ion count (TSIC) and the atomic ions ($H^{\pm}$, $C^{\pm}$, $O^{\pm}$) can give a first hint of a change in the sputtering or ionization probability due to gold deposition. Figure 6.5a shows the evolution of the TSIC for the PC polymer in the negative polarity as a function of the used polymer concentration and of the evaporated gold quantity. For a better comparison between the samples, the TSIC is normalized to the TSIC of the pristine polymer sample. Similar results can be found in the positive polarity and on the other polymers.

Copy for "Bibliothèque UCL"



(a) *PC - negative polarity*



(b) *PS - positive polarity*

Figure 6.5: *Evolution of the TSIC as a function of the evaporated gold quantity for different used concentration of PC and PS polymer solution.*

Copy for "Bibliothèque UCL"

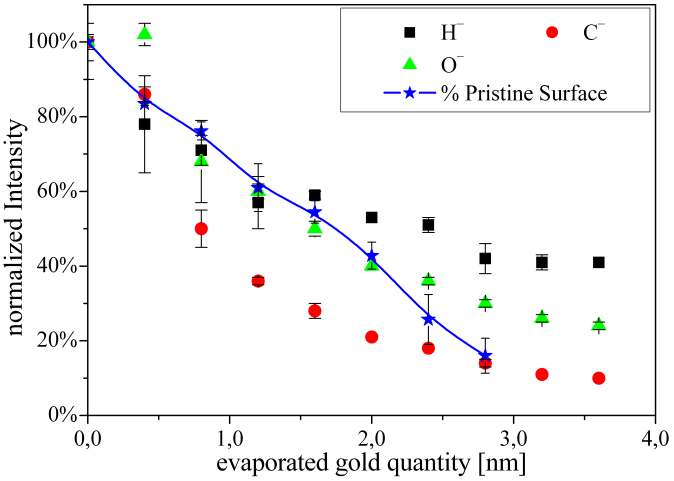
A first observation is that for thick layers the TSIC depends only little on the evaporated gold quantity (except for the PS in the positive polarity (↪ *Figure 6.5b*)). The maximal variation on all these thick oxygen-containing polymers (PC, PET-I, PMMA) is between 0.76 and 1.40. In the negative polarity, the average contribution of the Au_n^- ions to the TSIC is slightly below 10% (with a maxmimal contribution reaching 15% in the case of PS with 0.8 nm of evaporated gold), whereas in the positive polarity, the contributions of the Au_n^+ ions to the TSIC are all below 1%. Another observation is that the TSIC evolution of polymer samples, where the substrate has a provable influence (↪ *Chapter 6.2*) is different than on thick polymer samples. The observed difference of the TSIC evolution as a function of evaporated gold-quantity between thin and thick polymer layers can be attributed to the enhanced sputter yield due to the influence of the underlying substrate.

Interesting is also the evolution of the atomic species (H, C, O) of the polymer as a function of the gold quantity. On thick PC, PET-I or PMMA samples, these atomic anions show mainly a continuous decrease of their intensity with increasing gold coverage (↪ *Figure 6.6a*). For these polymers, the intensity decrease matches to the percentage of pristine polymer left at the sample surface, which was determined by electron microscopy image analysis (↪ *Chapter 5.2.2*). At higher evaporated gold-quantity, the intensity of the atomic species seems to become constant. In the positive polarity the evolution of these atomic cations is similar.

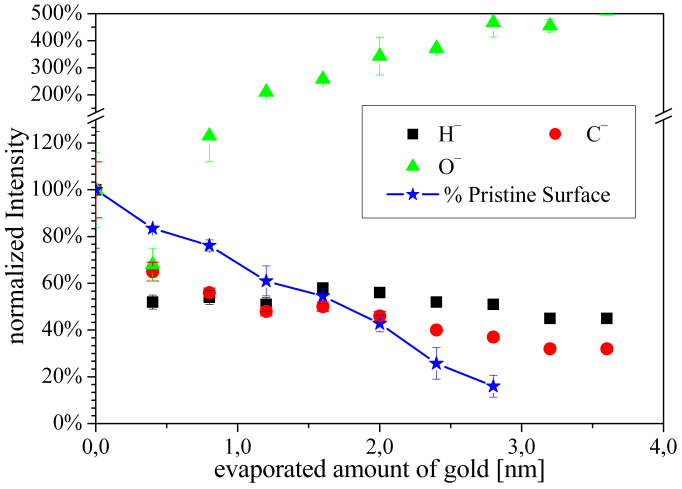
However the PS polymer shows different evolutions for TSIC and the atomic ions than the other polymers: Although the TSIC does not change significantly in the negative polarity (enhancement range: $0.96 - 1.12$), the TSIC continuously increase in the positive polarity (↪ *Figure 6.5b*). Furthermore the O^- intensity of PS (a polymer which theoretically does not contain any oxygen) increases continuously with increasing gold quantity (↪ *Figure 6.6b*). However the oxygen intensity is still very low compared to other polymer samples. The H^+ and C^+ ions show on the PS sample not a similar decrease as on the other polymers.

The fact that the TSIC evolution as a function of the evaporated gold quantity is significantly different on thin oxygen-containing polymers, is another hint that in these cases the substrate had an important impact

Copy for "Bibliothèque UCL"



(a) *PC - negative polarity*



(b) *PS - negative polarity*

Figure 6.6: *Change of the intensity of H^-, C^- and O^- as function of the evaporated gold quantity for thick PC and PS polymer samples in the negative polarity. The solid line indicates the remaining percentage of pristine polymer at the sample surface.*

Copy for "Bibliothèque UCL"

on the emitted ion intensities. The small variation of the negative TSIC of oxygen-containing polymers as a function of gold-quantity indicates that the presence of gold on the sample surface does not have significant influence on the product of sputtering and ionization probabilities. Nevertheless it can not be excluded that both probabilities vary simultaneously in an opposite way or that different fragments undergo different probability changes.

The intensity decrease of atomic ions with increasing gold coverage can be explained if one considers the formation of secondary ions (↪ *Chapter 3.2.3*). As secondary ions are mainly emitted from the top surface layer of the sample and the H, C and O ions are theoretically only present in the polymer sample and not in the gold deposit, the intensity of these ions is proportional to the surface of the uncovered polymer. However, for large gold coverage, it can not be excluded that also a part of the signal is induced by redeposition of emitted atoms, diffusion of small fragments onto the gold deposit or absorption of contamination present in the preparation/analysis chamber.

Recent MD simulations [79, 80] show that the presence of gold clusters on the polymer sample causes that the collision cascade, induced by a monoatomic primary ions, deposits more energy in the sample surface, which results in a higher sputter yield of polymer *fragments*. No statements about atomic ions have been made in these simulations so that the decrease of atomic ion intensities found here in the experiments, can be conscientiously correlated to the diminishing pristine polymer coverage at the sample surface. This behavior indicates that a collision cascade starting from the impact of the primary ion on a gold cluster does not reach the polymer surface with sufficient energy to break the polymer molecule into atomic fragments and to emit their ions towards vacuum (↪ *Chapter 3.2.3.C*). As no enhancement of the atomic ions can be observed in the negative polarity with increasing gold quantity, the presence of gold and its reduction of the local work function can be neglected for the atomic ion emission.

The different behavior of TSIC and atomic ions on the PS sample can be explained by the assumption that the oxygen or oxygen containing species, which are left in the analysis/preparation chamber, are adsorbed onto the sample. As the O^- intensity increases steadily with the gold coverage one can imagine that the oxygen is adsorbed rather

Copy for "Bibliothèque UCL"

onto the gold deposit than on the polymer. The relative stability of the H^+ and C^+ intensities can be explained either by the presence of an electronegative oxygen over the whole surface, which favors the positive ion emission [182], or by a different change in the molecular orbital level in the PS compared to the oxygen-containing polymers due to the presence of oxygen and/or gold.

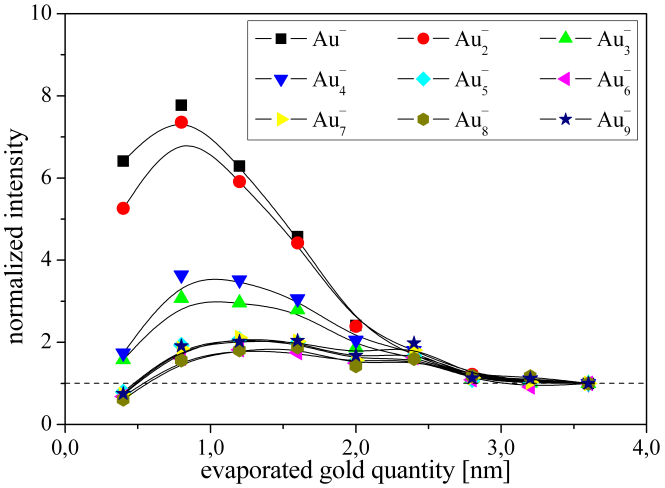
To complete this section about the evolution of atomic and inorganic cluster ions as a function of evaporated gold-quantity, a short summary of the results covering the variation of the $Au_n^{\pm}$-cluster intensities emitted from a metalized polymer samples is described hereafter.

In the negative polarity, the different gold cluster ions show the same behavior on all thick polymers: For small gold-quantities, the intensity of the Au_n^--clusters increases until an gold-quantity of $0.8 - 1.2$ nm followed by a slow intensity-decrease to a Au-cluster depending limiting value, which is assumed here to be close to the value obtained for pure Au sample. Based on that assumption, the intensities of each gold cluster are normalized by forming the ratio $I_{Au_n}(x\,nm)/I_{Au_n}(3.6\,nm)$, which allows a better comparison of the evolution of the different $Au_n^{\pm}$-clusters (↪ *Figure 6.7a*). In the positive polarity, the Au_n^+ cation intensities are 1-2 orders of magnitude smaller than the corresponding Au_n^- anion.

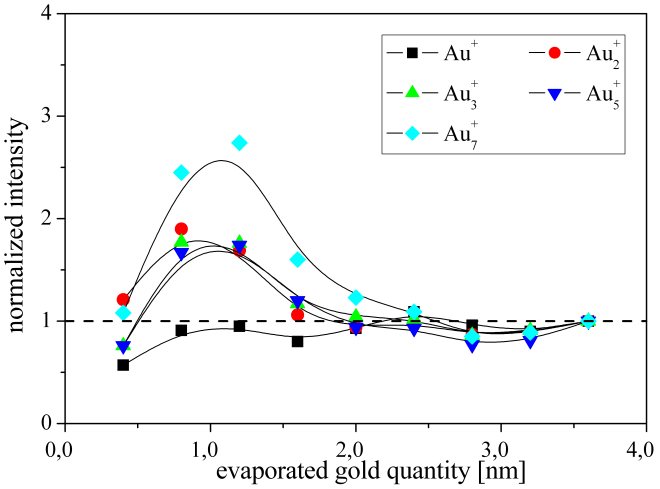
Contrarily to the negative polarity, the evolution of the Au_n-clusters as function of the evaporated gold quantity shows significant difference between the samples in the positive polarity. On the PC and PMMA samples, the Au_n^+ intensity pass through a maximum at $0.8 - 1.2$ nm of evaporated Au quantity before approaching an Au-cluster depending limiting value. In contrast, on the PS sample the Au_n^+ intensities steadily increase towards a limiting value, whereas no clear maximum can be observed on PET-I sample. Furthermore one realizes that, contrarily to the negative polarity, the maximum increase is higher for large Au_n^+-cluster than for light ones.

Beside a steady decrease of the absolute secondary $Au_n^{\pm}$ yields as the size of the Au_n cluster increases, a yield oscillation between adjacent Au-clusters can be observed (↪ *Figure 6.8*). Thereby the intensity of odd n clusters is generally greater that that of even $n-1$- and $n+1$-clusters. In the negative polarity, the yield decrease across the Au_n^--clusters becomes smaller with increasing evaporated gold quantity.

Copy for "Bibliothèque UCL"



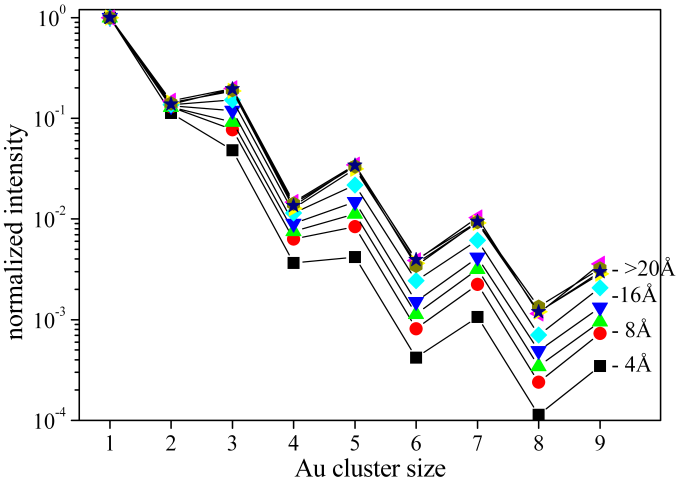
(a) *negative polarity*



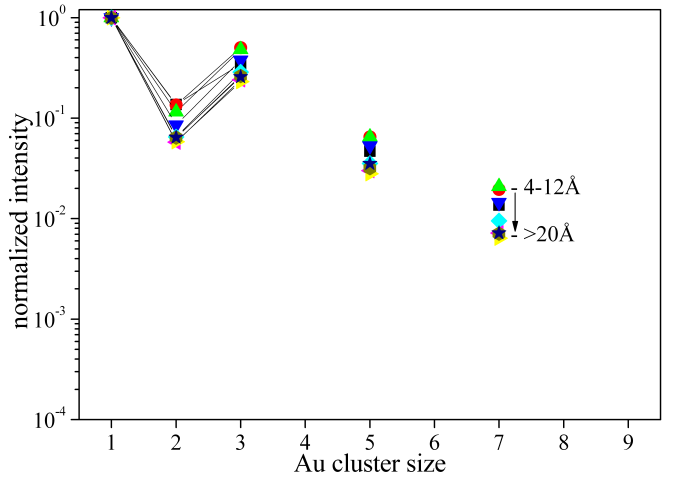
(b) *positive polarity*

Figure 6.7: *Normalized variation of the secondary ion intensity of* $Au_n^{\pm}$ *as a function of the evaporated gold quantity on PC. The normalization is based on the* $Au_n^{\pm}$ *intensity from the largest evaporated gold quantity.*

Copy for "Bibliothèque UCL"



(a) *negatitve polarity*



(b) *positive polarity*

Figure 6.8: *Normalized variation of the secondary ion intensity of $Au_n^{\pm}$ as a function of the Au-cluster size. The normalization is based on intensity of $Au^{\pm}$. Au_4^+ and Au_6^+ have not been observed.*

Copy for "Bibliothèque UCL"

Above 2 nm of evaporated gold-quantity, no further yield decrease is observed. Contrarily to the negative polarity, the yield decrease across the Au_n^+-clusters becomes greater with increasing evaporated gold quantity in the positive polarity.

The yield decrease of metallic clusters with n has been explained by MD simulations and the sputtering theory. However, the effect of the MCP detector efficiency, which decreases for increasing ion masses [253], can not be neglected. The lower intensity of gold cations in comparison to that of the anions can be explained by the fact that the electron affinity of a gold atom is much smaller that its ionization energy (↪ *Table 6.1*).

Atom	Ionization or VIP [eV]	Work Function [eV]	Electron affinity [eV]	Binding energy [eV]
H	13.60	-	0.75	-
C	11.26	5	1.26	-
O	13.62	-	1.46	-
Au	9.23	5.38	2.31	-
Au_2	9.51	-	2.02	2.20
Au_3	7.37	-	3.77	3.41
Au_4	8.11	-	2.70	5.81
Au_5	7.59	-	3.25	7.95
Au_6	8.55	-	3.30	11.0
Au_7	7.29	-	3.49	12.4
Au_8	8.21	-	2.96	15.2
Au_9	7.12	-	3.63	16.8

Table 6.1: *Ionization energies (or vertical ionization potentials for clusters), work functions and electron affinities for the different species occurring in the work. Values found in [236] and [254].*

The odd-even alternation, which has been observed regardless of the ion formation and detection methods [255–257], essentially reflects an electron pairing effect, resulting from the circumstance that each atom in the cluster contributes a single valence electron to the bonding orbital, so that the electron affinity of odd-size ionic clusters (even number of valence electrons) is higher than that of even-size ionic clusters, whereas

Copy for "Bibliothèque UCL"

the ionization energy (or vertical ionization potential) shows the inverse relation (lower ionization energy for odd-size ionic clusters) [258].

As plenty different physical parameters (ionization energy, electron affinity, binding energy, sputter yield) are able to change simultaneously, a clear and straightforward interpretation of the $Au_n^{\pm}$ evolutions as a function of the deposited gold quantity is not possible. However is it remarkable that the maximum of the $Au_n^{\pm}$-intensities corresponds to the maximum of the detected number of gold islands (↪ *Figure 5.24*).

As far as the evolution of the gold ions are described in the literature for MetA-SIMS experiments [76, 259], the observation in this work are consistent with the results found there. So assign Delcorte et al. [76] the exponential decay for large deposited gold quantity to the results of a bulk metallic crystal. The results here show an exponential decay too, but an exponential decay can be observed for all amount of deposited gold quantity and not only for large evaporated gold quantity. This contradictory statement can be resolved if one assumes that the small clusters observed during electron microscopy analysis (↪ *Chapter 5.2*) already behave mostly like bulk material.

6.4 Evolution of characteristic and gold-adducted fragments

As known from the literature and also observed in the previous chapters, the thickness of the polymer film influences the ion emission. In order to ensure that the substrate has no effect on the experiments only thick polymer layers are analyzed and studied here in a more detailed way. If the interaction with the substrate and charging effects can be excluded, similar results can be observed also for larger sample thicknesses.

In the case where the sample is an isolating bulk sample, on which a charge neutralization, e.g. by flooding the surface by low-energy electrons, is absolutely necessary, the metalization procedure leads not only to an enhancement of the signal intensity but makes also the charge neutralization superfluous [238]. Although the samples, which are evaluated hereafter represent bulk polymer samples, no sample charging has been observed during the analysis.

Copy for "Bibliothèque UCL"

As generally several hundreds of peaks are observed in a ToF-SIMS spectrum, a choice of the most important and characteristic fragments is done in a preliminary step (↪ *Chapter 6.4.1*). In the subsequent Section 6.4.2 the evolutions of the selected fragments as a function of the evaporated gold quantity are presented and discussed in detail for every polymer used in this study. In a further section the combinations of a characteristic fragment with a gold atom is examined (↪ *Chapter 6.4.3*). At the end of the sections the observed results are discussed and it is tried to clarify the observations with regard to different parameters (i.e. morphology, presence of oxygen, modification in sputter and/or ionization probability).

6.4.1 Selection of the characteristic fragments

In bulk polymers, only ions in the fingerprint region ($m/z < \mathbb{M}$), which are generated by fragmentation of the macromolecules, can be observed. This fingerprint pattern of the spectra allows the unambiguous identification of most of the polymer molecular structures. The basic assumption here is that the emitted ions are fragments which are directly related to the molecular structure of the polymers present at the surface. However, it has been shown that for some polymers such as polystyrene (PS), the molecular structure of some characteristic ions cannot be deduced directly from the macro-chain fragmentation, but requires important reorganizations of the emitted fragment. Among the numerous characteristic fragments of the polymers (↪ *Chapter A.2*), only the few ion fragments, which are listed in Table 6.2, are discussed here in details. The selected ions are the most intense ions across the fingerprint region of the molecule with a choice of simple hydrocarbons and oxygen-containing polymer fragments. A comparison with the spectra of pure gold (↪ *Chapter 4.2.2.C*) shows that due to the low intensity of the "contamination" fragments, the metalization procedure does not significantly influence the intensity of the selected characteristic fragments.

Copy for "Bibliothèque UCL"

Polarity	negative		positive	
	Label	Mass [u]	Label	Mass [u]
PC	C_4H^-	49.01	$C_6H_5^+$	77.04
	C_5^-	60.00	$C_9H_7^+$	115.06
	$C_6H_5O^-$	93.03	$C_9H_{11}O^+$	135.08
	$C_9H_9O^-$	133.07	$C_{13}H_9^+$	165.07
	$C_{14}H_{11}O_2^-$	211.08	$C_{14}H_{11}O^+$	195.08
PET-I	$C_6H_4^-$	76.03	$C_6H_4^+$	76.03
	$C_7H_5O^-$	105.02	$C_7H_4O^+$	104.01
	$C_7H_5O_2^-$	121.04	$C_8H_5O_3^+$	149.04
	$C_8H_5O_4^-$	165.01	$C_{10}H_7O_4^+$	191.01
	$C_{10}H_7O_4^-$	191.01	$C_{10}H_9O_4^+$	193.03
PMMA	CH_3O^-	31.02	$C_2H_3O_2^+$	59.01
	$C_4H_5O_2^-$	85.03	$C_4H_5O^+$	69.03
	$C_5H_9O_2^-$	101.06	$C_5H_9O^+$	85.07
	$C_9H_{13}O_4^-$	185.08	$C_5H_9O_2^+$	101.06
			$C_9H_{13}^+$	121.10
PS	C_4H^-	49.01	$C_4H_3^+$	51.02
	$C_5H_2^-$	62.02	$C_5H_3^+$	63.02
	C_6H^-	73.01	$C_6H_5^+$	77.04
	$C_7H_2^-$	86.02	$C_7H_7^+$	91.06
	$C_8H_5^-$	101.04	$C_9H_7^+$	115.06

Table 6.2: *Selected fragments of the different polymers among their vast number of characteristic fragments for the detailed discussion of the their intensities as a function of the evaporated gold quantity. The structure of the fragments can be found in the appendix A.2.*

6.4.2 Evolution of characteristic fragments as a function of the evaporated Au-quantity

In this section the intensity evolution of the selected characteristic ions as a function of the evaporated gold quantity is presented for all the four polymers used in this work. In general the indication of the secondary yield value is only needed if one wants to compare the secondary ion emission measured with different analysis parameters. As the analysis parameters are unchanged during the analysis of a whole sample series,

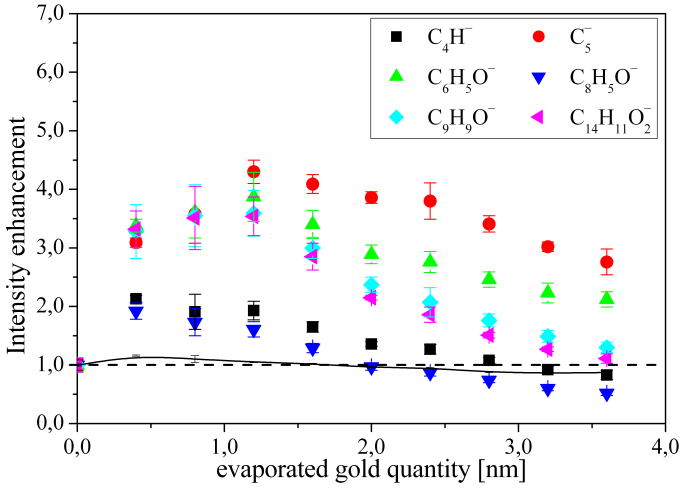
Copy for "Bibliothèque UCL"

the indication of the secondary yield value is waived here. Instead, the relative intensity variation of the characteristic fragments compared to the pristine sample is shown here as a function of evaporated gold quantity. For that, the secondary ion intensity of a fragment from a metalized sample is divided by the intensity of the same peak obtained from the pristine samples $\left(\frac{I_{Frag}(x\,Au)}{I_{Frag}(0)}\right)$. For a direct comparison also the evolution of the total secondary ion counts are plotted as a solid line in the graphs and in some graphs, also the evolution of the remaining polymer at the sample surface is represented by a dotted line. The evolution of other fragments, which are not characteristic for the polymer samples, are not investigated in this work. At the end of this section the observed enhancement and possible explanations are discussed.

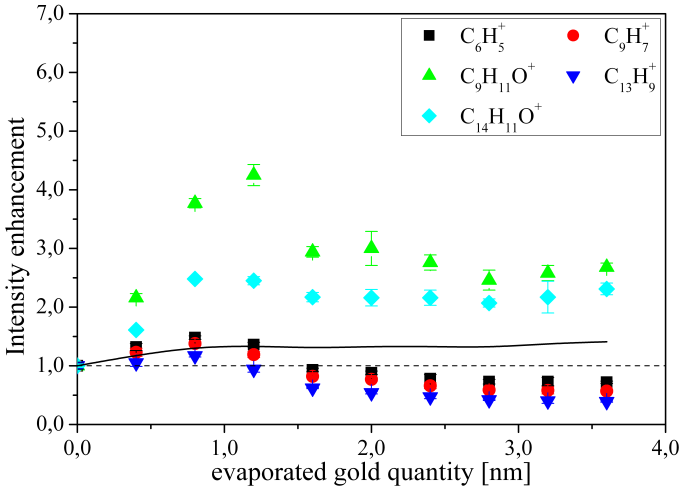
PC In the negative SI mode (↪ *Figure 6.9a*), one observes that the intensity of the fragments strongly increases to a maximum and then slowly decreases. For larger gold quantities, some fragments show also an yield enhancement <1 (net yield decrease). The maximum enhancement as well as the amount of gold at which the transition to the net yield decrease occurs, is fragment dependent. Most fragments in the negative polarity reach the maximum at a gold quantity of ≈ 1.2 nm. In the positive SI mode (↪ *Figure 6.9b*), only hydrocarbon fragments show a yield decrease at high evaporated gold quantity, while the yield enhancement of oxygen-containing fragments reaches a value of 2-3 at a higher gold coverage.

PET-I In the negative polarity (↪ *Figure 6.10a*) the maximum of the enhancement is reached between 0.8 and 1.2 nm and its position is similar for the fragments. The enhancement of the oxygen-containing fragments are quite similar whereas the simple hydrocarbon fragments exhibit a larger enhancement. At higher evaporated gold quantity, the enhancement of the fragments decreases towards unity. In the positive polarity there is a net yield decrease over the whole range of the evaporated gold quantity (↪ *Figure 6.10b*). A local maximum can be found at ≈ 0.8 nm but mainly the intensity decrease is similar to the decrease of the remaining polymer surface. There is no significant difference in the evolution of the secondary ion intensity between the hydrocarbons and oxygen-containing fragments.

Copy for "Bibliothèque UCL"



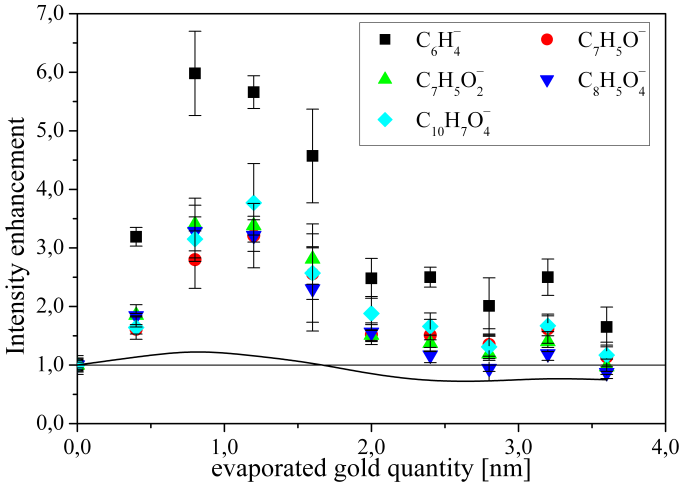
(a) *negative polarity*



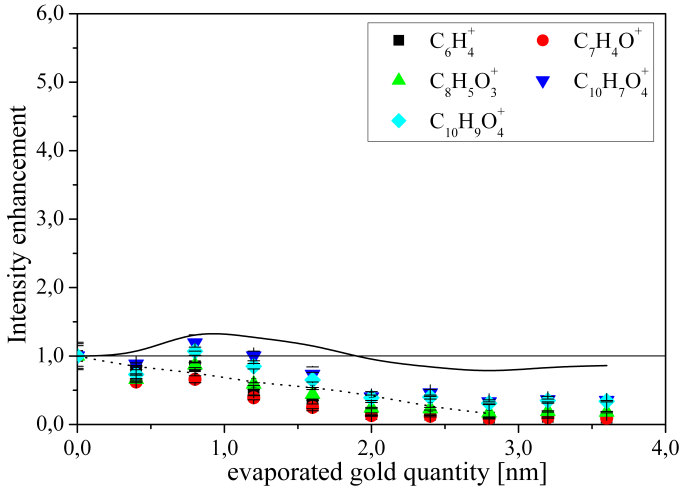
(b) *positive polarity*

Figure 6.9: *Secondary ion intensity variations of characteristic PC fragments in both polarities measured on a thick PC layer. The solid line represents the evolution of the total secondary ion counts.*

Copy for "Bibliothèque UCL"



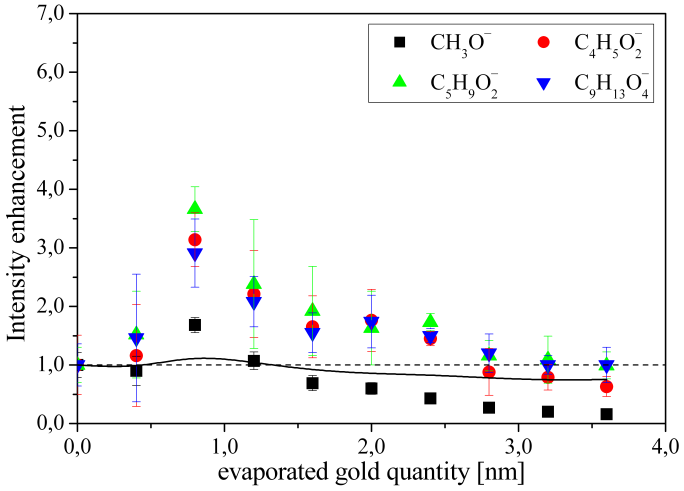
(a) *negative polarity*



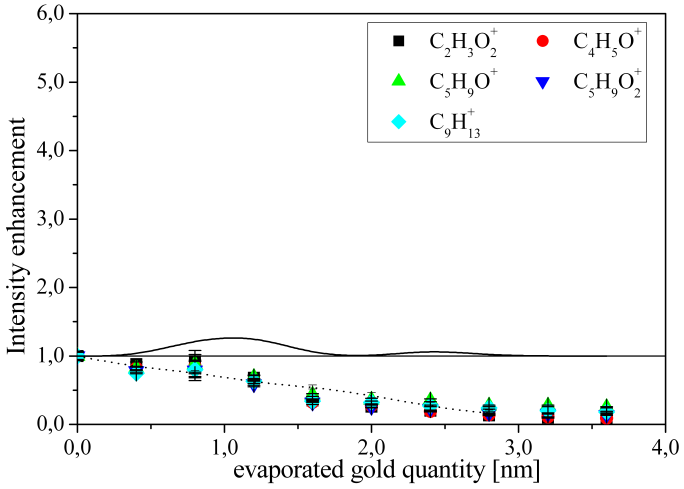
(b) *positive polarity*

Figure 6.10: *Enhancement of the secondary ion intensity for characteristic PET-I fragments in both polarities as a function of the evaporated gold quantity. The evolution of the total secondary ion counts and the remaining polymer at the sample surface are represented by a solid line and dotted line, respectively.*

Copy for "Bibliothèque UCL"



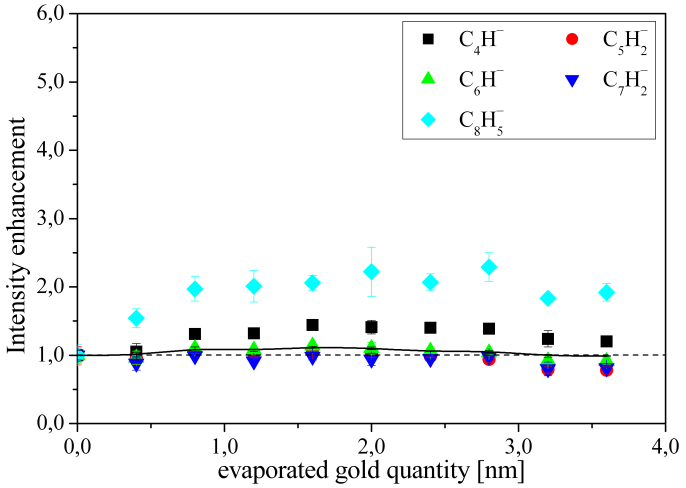
(a) *negative polarity*



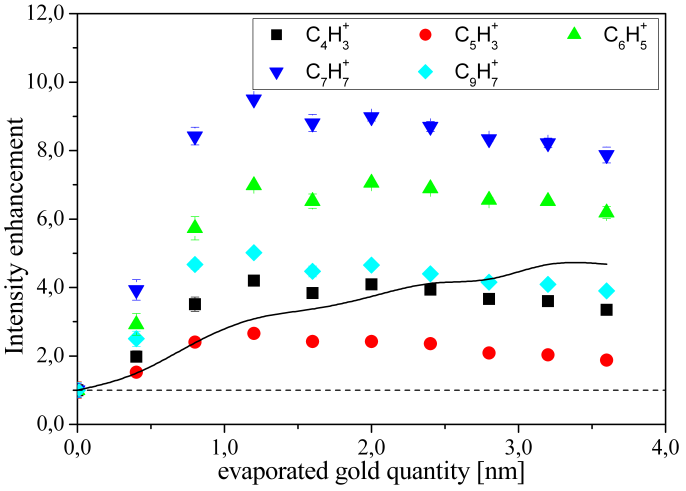
(b) *positive polarity*

Figure 6.11: *Variation of the secondary ion intensity of characteristic PMMA fragments in both polarities as a function of the evaporated gold quantity. The solid line and the dotted line represent the evolution of the total secondary ion counts and the remaining polymer at the sample surface, respectively.*

Copy for "Bibliothèque UCL"



(a) *negative polarity*



(b) *positive polarity*

Figure 6.12: *Enhancement of the secondary ion intensity for characteristic PS fragments in both polarities as a function of the evaporated gold quantity. The solid line represents the evolution of the total secondary ion counts.*

Copy for "Bibliothèque UCL"

PMMA As for the polycarbonate, the enhancement evolution of characteristic poly(methyl methacrylate) anions first pass through a maximum before a moderate decrease occurs (↪ *Figure 6.11a*). The position of the maximum is however slightly lower (≈ 0.8 nm) than on the PC sample. At higher evaporated gold quantity, a net yield decrease is observed. In the positive polarity no enhancement of the cations is observed at all (↪ *Figure 6.11b*) but the intensity decrease is similar to the decrease of the remaining polymer surface. At higher evaporated gold quantity, the net yield decrease stabilizes.

PS For most of the characteristic polystyrene anions (↪ *Figure 6.12a*) the observed yield enhancement is quite small. Contrarily to the other polymers no clear maximum is observed. In the positive SI mode (↪ *Figure 6.12b*) the intensity first increase until ≈ 1.2 nm and then for larger gold quantity only a slight decrease of the yield enhancement is observed. The yield enhancement of the characteristic cations is strongly fragment-dependent (enhancement between 2 and 10).

Discussion

The number of publications about MetA-SIMS is quite small, so that a comparison with the results obtained in this work is difficult. On the one hand, most of the papers handle light-weighted simple hydrocarbon polymers, so that only the polystyrene results here are comparable with the literature to some extend. The fact that the observed yield enhancement of the characteristic polystyrene fragments are lower here than those observed in the literature [9, 73, 76] can be attributed to the lower diffusion coefficient of higher molecular weight polymers over the gold nanoparticles. On the other hand, investigations describing oxygen-containing polymers or showing the results of the negative polarity are even sparser in the literature of MetA-SIMS, so that a reasonable comparison with former results is unpromising.

At the first sight, one might see that the evolution of the characteristic fragments and the total secondary ion count are similar. But a closer look reveals that neither the enhancement value of the TSIC nor the position of its maximum matches with the observation of the evolution of the characteristic fragments. The discrepancy

Copy for "Bibliothèque UCL"

between the TSIC evolution and the characteristic fragments indicates that the sample metalization induces a fragment-selective change in the sputtering/ionization probability, i.e. depending on whether the emitted ion is characteristic for the sample or not, the sputtering/ionization probability changes in a different way, so that the sum of the emitted fragment matches the (relative) constant total secondary ion count.

A further general observation is that, except for the polystyrene sample which shows the opposite behavior, the enhancement is larger in the negative polarity than in the positive polarity. Moreover the oxygen-containing fragments undergo a different enhancement than the hydrocarbon fragments on the oxygen-containing polymers. All this, in addition to the observed evolution of the atomic ions as a function of gold quantity (↪ *Chapter 6.3*) and the results obtained under different storage conditions (↪ *Chapter 6.5*) indicates that the presence of oxygen in- and/or outside the polymer molecule/fragment can have an influence on the emission enhancement.

Taking into account the surface morphology of the metalized sample (↪ *Chapter 5.2*) several conclusions can be made about the influences of the morphology parameters to the intensity enhancement of the characteristic fragments: As no linearity between the evaporated (or deposited) gold quantity and the enhancement is observed, the total amount of gold present at the sample surface is not responsible for the noticed enhancements. Since the gold coverage θ continuously increases as a function of evaporated gold quantity (↪ *Figure 5.23*) and such an evolution is not observed for the characteristic fragment enhancements, a correlation between the fragment enhancement and the gold coverage can be omitted too. With the same argumentation, a direct relation between the enhancement in ToF-SIMS and the mean area and diameter of the gold islands (↪ *Figures 5.25 and 5.27*) can be excluded. Also both morphology parameters, the number of gold islands per area N_i and the mean interface perimeter P_{mi}, which show in their evolution a maximum at ≈ 0.8 nm and $1.6 - 2.0$ nm respectively, can not serve alone as explanation for the observed enhancement evolution.

In the cases of PET-I$\oplus$ and PMMA$\oplus$, where the characteristic fragment intensities steadily decrease with ongoing metalization, the observed enhancement decrease can be allocated to the decrease of the pristine polymer that is available at the surface. This indicates that in

Copy for "Bibliothèque UCL"

these cases the creation process (pulverization and ionization) of the secondary ions does not change due to the presence of gold on the polymer surface.

For the case where the enhancement of the characteristic fragments passes through a maximum located between 0.8 and 1.2 nm of evaporated gold (↪ PC⊖, PET-I⊖, PMMA⊖) an other parameter than the gold coverage should be considered. Only the evolution of the number of gold islands per μm^2 (↪ *Figure 5.24*) fulfills the request of the maximum position. But this parameter shows a too fast fall off after its maximum, which is not observed on the enhancement evolution in ToF-SIMS. A resort of this dilemma would be a combination of multiple parameters.

Originating from the reflection that, on the one hand, a primary ion which impinges in the center of a gold islands does not emit any polymer fragments, and on the other hand, the available polymer surface decreases with ongoing metalization, the following assumption can be made: It exists a region at the boundary of each gold island, at which a starting collision cascade reaches the polymer/vacuum interface. Thereby the deposited energy in the polymer is in such that it is not enough to violently fragment the polymer into atoms but sufficient to emit characteristic polymer fragments. Thus the effective area, which gives rise to the emission of polymer fragments, is increased by this boundary area of the gold islands although the remaining polymer surface where the fragments are emitted decreases. Recent molecular dynamic simulations showed that the size of this boundary will be less than 3 nm [80].

Based on this assumption an equation, which models the observed SI enhancement in MetA-SIMS can be established (↪ *Equation 6.1*). This equation is composed of two terms. One describes the disappearing pristine polymer available at the sample surface by $(1 - \theta)$ where θ is the percentage of sample surface which is covered with gold. The other term handles the interface perimeter exposed to the S-SIMS analysis and which is assumed to enhance to SI intensities. Therefore the mean interface perimeter per islands P_{mi}, the number of gold islands per square micrometer N_i and the analyzed sample surface $A \cong 100 \times 100 \mu m^2$ are multiplied together.

Copy for "Bibliothèque UCL"

$$\text{Enhancement} = f_1 \cdot (1 - \theta) + f_2 \cdot (A \cdot N_i \cdot P_{mi}) \tag{6.1}$$

By dint of the solver function in Microsoft Excel the two factors f_1 and f_2 of the Equation 6.1 are adjusted in such a way that the divergence between the calculated enhancement and the SI enhancement observed in the ToF-SIMS analyses is minimized.

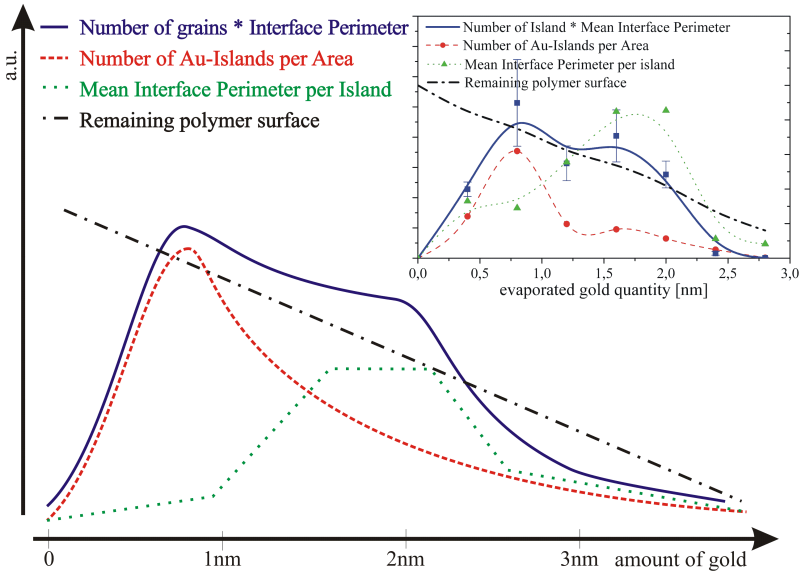


Figure 6.13: *Evolution of the morphology parameters "number of island per area", "mean interface perimeter" and "remaining polymer surface" as well as their combination. The inset shows the evolutions determined by the experimental data of the morphology parameters. In order to show all the data in a single graph, some parameters are multiplied by a constant factor. The exact values of the different parameters can be found in Section 5.2.2.*

In Figure 6.13 a sketch of the theoretical evolution of such a combination is depicted and the graph in the inset shows the evolution based on the experimentally determined morphology data. The steep decrease after the maximum at 0.8 nm of evaporated gold, which is

Copy for "Bibliothèque UCL"

observed on the plot of the number of grains per area disappears, but now a steep decrease occurs at ≈ 2 nm. This decrease is not observed in the enhancement evolution of the characteristic polymer fragments, and therefore the fit of the equation is only performed for lower evaporated gold quantities. For larger amount of gold the deviation becomes too large, which indicates that other additional parameters (not necessary morphology parameters) are becoming significant at these evaporated gold quantities. It can not be proved that the here-proposed model based on a combination of morphology parameters is complete even for low evaporated gold quantities. However the observed SI enhancement at low gold coverage are well described by the model presented above.

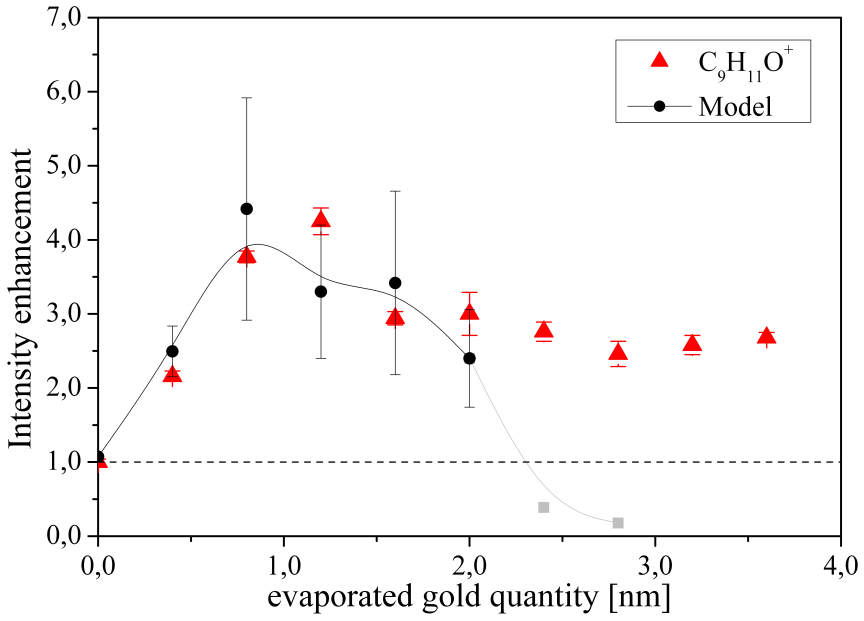


Figure 6.14: *Comparison of the calculated enhancement by the Equation 6.1 with the SI enhancement observed in S-SIMS for one characteristic PC fragment in the positive polarity.*

Figure 6.14 shows the application of the model to a characteristic fragment ($C_9H_{11}O^+$) of the PC in the positive polarity. For most of the studied fragments similar matches are obtained. In Table 6.3

Copy for "Bibliothèque UCL"

the factors f_1 and f_2 of the Equation 6.1 are denoted for the studied characteristic polymer fragments (↪ *Table 6.2*). Except for the PC$\ominus$ the values of the factor f_1 are very close to unity, whereas the value of the factor f_2, which can be interpreted as a kind of exaltation coefficient, are between $10^{-9}\mu m^{-1}$ and $10^{-6}\mu m^{-1}$. The fact that the factor f_1 is close to unity shows clearly the direct relation between the diminishing polymer surface and the SI "enhancement" (or rather a direct correlation of the net yield decrease and the diminishing polymer surface due to the ongoing gold coverage). In the case of PS$\oplus$ the fitting errors are large, which indicates that the developed model is not adequate for all samples and that on some samples other non-morphologic influences are dominant.

Nevertheless, as there exists different kinds of yield enhancement evolutions, the entire enhancement can not be completely explained by morphology effect. For instance, the enhancement evolution on the PS sample differs from the other polymers. Contrarily to the other polymers, the enhancement in the positive polarity is larger than the enhancement in the negative polarity. However, there is also a similarity: After a steep increase in the intensity in the positive polarity, a slow decrease is observed here too, but even at a large evaporated gold quantity, the fragments do not show a net decrease at all. Hence as the gold deposition has been performed in the same conditions than for the other polymers and no significant difference in the morphology between the polymers have been observed. The only difference in the PS system is the absence of oxygen inside the polymer molecule. So the presence of the gold can not be the only cause for the observed enhancements.

Compared to the pristine PS sample, the metalization procedure induces that a huge amount of oxygen is added to the surface by adsorption. This additional oxygen, which is known to enhance the cation ionization, may be the origin for the observed enhancement in the positive polarity on the PS sample. As the other polymers already possess at least one oxygen atom inside their monomer molecule, the added quantity of oxygen due adsorption after the metalization is very small and may not have an influence on their intensity enhancement.

Copy for "Bibliothèque UCL"

PC					
negative polarity					
	C_4H^-	C_5^-	$C_6H_5O^-$	$C_9H_9O^-$	$C_{14}H_{11}O_2^-$
f_1	1.29	1.27	1.45	1.47	1.51
$f_2{}^*$	2.56	7.96	6.72	6.01	5.72
positive polarity					
	$C_6H_5^+$	$C_9H_7^+$	$C_9H_{11}O^+$	$C_{13}H_9^+$	$C_{14}H_{11}O^+$
f_1	1.10	1.08	1.07	1.05	0.99
$f_2{}^*$	1.35	1.08	7.01	0.57	4.25
PET-I					
negative polarity					
	$C_6H_4^-$	$C_7H_5O^-$	$C_7H_5O_2^-$	$C_8H_5O_4^-$	$C_{10}H_7O_4^-$
f_1	1.16	0.99	1.01	1.06	0.99
$f_2{}^*$	10.41	4.84	5.60	5.04	5.55
positive polarity					
	$C_6H_4^+$	$C_7H_4O^+$	$C_8H_5O_3^+$	$C_{10}H_7O_4^+$	$C_{10}H_9O_4^+$
f_1	1.02	0.96	0.94	0.98	0.94
$f_2{}^*$	0.31	0.50	0.03	0.67	0.47
PMMA					
negative polarity					
	CH_3O^-	$C_4H_5O_2^-$	$C_5H_9O_2^-$	$C_9H_{13}O_4^-$	
f_1	0.95	0.83	0.90	0.97	
$f_2{}^*$	1.21	4.28	4.90	3.85	
positive polarity					
	$C_2H_3O_2^+$	$C_4H_5O^+$	$C_5H_9O^+$	$C_5H_9O_2^+$	$C_9H_{13}^+$
f_1	1.04	1.04	1.00	1.01	0.99
$f_2{}^*$	0.07	0.07	0.02	0.22	0.16
PS					
negative polarity					
	C_4H^-	$C_5H_2^-$	C_6H^-	$C_7H_2^-$	$C_8H_5^-$
f_1	0.94	0.97	0.95	0.95	1.00
$f_2{}^*$	1.92	1.08	1.26	0.91	3.56
positive polarity					
	fitting errors too large for f_1 and $f_2{}^*$				

Table 6.3: *Parameters f_1 and f_2 of the Equation 6.1 obtained after fitting the intensity enhancements of the different fragments and polymers. (* The unit of f_2 is $[\cdot 10^{-7}\mu m^{-1}]$)*

Copy for "Bibliothèque UCL"

To verify the assumption that beyond a change in the sputtering process due to the deposited gold, the evaporated gold and / or adsorbed oxygen also influence the ionization probability, complex calculations are needed. These theoretical investigations about the change in the molecular orbital structure and thus a change in the work function of the polymer due to the presence of gold or oxygen may be subject of an dedicated research work.

In order to reveal other yield enhancing causes, it is checked if the metalization changes the relative intensity of the fragments and thus favors the emission of special fragments. For that the ratio of the intensity of different characteristic fragments is calculated, and due to a limited number of studied polymers only limited unambiguous statements are possible.

The fragments of PC and PET-I show opposite behavior: Whereas with ongoing gold deposition the enhancement of oxygen-containing fragments is higher on the PC sample than the enhancement of the simple hydrocarbon fragments, on the PET-I sample it is the opposite behavior: the hydrocarbon fragments show a larger yield increase after gold deposition compared to the oxygen-containing fragments. Characteristic fragments containing an oxonium group $\equiv O^+$ always show a lower enhancement compared to other characteristic fragments. The ratio $C_{10}H_9O_4^+/C_{10}H_7O_4^+$ in the positive polarity shows that there is no significant difference between the emission of the protonated and the deprotonated monomer cation of the PET-I polymer. Unfortunately no detection of (de)protonated monomers was observed on the other polymers. As no information about the molecular weight of the PET-I sample is available, I suppose that therefore the molecular weight of this sample is significantly lower than those of the other polymers.

For a more detailed examination of the influence of the functional group on the fragment emission behavior, which could explain the different observed enhancement of the fragments, a study of polymers with a common backbone chain and various functional groups should be realized.

Copy for "Bibliothèque UCL"

6.4.3 Evolution of gold-adducted fragments as a function of the evaporated gold quantity

Polymer	Polarity	Label	Mass	$\mathcal{Me} + \mathfrak{Char}\ldots$
PC	negative	$[Au + C_4]^-$	244.97	–H
		$[Au + C_4H_2]^-$	246.98	+H
		$[Au + C_6H_4O]^-$	288.99	–H
		$[Au + C_9H_8O]^-$	329.02	–H
		$[Au + C_{14}H_{10}O_2]^-$	407.03	–H
	positive	$[Au + C_6H_4]^+$	273.00	–H
		$[Au + C_9H_{10}O]^+$	331.04	–H
PET-I	negative	$[Au + C_6H_4]^-$	273.00	–
		$[Au + C_7H_4O]^-$	300.99	–H
		$[Au + C_7H_4O_2]^-$	316.98	–H
		$[Au + C_8H_4O_2]^-$	328.98	–[OH + O]
	positive	$[Au + C_6H_4]^+$	273.00	–
		$[Au + C_7H_5O]^+$	302.00	+H
		$[Au + C_8H_4O_3]^+$	344.97	–H
PMMA	negative	$[Au + CH_3O]^-$	227.98	–
		$[Au + C_5H_8O_2]^-$	297.01	–H
		$[Au + C_9H_{12}O_4]^-$	381.02	–H
	positive	$[Au + C_2H_2O_2]^+$	254.96	–H
		$[Au + C_4H_4O]^+$	264.99	–H
		$[Au + C_5H_8O]^+$	281.02	–H
		$[Au + C_5H_8O_2]^+$	297.01	–H
PS	negative	$[Au + C_4]^-$	244.97	–H
		$[Au + C_4H_2]^-$	246.98	+H
		$[Au + C_6]^-$	268.97	–H
		$[Au + C_6H_6]^-$	275.01	not charac.
	positive	$[Au + C_6H_5]^+$	274.01	–
		$[Au + C_7H_6]^+$	287.01	–H
		$[Au + C_7H_8]^+$	289.03	+H
		$[Au + C_8H_8]^+$	301.03	+H

Table 6.4: *Anionized and cationized characteristic fragments of the different polymers. Their relation with the characteristic fragment of the pristine polymer (↪ Table 6.2) is denoted in the last column.*

Copy for "Bibliothèque UCL"

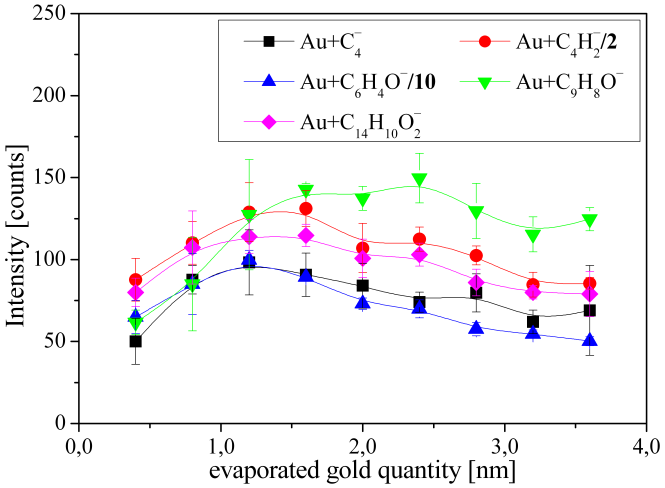
Regarding the detection of gold-adduct ions, opposite results are reported in the literature. Overall the published results show that heavy-weighted organic samples hardly emit metal-adduct ions. Therefore it is not surprising that in this work too, only a few gold-adduct ions could be observed. In Table 6.4 the most intense anionized and cationized characteristic fragments are listed as well as their relation with the characteristic fragment of the pristine polymer. In the figures 6.15 to 6.18 the intensity evolution of the detected anionized/cationized fragments for the different polymers are presented. In order to show the evolutions of the gold-adducted characteristic fragments of one polymer in a single graph, some fragment intensities are multiplied by a factor.

PC Mainly the intensity of the anionized PC fragments increases to its maximum at ≈ 1.2 nm of evaporated gold quantity before it slowly decrease to its initial intensity ($\hookrightarrow$ *Figure 6.15a*). In the positive polarity ($\hookrightarrow$ *Figure 6.15b*) only two cationized fragments based on the characteristic fragments could be observed: The simple cationized hydrocarbon fragment shows a maximum at $0.8 - 1.2$ nm, whereas the intensity of the oxygen-containing fragment steadily increases.

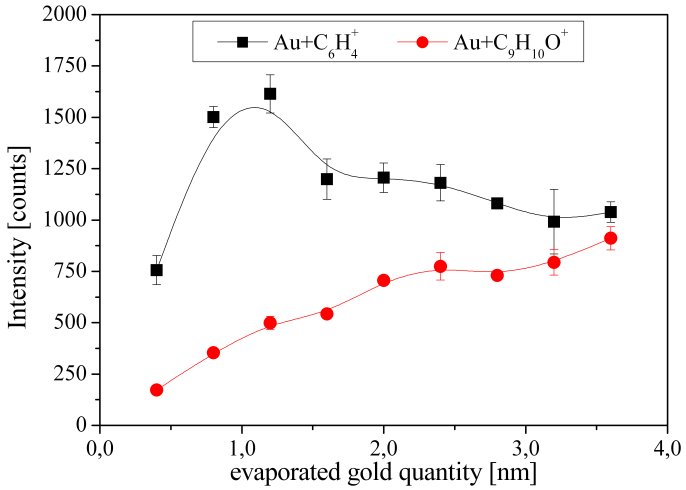
PET-I In the negative polarity ($\hookrightarrow$ *Figure 6.16a*), the most intense of the gold-adducted characteristic fragment is the simple hydrocarbon fragment. That fragments show a maximum at ≈ 1.2 nm. The intensity of the oxygen-containing fragments raises until the evaporated gold quantity of ≈ 1.2 nm and then stays relatively constant. In the positive polarity ($\hookrightarrow$ *Figure 6.16b*), all gold-adducted characteristic fragments pass through a maximum at ≈ 0.8 nm of evaporated gold quantity. At higher gold quantity the intensity seems to level. Here too, the simple gold-adducted hydrocarbon fragment is the most intense one.

PMMA The anionized-characteristic fragments pass through a maximum at 0.8 nm of evaporated gold quantity before the intensity steadily decreases ($\hookrightarrow$ *Figure 6.17a*). In the positive polarity the maximum of the intensities is rather reached at 1.2 nm ($\hookrightarrow$ *Figure 6.17b*).

Copy for "Bibliothèque UCL"



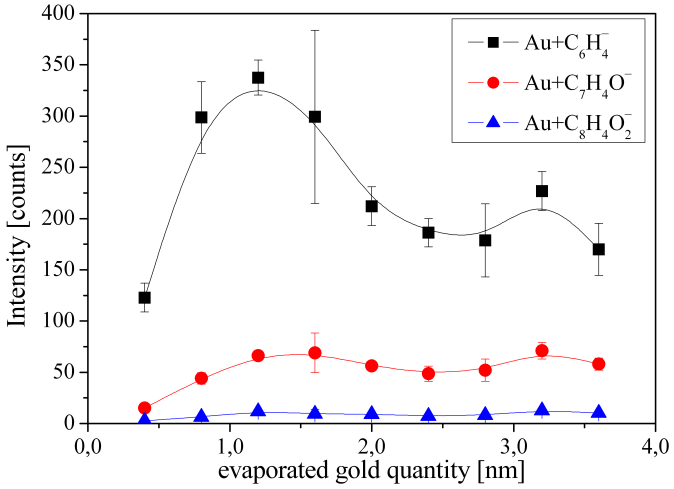
(a) *negative polarity*



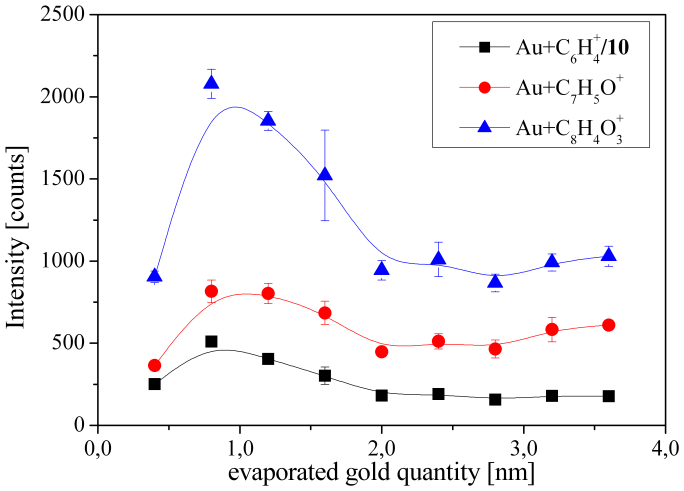
(b) *positive polarity*

Figure 6.15: *Intensity of anionized and cationized characteristic PC fragments as a function of evaporated gold quantity.*

Copy for "Bibliothèque UCL"



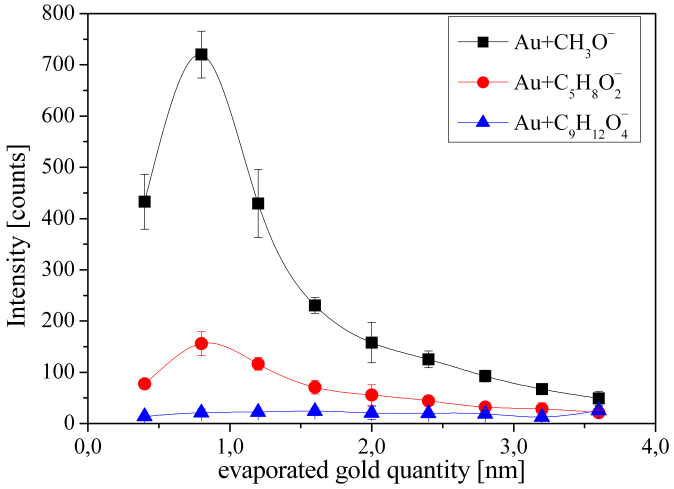
(a) *negative polarity*



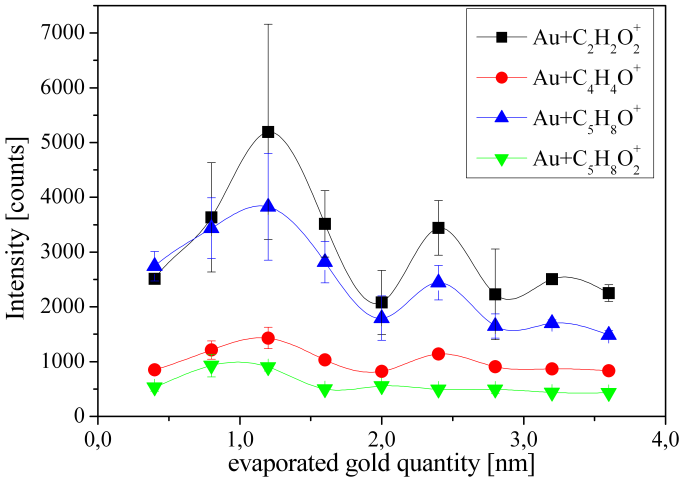
(b) *positive polarity*

Figure 6.16: *Intensity of anionized and cationized characteristic PET-I fragments as a function of evaporated gold quantity.*

Copy for "Bibliothèque UCL"



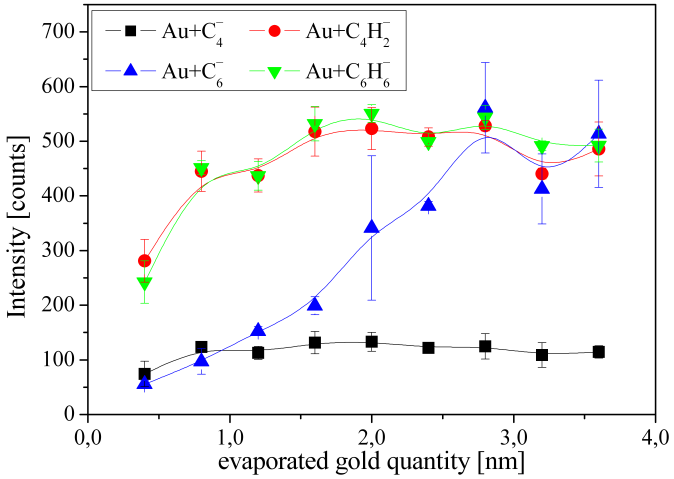
(a) *negative polarity*



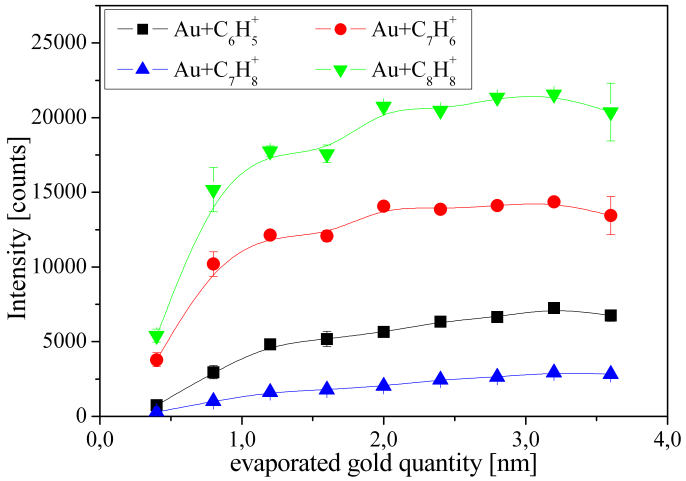
(b) *positive polarity*

Figure 6.17: *Intensity of anionized and cationized characteristic PMMA fragments as a function of evaporated gold quantity.*

Copy for "Bibliothèque UCL"



(a) *negative polarity*



(b) *positive polarity*

Figure 6.18: *Intensity of anionized and cationized characteristic PS fragments as a function of evaporated gold quantity.*

Copy for "Bibliothèque UCL"

PS In the negative polarity (↪ *Figure 6.18a*), the intensity of most gold-adducted fragments increases steadily. Some fragments seem to level above 2.0 nm other fragments only above 2.8 nm. The intensity of cationized characteristic fragments steadily increases and seams to reach a limiting value for high evaporated gold quantity (↪ *Figure 6.18b*).

Discussion about gold-adducted fragments

In order to gain some additional information about the emission process or the stability of the emitted ions, the ratio $\frac{(\mathcal{M}e+\mathfrak{Char})^{\pm}}{\mathfrak{Char}^{\pm}}$ between the anionized/cationized fragments and their corresponding characteristic polymer fragment is calculated (↪ *Table 6.5*).

Polymer	Polarity	Order of the Ratios
PC	negative	$\frac{AuC_6H_4O^-}{C_6H_5O^-} > \frac{AuC_6H_4^-}{C_6H_4^-} > \frac{AuC_4H_2^-}{C_4H^-} > \frac{AuC_{14}H_{10}O_2^-}{C_{14}H_{11}O_2^-}$
	positive	$\frac{AuC_6H_4^+}{C_6H_5^+} > \frac{AuC_9H_{10}O^+}{C_9H_{11}O^+}$
PET-I	negative	$\frac{AuC_7H_4O^-}{C_7H_5O^-} > \frac{AuC_6H_4^-}{C_6H_4^-} > \frac{AuC_7H_4O_2^-}{C_7H_5O_2^-}$
	positive	$\frac{AuC_6H_4^+}{C_6H_4^+} > \frac{AuC_8H_4O_3^+}{C_8H_5O_3^+} > \frac{AuC_7H_5O^+}{C_7H_4O^+}$
PMMA	negative	$\frac{AuC_7H_4O^-}{C_7H_5O^-} > \frac{AuC_6H_4^-}{C_6H_4^-} > \frac{AuC_7H_4O_2^-}{C_7H_5O_2^-}$
	positive	$\frac{AuC_5H_8O^+}{C_5H_9O^+} > \frac{AuC_2H_2O_2^+}{C_2H_3O_2^+} > \frac{AuC_5H_8O_2^+}{C_5H_8O_2^+} > \frac{AuC_4H_4O^+}{C_4H_5O^+}$
PS	negative	$\frac{AuC_6^-}{C_6H_5^-} > \frac{AuC_4H_2^-}{C_4H^-} > \frac{AuC_4^-}{C_4H^-}$
	positive	$\frac{AuC_8H_8^+}{C_8H_7^+} > \frac{AuC_6H_5^+}{C_6H_5^+} > \frac{AuC_7H_6^+}{C_7H_7^+} > \frac{AuC_7H_8^+}{C_7H_7^+}$

Table 6.5: *Order of the ratios for the different polymers in the both polarities.*

A general observation is that the intensity of the gold-adducted fragments is always lower than the corresponding characteristic fragment, so that these ratios are all below unity. As a consequence of these low intensities of the gold-adducted characteristic fragments, no additional information for sample characterization is provided and thus these signals are limited usable for an analytical exploitation of real-world samples. The discrepancy of this observation to those found in the literature, where the intensity of the cationized fragments is larger

Copy for "Bibliothèque UCL"

than the intensity of their corresponding fragments, can be attributed to the fact that in this work high-mass polymers are studied.

A further general remark is that in the negative polarity mostly the deprotonated gold-adducted fragment is more intense than the protonated fragment, which often could even not be observed. In the case of simple gold-adducted hydrocarbon fragments (such as $[Au + C_xH_y]^-$) the intensity of the protonated fragments is higher. This behavior can be observed on the polycarbonate (↪ *Figure 6.15*) and the polystyrene (↪ *Figure 6.18*) samples. The opposite behavior occurs in the positive polarity (↪ *Figure 6.18*). A significant influence of gold-adducted hydrocarbon fragments that are added during the metalization process can be negligated due to the low contamination level added by the evaporation (↪ *Chapter 4.2.2.C*). However this error source can not be completely ruled out.

These different behaviors of the gold-adducted fragments can be also picked out from Table 6.5, where the order of the ratios values is denoted. Furthermore, one observes in the negative polarity that the ratio value of fragments containing one oxygen atom is higher than the ratio value of simple hydrocarbon fragments, which on their side have a higher ratio value than the fragments containing two oxygen atoms. In the positive polarity, the ratio value of hydrocarbon fragments is higher than those of the fragments containing one or more oxygen atoms.

The comparison of these results with those in the literature proves to be difficult because on the one side the total number of MetA-SIMS publication is limited, and on the other side only the evolution of cationized fragments emitted from low weighted simple polymers without oxygen have been investigated. For those polymers, the intensity of the cationized fragments continuously increase with ongoing evaporated gold quantity and in some cases steeply decrease for very high deposited amount of gold [9, 70, 73]. The fact that in this work no such high gold quantity are evaporated on the sample may explain why this decrease is not observed in this work. In the negative polarity, no comparison at all with the literature can be made, because no results about the intensity of anionized fragments have been published up to now.

Copy for "Bibliothèque UCL"

6.4.4 Conclusions of the characteristic and gold-adducted fragment evolutions

The different evolution of the TSIC and the characteristic fragment intensities as a function of the evaporated gold quantity indicates that the sample metalization induces a fragment-selective change in the sputtering/ionization probability. The enhancement evolution of some polymers is successfully described by a model based on the evolution of different morphology parameters of the gold deposit.

Nevertheless as there exists different kinds of yield enhancement evolutions (different absolute enhancement of the fragments and different behavior of the enhancement in the both polarities), the entire enhancement can not only be explained by one factor or model. Overall the intensity enhancement of the characteristic fragments seams to be an combination of positive (+) and negative (−) effects between different parameters:

−: The available polymer at the sample surface decreases with increasing evaporated gold quantity. This leads to a logical decrease of the formation probability of the characteristic ions.

+: The gold deposition modifies the deposited energy distribution of the primary ion in the polymer surface, so that the sputter probability can increase.

±: Furthermore, the different enhancement behavior of the fragments in both polarities is an indication that the presence of gold (and oxygen) also change the ionization probability (in a positive or negative way).

Based on the observations made in the literature and especially made in this work, some statements about the change of the *Pulverization* and *Ionization* probabilities are made here after. The different observations made about the change in the secondary ion emission process are denoted in the following table as well as their influence on the pulverization and ionization probability. Also the chapter/page, where the indication/statement is described in a more detail can be found in the following listing.

Copy for "Bibliothèque UCL"

• The metallic substrate on which a monolayer of the analyte is deposited acts as an external source for the analyte molecule ionization (↪ *Chapter 2.1.2*). Furthermore a high atomic mass substrate has the effect that the projectile energy is reflected towards the vacuum, which leads to a higher pulverization probability and thus a higher secondary ion emission.

Pulverization & Ionization

• For thicker analyte layers onto a metallic substrate where the collision cascade still reach the underlying substrate (↪ *Chapter 6.2*), a part of the projectile energy can also be reflected towards sample surface. In this case the substrate can not act as an ionization agent anymore.

Pulverization

• The continuous decrease of the atomic species intensity with increasing gold coverage (↪ *Chapter 6.3*) is not the result of a change in the pulverization or ionization probability. Some characteristic polymer fragment ions show the same behavior (↪ *Figures 6.10b and 6.11b*). These intensity decreases are only due to the reduced polymer quantity at the sample surface.

diminishing pristine polymer coverage

• The discrepancy between the TSIC evolution and the characteristic fragments (↪ *Figures 6.9-6.12*) indicates that the sample metalization induces a fragment-selective change in the sputtering/ionization probability. Only with this observation a more detailed statement about the probability changes can not be made.

Pulverization & Ionization

• The different yield enhancement of the various characteristic fragments (↪ *Figures 6.9-6.12*) can be allocated to a change in the pulverization probability. Additional observations allow a further distinction in the change of the emission process (see below).

Pulverization & Ionization

Copy for "Bibliothèque UCL"

• The hypothetic model established in the literature (↪ *Chapter 2.1.5*) as well as the model developed here (↪ *Chapter 2.1.5*) for the yield enhancement in MetA-SIMS state that the energy deposition is different around the deposited gold islands so that the pulverization probability is changed. These models do not make any statements about changes in the ionization probability. However the presence of gold also have an influence on the ionization probability of the secondary ions (see below). *Pulverization*

• The significant different behavior in both polarities of the characteristic fragment ions as a function of the evaporated gold quantity (↪ *Figures 6.9-6.12*) can be allocated to a different ionization behavior of the characteristic fragments due to the presence of gold. *Ionization*

• On some samples (e.g. ↪ *Figure 6.9*), the oxygen-containing fragments undergo a different enhancement evolution than the hydrocarbon fragments. This difference can only be explained by different ionization probabilities between the different fragments. *Ionization*

• As the morphology results obtained by SEM and TEM are similar (↪ *Chapter 5.2.2*), one can assume that the size and shape of the gold islands are stable across the time. In combination with the observations that the secondary ion yield enhancement varies across storage time (↪ *Chapter 6.5*), one may assume either that the polymer chains migrate on the top of the gold islands or the gold islands diffuse into the polymer with time. In both cases, the sample behaves similar to a monolayer deposited on a gold layer. As only the position of the gold islands have changed slightly, it is justified to assume the ionization probability keeps unchanged. *Pulverization*

Copy for "Bibliothèque UCL"

Ionization

• The observations of the secondary yield enhancement in different storage conditions indicate that the adsorption of oxygen plays a significant role (e.g. ↪ *Figure 6.22*). As the mass of the oxygen is small, the change of the pulverization probability due to the oxygen adsorption can be neglected and one can assume that only the electronegativity of the oxygen influences the observed secondary ion yield enhancement.

The made observations in the different experiments suggest that the presence of the gold influences the secondary ion emission process in MetA-SIMS. The individual results alone do not allow to draw conclusions on the variation of the pulverization and ionization probabilities. With the numerous experiments in well defined conditions and by a combination of different observations, this work allows differentiating the various processes that induce changes in the pulverization/ionization due to the metalization. Although the ionization seams to be the dominant factor for the yield enhancement in MetA-SIMS, the exact ionization mechanism (↪ *Chapter 3.2.3*) remains unclear.

The limited number of MetA-SIMS literature makes a comparison of the results difficult. As in these publications most times only light-weighted simple hydrocarbon polymers are studied, they report a larger enhancement due to the higher diffusion of the molecules onto the gold nanoparticles.

Furthermore it should also be mentioned that, contrarily to the literature, where principally $^{69}Ga^+$ primary ions are used, here the ToF-SIMS analyses are done using a $^{40}Ar^+$ primary ion beam. Although the secondary ion yield on pristine PS is slightly larger using the $^{40}Ar^+$ primary ions than using $^{69}Ga^+$, the secondary yield enhancement as well as the absolute secondary ion yield after gold metalization is larger with $^{69}Ga^+$ primary ions [71]. For $^{132}Xe^+$ and $^{209}Bi^+$ primary ions the secondary yield of the fragments is already higher than for $^{40}Ar^+$ ions, even without metalization. However, for these primary ions the metalization procedure result in a lower enhancement than for $^{40}Ar^+$ and $^{69}Ga^+$ primary ions [71].

Copy for "Bibliothèque UCL"

6.5 Evolution in Time and Storage

Some preliminary experiments have been performed to check the evolution of the characteristic fragments in different time- and environment storage conditions. Therefore, different thick polymer samples were metalized with an amount of gold ($\approx$ 2 nm) and stored for various times either in vacuum ($< 10^{-5}\, mbar$) or atmospheric conditions. To compensate the variation of the instrumental factors across the days, the intensity of the samples, which where stored in different conditions, are corrected in the way that their TSIC are similar, so that a comparison of the intensities became possible. As the instrument was not optimized for these kind of long-term analysis, the presented analysis should only be taken as introduction for further investigations in future.

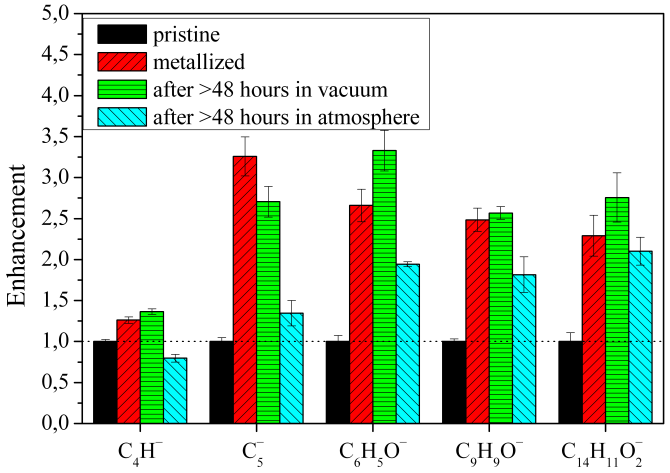
Representative for the different oxygen-containing polymers, the results of the polycarbonate samples are presented here. Figure 6.19 shows the enhancement variations of characteristic fragments of the pristine, the metalized, the *in-situ*-stored and the *ex-situ*-stored sample for both polarities.

One can observe that most characteristic peaks of the sample which were stored *in-situ* for some days exhibit similar or slightly increasing enhancement compared to the enhancement directly observed after the metalization. An outlier is the fragment $C_{14}H_{11}O^+$, which shows a significantly larger enhancement after the storage time. On the other hand the samples stored *ex-situ* for some days show a different and incoherent behavior: Some of the fragments exhibit a lower, other an higher enhancement compared to the enhancement observed for the same time *in-situ* storage.

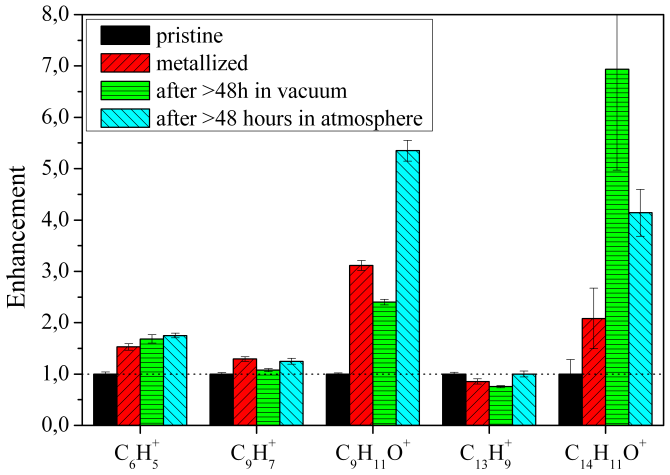
The intensity evolution of characteristic fragments with time for vacuum storage conditions is shown in Figure 6.20, which represents the variation of characteristic secondary ions intensities of a PC sample stored *in-situ* and analyzed at different times after its metalization. The different fragment enhancement in Figure 6.20 compared to the observed enhancements in Figure 6.19 is due to uncertainties of the metalization process in these experiment series.

One observes different behaviors of the fragments over storage time: The enhancements of some fragments show an increase, some of them a decrease. Most of the fragments do not undergo a significant change in

Copy for "Bibliothèque UCL"



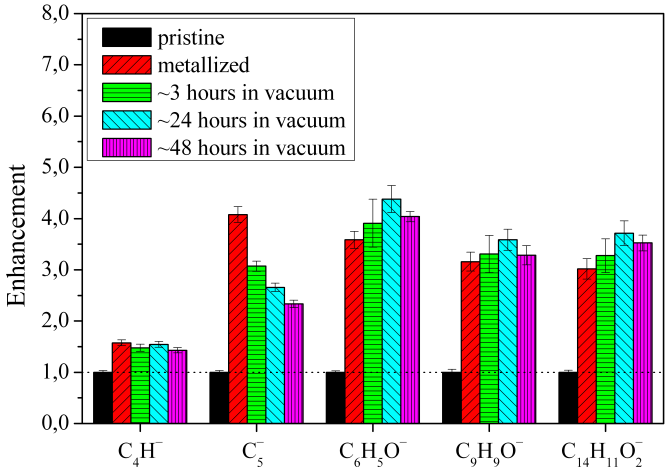
(a) *negative polarity*



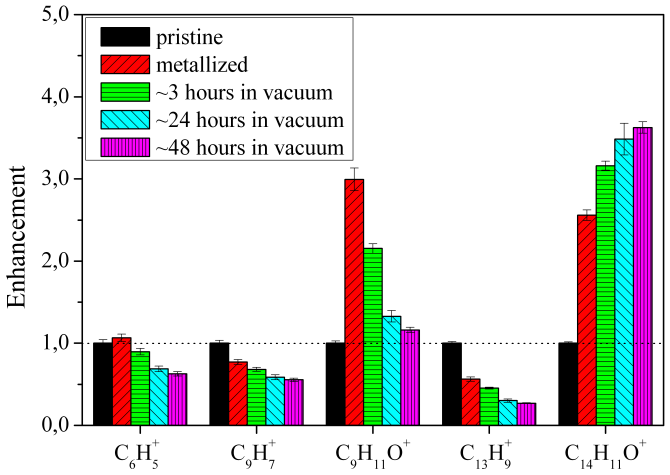
(b) *positive polarity*

Figure 6.19: *Variation of the secondary ion intensity of characteristic fragments of a thick PC sample under different storage conditions.*

Copy for "Bibliothèque UCL"



(a) *negative polarity*



(b) *positive polarity*

Figure 6.20: *Variation of the secondary ion intensity of characteristic fragments of a thick PC sample for various* in-situ *storage time.*

Copy for "Bibliothèque UCL"

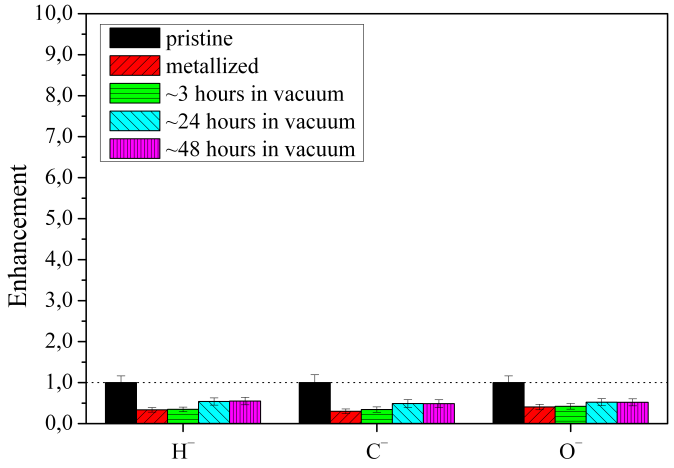
their enhancement. However other polymers (e.g. PMMA, PS) show a different behavior: For short storage time, the enhancement variation is negligible and for longer storage time the ion intensities increase.

In Chapter 6.3, it was assumed that oxygen is adsorbed onto the sample surface, which then, especially for the PS sample, influences the atomic ion intensity. In order to confirm or contradict this hypothesis, the ion intensities evolution of polystyrene sample under different storage condition is discussed here in more detail.

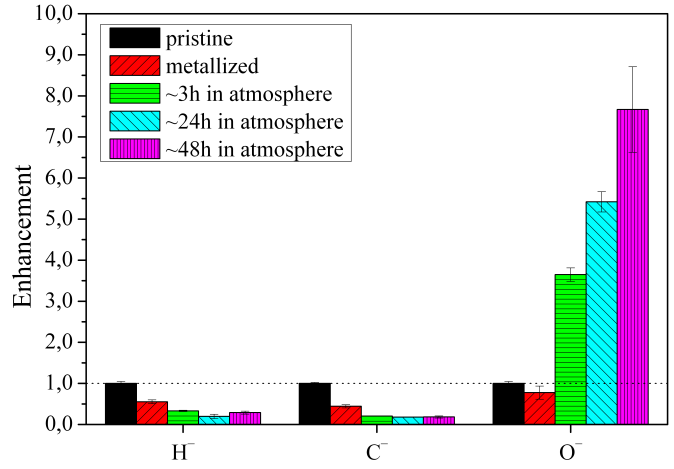
In Figure 6.21 the evolution of the atomic anions for different *in-situ* and *ex-situ* storage time is shown. Even for a short storage time one sees a remarkable increase of the oxygen intensity for the sample which was stored *ex-situ*. The change of the O^--intensity during metalization as well as for short *in-situ* storage time (≈ 3 h) is not significant. For longer *in-situ* storage time a slight increase of the oxygen is observed too but the increase is negligible compared to the increase that occurs even for a short *ex-situ* storage time. This kind of evolution of the O^- intensity is not observed on the other investigated polymers. The other atomic ions ($H^\pm$, $C^\pm$) do not show a significant difference for different storage conditions. Although a large O^- peak is observed on the pure gold spectrum (↪ *Figure 4.14*), the intensity of this peak is in the range of the intensity for the in-situ stored sample, described in this section. As the intensity of the O^- does not vary with the amount of deposited gold, this observation indicates that the observed oxygen signal is due to an adsorption of oxygen or oxygen-containing molecules after the metalization procedure. The O^- intensity increase of an ex-situ stored sample can reach up to a factor 10.

Regarding the characteristic fragments of the polystyrene sample, one observes similar differences between the storage environment in the negative polarity (↪ *Chapter 6.22*): For short *in-situ* storage-time the enhancement does not change significantly, whereas a longer storage slightly increases the intensity. On the other hand, when the sample is stored *ex-situ*, the enhancement is, compared to the *in-situ* stored sample, significantly increased for all storage times. But, in contrary to all expectations, in the positive polarity no significant difference between the storage conditions can be observed (↪ *Chapter 6.23*). A close look on the spectrum reveals that the intensity of the saturated hydrocarbonate fragments have increased disproportionally after each

Copy for "Bibliothèque UCL"



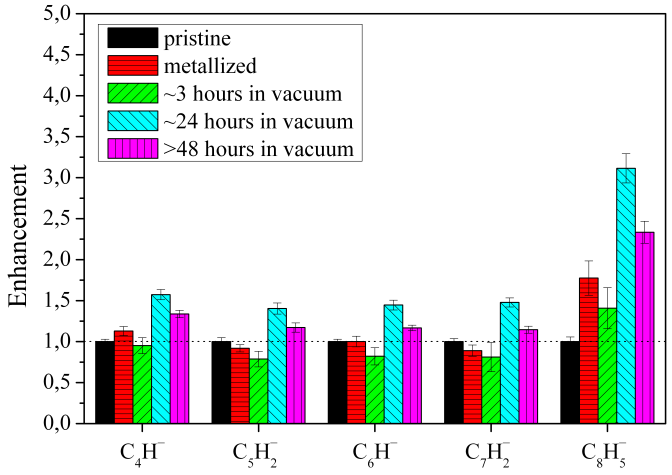
(a) *vacuum*



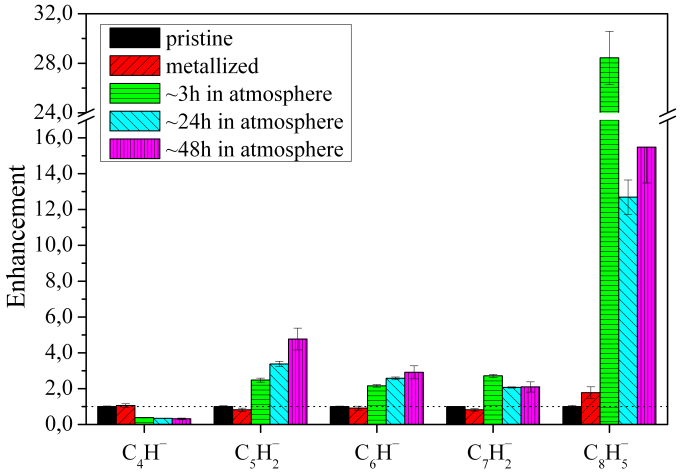
(b) *atmosphere*

Figure 6.21: *Variation of the secondary ion intensity of atomic ions from a thick PS in the negative polarity under different storage conditions and for various storage times.*

Copy for "Bibliothèque UCL"



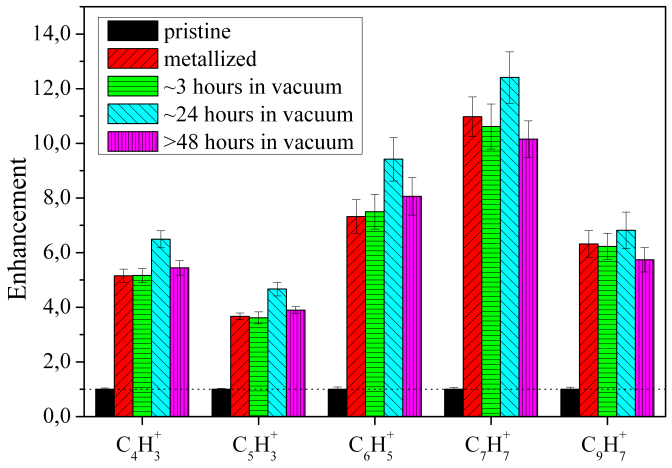
(a) *vacuum*



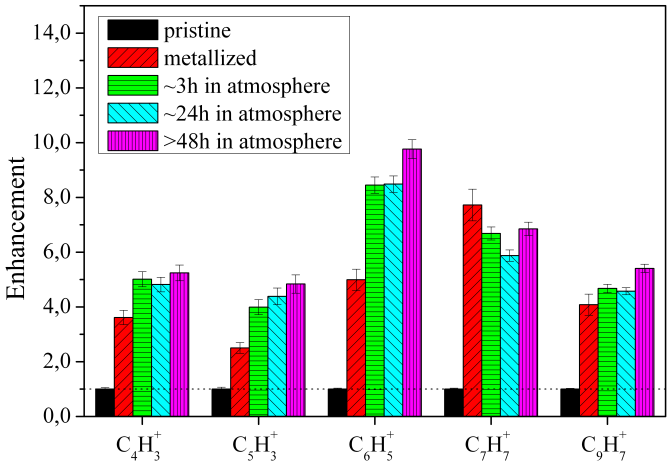
(b) *atmosphere*

Figure 6.22: *Variation of the secondary ion intensity of characteristic fragments of PS in the negative polarity under different storage conditions.*

Copy for "Bibliothèque UCL"



(a) *vacuum*



(b) *atmosphere*

Figure 6.23: *Variation of the secondary ion intensity of characteristic fragments of PS in the positive polarity under different storage conditions.*

Copy for "Bibliothèque UCL"

atmosphere storage. On the other polymer samples, which were stored ex-situ also some additional peaks are observed. This indicates that, although the samples were conscientiously stored in the sample holder box significant amount of organic contamination is adsorbed on the surface during the sample manipulation (storage, pumping, venting). However, no further investigations about the origin of this additional peaks have been performed because these studies would be far behind the scope of this work. Overall one may conclude that there is no evidence in the observations that the polymer molecules migrate onto the gold islands.

The time dependency of the ion intensity emitted from metalized sample has also been observed by Adriaensen et al., but unfortunately they do not make any statements at all in their papers about their sample storage conditions (*in-situ* or *ex-situ*) [66, 68, 72]. They presume that the change in the secondary ion yield is due to surface rearrangements, which occur with time on the metal evaporated samples. The results here confirm the common hypothesis that the structure of the sample surface is not stable. As the morphology of the overlayer is stable over time (↪ *Chapter 5.2.2*) either a diffusion of the gold clusters into the bulk polymer or a migration of polymer chains over the gold clusters must occur in order to explain the observed intensity change. A diffusion of large gold islands, such as seen by electron microscopy analysis (↪ *Chapter 5.2.2*), is however not very probable. However the evaluation of the metalized polystyrene samples stored *in-situ* and *ex-situ* confirms the hypothesis of oxygen adsorption made in Chapter 6.3. Furthermore these results on the polystyrene samples give indication that the presence of oxygen has a clear influence on the enhancement of the characteristic fragments.

In any case, the time elapsed between the metalization procedure and the analysis can considerably change the ion intensities. Unfortunately, in all papers handling the MetA-SIMS effect no statements at all about the environmental and temporal conditions between the metalization and the analysis is made, which makes it difficult to compare the results among themselves. Especially when light-weighted polymers are analyzed, where the polymer chain mobility is high, the time-effect could have an important impact on the results. Another thing is the difference in the time evolution of the ion intensities between the positive and the negative polarity, which indicates that an additional parameter

Copy for "Bibliothèque UCL"

(such as oxygen adsorption) could have an influence. In all the papers handling the time-effect, only the intensity evolution of the cations and no investigations about this effect in the negative polarity have been carried out up to now.

Although some rudimentary system was installed to heat the preparation chamber and thus, contrarily to existing work [72, 260], to heat the sample *in-situ*, the exact temperature of the samples could no be determined. As increasing temperature raises the polymer mobility and thus the surface rearrangement, this could be an issue for further researches.

Copy for "Bibliothèque UCL"

Copy for "Bibliothèque UCL"

Chapter 7

Summary and Conclusions

A less sample-restricted preparation method for S-SIMS analysis, called metal-assisted SIMS (MetA-SIMS), consists in coating the sample surface with a small amount of a noble metal prior to the SIMS analysis. Up to now only a limited number of special organic samples have been studied with this method, which allows an enhanced spectral as well as an imaging analysis of real-world samples. The investigation in this work is to find out the optimal conditions for MetA-SIMS for various common polymers used in the industries as well as to give further fundamental insights into the ion emission process due to a gold deposition onto the samples.

In order to correlate the ToF-SIMS results with the structure of the deposited gold, a detailed evaluation of the gold morphology on polymer samples has been performed. First, the exact quantity of the deposited gold is determined by XPS. Two independent evaluation methods of XPS spectra reveal no significant difference between the different polymers and give similar values for the deposited gold amount so that similar sticking coefficients, which are far below unity for all polymers are obtained for gold onto these polymers. Thereby the reconstruction of the experimental XPS spectra on the metalized samples, and confirmed by other experimental results, assumes an organic layer on the top. The determination of the exact gold quantity on the polymer surface, which was up to now not considered in former MetA-SIMS studies, is essential for the sample characterization in MetA-SIMS.

Copy for "Bibliothèque UCL"

Conscientious evaluation of the AFM measurements reveals that the morphology of the deposited gold exhibits a similar structure evolution with increasing gold-deposition. Although an obvious evolution of the surface texture has been observed, a quantitative evaluation failed due to the wavy polymer surface and the relatively large size of the AFM tip.

The "real" structure of the gold morphology has been revealed by the electron microscope images. A good linearity between the gold surface coverage and the evaporated gold amount has been observed. In the initial stage of gold deposition, new isolated islands are formed, so that the density of gold cluster first strongly increases with the deposited gold quantity and the mean area of the gold islands does not change significantly. With ongoing metalization, the grain area increases either by island growing or by coalescence of existing gold islands, so that the density of gold islands decreases and the mean area of the islands increases. The interface perimeter per grain between the gold and the polymer does not vary significantly in the initial stage of gold deposition, reaches a maximum value and subsequently decreases again. Due to the fact that the surface coverage increases slower with the evaporated gold amount than the deposited gold quantity, the Volmer-Weber growth mechanism of gold onto polymer surface is confirmed. A simple mathematical model, which is confirmed by XPS measurements of the island height, indicates that the gold islands have an half-ellipsoidal form.

Analyses of various polymer thickness deposited on different substrates reveal that the collision cascade permeates the polymer samples and reaches the underlying substrate if the polymer thickness is too low. As consequence a larger part of the collision cascade is reflected back towards the sample surface so that a larger amount of the energy induced by the ion bombardment is deposited in a surface near region, and thus more fragments are emitted from the sample. On the basis of these results, the further study is performed on thick polymer samples to ensure that the collision cascade fully develops inside the polymer layer and so the analysis of a bulk polymer sample is made.

Beyond a relatively constant total secondary ion count (TSIC) with increasing gold coverage, the yield of the atomic ions proportionally decreases. This can be explained by the fact that the atomic ions

Copy for "Bibliothèque UCL"

are created close to the impact point of the primary ion, and by the assumption that an impact on a gold cluster does not create a collision cascade that reaches the polymer surface with sufficient energy to break the polymer molecule into atomic fragments and emit their ions towards vacuum. Furthermore this decrease of the atomic ion yields indicates that the presence of gold and the reduction of the local work function can be neglected for the emission of the atomic ions. Although recent MD simulations show that the presence of gold clusters on the polymer sample causes a wider collision cascade and thus a larger energy deposition in the sample surface, neither a statement about atomic ions has been made in these simulations nor the exact distribution of the deposited energy as a function of the distance from the impact point is known.

With ongoing metalization, one observes that the maximum of the $Au_n^{\pm}$-yields coincides with the maximum of the detected number of gold islands. Furthermore, one observes a steady decrease of the absolute secondary $Au_n^{\pm}$ yields as the size of the Au_n-cluster increases, combined with an yield oscillations between adjacent Au-clusters. This odd-even alternation, which has been observed regardless of the ion formation and detection methods, essentially reflects an electron pairing effect and the exponential decay is due to the presence of a bulk metallic crystal. Concerning this decay, the small Au clusters, which were observed with electron microscopies, already behave mostly like bulk material.

As no correlation between the TSIC and the secondary ion yield of the characteristic fragments are found, the sample metalization induces a fragment-selective enhancement. A general observation is that, except for the polystyrene sample which shows the opposite behavior, the yield enhancement of the characteristic fragments is larger in the negative polarity than in the positive polarity. Furthermore the oxygen-containing fragments undergo a different enhancement than the hydrocarbon fragments.

Considering that, on the one hand a primary ion that impinges in the center of a gold island does not emit any polymer fragments, and on the other hand the decrease of the available polymer surface with ongoing metalization, one can assume that there exists a region at the periphery of each gold island at which a starting collision cascade reaches the polymer/vacuum interface. Thereby the deposited energy

Copy for "Bibliothèque UCL"

in the polymer is such that it is not enough to violently fragment the polymer into atoms but sufficient to emit characteristic polymer fragments. The model, which is proposed in this work and which is based on a combination of three morphology parameters, depicts quite well the SI yield enhancement for small evaporated gold-quantities. Above 2nm Au equivalent thickness, the hypothesis of the combined morphology parameters does not reflect the observed enhancement, so that one must assume that for larger gold quantity other additional parameters (not necessary morphology parameters) are becoming significant.

The different yield enhancement evolution on the PS sample, the observed evolution of the atomic ions as a function of gold quantity, the relative yield change between the fragments and the results obtained under different storage conditions are indications that other parameters (oxygen adsorption, polymer surface diffusion, functional group, ...) have an influence on the yield enhancement too. Also the different behaviors of gold-adducted fragments and their ratio to their corresponding fragments show that the presence of oxygen inside and outside the fragment may have an influence on the yield enhancement. Furthermore, the low yields of the gold-adducted fragments, means that these fragments provide no additional information for sample characterization and thus these signals are of very limited use for an analytical exploitation of real-world samples.

Overall the intensity enhancement of the characteristic fragments is a combination of different effects, such as reduction of the available polymer at the sample surface as well as modification of sputtering and ionization probabilities. The results in this work indicate that the ionization process is the dominant factor for the secondary ion yield enhancement in MetA-SIMS.

The number of publications about MetA-SIMS is quite small, so that a comparison with the results obtained in this work is difficult. As most of the time light-weighted simple hydrocarbon polymers are studied in those papers, only the polystyrene results here are somewhat comparable with the literature. The fact that the observed yield enhancement of the characteristic polystyrene fragments are lower here than those observed in the literature can be attributed to the lower diffusion coefficient of higher molecular weight polymers over the gold nanoparticles. Also the low yield of the gold-adducted fragments can be attributed to the high

Copy for "Bibliothèque UCL"

molecular weight of the samples analyzed in this work. Although the time dependency of the ion intensity emitted from metalized samples has been described in the literature, no statements at all about sample storage conditions can be found in these publications. In any case, the time elapsed between the metalization procedure and the analysis as well as the storage conditions can considerably change the ion intensities. As most studies use $^{69}Ga^{+}$ as primary ion, which results in a larger yield enhancement than with $^{40}Ar^{+}$ primary ions, a direct comparison of the secondary ion yields is not possible. Furthermore, studies describing oxygen-containing polymers are even sparser and investigations of the ion emission in the negative polarity are, to all practical purposes, non-existent in MetA-SIMS, so that a comparison with former results is not possible.

As a general conclusion, the results obtained up to now indicate that the MetA-SIMS method is only of limited use for analysis of real-world samples. On the one side, the metalization of the organic bulk sample makes the neutralization by low-energy electron bombardment superfluous and may increase the secondary ion yield. On the other side, extreme caution is required for the interpretation of the results, especially when samples are prepared in a different way, not metalized together or have a complete different nature. In this case a detailed study of the overlayer morphology should also be performed, in order to estimate and verify that the same amount of metal and the same overlayer structure is present on every sample. However, the MetA-SIMS procedure gives new insights on the fundamental ion emission process after primary ion impact.

After this work, there are still a lot of open questions concerning the origin of the yield enhancement in MetA-SIMS, so that at last, I denote some, in my eyes, interesting topics for future research:

- Molecular dynamic simulations that plot the deposited energy deposition as a function of the distance from the impact point of the primary ion could confirm if the decrease of the atomic ion intensity is due to limitation of the collision cascade. Furthermore the deposited energy distribution on gold covered samples may reveal the influence of the pulverization process in MetA-SIMS.

Copy for "Bibliothèque UCL"

- Experiments, where the gold surface coverage is changed independently to the size of the gold islands and thus independent to the mean interface perimeter, could confirm the hypothesis that the interface perimeter influences the yield enhancement. Such kind of experiments may allow to determine the influence of the pulverization in MetA-SIMS because the ratio of of the deposited energy in the surface layer to the energy deposited deep inside the sample can be changed independently to the deposited gold quantity.

- Theoretical calculation of the molecular orbital structure could clarify how the work function (molecular orbital configuration) of the polymer changes if gold and/or oxygen is added to the system. This knowledge would clarify the ionization mechanism in MetA-SIMS.

- A study of polymers with common backbone chain and various functional groups could reveal if the functional group has an influence on the yield enhancement. These experiments would not only have a practical aspect in analyzing and comparing similar polymers with different functional groups by MetA-SIMS, but the study would also allow to reveal the influence of the functional group on the ionization mechanism in MetA-SIMS.

- A more rigorous and complete study on the yield enhancement as a function of the sample storage conditions and times could reveal the influence of the polymer chain diffusion over the gold islands as well as the influence of the adsorbed oxygen. Sample heating could increase the polymer diffusion and bring out the influence of the glass transition temperature on the yield enhancement. These experiments, which can also reveal the influence of the pulverization process, are in interest of a practical use of MetA-SIMS, in order to find the optimal storage condition and time period for the SIMS analysis after the metalization.

- Although some publications, which handle the nature of the metal, already exist [56, 68, 73], additional and more detailed studies with different metals should be taken into consideration in order to clarify the influence of the mass on the deposited energy in the near surface region and thus on the yield enhancement. The nature

Copy for "Bibliothèque UCL"

of the deposited metal has an influence on the pulverization and ionization mechanisms.

- As the influence of adsorbed oxygen turned out to have an impact on the yield enhancement, one should investigate if a surface flooding (saturation) with oxygen gas lead to an yield enhancement. For the analysis of metals and semiconductor samples, this analysis protocol is already known to emphasize the secondary ion yield [152, see page 218ff] and recently it was shown for various organic molecules that the injection of water vapor close to the surface also leads to an enhancement of the secondary ion intensities [261]. The flooding of the sample with oxygen would bring an additional practical application for MetA-SIMS and even in general for organic sample analysis in S-SIMS. Furthermore, as the mass of oxygen does not change the pulverization behavior of the primary ion, a detailed study could reveal the influence of the oxygen added to the sample on the ionization process.

Copy for "Bibliothèque UCL"

Copy for "Bibliothèque UCL"

Bibliography

[1] A. Benninghoven, D. Jaspers and W. Sichtermann: *Secondary-ion emission of amino acids* - Appl. Phys. B: Lasers Opt. **11** (1976) 35–39. (DOI: 10.1007/BF00895013)

[2] A. Benninghoven and W. Sichtermann: *Detection, identification, and structural investigation of biologically important compounds by secondary ion mass spectrometry* - Anal. Chem. **50** (1978) 1180 – 1184. (DOI: 10.1021/ac50030a043)

[3] H. Grade, N. Winograd and R.G. Cooks: *Cationization of Organic Molecules in Secondary Ion Mass Spectrometry* - J. Am. Chem. Soc. **99** (1977) 7725–7726. (DOI: 10.1021/ja00465a062)

[4] B. Hagenhoff, D. Van Leyen, E. Niehuis and A. Benninghoven: *Time-of-flight secondary ion mass spectrometry of insulators with pulsed charge compensation by low-energy electrons* - J. Vac. Sci. Technol. A **7** (1989) 3056–3064. (DOI: 10.1116/1.576315)

[5] R. Michel-Choi, *New Substrates for Polymer Cationization with Time-of-Flight Secondary Ion Mass Spectrometry*, Eidgenössischen Technischen Hochschule Zürich, (1998).

[6] A.I. Gusev, B.K. Choi and D.M. Hercules: *Improvement of signal intensities in static secondary-ion mass spectrometry using halide additives and substrate modification* - J. Mass Spectrom. **33** (1998) 480 – 485. (DOI: 10.1002/(SICI)1096-9888(199805)33:5<480::AID-JMS644>3.0.CO;2-B)

[7] K.J. Wu and R.W. Odom: *Matrix-Enhanced Secondary Ion Mass Spectrometry: A Method for Molecular Analysis of Solid Surfaces* - Anal. Chem. **68** (1996) 873–882. (DOI: 10.1021/ac950717i)

[8] R.W. Linton, M.O. Mawn, A.M. Belu, J.M. DeSimone, M.O. Hunt Jr., Y.Z Menceloglu, H.G. Cramer and A. Benninghoven: *Time-of-flight secondary ion mass spectrometric analysis of polymer surfaces and additives* - Surf. Interface Anal. **20** (1993) 991–999. (DOI: 10.1002/sia.740201210)

[9] A. Delcorte, N. Médard and P. Bertrand: *Organic Secondary Ion Mass Spectrometry Sensitivity Enhancement by Gold Deposition* - Anal. Chem. **74** (2002) 4955–4968. (DOI: 10.1021/ac020125h)

Copy for "Bibliothèque UCL"

[10] H. Grade and R.G. Cooks: *Secondary Ion Mass Spectrometry. Cationization of Organic Molecules with Metals* - J. Am. Chem. Soc. **100** (1978) 5615–5621. (DOI: 10.1021/ja00486a006)

[11] Keyang Xu, Andrew Proctor and David M. Hercules: *Time-of-flight secondary ion mass spectrometry (TOF-SIMS) of polyisoprenes* - Mikrochim. Acta **122** (1996) 1–15. (DOI: 10.1007/BF01252400)

[12] Anthony J. Nicola, David C. Muddiman and David M. Hercules: *Enhancement of Ion Intensity in Time-of-Flight Secondary-Ionization Mass Spectrometry* - J. Am. Soc. Mass Spectrom. **7** (1996) 467–472. (DOI: 10.1016/1044-0305(96)00006-2)

[13] A. Delcorte, X. Vanden Eynde, P. Bertrand, J.C. Vickerman and B.J. Garrison: *KeV particle-induced emission and fragmentation of polystyrene molecules adsorbed on silver-insights from molecular dynamics* - J. Phys. Chem. B **104** (2000) 2673–2691. (DOI: 10.1021/jp993539w)

[14] A. Delcorte and B.J. Garrison: *High Yield Events of Molecular Emission Induced by Kiloelectronvolt Particle Bombardment* - J. Phys. Chem. B **104** (2000) 6785–6800. (DOI: 10.1021/jp001374h)

[15] B. Arezki, A. Delcorte and P. Bertrand: *Kinetic energy distributions of molecular and cluster ions sputtered from self-assembled monolayers of octanethiol on gold* - Nucl. Instr. Meth. Phys. Res. B **193** (2002) 755–761. (DOI: 10.1016/S0168-583X(02)00899-6)

[16] A. Delcorte and P. Bertrand: *Metal Salts for Molecular Ion Yield Enhancement in Organic Secondary Ion Mass Spectrometry: A Critical Assessment* - Anal. Chem. **77** (2005) 2107–2115. (DOI: 10.1021/ac040158s)

[17] A. Delcorte: *Matrix-enhanced secondary ion mass spectrometry: The Alchemist's solution?* - Appl. Surf. Sci. **252** (2006) 6582–6587. (DOI: 10.1016/j.apsusc.2006.02.076)

[18] D. van Leyen, M. Deimel, B. Hagenhoff and A. Benninghoven: *Secondary Ion Formation from Polymer Materials: A Systematic Investigation* - Proc. SIMS **7** (1989).

[19] R. Möller, A. Schnieders, G. Kortenbruck and A. Benninghoven: *Sputtering of Organic Molecules: Comparison of secondary neutral an ion emission* - Proc. SIMS **10** (1997) 943–946.

[20] J.-C. Canry and J.C. Vickerman: *Mixed Self-assembled monolayers of Dodecanethiol and octadecanethiol on silver and Gold: A ToF SIMS Intvestigation* - Proc. SIMS **10** (1997) 623–626.

[21] A. Benninghoven: *Secondary Ion Mass Spectrometry of Organic Compounds* - Proc. SIMS **3** (1982) 438–441.

Copy for "Bibliothèque UCL"

[22] A. Delcorte, I. Wojciechowski, X. Gonze, B.J. Garrison and P. Bertrand: *Single and double cationization of organic molecules in SIMS* - Int. J. Mass Spectrom. **214** (2002) 213–232. (DOI: 10.1016/S1387-3806(01)00554-1)

[23] A. Delcorte and P. Bertrand: *Sputtering of parent-like ions from large organic adsorbates on metals under keV ion bombardment* - Surf. Sci. **412-413** (1998) 97–124. (DOI: 10.1016/S0039-6028(98)00373-2)

[24] A. Delcorte, I. Wojciechowski, X. Gonze, B.J. Garrison and P. Bertrand: *The formation of singly and doubly cationized oligomers in SIMS* - Appl. Surf. Sci. **203-204** (2003) 106–109. (DOI: 10.1016/S0169-4332(02)00709-2)

[25] I. Wojciechowski, A. Delcorte, X. Gonze and P. Bertrand: *Mechanism of metal cationization in organic SIMS* - Chem. Phys. Lett. **346** (2001) 1–8. (DOI: 10.1016/S0009-2614(01)00931-9)

[26] A. Delcorte and P-Bertrand: *Kinetic energy distributions of secondary molecular ions from thin organic films under ion bombardment* - Nucl. Instr. Meth. Phys. Res. B **115** (1996) 246–250. (DOI: 10.1016/0168-583X(95)01563-9)

[27] A. Delcorte, B.G. Segda and P. Bertrand: *ToF-SIMS analyses of polystyrene and dibenzanthracene: Evidence of the fragmentation and metastable decay processes in the molecular secondary ion emission (see also erratum)* - Surf. Sci. **381** (1997) 18–32. (DOI: 10.1016/S0039-6028(97)00070-8)

[28] A. Delcorte and P. Bertrand: *Influence of chemical structure and beam degradation on the kinetic energy of molecular secondary ions in keV ion sputtering of polymers* - Nucl. Instr. Meth. Phys. Res. B **135** (1998) 430–435. (DOI: 10.1016/S0168-583X(97)00652-6)

[29] A. Delcorte, B.G. Segda and P. Bertrand: *Erratum to: "ToF-SIMS analyses of polystyrene and dibenzanthracene: Evidence of the fragmentation and metastable decay processes in the molecular secondary ion emission" [Surf. Sci. 381 (1997) 18]* - Surf. Sci. **389** (1997) 393–394. (DOI: 10.1016/S0039-6028(97)00468-8)

[30] A. Delcorte and P. Bertrand: *Energy distributions of hydrocarbon secondary ions from thin organic films under keV ion bombardment: Correlation between kinetic and formation energy of ions sputtered from triosenic acid* - Nucl. Instr. Meth. Phys. Res. B **117** (1996) 235–242. (DOI: 10.1016/0168-583X(96)00306-0)

[31] A. Delcorte, X. Vanden Eynde, P. Bertrand and D.F. Reich: *Influence of the primary ion beam parameters (nature and energy and angle) on the kinetic energy distribution of molecular fragments sputtered from PET by keV ions* - Int. J. Mass Spectrom. **189** (1999) 133–146. (DOI: 10.1016/S1387-3806(99)00063-9)

[32] H.M. Urbassek: *Sputtering of Molecules* - Nucl. Instr. Meth. Phys. Res. B **18** (1987) 587–595. (DOI: 10.1016/S0168-583X(86)80093-3)

Copy for "Bibliothèque UCL"

[33] G.J. Leggett and J.C. Vickerman: *An empirical model for ion formation from polymer surfaces during analysis by secondary ion mass spectrometry* - Int. J. Mass Spectrom. Ion Proc. **122** (1992) 281–319. (DOI: 10.1016/0168-1176(92)87021-6)

[34] A. Licciardello, S. Pignataro, A. Leute and A. Benninghoven: *Dimerization of Polystyrene during Static SIMS Measurements* - Surf. Interface Anal. **20** (1993) 549–551. (DOI: 10.1002/sia.740200611)

[35] A. Delcorte, L.T. Weng and P. Bertrand: *Secondary molecular ion emission from aliphatic polymers bombarded with low energy ions: Effects of the molecular structure and the ion beam induced surface degradation* - Nucl. Instr. Meth. Phys. Res. B **100** (1995) 213–216. (DOI: 10.1016/0168-583X(94)00842-6)

[36] K. Wien: *TOF-SIMS analysis of polymers* - Nucl. Instr. Meth. Phys. Res. B **131** (1997) 38–54. (DOI: 10.1016/S0168-583X(97)00147-X)

[37] K.D. Krantzman, Z. Postawa, B.J. Garrison, N. Winograd, S.J. Stuart and J.A. Harrison: *Understanding collision cascades in molecular solids* - Nucl. Instr. Meth. Phys. Res. B **180** (2001) 159–163. (DOI: 10.1016/S0168-583X(01)00411-6)

[38] P. Bertrand, A. Delcorte and B.J. Garrison: *Molecular SIMS for organic layers: new insights* - Appl. Surf. Sci. **203-204** (2003) 160–165. (DOI: 10.1016/S0169-4332(02)00722-5)

[39] A. Delcorte and P. Bertrand: *Metastable decay of molecular fragment ions sputtered from hydrocarbon polymers under keV ion bombardment* - Int. J. Mass Spectrom. **184** (1999) 217–231. (DOI: 10.1016/S1387-3806(99)00012-3)

[40] B.J. Garrison: *Organic Molecule Ejection from Surfaces due to Heavy Particle Bombardment* - J. Am. Chem. Soc. **104** (1982) 6211–6217. (DOI: 10.1021/ja00387a009)

[41] A. Delcorte, P. Bertrand, J. C. Vickerman and B. J. Garrison: *How do large organic molecules sputter? Insights from ToF-SIMS and molecular dynamics simulations* - Proc. SIMS **12** (2000) 27–32.

[42] R.S. Taylor and B.J. Garrison: *Molecular Dynamics Simulations of keV Particle Bombardment: Correlation of Intact Molecular Ejection with Adsorbate Size* - Chem. Phys. Lett. **230** (1994) 495–500. (DOI: 10.1016/0009-2614(94)01196-6)

[43] R.S. Taylor and B.J. Garrison: *A microscopic view of particle bombardment of organic films* - Int. J. Mass Spectrom. Ion Proc. **143** (1995) 225–233. (DOI: 10.1016/0168-1176(94)04120-V)

[44] F. Honda, G.M. Lancaster, Y. Fukuda and J.W. Rabalais: *SIMS study of the mechanism of cluster formation during ion bombardment of alkali halides* - J. Chem. Phys. **69** (1978) 4931. (DOI: 10.1063/1.436480)

Copy for "Bibliothèque UCL"

[45] S.J. Pachuta and R.G. Cooks: *Mechanisms in molecular SIMS* - Chem. Rev. **87** (1987) 647 – 669. (DOI: 10.1021/cr00079a009)

[46] H.T. Jonkman, J. Michl, R.N. King and J.D. Andrade: *Low-temperature secondary positive ion mass spectrometry of neat and argon-diluted organic solids* - Anal. Chem. **50** (1978) 2078–2082. (DOI: 10.1021/ac50036a034)

[47] R.J. Day, S.E. Unger and R.G. Cooks: *Molecular Secondary Ion Mass Spectrometry* - Anal. Chem. **52** (1980) 557A–565A. (DOI: 10.1021/ac50054a002)

[48] B.J. Garrison, A. Delcorte and K.D. Krantzman: *Molecule Liftoff from Surfaces* - Acc. Chem. Res. **33** (2000) 69–77. (DOI: 10.1021/ar970135i)

[49] R. Chatterjee, Z. Postawa, N. Winograd and B.J. Garrison: *Molecular Dynamics Simulation Study of Molecular Ejection Mechanisms: keV Particle Bombardment of C6H6/Ag{111}* - J. Phys. Chem. B **103** (1999) 151–161. (DOI: 10.1021/jp9833045)

[50] A. Delcorte: *Modeling keV particle interaction with molecular and polymeric samples* - Nucl. Instr. Meth. Phys. Res. B **236** (2005) 1–10. (DOI: 10.1016/j.nimb.2005.03.242)

[51] K. Beardmore and R. Smith: *Ion bombardment of polyethylene* - Nucl. Instr. Meth. Phys. Res. B **102** (1995) 223–227. (DOI: 10.1016/0168-583X(95)80145-C)

[52] A. Delcorte, P. Bertrand and B.J. Garrison: *A microscopic view of organic sample sputtering* - Appl. Surf. Sci. **203-204** (2003) 166–169. (DOI: 10.1016/S0169-4332(02)00724-9)

[53] N. Winograd and B.J. Garrison: *Molecular desorption and secondary ion mass spectrometry (Desorption ionization/prozesses)* - Int. J. Mass Spectrom. **212** (2001) 467–475. (DOI: 10.1016/S1387-3806(01)00510-3)

[54] A. Delcorte and B.J. Garrison: *Kiloelectronwolt Argon-Induced Molecular Desorption from a Bulk Polystyrene Solid* - J. Phys. Chem. B **108** (2004) 15652–15661. (DOI: 10.1021/jp0402131)

[55] R. Zaric, B. Pearson, K.D. Krantzman and B.J. Garrison: *Molecular dynamics simulations to explore the effect of projectile size on the ejection of organic targets from metal surfaces* - Int. J. Mass Spectrom. Ion Proc. **174** (1998) 155–166. (DOI: 10.1016/S0168-1176(97)00299-1)

[56] A. Delcorte, J. Bour, F. Aubriet, J.-F. Muller and P. Bertrand: *Sample Metallization for Performance Improvement in Desorption/Ionization of Kilodalton Molecules: Quantitative Evaluation, Imaging Secondary Ion MS, and Laser Ablation* - Anal. Chem. **75** (2003) 6875–6885. (DOI: 10.1021/ac0302105)

[57] K.S.S. Liu, C.W. Yong, B.J. Garrison and J.C. Vickerman: *Molecular Dynamics Simulations of Particle Bombardment Induced Desorption Processes: Alkanethiolates on Au(111)* - J. Phys. Chem. B **103** (1999) 3195–3205. (DOI: 10.1021/jp984071k)

Copy for "Bibliothèque UCL"

[58] I.S. Gilmore and M.P. Seah: *Investigating the difficulty of eliminating flood gun damage in ToF-SIMS* - Appl. Surf. Sci. **203-204** (2003) 600–604. (DOI: 10.1016/S0169-4332(02)00774-2)

[59] I.S. Gilmore and M.P. Seah: *Electron flood gun damage in the analysis of polymers and organics in time-of-flight SIMS* - Appl. Surf. Sci. **187** (2002) 89–100. (DOI: 10.1016/S0169-4332(01)00787-5)

[60] I.S. Gilmore and M.P. Seah: *Static SIMS: towards unfragmented mass spectra - the G-SIMS procedure* - Appl. Surf. Sci. **161** (2000) 465–480. (DOI: 10.1016/S0169-4332(00)00317-2)

[61] F.M. Green, I.S. Gilmore and M.P. Seah: *G-SIMS and SMILES: Simulated fragmentation pathways for identification of complex molecules, amino acids and peptides* - Appl. Surf. Sci. **255** (2008) 852–855. (DOI: 10.1016/j.apsusc.2008.05.087)

[62] A. Karen and A. Benninghoven: *TOF-SIMS Analysis of Metals on Polymers* - Proc. SIMS **9** (1994) 789–791.

[63] H. Yanashima, M. Sado and M. Minobe: *Surface Analysis of Molded Polymers by TOF-SIMS: Effects of Metal Evaporation on Ion Intensity* - Proc. SIMS **10** (1996) 751.

[64] I.V. Bletsos, D.M. Hercules, J.M. Magill, D. vanLeyen, E. Niehuis and A. Benninghoven: *Time-of-Flight Secondary Ion Mass Spectrometry: Detection of Fragments from Thick Polymer Film in the Range m/z <=4500* - Anal. Chem. **60** (1988) 938–944. (DOI: 10.1021/ac00160a021)

[65] A.M. Belu, M.P. Mawn and R.W. Linton: *Investigation of Ion Formation and Desorption in TOF-SIMS using Polymers* - Proc. SIMS **9** (1994) 781.

[66] L. Adriaensen, F. Vangaever and R. Gijbels: *Metal-Assisted Secondary Ion Mass Spectrometry: Influence of Ag and Au Deposition on Molecular Ion Yields* - Anal. Chem. **76** (2004) 6777–6785. (DOI: 10.1021/ac049108d)

[67] A. Delcorte and B. Bertrand: *Interest of silver and gold metallization for molecular SIMS and SIMS imaging* - Appl. Surf. Sci. **231-232** (2004) 250–255. (DOI: 10.1016/j.apsusc.2004.03.029)

[68] L. Adriaensen, F. Vangaever and R. Gijbels: *Organic SIMS: The influence of time on the ion yield enhancement by silver and gold deposition* - Appl. Surf. Sci. **231-232** (2004) 256–260. (DOI: 10.1016/j.apsusc.2004.03.031)

[69] L. Adriaensen, F. Vangaever, J. Lenaerts and R. Gijbels: *S-SIMS and MetA-SIMS study of organic additives in thin polymer coatings* - Appl. Surf. Sci. **252** (2006) 6628–6631. (DOI: 10.1016/j.apsusc.2006.02.275)

[70] A. Delcorte, S. Yunus, N. Wehbe, N. Nieuwjaer, C. Poleunis, A. Felten, L. Houssiau, J.-J. Pireaux and P. Bertrand: *Metal-Assisted Secondary Ion mass Spectrometry using Monoatomic (Ga+, In+) and Fullerene Projectiles* - Anal. Chem. **79** (2007) 3673–3689. (DOI: 10.1021/ac062406l)

Copy for "Bibliothèque UCL"

[71] A. Heile, N. Wehbe, A. Delcorte, P. Bertrand, A. Felten, L. Houssiau, J.-J. Pireux, R. de Mondt, l. Van Vaeck, D. Lipinsky and H.F. Arlinghaus: *Metal-Assisted SIMS and Cluster Ion Bombardment for Ion Yield Enhancement* - Appl. Surf. Sci. **255** (2008) 941–943. (DOI: 10.1016/j.apsusc.2008.05.007)

[72] R. De Mondt, L. Adriaensen, F. Vangaever, J. Lenaerts, L. Van Vaeck and R. Gijbels: *Empirical evaluation of metal deposition for the analysis of organic compounds with static secondary ion mass spectrometry (S-SIMS)* - Appl. Surf. Sci. **252** (2006) 6652–6655. (DOI: 10.1016/j.apsusc.2006.02.110)

[73] A. Prabhakaran, S. Yunus, N. Wehbe, P. Bertrand and A. Delcorte: *Secondary Ion Yield Enhancement in organic samples due to Au/Pt nanoparticle condensation and their substrate effects* - Surf. Interface Anal. **43** (2011) 74–77. (DOI: 10.1002/sia.3477)

[74] M. Inoue and A. Murase: *Molecular weight evaluation of poly-dimethylsiloxane on solid surfaces using silver deposition-TOF-SIMS;* - Appl. Surf. Sci. **231-232** (2004) 296–301. (DOI: 10.1016/j.apsusc.2004.03.066)

[75] A. Marcus and N. Winograd: *Metal Nanoparticle Deposition for ToF-SIMS Signal Enhancement of Polymers* - Anal. Chem. **78** (2006) 141–148. (DOI: 10.1021/ac0513921)

[76] A. Delcorte, C. Poleunis and P. Bertrand: *Stretching the limits of static SIMS with* C_{60}^{+} - Appl. Surf. Sci. **252** (2006) 6494–6497. (DOI: 10.1016/j.apsusc.2006.02.259)

[77] S.L. Luxembourg and R.M.A. Heeren: *Fragmentation at and above surfaces in SIMS: Effects of biomolecular yield enhancing surface modifications* - Int. J. Mass Spectrom. **253** (2006) 181–191. (DOI: 10.1016/j.ijms.2005.12.048)

[78] Stefan Libertus Luxembourg. *Mass Microscopy: Imaging Biomolecules on Surfaces.* PhD thesis, Universiteit Utrecht, (December 2005).

[79] O. Restrepo, A. Prabhakaran, K. Hamraoui, N. Wehbe, S. Yunus, P. Betrand and A. Delcorte: *Mechanisms of Metal-Assisted Secondary Ion Mass Spectrometry: A Mixed Theoretical and Experimental Study* - Surf. Interface Anal. **42** (2010) 1030–1034. (DOI: 10.1002/sia.3203)

[80] Oscar Restrepo and A. Delcorte: *Molecular dynamics study of metal-organic samples bombarded by kiloelectronvolt projectiles* - Surf. Interface Anal. **43** (2011) 70–73. (DOI: 10.1002/sia.3411)

[81] G. McCombie and R. Knochenmuss: *Enhanced MALDI Ionization Efficiency at the Metal-Matrix Interface: Practical and Mechanistic Consequences of Sample Thickness and Preparation Method* - J. Am. Soc. Mass Spectrom. **17** (2006) 737–745. (DOI: 10.1016/j.jasms.2006.02.005)

[82] A. Heile, C. Muhmann, D. Lipinsky and H.F. Arlinghaus: *Investigations of secondary ion yield enhancing methods in combination.* - Surf. Interface Anal. **43** (2011) 20–23. (DOI: 10.1002/sia.3556)

Copy for "Bibliothèque UCL"

[83] G. Gillen and A. Fahey: *Secondary ion mass spectrometry using cluster primary ion beams* - Appl. Surf. Sci. **203-204** (2003) 209–213. (DOI: 10.1016/S0169-4332(02)00627-X)

[84] D. Touboul, F. Halgand, A. Brunelle, R. Kersting, E. Tallarek, B. Hagenhoff and O. Laprévote: *Tissue Molecular Ion Imaging by Gold Cluster Ion Bombardment* - Anal. Chem. **76** (2004) 1550–1559. (DOI: 10.1021/ac035243z)

[85] N. Winograd: *The Magic of Cluster SIMS* - Anal. Chem. **77** (2005) 142A–149A. (DOI: 10.1021/ac053355f)

[86] D.E. Weibel, N. Lockyer and J.C. Vickerman: *C60 cluster ion bombardment of organic surfaces* - Appl. Surf. Sci. **231-232** (2004) 146–152. (DOI: 10.1016/j.apsusc.2004.03.098)

[87] N. Winograd, Z. Postawa, J. Cheng, C. Szakal, J. Kozole and B.J. Garrison: *Improvements in SIMS continue. Is the end in sight?* - Appl. Surf. Sci. **252** (2006) 6836–6843. (DOI: 10.1016/j.apsusc.2006.02.142)

[88] E.A. Jones, J.S. Fletcher, C.E. Thompson, D.A. Jackson, N.P. Lockyer and J.C. Vickerman: *ToF-SIMS analysis of bio-systems: Are polyatomic primary ions the solution?* - Appl. Surf. Sci. **252** (2006) 6844–6854. (DOI: 10.1016/j.apsusc.2006.02.145)

[89] Z. Postawa: *Sputtering simulations of organic overlayers on metal substrates by monoatomic and clusters projectiles* - Appl. Surf. Sci. **231-232** (2004) 22–28. (DOI: 10.1016/j.apsusc.2004.03.019)

[90] *Interaction of keV monoatomic and fullerene ions with organic materials: Recent experiments and simulations*, ISBN 141, (2006).

[91] J.A. Townes, A.K. White, E.N. Wiggins, K.D. Krantzman, B.J. Garrison and N. Winograd: *Mechnism for Increased Yield with SF_5^+ Projectiles in Organic SIMS: The Substrate Effect* - J. Phys. Chem. A **103** (1999) 4587–4589. (DOI: 10.1021/jp9907138)

[92] R.D. Harris, M.J. Van Stipdonk and E.A. Schweikert: *Kiloelectron volt cluster impacts: prospects for cluster-SIMS* - Int. J. Mass Spectrom. Ion Proc. **174** (1998) 167–177. (DOI: 10.1016/S0168-1176(97)00300-5)

[93] B. Czerwinski, A. Delcorte, B.J. Garrison, B. Samson, N. Winograd and Z. Postawa: *Sputtering of thin benzene and polystyrene overlayers by keV Ga and C60 bombardment* - Appl. Surf. Sci. **252** (2006) 6419–6422. (DOI: 10.1016/j.apsusc.2006.02.202)

[94] A. Heile, N. Wehbe, A. Delcorte, P. Bertrand, A. Felten, L. Houssiau, J.-J. Pireaux, R. De Mondt, L. Van Vaeck, D. Lipinsky and H. F. Arlinghaus: *Investigation of methods to enhance the secondary ion yields in TOF-SIMS of organic samples* - Surf. Interface Anal. **40** (2008) 538–542. (DOI: 10.1002/sia.2810)

Copy for "Bibliothèque UCL"

[95] K.L. Mittal, editor: *Metallized Plastics: Fundamentals and Applications*. M. Dekker, (1998).

[96] J.J. Pireaux: *Is there an interaction at the aromatic site(s) in a metal/polymer interface? An XPS and HREELS review* - Synth. Met. **67** (1994) 39–46. (DOI: 10.1016/0379-6779(94)90009-4)

[97] F. Faupel, R. Willecke and A. Thran: *Diffusion of metals in polymers* - Mater. Sci. Eng. **R22** (1998) 1–55. (DOI: 10.1016/S0927-796X(97)00020-X)

[98] V. Zaporojtchenko, T. Strunskus, K. Behnke, C. v. Bechtolsheim, M. Kiene and F. Faupel: *Metal/polymer interfaces with designed morphologies* - J. Adhes. Sci. Technol. **14** (2000) 467–490. (DOI: 10.1163/156856100742609)

[99] Z. Zhang and M.G. Lagally: *Atomistic Processes in the Early Stages of Thin-Film Growth* - Science **276** (1997) 377–383. (DOI: 10.1126/science.276.5311.377)

[100] M.C. Barnes, D.-Y. Kim, H.S. Ahn, C.O. Lee and N.M. Hwang: *Deposition mechanism of gold by thermal evaporation: approach by charged cluster model* - J. Cryst. Growth **213** (2000) 83–92. (DOI: 10.1016/S0022-0248(00)00359-6)

[101] A. Thran, M. Kiene, V. Zaporojtchenko and F. Faupel: *Condensation Coefficients of Ag on Polymers* - Phys. Rev. Lett. **82** (Mar 1999) 1903–1906. (DOI: 10.1103/PhysRevLett.82.1903)

[102] V. Zaporojtchenko, K. Behnke, A. Thran, T. Strunskus and F. Faupel: *Condensation coefficients and initial stages of growth for noble metals deposited onto chemically different polymer surfaces* - Appl. Surf. Sci. **144-145** (1999) 355–359. (DOI: 10.1016/S0169-4332(98)00826-5)

[103] V. Zaporojtchenko, K. Behnke, T. Strunskus and F. Faupel: *Determination of condensation coefficients of metals on polymer surfaces* - Surf. Sci. **454-456** (2000) 412–416. (DOI: 10.1016/S0039-6028(00)00234-X)

[104] R.L.W. Smithson, D.J. McClure and D.F. Evans: *Effects of polymer substrate surface energy on nucleation and growth of evaporated gold films* - Thin Solid Films **307** (1997) 110–112. (DOI: 10.1016/S0040-6090(97)00310-6)

[105] V. Zaporojtchenko, T. Strunskus, K. Behnke, C. v. Bechtolsheim, A. Thran and F. Faupel: *Formation of metal-polymer interfaces by metal evaporation: influence of deposition parameters and defects* - Microelectron. Eng. **50** (2000) 465–471. (DOI: 10.1016/S0167-9317(99)00316-0)

[106] N. Jones, M. Stoilovic, C. Lennard and C. Roux: *Vacuum metal deposition: factors affecting normal and reverse development of latent fingerprints on polyethylene substrates* - Forens. Sci. Int. **115** (2001) 73–88. (DOI: 10.1016/S0379-0738(00)00310-8)

Copy for "Bibliothèque UCL"

[107] J.A Venables: *Atomic processes in crystal growth* - Surf. Sci. **299-300** (1994) 798–817. (DOI: 10.1016/0039-6028(94)90698-X)

[108] V. Zaporojtchenko, J. Zekonyte, A. Biswas and F. Faupel: *Controlled growth of nano-size metal clusters on polymers by using VPD method* - Surf. Sci. **532-535** (2003) 300–305. (DOI: 10.1016/S0039-6028(03)00128-6)

[109] V. Zaporojtchenko, J. Zekonyte, S. Wille, U. Schuermann and F. Faupel: *Tailoring of the PS surface with low energy ions: Relevance to growth and adhesion of noble metals* - Nucl. Instr. Meth. Phys. Res. B **236** (July 2005) 95–102. (DOI: 10.1016/j.nimb.2005.03.261)

[110] F. Parmigiani, G. Samoggia and G.P. Ferraris: *Optical properties of sputtered gold clusters* - J. Appl. Phys. **57** (1985) 2524–2528.

[111] P.A. Gollier and P. Bertrand: *Diffusion of Copper in Polymer during the Metallization of PET* - J. Adhesion **58** (1996) 173–183. (DOI: 10.1080/00218469608015198)

[112] A. Patnaik and C. Li: *Interface configuration in gold/polycarbonate bilayer structure: an in situ study through Ar+ ion depth profiling* - Appl. Surf. Sci. **140** (1999) 197–203. (DOI: 10.1016/S0169-4332(98)00591-1)

[113] S. Nowak, R. Mauron, G. Dietler and L. Schlapbach: *XPS-Study of Metal-Polymer Interfaces after Polymer Surface Treatment by Ion and Plasma Techniques* - Metallized Plastics **2** (1991) 233–244.

[114] B. Lewis: *Nucleation theory: present status and outstanding problems* - Thin Solid Films **50** (1978) 233–240. (DOI: 10.1016/0040-6090(78)90109-8)

[115] M.S. Kunz, K.R. Shull and A.J. Kellock: *Morphologies of discontinuous gold films on amorphous polymer substrates* - J. Appl. Phys. **72** (1992) 4458–4460. (DOI: 10.1063/1.352362)

[116] G.M. Pound, M.T. Simnad and L. Yang: *Heterogeneous Nucleation of Crystals from Vapor* - J. Chem. Phys. **22** (1954) 1215–1219. (DOI: 10.1063/1.1740336)

[117] T.L. Morkved, P. Wiltzius, H-M. Jaeger, D.G. Grier and T.A. Witten: *Mesoscopic self-assembly of gold islands on diblock-copolymer films* - Appl. Phys. Lett. **64** (1994) 422–424. (DOI: 10.1063/1.111118)

[118] Y. Travaly and P. Bertrand: *Static SIMS Investigation of Metal/Polymer Interfaces* - Surf. Interface Anal. **23** (1995) 328–334. (DOI: 10.1002/sia.740230509)

[119] X. Dai, M. Stoilovic, C. Lennard and N. Speers: *Vacuum metal deposition: Visualisation of gold agglomerates using TEM imaging* - Forens. Sci. Int. **168** (2007) 219–222. (DOI: 10.1016/j.forsciint.2006.01.012)

Copy for "Bibliothèque UCL"

[120] R.P. Netterfield, P.J. Martin, R.M. Sainty, R.M. Duffy and C.G. Pacey: *Characterization of growing thin films by in situ ellipsometry, spectral reflectance and transmittance measurements, and ion-scattering spectrometry* - Rev. Sci. Instrum. **56** (1985) 1995–2003. (DOI: 10.1063/1.1138408)

[121] V. Svorcik, J. Zehentner, V. Rybka, P. Slepicka and V. Hnatowicz: *Characterization of thin gold layers on polyethyleneterephthalate: transition from discontinuous to continuous, homogenous layer.* - Appl. Phys. A **75** (2002) 541–544. (DOI: 10.1007/s003390101024)

[122] V. Svorcik, V. Rybka, M. Maryska, M. Spirkova, J. Zahentner and V. Hnatowicz: *Microscopic study of ultra-thin gold layers on polyethyleneterephthalate* - Eur. Polym. J. **40** (2004) 211–217. (DOI: 10.1016/j.eurpolymj.2003.08.007)

[123] C. Charton and M. Fahland: *Growth of Ag films on PET deposited by magnetron sputtering* - Vacuum **68** (2003) 65–73. (DOI: 10.1016/S0042-207X(02)00289-0)

[124] D. H. Cole, K. R. Shull, L.E. Rehn and P. Baldo: *Metal-Polymer Interactions in a Polymer/Metal Nanocomposite* - Phys. Rev. Lett. **78** (1997) 5006–5009. (DOI: 10.1103/PhysRevLett.78.5006)

[125] K. Akamatsu and S. Deki: *Characterization and optical properties of gold nanoparticles dispersed in nylon 11 thin films* - J. Mater. Chem. **7** (1997) 1773 – 1777. (DOI: 10.1039/a703055j)

[126] J. Erichsen, J. Kanzow, U. Schürmann, K. Dolgner, K. Günther-Schade, Thomas Strunskus, V. Zaporojtchenko and F. Faupel: *Investigation of the Surface Glass Transition Temperature by Embedding of Noble Metal Nanoclusters into Monodisperse Polystyrenes* - Macromolecules **37** (2004) 1831–1838. (DOI: 10.1021/ma0353080)

[127] S. Norrman, T. Andersson, C.G. Granqvist and O. Hunderi: *Optical properties of discontinuous gold films* - Phys. Rev. B **18** (1978) 674–695. (DOI: 10.1103/PhysRevB.18.674)

[128] J.C. Moreira and N.R. Demarquette: *Influence of temperature, molecular weight, and molecular weight dispersity on the surface tension of PS, PP, and PE. I. Experimental* - J. Appl. Polym. Sci. **82** (2001) 1907–1920. (DOI: 10.1002/app.2036)

[129] C.J. Robinson: *The effects of a glow discharge on the nucleation characteristics of gold on polymer substrates* - Thin Solid Films **57** (1979) 285–289. (DOI: 10.1016/0040-6090(79)90164-0)

[130] N. Marin and Y. Serruys: *Diffusion of metals deposited on a polyimide film (Kapton) under and out of irradiation* - Nucl. Instr. Meth. Phys. Res. B **105** (1995) 175–180. (DOI: 10.1016/0168-583X(95)00551-X)

Copy for "Bibliothèque UCL"

[131] A.M. Bittner: *Clusters on soft matter surfaces* - Surf. Sci. Rep. **61** (2006) 383–428. (DOI: 10.1016/j.surfrep.2006.03.003)

[132] V. Papaefthimiou, A. Siokou and S. Kennou: *A study of the interface formation between gold and a thin conjugated oligomer film* - Surf. Sci. **532-535** (2003) 255–260. (DOI: 10.1016/S0039-6028(03)00155-9)

[133] Y.C. Jean, R. Zhang, H. Cao, J.-P. Yuan, C.-M. Huang, B. Nielsen and P. Asoka-Kumar: *Glass transition of polystyrene near the surface studied by slow-positron-annihilation spectroscopy* - Phys. Rev. B **56** (1997) R8459–R8462. (DOI: 10.1103/PhysRevB.56.R8459)

[134] K.F. Mansfield and D.N. Theodorou: *Molecular dynamics simulation of a glassy polymer surface* - Macromolecules **24** (1991) 6283–6294. (DOI: 10.1021/ma00023a034)

[135] A.M. Mayes: *Glass Transition of Amorphous Polymer Surfaces* - Macromolecules **27** (1994) 3114–3115. (DOI: 10.1021/ma00089a033)

[136] J. Bachnagel and K. Binder: *On the influence of hard walls on structural properties in polymer glass simulation* - Macromolecules **28** (1995) 6808–6818. (DOI: 10.1021/ma00124a016)

[137] D.S. Fryer, R.D. Peters, E.Jun Kim, J.E. Tomaszewski, J.J. de Pablo, P.F. Nealey, C.C. White and Wen li Wu: *Dependence of the Glass Transition Temperature of Polymer Films on Interfacial Energy and Thickness* - Macromolecules **34** (2001) 5627–5634. (DOI: 10.1021/ma001932q)

[138] RAL Jones: *The dynamics of thin polymer films* - Curr. Opin. Colloid Interface Sci. **4** (1999) 153–158. (DOI: 10.1016/S1359-0294(99)00025-4)

[139] L. Xie, G.B. DeMaggio, W.E. Frieze, J. DeVries, D.W. Gidley, H.A. Hristov and A.F. Yee: *Positronium Formation as a Probe of Polymer Surfaces and Thin Films* - Phys. Rev. Lett. **74** (1995) 4947–4950. (DOI: 10.1103/PhysRevLett.74.4947)

[140] J.L. Keddie, R.A.L. Jones and R.A. Cory: *Interface and surface effects on the glass-transition temperature in thin polymer films* - Faraday Discuss. **98** (1994) 219 – 230. (DOI: 10.1039/FD9949800219)

[141] J.L. Keddie, R.A.L. Jones and R.A. Cory: *Size-Dependent Depression of the Glass Transition Temperature in Polymer Films* - Europhys. Lett. **27** (1994) 59–64. (DOI: 10.1209/0295-5075/27/1/011)

[142] J.A. Forrest: *A decade of dynamics in thin films of polystyrene: Where are we now?* - Eur. Phys. J. E **8** (2002) 261–266. (DOI: 10.1140/epje/i2002-10005-5)

[143] S. Hajati, V. Zaporojtchenko, F. Faupel and S. Tougaard: *Characterization of Au nano-cluster formation on and diffusion in polystyrene using XPS peak shape analysis* - Surf. Sci. **601** (2007) 3261–3267. (DOI: 10.1016/j.susc.2007.06.001)

Copy for "Bibliothèque UCL"

[144] G.J. Kovacs and P.S. Vincett: *Formation and thermodynamic stability of a novel class of useful materials: Close-packed monolayers of submicron monodisperse spheres just below a polymer surface* - J. Colloid Interface Sci. **90** (1982) 335–351. (DOI: 10.1016/0021-9797(82)90302-2)

[145] G.J. Kovacs, P.S. Vincett, C. Tremblay and A.L. Pundsack: *Vacuum deposition onto softenable substrates: Formation of novel subsurface structures* - Thin Solid Films **101** (1983) 21–40. (DOI: 10.1016/0040-6090(83)90490-X)

[146] A. Mackova, V. Periina, V. Svorcik and J. Zemek: *RBS, ERDA and XPS study of Ag and Cu diffusion in PET and PI polymer foils* - Nucl. Instr. Meth. Phys. Res. B **240** (2005) 303–307. (DOI: 10.1016/j.nimb.2005.06.157)

[147] P.-A. Gollier and P. Bertrand: *Cyclic oligomer segregation at the metallized PET surface* - J. Adhes. Sci. Technol. **16** (2002) 1–13. (DOI: 10.1163/15685610252771121)

[148] P.-A. Gollier and P. Bertrand. *Annealing Behaviour of metallized PET: Influence of Deposition Parameters.* In Proc, editor, *Proc*, (1997).

[149] J.J. Thomson: Philos. Mag.**21** (1911) 225.

[150] A. Benninghoven: *Analysis of Submonolayers on Silver by Negative Secondary Ion Emission* - Phys. Status Solidi (b) **34** (1969) K169–K171. (DOI: 10.1002/pssb.19690340267)

[151] A. Benninghoven: *Observing surface oxidation of molybdenum with the statical method of secondary ion mass spectroscopy* - Chem. Phys. Lett. **6** (1970) 626–628. (DOI: doi:10.1016/0009-2614(70)85243-5)

[152] A. Benninghoven, G.G. Rüdenauer and H.W. Werner, *Secondary Ion Mass Spectrometry: Basic Concepts, Instrumental Aspects, Applications and Trends*, ISBN 86. J. Wiley & Sons, p.j. elving and j.d. winefordner and i.m. kolthoff edition, (1987).

[153] S.J. Stranick, S.V. Atre, A.N. Parikh, M.C. Wood, D.L. Allara, N. Winograd and P.S. Weiss: *Nanometer Scale Phase Separation in Mixed Composition Self-Assembled Monolayers* - Nanotechnology **7** (1996) 438–442. (DOI: 10.1088/0957-4484/7/4/025)

[154] M.L. Pacholski and N. Winograd: *Imaging with Mass Spectrometry* - Chem. Rev. **99** (1999) 2977–3005. (DOI: 10.1021/cr980137w)

[155] B. Hagenhoff: *High Resolution Surface Analysis by ToF-SIMS* - Mikrochim. Acta **132** (2000) 259–271. (DOI: 10.1007/s006040050019)

[156] A. Adriaens, L. Van Vaeck and F. Adams: *Static Secondary Ion Mass Spectrometry (S-SIMS) Part 2: Material Science Applications* - Mass. Spec. Rev. **18** (1999) 48–81. (DOI: 10.1002/(SICI)1098-2787(1999)18:1<48::AID-MAS2>3.0.CO;2-I)

Copy for "Bibliothèque UCL"

[157] C.W. Magee, F.A. Stevie and R.G. Wilson, *Secondary Ion Mass Spectrometry - A Practical Handbook For Depth Profiling And Bulk Impurity Analysis*. John Wiley & Sons, Inc., (1989).

[158] M. Betti: *Isotope ratio measurements by secondary ion mass spectrometry (SIMS) and glow discharge mass spectrometry (GDMS)* - Int. J. Mass Spectrom. **242** (2005) 169–182. (DOI: 10.1016/j.ijms.2004.11.022)

[159] S.L. Chryssoulis and S.S. Dimov: *Optimized conditions for selective gold flotation by ToF-SIMS and ToF-LIMS* - Appl. Surf. Sci. **231-232** (2004) 265–268. (DOI: 10.1016/j.apsusc.2004.03.058)

[160] S. Aoyagi, S. Hiromoto, T. Hannawa and M. Kudo: *ToF-SIMS investigation of metallic material surface after culturing cells* - Appl. Surf. Sci. **231-232** (2004) 470–474. (DOI: 10.1016/j.apsusc.2004.03.181)

[161] J.-L. Guerquin-Kern, T.-D. Wu, C. Quintana and A. Croisy: *Progress in analytical imaging of the cell by dynamic secondary ion mass spectrometry (SIMS microscopy)* - Biochim. Biophys. Acta **1724** (2005) 228–238. (DOI: 10.1016/j.bbagen.2005.05.013)

[162] S. Parry and N. Winograd: *Hight-Resolution ToF-SIMS Imaging of Eukaryotic Cells Preserved in a Trehalose Matrix* - Anal. Chem. **77** (2005) 7950–7957. (DOI: 10.1021/ac051263k)

[163] C.Galli Marxer, M.L. Kraft, P.K. Weber, I.D. Hutcheon and S.G. Boxer: *Supported Membrane Composition Analysis by Secondary Ion Mass Spectrometry with High Lateral Resolution* - Biophys. J. **88** (2005) 2965–2975. (DOI: 10.1529/biophysj.104.057257)

[164] C. Brüning, S. Hellweg, S. Dambach, D. Lipinsky and H.F. Arlinghaus: *Improving the interpretation of ToF-SIMS measurements on absorbed proteins using PCA* - Surf. Interface Anal. **38** (2006) 191–193. (DOI: 10.1002/sia.2233)

[165] R.M.A. Heeren, L.A. McDonnell, E. Amstalden, S.L. Luxembourg, A.F.M. Altelaar and S.R. Piersma: *Why don't biologists use SIMS? A critical evolution of imaging MS* - Appl. Surf. Sci. **252** (2006) 6827–6835. (DOI: 10.1016/j.apsusc.2006.02.134)

[166] L.A. McDonnell, R.M.A. Heeren, R.P.J. de Lange and I.W. Fletcher: *Higher Sensitivity Secondary Ion Mass Spectrometry of Biological Molecules for High Resolution, Chemically Specific Imaging* - J. Am. Soc. Mass Spectrom. **17** (2006) 1195–1202. (DOI: 10.1016/j.jasms.2006.05.003)

[167] X. Dong, A. Gusev and D.M. Hercules: *Characterization of Polysiloxanes with Different Functional Groups by Time-of-Flight Secondary Ion Mass Spectrometry* - J. Am. Soc. Mass Spectrom. **9** (1998) 292–298. (DOI: 10.1016/S1044-0305(98)00003-8)

Copy for "Bibliothèque UCL"

[168] K. Reihs, M. Voetz, M. Kruft, D. Wolany and A. Benninghoven: *Molecular weight determination of bulk polymer surfaces by static secondary ion mass spectrometry* - Fresen. J. Anal. Chem. **358** (1997) 93–95. (DOI: 10.1007/s002160050353)

[169] F.-R. Lang, Y. Pitton, H. J. Mathieu, D. Landolt and E. M. Moser: *Surface analysis of polyethyleneterephthalate by ESCA and TOF-SIMS* - Fresen. J. Anal. Chem. **358** (1997) 251–254. (DOI: 10.1007/s002160050398)

[170] W.E. Wallace and C.M. Guttman: *Data Analysis Methods for Synthetic Polymer Mass Spectrometry: Autocorrelation* - J. Res. Natl. Inst. Stand. Technol. **107** (2002) 1–17.

[171] R.J. Composto, R.M. Walters and J. Genzer: *Application of ion scattering techniques to characterize polymer surfaces and interfaces* - Mater. Sci. Eng. **R38** (2002) 107–180. (DOI: 10.1016/S0927-796X(02)00009-8)

[172] M. Inoue, A. Murase and M. Sugiura: *Molecular Weight Evaluation of Poly(dimethylsiloxane) on Solid Surfaces Using Silver Deposition/TOF-SIMS* - Anal. Sci. **20** (2004) 1623. (DOI: 10.2116/analsci.20.1623)

[173] L. Kailas and P. Bertrand: *End group effect on surface and interfacial segregation in PS-PMMA blend thin films* - Appl. Surf. Sci. **252** (2006) 6648–6651. (DOI: 10.1016/j.apsusc.2006.02.270)

[174] A. Delcorte, P. Bertrand, E. Wischerhoff and A. Laschewsky: *Adsorption of Polyelectrolyte Multilayers on Polymer Surfaces* - Langmuir **13** (1997) 5125–5136. (DOI: 10.1021/la970105o)

[175] A. Delcorte, S. Befahy, C. Poleunis, M. Troosters and P. Bertrand. *ToF-SIMS study of adherence improvement for metallized silicone films.* In *3rd internation Symposium on Adhesion Aspects of Thin Films (including Adhesion measurement and Metallized Plastics)*, (2003).

[176] Th. Gross, I. Retzko, J. Friedrich and W. Unger: *Time-of-flight-SIMS and XPS characterization of metal doped polymers* - Appl. Surf. Sci. **203-204** (2003) 575–579. (DOI: 10.1016/S0169-4332(02)00769-9)

[177] Y. Lee, S. Han and M.-H. Kwon: *ToF-SIMS study of modified polymer surfaces* - Appl. Surf. Sci. **231-232** (2004) 278–282. (DOI: 10.1016/j.apsusc.2004.03.144)

[178] F. Zanderigo, S. Ferrari, G. Queirolo, C. Pello and M. Borgini: *Quantitative ToF-SIMS analysis of metal contamination on silicon wafers* - Mater. Sci. Eng., B **73** (2000) 173–177. (DOI: 10.1016/S0921-5107(99)00456-0)

[179] M. Inoue, A. Murase, M. Yamamoto and S. Kubo: *Analysis of volatile nanoparticles emitted from diesel engine using TOF-SIMS and metal-assisted SIMS (MetA-SIMS)* - Appl. Surf. Sci. **252** (2006) 7014–7017. (DOI: 10.1016/j.apsusc.2006.02.169)

Copy for "Bibliothèque UCL"

[180] C. Poleunis, A. Delcorte and P. Bertrand: *Determination of organic contaminations on Si wafer surfaces by static ToF-SIMS: Improvement of the detection limit with C_{60}^+ primary ions* - Appl. Surf. Sci. **252** (2006) 7258–7261. (DOI: 10.1016/j.apsusc.2006.02.267)

[181] S. Verdier, J.B. Metson and H.M. Dunlop: *Static SIMS studies of the oxides and hydroxides of aluminium* - J. Mass Spectrom. **42** (2007) 11–19. (DOI: 10.1002/jms.1121)

[182] P. Williams: *The sputtering process and sputtered ion emission* - Surf. Sci. **90** (1979) 588–634. (DOI: 10.1016/0039-6028(79)90363-7)

[183] R. Smith, D. Ramasawmy and S.D. Kenny: *A molecular dynamics model for the Coulomb explosion* - Nucl. Instr. Meth. Phys. Res. B **228** (2005) 330–336. (DOI: 10.1016/j.nimb.2004.10.066)

[184] P. Sigmund, I.S. Bitensky and J. Jensen: *Molecule and cluster bombardment: energy loss, trajectories and collision cascades* - Nucl. Instr. Meth. Phys. Res. B **112** (1996) 1–11. (DOI: 10.1016/0168-583X(95)01125-0)

[185] Y. Le Beyec: *Cluster impacts at keV and MeV energies: Secondary emission phenomena* - Int. J. Mass Spectrom. Ion Proc. **174** (1998) 101–117. (DOI: 10.1016/S0168-1176(97)00294-2)

[186] D. Jacquet and Y. Le Beyec: *Cluster impacts on solids* - Nucl. Instr. Meth. Phys. Res. B **193** (2002) 227–239. (DOI: 10.1016/S0168-583X(02)00755-3)

[187] A. von Hippel: *Zur Theorie der Kathodenzerst´aubung* - Annalen der Physik **386** (1926) 1043–1075. (DOI: 10.1002/andp.19263862510)

[188] C.H. Townes: *Theory of Cathode Sputtering in Low Voltage Gaseous Discharges* - Phys. Rev. **65** (1944) 319 – 327. (DOI: 10.1103/PhysRev.65.319)

[189] M.W. Thompson and R.S. Nelson: *Evidence for heated spikes in bombarded gold from the energy spectrum of atoms ejected by 43 keV Ar and Xe ions* - Philos. Mag. **7** (1962) 2015–2026. (DOI: 10.1080/14786436208214470)

[190] G.Betz and K. Wien: *Energy and angular distributions of sputtered particles* - Int. J. Mass Spectrom. Ion Proc. **140** (1994) 1–110. (DOI: 10.1016/0168-1176(94)04052-4)

[191] P. Sigmund, *Sputtering by Particle Bombardment I.* Springer Verlag, Berlin, (1981).

[192] P. Sigmund: *Theory of Sputtering. I. Sputtering Yield of Amorphous and Polycrystalline Targets* - Phys. Rev. **184** (1969) 383 – 416. (DOI: 10.1103/PhysRev.184.383)

[193] M.W. Thompson: *Atomic collision cascades in solids* - Vacuum **66** (2002) 99–114. (DOI: 10.1016/S0042-207X(02)00179-3)

Copy for "Bibliothèque UCL"

[194] G. Slodzian: *Some problems encountered in secondary ion emission applied to elementary analysis* - Surf. Sci. **48** (1975) 161–186. (DOI: 10.1016/0039-6028(75)90315-5)

[195] G. Blaise: *Similarities in photon and ion emissions induced by sputtering* - Surf. Sci. **60** (1976) 65–75. (DOI: 10.1016/0039-6028(76)90006-6)

[196] G.E. Thomas: *Letter to the Editor* - Radiat. Eff. Defects Solids **31** (1977) 185–186. (DOI: 10.1080/00337577708233276)

[197] C. Plog and W. Gerhard: *Secondary ion production by latent energy of neutrally emitted particles* - Surf. Sci. **152-153** (1985) 127–134. (DOI: 10.1016/0039-6028(85)90135-9)

[198] A. Benninghoven: *Some aspects of secondary ion mass spectrometry of organic compounds* - Int. J. Mass Spectrom. Ion Phys. **53** (1983) 85–99. (DOI: 10.1016/0020-7381(83)85104-3)

[199] W. Lange, M. Jirikowsky and A. Benninghoven: *Secondary ion emission from UHV-deposited amino acid overlayers on metals* - Surf. Sci. **136** (1984) 419–436. (DOI: 10.1016/0039-6028(84)90621-6)

[200] R.G. Cooks and K.L. Busch: *Matrix effects, internal energies and MS/MS spectra of molecular ions sputtered from surfaces* - Int. J. Mass Spectrom. Ion Phys. **53** (1983) 111–124. (DOI: 10.1016/0020-7381(83)85106-7)

[201] D.E. David, T.F. Magnera, R. Tian, D. Stulik and J. Michl: *Cluster ions from keV-energy ion and atom bombardment of frozen gases* - Nucl. Instr. Meth. Phys. Res. B **14** (1986) 378–391. (DOI: 10.1016/0168-583X(86)90133-3)

[202] W. Forst, *Unimolecular Reactions: A Concise Introduction.* Cambridge University Press, (2003).

[203] V. R. Deline, W. Katz, C.A. Evans Jr. and P. Williams: *Mechanism of the SIMS matrix effect* - Appl. Phys. Lett. **33** (1978) 832–835. (DOI: 10.1063/1.90546)

[204] T. Wirtz and H.-N. Migeon: *Work function shifts and variations of ionization probabilities occurring during SIMS analyses using an in situ deposition of* Cs^0 - Surf. Sci. **561** (2004) 200–207. (DOI: 10.1016/j.susc.2004.05.068)

[205] P. Philipp, T. Wirtz, H.-N. Migeon and H. Scherrer: *SIMS analysis with neutral cesium deposition: Negative secondary ion sensitivity increase and quantification aspects* - Int. J. Mass Spectrom. **253** (2006) 71–78. (DOI: 10.1016/j.ijms.2006.02.018)

[206] T. Wirtz and H.-N. Migeon: *Storing Matter: A new quantitative and sensitive analytical technique* - Appl. Surf. Sci. **255** (2008) 1498–1500. (DOI: 10.1016/j.apsusc.2008.05.109)

Copy for "Bibliothèque UCL"

[207] P. Philipp, B. Douhard, F. Lacour, T. Wirtz, L. Houssiau, J.-J. Pireaux and H.-N. Migeon: *The Storing Matter technique: preliminary results on PS and PVC* - Appl. Surf. Sci. **255** (2008) 866–869. (DOI: 10.1016/j.apsusc.2008.05.070)

[208] P. Philipp, F. Lacour, T. Wirtz, L. Houssiau, J.-J. Pireaux, G.Slodzian and H.-N. Migeon: *The Storing Matter Technique: Application to Inorganic Samples* - Appl. Surf. Sci. **255** (2008) 1501–1504. (DOI: 10.1016/j.apsusc.2008.05.075)

[209] G. Binnig, C.F Quate and Ch. Gerber: *Atomic force microscope* - Phys. Rev. Lett. **56** (1986) 930–933. (DOI: 10.1103/PhysRevLett.56.930)

[210] S. Siaua, A.Vervaeta, A.Van Calstera, I.Swennenb and E. Schacht: *Influence of wet chemical treatments on the evolution of epoxy polymer layer surface roughness for use as a build-up layer* - Appl. Surf. Sci. **237** (2004) 456–461. (DOI: 10.1016/j.apsusc.2004.06.111)

[211] F. Kienberger, R. zhu, R. Moser, C. Rankl, D. Blaas and P. Hinterdorfer: *Dynamic force microscopy for imaging of viruses under physiological conditions* - Biol. Proced. Online **6** (2004) 120–128. (DOI: 10.1251/bpo80)

[212] V.M. De Cupere and P.G. Rouxhet: *Surface crystallization of poly(ethylene terephtalate) studied by atomic force microscopy* - Polymer **43** (2002) 5571–5576. (DOI: 10.1016/S0032-3861(02)00394-4)

[213] H.-J. Butt, B. Cappella and M-Kappl: *Force measurments with the atomic force microscope: Technique, interpretation and applications* - Surf. Sci. Rep. **59** (2005) 1–152. (DOI: 10.1016/j.surfrep.2005.08.003)

[214] B. Li, M. Fujii, K. Fukada, T. Kato and T Seimiya: *In situ AFM observation of heterogeneous growth of adsorbed film on cleaved mica surface (Letter)* - Thin Solid Films **312** (1998) 20–23. (DOI: 10.1016/S0040-6090(97)00448-3)

[215] F. Deligny. *Etude et réalisation de la commande électronique d'un microscope à force atomique combiné un micoscope électronique à balayage.* PhD thesis, Université de Reims Champagne Ardenne, Laboratoire de Microscopies et d'Etudes des Nanostructures, (1999).

[216] E.P. Wojcikiewicz, X. Zhang and V.T. Moy: *Force and Compliance Measurements on Living Cells using Atomic Force Microscopy (AFM)* - Biol. Proced. Online **6** (2004) 1–9. (DOI: 10.1251/bpo67)

[217] A. Majumdar and P.I. Oden: *Nanometer-scale lithography using the atomic force microscope* - Appl. Phys. Lett. **61** (1992) 2293–2295. (DOI: 10.1063/1.108268)

[218] L.L. Sohn and R.L. Willett: *Fabrication of nanostructures using atomic-force-microscope-based lithography* - Appl. Phys. Lett. **67** (1995) 1552–1554. (DOI: 10.1063/1.114731)

Copy for "Bibliothèque UCL"

[219] J. Kuppers, T. Schimmel, R. Kladny and V. Popp: *Structuring of mica surfaces with a vibrating AFM tip* - Surf. Sci. **401** (1998) 105–111. (DOI: 10.1016/S0039-6028(97)00917-5)

[220] F.S. Teixeira, R.D. Mansano, M.C. Salvadori, M. Cattani and I.G. Brown: *Atomic force microscope nanolithography of polymethylmethacrylate polymer* - Rev. Sci. Instrum. **78** (2007) 053702. (DOI: 10.1063/1.2736311)

[221] E.S. Snow and P.M. Campbell: *Fabrication of Si nanostructures with an atomic force microscope* - Appl. Phys. Lett **64** (1994) 749–751. (DOI: 10.1063/1.111746)

[222] I.A. Mack, *Elektrochemische Nanostrukturierung von Nickel und Kupfer: Induziertes Abscheiden und Aufl'osen mit der AFM-Spitze*, Universität Karlsruhe, (2002).

[223] B. Cappella and G. Dietler: *Force-distance curves by atomic force microscopy* - Surf. Sci. Rep. **34** (1999) 1–104. (DOI: 10.1016/S0167-5729(99)00003-5)

[224] K.I. Shiramine, S. Muto, T. Shibayama, N. Sakaguchi, H. Ichinose, T. Kozaki, S. Sata, Y. Nakata, N. Yokoyama and M. Taniwaki: *Tip artifact in atomic force microscopy observations of InAs quantum dots grown in Stranski–Krastanow mode* - J. Appl. Phys. **101** (2007) 33527–33531. (DOI: 10.1063/1.2434806)

[225] C. Simon. *Caractérisation de surfaces organiques moléculaires et polymères par SIMS statique: Effet de la métalisation.* PhD thesis, Université de Metz, (1996).

[226] A.G. Emslie, F.T. Bonner and L.G. Peck: *Flow of a Viscous Liquid on a Rotating Disk* - J. Appl. Phys. **29** (1958) 858–862. (DOI: 10.1063/1.1723300)

[227] D. Meyerhofer: *Characteristics of resist films produced by spinning* - J. Appl. Phys. **49** (1978) 3993–3997. (DOI: 10.1063/1.325357)

[228] C.J. Lawrence: *The mechanics of spin coating of polymer films* - Phys. Fluids **31** (1988) 2786–2795. (DOI: 10.1063/1.866986)

[229] Image Metrology. *The Scanning Probe Image Processor (SPIP): User's and Reference Guide v.4.4*, (2007). www.imagemet.com.

[230] A. Delcorte, P. Bertrand, X. Arys, A. Jonas, E. Wischerhoff, B. Mayer and A. Laschewsky: *ToF-SIMS study of alternate polyelectrolyte thin films: Chemical surface characterization and molecular secondary ions sampling depth* - Surf. Sci. **366** (1996) 149–165. (DOI: 10.1016/0039-6028(96)00779-0)

[231] S. Tanuma, C.J. Powell and D.R. Penn: *Calculation of electron inelastic paths: V. Data for 14 organic compounds over the 50-2000eV range* - Surf. Interface Anal. **21** (1993) 165–176. (DOI: 10.1002/sia.740210302)

[232] F. Bernoux, J.-P. Piel, B. Castellon, P. Boher, J.-L. Stehlé, C. Defranoux and J.-H. Lecat: *Ellipsométrie - Théorie, Instrumentation et applications* - Techniques de l'Ingénieur **R6** 490 1–11 & 491 1–10.

Copy for "Bibliothèque UCL"

[233] C.B. Walsh and E.I. Franses: *Ultrathin PMMA films spin-coated from toluene solutions* - Thin Solid Films **429** (2003) 71–76. (DOI: 10.1016/S0040-6090(03)00031-2)

[234] B.-Ch. Schwede, *The Münster High Mass Resolution Static SIMS Library*, ISBN Revision 1.10. ION-TOF GmbH, (May 1999).

[235] C.B. Alcock, V.P. Itkin and M.K. Horrigan: *Vapor Pressure Equations for the Metallic Elements: 298-2500 K* - Can. Metall. Q. **23** (1984) 309–313.

[236] D.R. Lide, *Handbook of Chemistry and Physics - 84th Edition*. CRC Press, (2004).

[237] Bal-Tec. *Film Thickness and Rate Monitor QSG 060 (Manual)*, (1993).

[238] L. Nittler, *Cationisation des polymères en fonction de la structure du dépôt métallique*, UCL-PCPM / CRP-Gabriel Lippmann - LAM, (sep 2005).

[239] Fouad Wahoud, Taoufiq Mouhib, Jean-Nicolas Audinot, A. Delcorte and Henri-Noël Migeon: *Study of charge effect during Cs^+ sputtering of polystyrene in the pre-equilibrium regime* - Surf. Interface Anal. **43** (2011) 201–203. (DOI: 10.1002/sia.3419)

[240] D. Briggs, A. Brown and J.C. Vickerman, *Handbook of static secondary ion mass spectrometry (SIMS)*, ISBN 0-471-91627-7. John Wiley&Son, (1989).

[241] J.G. Newman, B.A. Carlson, R.S. Michael and J.F. Moulder, *Static SIMS Handbook of Polymer Analysis*, ISBN 0-962-70261-7. Perking-Elmer Corporation, Physical Electronics Division, (1991).

[242] V.L. Mironov, *Fundamentals of Scanning Probe Microscopy*. The Russian Academy of Science, (2004). Textbook for students of the senior courses of higher educational institutions.

[243] J.A. Gallego-Juarez: *Piezoelectric ceramics and ultrasonic transducers* - J. Phys. E: Sci. Instrum. **22** (1989) 804–816. (DOI: 10.1088/0022-3735/22/10/001)

[244] S. Tougaard: *Quantitative analysis of the inelastic background in surface electron spectroscopy* - Surf. Interface Anal. **11** (1988) 453–472. (DOI: 10.1002/sia.740110902)

[245] S. Tougaard and A. Jablonski: *Quantitative XPS: Influence of Elastic Electron Scattering in Quantification by Peak Shape Analysis* - Surf. Interface Anal. **25** (1998) 404–408. (DOI: 10.1002/(SICI)1096-9918(199706)25:6<404::AID-SIA250>3.0.CO;2-A)

[246] S. Tougaard: *Practical algorithm for background substraction* - Surf. Sci. **216** (1989) 343–360. (DOI: 10.1016/0039-6028(89)90380-4)

Copy for "Bibliothèque UCL"

[247] Tougaard and H.S. Hansen: *Non-destructive depth profiling through quantitative analysis of surface electron spectra* - Surf. Interface Anal. **14** (1989) 730–738. (DOI: 10.1002/sia.740141109)

[248] S. Tougaard: *Inelastic background correction and quantitative surface analysis* - J. Electron Spectrosc. Relat. Phenom. **52** (1990) 243–271. (DOI: 10.1016/0368-2048(90)85022-2)

[249] S. Tougaard: *Surface nanostructure determination by X-ray photoemission spectroscopy peak shape analysis* - J. Vac. Sci. Technol. A **14** (1996) 1415–1423. (DOI: 10.1116/1.579963)

[250] S. Tougaard: *Accuracy of the non-destructive surface nanostructure quantification technique based on analysis of the XPS or AES peak shape* - Surf. Interface Anal. **26** (1998) 249. (DOI: 10.1002/sia.740141109)

[251] M. Haruta: *Size- and support-dependency in the catalysis of gold* - Catalysis Today **36** (1997) 153–166. (DOI: 10.1016/S0920-5861(96)00208-8)

[252] Program. *S.R.I.M. - The Stopping and Range of Ions in Matter.* http://www.srim.org/.

[253] K.J. Taylor, C.L. Pettiette-Hall, O. Cheshnovsky and R.E. Smalley: *Ultraviolet photoelectron spectra of coinage metal clusters* - J. Chem. Phys. **96** (1992) 3319–3329. (DOI: 10.1063/1.461927)

[254] Xi-Bo Li, Hong-Yan Wang, Xiang-Dong Yang, Zheng-He Zhu and Yong-Jian Tang: *Size dependence of the structures and energetic and electronic properties of gold clusters* - J. Chem. Phys. **126** (2007) 84505. (DOI: 10.1063/1.2434779)

[255] I. Katakuse, T. Ichihara, Y. Fujita, T. Matsuo, T. Sakurai and H. Matsuda: *Mass distributions of copper, silver and gold clusters and electronic shell structure* - Int. J. Mass Spectrom. Ion Proc. **67** (1985) 229–236. (DOI: 10.1016/0168-1176(85)80021-5)

[256] I. Katakuse, T. Ichihara, Y. Fujita, T. Matsuo, T. Sakurai and H. Matsuda: *Mass distributions of negative cluster ions of copper, silver, and gold* - Int. J. Mass Spectrom. Ion Proc. **74** (1986) 33–41. (DOI: 10.1016/0168-1176(86)85021-2)

[257] C. Stoermer, J. Friedrich and M.M. Kappes: *Observation of multiply charged cluster anions upon pulsed UV laser ablation of metal surfaces under high vacuum* - Int. J. Mass Spectrom. **206** (2001) 63–78. (DOI: 10.1016/S1387-3806(00)00390-0)

[258] M. Fallavier, R. Kirsch, S.N. Morozov, J.C. Poizat, J.P. Thomas and N. Wehbe: *Intense emission of cluster anions from gold targets under impact of keV/u gold clusters* - Phys. Rev. B **68** (2003) 140102–140105. (DOI: 10.1103/PhysRevB.68.140102)

Copy for "Bibliothèque UCL"

[259] N. Wehbe, T. Mouhib, A. Prabhakaran, P. Bertrand and A. Delcorte: *Influence of the Organic Layer Thickness in (Metal-Assisted) Secondary Ion Mass Spectrometry Using Ga^+ and C_{60}^+ Projectiles* - J. Am. Soc. Mass Spectrom. **20** (2009) 2294–2303. (DOI: 10.1016/j.jasms.2009.08.022)

[260] R. De Mondt. *Statische Secundaire Ionen Massaspectrometrie: Methode Ontwikkeling en Toepassing op Grafische Materialen.* PhD thesis, Universiteit Antwerpen, (2007).

[261] T. Mouhib, A. Delcorte, C. Poleunis and P. Bertrand: *Organic secondary ion mass spectrometry: signal enhancement by water vapour injection* - Journal of the American Society for Mass Spectrometry **.** (2010) . (DOI: 10.1016/j.jasms.2010.08.013)

Copy for "Bibliothèque UCL"

List of Figures

2.1 Schematic diagram of the basic processes occurring in the initial stages of metal/polymer interface formation by physical vapor deposition (modified from [98]). Sketched are: (a) adsorption of atoms and clusters, (b) desorption, (c) surface diffusion, (d) nucleation of critical clusters, (e) aggregation, (f) edge diffusion, (g) dissociation, (h) diffusion into the bulk, (i) aggregation in the bulk. 23

2.2 Schematic cross-section views of the three primary modes of thin film growth: (a) Volmer-Weber (island formation), (b) Frank-van der Merwe (layer-by-layer), and (c) Stranski-Krastanov (layer-plus-island). For each growth mode different amounts of surface coverage (expressed in monolayer (ML)) are shown. 28

3.1 Principle of the SIMS technique: Impinging primary ions interact with the atoms in the sample and the hereby created secondary ions are analyzed in a mass spectrometer. 38

3.2 Different Models of energy deposition: a) Collision Cascade - b) Hot Spot - c) Single-knock out. For more details refer to Section 3.2.2 (adapted from [190] ([191]). 40

3.3 Nascent Ion Model for metal oxides. As a result of the collision cascade, a neutral molecule leaves the surface and dissociates at some distance, producing a metal cation and an oxygen anion. 42

3.4 Precursor model: The energy transfer to preformed ion (precursor) and the subsequent emission of parentlike secondary ions (adapted from [152]). 43

3.5 Summary of the processes thought to occur in the Desorption-Ionization Model (adapted from [200]). 44

3.6 Model for the formation of secondary ions observed in a polymer sample in SIMS (adapted from [33]). 45

3.7 The impact of a primary ion on a surface results in the emission of secondary particles and the damage of the surface molecules in an area σ around the impact point (adapted from [152]). 46

Copy for "Bibliothèque UCL"

3.8 The Lennard-Jones potential (black line) is the sum of the attractive potential (blue) and the repulsive potential (red). Furthermore the regions for the different type of AFM measurements, which are described in Chapter 4.4.3, are indicated in the graph. 51

3.9 A typical force-distance curve $\Delta\ Z = f(z)$. The red line shows the approach of the tip to the sample and the blue line indicates the acting forces on the tip when it is retracting from the surface. The inlets show the bending of the cantilever at different points of the curve. For a more detailed description see the text in Chapter 3.3.2. 52

3.10 Formation of artifacts in an AFM measurements due to the tip apex dimension and size of the surface structures. The measured topography of the sketched sample is drawn in a thick solid line. The measured elevation is broader than the real structure. The depth of too small cavities are not measured accurately. 53

3.11 Principle of XPS and Auger: a) Excitation of an inner shell electron by a radiation of energy $h\nu$ - b) Ejection of a photoelectron which leaves a hole in the inner $1s$ shell - c) Ejection of an Auger electron KL_1L_2. 55

3.12 Scheme of electron-matter interactions arising from the impact of an electron beam onto a specimen. a) A signal below the specimen is only observable if the thickness is thin enough to allow some electrons to pass through. b) In thick samples the interaction volume has a pear-like shape. 58

4.1 Preparation of the polymer film samples. See text for a detailed description of the preparation method. 63

4.2 The four process phases in spin-coating. See text for a detailed description of the spincoating process. 64

4.3 AC-AFM topography (fov: $2 \times 2\mu m^2 \times 6$nm): Different pristine polycarbonate samples 68

4.4 Most commonly used roughness parameter (S_a, S_q and S_{sk}) for the pristine samples prepared either as bulk or by spin-coating. 70

4.5 Evolution of the silicon substrate signal in ToF-SIMS as a function of the PC polymer concentration of the solution used for spincoated sample preparation. 71

4.6 Schematic setup of the ellipsometry experiment 71

4.7 (a) and (b) show the fitting plots for a polycarbonate film. The red lines indicate the expected signal from the model, whereas the other lines represent the measurement. 72

4.8 Evolution of the polymer thickness as a function of the solution concentration for the different spincoated polymers. The data points are fitted by the equation $d_s = k \cdot c^{\alpha}$ using the parameters denoted in Table 4.6. 73

Copy for "Bibliothèque UCL"

4.9 Comparison of the relative intensities of the characteristic negative secondary ions of polystyrene between the samples prepared by spin-coating and the data in the Münster High Mass Resolution Static SIMS Library [234]. 74

4.10 ToF-SIMS spectra in positive polarity of the 4 polymers (in each graph from top to bottom: PC, PET-I, PMMA, PS) with a ≈ 1 nm nominal thickness deposition of gold by sputtering. The mass of the peaks as well as their probable Label are noted in Table 4.7. 76

4.11 Vapor pressure of different metals. The solid line represents the vapor pressure of solids. The dotted line correspond to the vapor pressure of the liquid metal. The melting temperature of the elements as well as the corresponding vapor pressure are noted in the inset. 79

4.12 Side view of the first geometry of the evaporation system. 81

4.13 Final position of the evaporation cell 83

4.14 ToF-SIMS spectrum in the negative polarity of a thick (≈ 13 nm) gold deposit on native silicon. The mass of the peaks as well as their probable label are noted in Table 4.10. 86

4.15 ToF-SIMS spectrum in the positive polarity of a thick (≈ 13 nm) gold deposit on native silicon. The mass of the peaks as well as their probable label are noted in Table 4.10. 87

4.16 Temperature rise as a function of the power of the evaporation source. The gray area marks the power during evaporation of gold. 89

4.17 Confoval Microcopy (fov: $100 \times 100 \mu m^2 \times \approx 50$nm): Topography of pristine and heat-treated spincoated polystyrene - measurements kindly provided by Novelis Luxembourg S.A. 90

4.18 Roughness parameter for the pristine polymer (PS) and the heat-treated pristine polymer. 90

4.19 Draft of the main components of a SIMS. 92

4.20 Photo of the ToF-SIMS III instrument at the SAM department of the CRP-Gabriel Lippmann. 95

4.21 a) Main AFM components and b) Laser spot deviation due to cantilever deformation (adapted from [242]). 97

4.22 Photography of the AFM instrument in the CRP-GL 99

4.23 Typical components of an XPS instrument: Schematics of a) a twin anode X-ray source - b) Hemispherical electron energy analyzer used in the Thermo VG Microlab 350. 102

5.1 Sections through samples: (a) polymer sample with an overlayer - (b) polymer sample with an overlayer and a contamination layer. The values for the sensitivity factors σ_i and the inelastic mean free path lengths λ_i^j are noted in Table 5.2. 112

Copy for "Bibliothèque UCL"

5.2 Au-Thickness determined by XPS with the 2 layers model without reconstruction. The bold diagonal line represent the unit sticking coefficient. 113

5.3 Examples of the $C1s$ reconstruction for the different metalized polymers (PET-I and PS) by dint of a pristine polymer and a contamination samples. The nominal thickness of the evaporated gold layer is ≈ 0.9 nm. Between the elaboration and the XPS characterization, the metalized sample was stored several weeks in the lab atmosphere. 116

5.4 Au-Thickness determined by XPS with the 3 layers model with the reconstruction of the $C1s$ peak. The bold diagonal line represents the unit sticking coefficient. 117

5.5 Thickness of the contamination layer determined by the three layer model. 118

5.6 Distortion of the energy spectrum depending on the distance the electrons travel on their way out of the solid. 119

5.7 $QUASES^{™}$ -Models: a) Top layer (buried layer with $d_S = 0$) - b) Island (Passive Substrate) - c&d) *buried layer*. 120

5.8 Example of fitting a $Au4f$ XPS spectrum of a metalized (≈ 3.3 nm polycarbonate film with the $QUASES^{™}$ program. The insets show the results obtained from the different models ($\hookrightarrow$ *Figure 5.7*). 121

5.9 Scale factor s_f determined by $QUASES^{™}$ with the *buried layer* with $d_S = 0$. The scalefactor can be interpreted as coverage percentage. . . 122

5.10 Height of the gold islands determined by $QUASES^{™}$ with the *buried layer* with $d_S = 0$. 123

5.11 Scalefactor $s_f \hat{=}$ surface coverage θ. 124

5.12 Average height of the gold islands, which are determined by evaluating with the *buried layer* model in the $QUASES^{™}$ program. 125

5.13 Average depth below the surface of the gold structure (corresponds to the contamination thickness). The data was evaluated by using the *buried layer* model in the $QUASES^{™}$ program. 126

5.14 Deposited gold quantity as a function of the evaporated gold quantity, which is measured by the QCM. The deposited quantity is determined by multiplying the average height of the islands with the surface coverage obtained from the $QUASES^{™}$ program. The bold diagonal line represents the unit sticking coefficient. 127

5.15 AC-AFM topography (field of view (fov): $500 \times 500nm^2$): Image transformations - plane correction: a) raw data - b) correction plane - c) leveled image. 132

5.16 AC-AFM topography (fov: $500 \times 500nm^2$): Image transformations - noise reduction: a) leveled image - b) median filter - c) noise-free image. 132

Copy for "Bibliothèque UCL"

5.17 AC-AFM topography (fov: $500 \times 500nm^2$): Image transformations - polynomial subtraction: a) median filtered image - b) polynomial plane - c) final image. 133

5.18 AC-AFM topography (fov: $500 \times 500nm^2$) of PC with different amount of deposited gold (from a) pristine sample to g) 4.4 nm of gold. The color scale on these AFM topography images is from 0 to 2.2 nm. . . . 134

5.19 AC-AFM topography and phase (fov: $500 \times 500nm^2$) of metalized PS: a)-c) topography (color range: $0 - 2.5$ nm) - d)-f) phase images (color range: $0 - 1.2$ V). The amount of evaporated gold is noted below the images. g)-i)For an enhanced perception of the topography of the samples, a 3D representation of the same AFM data is shown (color range: adapted on the individual maximal z-range). 136

5.20 Average roughness S_a of the different polymers as a function of the evaporated amount of gold. The position and the size of the error bars are calculated on the basis of all the data. 138

5.21 SEM images (fov: $\approx 600 \times 440nm^2$): spincoated PS with different gold amounts. These images were acquired with the JSM-7500F from Jeol Ltd.. 139

5.22 TEM images (fov: $\approx 300 \times 300nm^2$): dried PS with different gold amount. These images were acquired with the LEO 922 Omega from LEO. In the upper left corner of each image, each detected grain by SPIP™ is indicated by an individual color. 141

5.23 Gold coverage percentage of PS samples as a function of the deposited gold amount. The different symbols correspond to the different analysis technique (▲: SEM and ■: TEM). The error bars are calculated on the basis of all the data. 142

5.24 Density of detected gold grains as a function of the evaporated amount of gold. The different symbols correspond to the different analysis technique (▲: SEM and ■: TEM). The error bars are calculated on the basis of all the data. 143

5.25 Evolution of the normalized distributions of the detected grain area as a function of the evaporated gold amount (Normalized to the total number of detected grains). The histogram represents the grain area distribution for a 1.2 nm amount of gold. The associated fit with a gamma function ($f(x) = a \cdot x^{p-1} \cdot e^{-b \cdot x}$) is better than $r^2 = 0.90$. . . . 144

5.26 Expectation values of the grain *area* as a function of the evaporated gold amount on PS. 146

5.27 Expectation values of the grain *diameter* as a function of the evaporated gold amount on PS. 147

5.28 Expectation values of the grain *interface perimeter* as a function of the evaporated gold amount on PS. 148

Copy for "Bibliothèque UCL"

5.29 Averaged height calculated with the assumption of ellipsoid-formed Au islands as a function of evaporated gold quantity (↪ *Equation 5.10*). For comparison, the height of the Au islands determined by XPS measurements (↪ *Chapter 5.1.1*) are shown too. 150

5.30 TEM images (fov: $\approx 300\times300nm^2$): sliced PC with different amount of evaporated gold. The images were acquired with the LEO 922 Omega from LEO. 151

5.31 TEM images (fov: $\approx 300 \times 300nm^2$) of metalized PC slices prepared by microtome. The amount of evaporated gold was ≈ 2.0 nm. 152

5.32 Schematic evolution of different morphology results. The lower frame shows that under certain circumstances, the AFM tip can not follow the surface profile. 155

6.1 Flow diagramm of the analysis procedure. 159

6.2 Enhancement $\frac{I_{Frag}(Au)}{I_{Frag}(Si)}$ of some characteristic fragments of the PC and PS polymers as a function of the concentration of the polymer solution used for spincoating. The measured thickness of the polymer layers is noted in brackets. 160

6.3 SRIM/TRIM Ratio $\frac{Y_C(Au)}{Y_C(Si)}$ of the sputtered C-Atoms on the different polymers as a function of polymer thickness. H and O atoms show a similar evolution. Simulation-Parameter: 10 keV ^{40}Ar - 45° incidence. 163

6.4 SRIM/TRIM evolution of the longitudinal ion-range on different substrates/polymer combinations as a function of the polymer thickness. Simulation-Parameter: 10 keV ^{40}Ar - 45° incidence. 164

6.5 Evolution of the TSIC as a function of the evaporated gold quantity for different used concentration of PC and PS polymer solution. 165

6.6 Change of the intensity of H^-, C^- and O^- as function of the evaporated gold quantity for thick PC and PS polymer samples in the negative polarity. The solid line indicates the remaining percentage of pristine polymer at the sample surface. 167

6.7 Normalized variation of the secondary ion intensity of $Au_n^{\pm}$ as a function of the evaporated gold quantity on PC. The normalization is based on the $Au_n^{\pm}$ intensity from the largest evaporated gold quantity. 170

6.8 Normalized variation of the secondary ion intensity of $Au_n^{\pm}$ as a function of the Au-cluster size. The normalization is based on intensity of $Au^{\pm}$. Au_4^+ and Au_6^+ have not been observed. 171

6.9 Secondary ion intensity variations of characteristic PC fragments in both polarities measured on a thick PC layer. The solid line represents the evolution of the total secondary ion counts. 177

Copy for "Bibliothèque UCL"

6.10 Enhancement of the secondary ion intensity for characteristic PET-I fragments in both polarities as a function of the evaporated gold quantity. The evolution of the total secondary ion counts and the remaining polymer at the sample surface are represented by a solid line and dotted line, respectively. 178

6.11 Variation of the secondary ion intensity of characteristic PMMA fragments in both polarities as a function of the evaporated gold quantity. The solid line and the dotted line represent the evolution of the total secondary ion counts and the remaining polymer at the sample surface, respectively. 179

6.12 Enhancement of the secondary ion intensity for characteristic PS fragments in both polarities as a function of the evaporated gold quantity. The solid line represents the evolution of the total secondary ion counts. 180

6.13 Evolution of the morphology parameters "number of island per area", "mean interface perimeter" and "remaining polymer surface" as well as their combination. The inset shows the evolutions determined by the experimental data of the morphology parameters. In order to show all the data in a single graph, some parameters are multiplied by a constant factor. The exact values of the different parameters can be found in Section 5.2.2. 184

6.14 Comparison of the calculated enhancement by the Equation 6.1 with the SI enhancement observed in S-SIMS for one characteristic PC fragment in the positive polarity. 185

6.15 Intensity of anionized and cationized characteristic PC fragments as a function of evaporated gold quantity. 191

6.16 Intensity of anionized and cationized characteristic PET-I fragments as a function of evaporated gold quantity. 192

6.17 Intensity of anionized and cationized characteristic PMMA fragments as a function of evaporated gold quantity. 193

6.18 Intensity of anionized and cationized characteristic PS fragments as a function of evaporated gold quantity. 194

6.19 Variation of the secondary ion intensity of characteristic fragments of a thick PC sample under different storage conditions. 202

6.20 Variation of the secondary ion intensity of characteristic fragments of a thick PC sample for various *in-situ* storage time. 203

6.21 Variation of the secondary ion intensity of atomic ions from a thick PS in the negative polarity under different storage conditions and for various storage times. 205

6.22 Variation of the secondary ion intensity of characteristic fragments of PS in the negative polarity under different storage conditions. 206

Copy for "Bibliothèque UCL"

6.23 Variation of the secondary ion intensity of characteristic fragments of PS in the positive polarity under different storage conditions. 207

A.1 Molecular structure and properties of polycarbonate A-5

A.2 Spectra of polycarbonate in the negative and positive polarities. The peaks mark by a * indicates characteristic peaks found in the literature. # indicates the position of the monomer. ‡ indicates the position of the characteristic peaks which are evaluated in this work. A-6

A.3 Contributions of the $C1s$ XPS peak of a pristine PC sample. A-9

A.4 Molecular structure of a) polyethylene terephthalate (PET) and b) polyethylene isophthalate (PET-I). A-10

A.5 Spectra of poly(etylene terephthalate) isophthalate in the negative and positive polarities. The peaks mark by a * indicates characteristic peaks found in the literature. # indicates the position of the monomer. ‡ indicates the position of the characteristic peaks which are evaluated in this work. A-11

A.6 Contributions of the $C1s$ XPS peak of a pristine PET-I sample. A-13

A.7 Molecular structure and properties of PMMA A-14

A.8 Spectra of PMMA in the negative and positive polarities. The peaks mark by a * indicates characteristic peaks found in the literature. # indicates the position of the monomer. ‡ indicates the position of the characteristic peaks which are evaluated in this work. A-15

A.9 Contributions of the $C1s$ XPS peak of a pristine PMMA sample. . . . A-18

A.10 Molecular structure and properties of polystyrene A-19

A.11 Spectra of polysytrene in the negative and positive polarities. The peaks mark by a * indicates characteristic peaks found in the literature. # indicates the position of the monomer. ‡ indicates the position of the characteristic peaks which are evaluated in this work. A-20

A.12 Contributions of the $C1s$ XPS peak of a pristine PS sample. A-22

Copy for "Bibliothèque UCL"

List of Tables

3.1 Overview of the capabilities and limitations of surface-analytical techniques available at the CRP-Gabriel Lippmann. 36

4.1 List of the used polymer in form of thin films. 63

4.2 List of the spincoated polymers which were studied in this work. Also mentioned are the internal reference # and the structure of the monomer. 66

4.3 The different polymers under study with their supplier, their suitable solvent, their weight average molecular weight, their glass transition temperature T_G and their typical surface energy. 67

4.4 Parameters for the spincoater used for the sample preparation in this work. 67

4.5 Optical constants (thickness and refracting index $\tilde{n}$) for the components of the ellipsometric model ($\hookrightarrow$ *Figure 4.6*). 72

4.6 Thickness fitting parameters for the different polymers 74

4.7 List of intense peaks observed on all polymers after the gold deposition by sputtering ($\hookrightarrow$ *Figure 4.10*). In the case where an indisputable association to an ion is possible, the label of this ion is noted. 77

4.8 Distribution of the gold thickness on Si samples to check the homogeneity of the evaporation. The thickness was determined by profilometry by averaging six points of measurements on each sample . 84

4.9 Distribution of the gold thickness on InP samples to check the homogeneity of the evaporation for small evaporated gold quantity. The thickness was determined by XPS analysis by averaging three points of measurements 84

4.10 List of intense peaks observed on a thick (≈ 13 nm) gold deposit on naitive silicon. In the case where an indisputable association to an ion is possible the label of this ion is noted. 88

4.11 Main characteristic parameters of the Pointprobe® cantilever from NanoWorld AG (from Datasheet). 100

4.12 Pass energy for the different type of acquired spectra. 104

Copy for "Bibliothèque UCL"

4.13 Comparison of theoretic characteristics of different electron guns. . . . 105

5.1 Limits of the $C1s$ and $Au4f$ peaks used for the reconstruction and thickness evaluation. 111

5.2 Values for the sensitivity factor of Au (σ_o) and of C (σ_c, σ_s). λ_i^j is the inelastic mean free path in layer j for electrons emitted from the layer i. The values for the inelastic mean free path are calculated by the TPP2M formula [231]. 112

5.3 Sticking coefficients for gold on different polymers determined by the two layer model. 113

5.4 Theoretical and experimental percentage of the different $C1s$ peak contribution of the different polymers and the contamination on a thick Au layer. $C1s$ peak contribution graphs of the different polymers are shown in Annexe A.2. 114

5.5 Sticking coefficients for gold on different polymers determined by the three layer model. 117

5.6 Sticking coefficients for gold on different polymers determined by the *buried layer* model. 127

5.7 Main characteristic parameters for the AFM analysis and the utilized Pointprobe® cantilever from NanoWorld AG. 131

6.1 Ionization energies (or vertical ionization potentials for clusters), work functions and electron affinities for the different species occurring in the work. Values found in [236] and [254]. 172

6.2 Selected fragments of the different polymers among their vast number of characteristic fragments for the detailed discussion of the their intensities as a function of the evaporated gold quantity. The structure of the fragments can be found in the appendix A.2. 175

6.3 Parameters f_1 and f_2 of the Equation 6.1 obtained after fitting the intensity enhancements of the different fragments and polymers. (* The unit of f_2 is $[\cdot 10^{-7}\mu m^{-1}]$) 187

6.4 Anionized and cationized characteristic fragments of the different polymers. Their relation with the characteristic fragment of the pristine polymer ($\hookrightarrow$ *Table 6.2*) is denoted in the last column. 189

6.5 Order of the ratios for the different polymers in the both polarities. . . 195

A.1 Properties of Gold. Mass spectra of the evaporated gold can be found in Chapter 4.2.2.C. A-4

A.2 Characteristic fragments of PC in the negative polarity A-7

A.3 Characteristic fragments of polycarbonate in the positive polarity . . . A-8

Copy for "Bibliothèque UCL"

A.4 Theoretical and experimental percentage of the different $C1s$ XPS peak contribution of a pristine PC sample. A-9

A.5 Characteristic fragments of poly(etylene terephthalate) in the negative polarity A-12

A.6 Characteristic fragments of poly(etylene terephthalate) in the positive polarity A-12

A.7 Theoretical and experimental percentage of the different $C1s$ XPS peak contribution of a pristine PET-I sample. A-13

A.8 Characteristic fragments of PMMA in the negative polarity A-16

A.9 Characteristic fragments of PMMA in the positive polarity A-17

A.10 Theoretical and experimental percentage of the different $C1s$ XPS peak contribution of a pristine PMMA sample. A-18

A.11 Characteristic fragments of polystyrene in the negative polarity A-19

A.12 Characteristic fragments of polystyrene in the positive polarity A-21

A.13 Theoretical and experimental percentage of the different $C1s$ XPS peak contribution of a pristine PS sample. A-22

Copy for "Bibliothèque UCL"

Copy for "Bibliothèque UCL"

Appendix A

Appendices

A.1 Glossary

$\alpha_{\mathbf{q}}$	angle between evaporation source and the normal of the QCM
$\alpha_{\mathbf{s}}$	angle between evaporation source and sample
A	(bombarded) surface
AES	Auger Electron Spectroscopy
AFM	Atomic Force Microscopy
β	take off angle
BSE	BackScattered Electron
$\mathfrak{Char}$	characteristic fragment of the sample
C	condensation coefficient
c	concentration
$\mathbf{\Delta}$	phase shift after reflection
$\mathbf{d}$, $\mathbf{d_o}$	thickness (of the gold deposition)
$\mathbf{d_c}$	thickness of the organic overlayer
$\mathbf{d_s}$	thickness of the substrate
$\mathbf{D_p}$	primary ion fluence
$\mathbf{D_s}$	surface diffusion coefficient
e	elemental charge
$\epsilon^{\pm}$	ionization probability
$\mathbf{E_{kin}}$	kinetic energy
$\mathbf{E_B}$	binding energy

Copy for "Bibliothèque UCL"

$\mathbf{f}$	evaporation rate
$\mathbf{F_T}$	tooling factor
$\mathbf{F_N}$, $\mathbf{F_L}$	normal force, lateral force
FWHM	Full Width at Half Maximum
fov	Field of view
γ, $\gamma_{\mathbf{M}}$,$\gamma_{\mathbf{MP}}$, $\gamma_{\mathbf{P}}$	surface tension
$\mathbf{h}\nu$	photon energy
$\mathbf{I_A}$	photoelectron current
$\mathbf{I_{Frag}}$	secondary ion intensity of a fragment
$\mathbf{I_p}$	primary ion current
$\mathbf{J}$	X-ray flux density
λ, $\lambda_{\mathbf{A}}$	inelastic mean free path
$\mathbf{L_q}$	evaporation source-sample distance
$\mathbf{L_s}$	evaporation source-QCM distance
LFM	Lateral Force Microscope
$\mathbf{m}$	mass
$\mathbf{m/q}$	mass / charge number for secondary ions
$\mathbf{M_n}$	number average molar mass $\frac{\sum n_i M_i^2}{\sum n_i}$
$\mathbf{M_w}$	weight average molar mass $\frac{\sum n_i M_i}{\sum n_i M_i}$
$\mathbb{M}$	molecule / monomer
$(\mathbb{M}$ $-\mathbf{H})^{\pm}$	deprotonated parent ion
$(\mathbb{M}$ $+\mathbf{H})^{\pm}$	protonated parent ion
Me	metal atom
$(\mathit{Me} + \mathfrak{Char})^{-}$	anionized characteristic ion of the sample
$(\mathit{Me} + \mathfrak{Char})^{+}$	cationized characteristic ion of the sample
ME-SIMS	Matrix Enhanced Secondary Ion Mass Spectroscopy
MetA-SIMS	Metal assisted Secondary Ion Mass Spectroscopy
MP	Mega Pixel (camera sensor)
$\tilde{\mathbf{n}}$	refracting index
$\mathbf{N_i}$	number of gold islands per square micrometer
$\mathbf{\Phi}$	work function
$\mathbf{\Psi}$	amplitude ratio of the light components
$\mathbf{p}$	pressure
$\mathbf{P_{mi}}$	mean interface perimeter between polymer and gold islands

Copy for "Bibliothèque UCL"

PC	Poly(carbonate)
PET	Poly(Ethylene Terephthalate)
PET-I	Poly(Ethylene Terephthalate)-Isopthalate
PMMA	Poly(Methyl MethAcrylate)
PS	Poly(Styrene)
q	electric charge
QCM	Quartz Crystal Microbalance
r	(radial) distance
R	radii of the AFM tip apex
$\mathbf{R_m}$	mass resolution
σ	damage cross section
$\sigma_\mathbf{i}$	interaction cross section
$\sigma_\mathbf{c}$, $\sigma_\mathbf{o}$, $\sigma_\mathbf{s}$	specific sensitivity factor
$\mathbf{S_a}$	average roughness
$\mathbf{s_f}$	scale factor
$\mathbf{S_{ku}}$	surface kurtosis
$\mathbf{S_q}$	root mean square roughness
$\mathbf{S_{sk}}$	surface skewness
SE	Secondary Electron
SI	Secondary Ion
SIMS	Secondary Ion Mass Spectrometry
SNOM	Scanning Near-field Optical Microscope
SPM	Scanning Probe Microscope
t	time
T	temperature
$\mathbf{T_G}$	glass-transition temperature
θ	coverage
TSIC	Total Secondary Ion Count
U	potential
UHV	Ultra High Vacuum
$\mathbf{v_0}$	initial velocity
w	width
XPS	X-ray Photoelectron Spectroscopy
Y, $\mathbf{Y_{Frag}}$	sputter yield (of a fragment)
ζ	equilibrium distance
$\mathbf{\Delta Z}$	cantilever bending
z	tip-sample distance
$\mathbf{Z_A}$	atomic number

Copy for "Bibliothèque UCL"

A.2 Characteristic peaks

Although the ion bombardment create numerous fragments, only a few of them are characteristic for the analyzed polymer. The most intense and characteristic of these fragments as well as their formula structure are listed in the following sections. These data are regrouped form different reference books [234, 240, 241]. Furthermore a small description of the polymer as well as some properties of them are given. Also an acquired spectrum is presented for each polymer in both polarities as well as a graph showing the contributions in XPS of $C1s$ peak is shown. In Table A.1 some properties of gold, which is used in this work for polymer metalization, are noted.

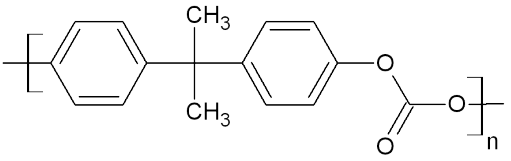
Formula	Au
Monoisotopic Mass	196.96 u
Atomic radius	144 pm
Melting Temperature	1064 °C
Boiling Temperature	2856 °C
Density	19.30 $\frac{g}{cm^3}$
Surface free energy	$\approx$ 1100 $\frac{mJ}{m^2}$

Table A.1: *Properties of Gold. Mass spectra of the evaporated gold can be found in Chapter 4.2.2.C.*

Copy for "Bibliothèque UCL"

A.2.1 Polycarbonate

Polycarbonates, which received their name due to the carbonate ester functional group, belong to the group of thermoplastic polymers. The most common type of polycarbonate plastic is made from bisphenol A (BPA). As they are easily worked, moulded, and thermoformed, these plastics are very widely used in the modern chemical industry. Its main features (high impact-resistance, temperature resistance, highly transparent to visible light and better light transmission characteristics) make the polymer attractive for housewares, laboratories and industries.



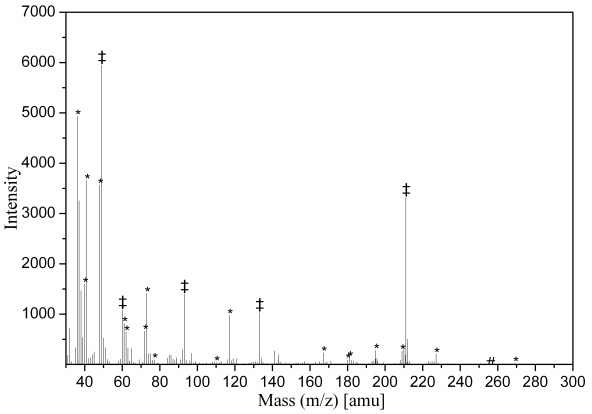
(a) *Molecular structure*

Molecular formula	$C_{16}H_{14}O_3$
Monoisotopic Mass	254.09 u
Melting Temperature	267 °C
Glass transition temperature	150 °C
Refracting index	1.582
Density	1.21 $\frac{g}{cm^3}$
Surface free energy	34 $\frac{mJ}{m^2}$

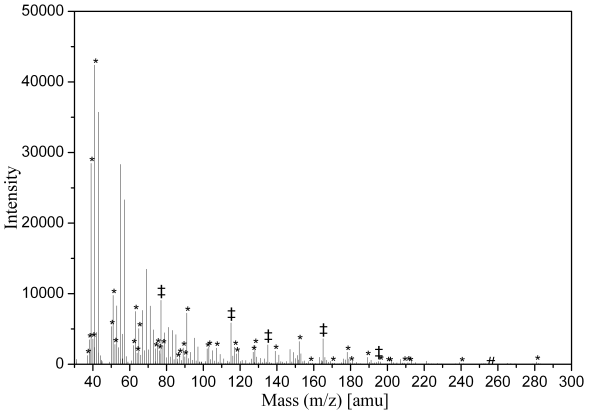
(b) *Properties of polycarbonate*

Figure A.1: *Molecular structure and properties of polycarbonate*

Copy for "Bibliothèque UCL"



(a) *negative polarity*



(b) *positive polarity*

Figure A.2: *Spectra of polycarbonate in the negative and positive polarities. The peaks mark by a * indicates characteristic peaks found in the literature. # indicates the position of the monomer. ‡ indicates the position of the characteristic peaks which are evaluated in this work.*

Copy for "Bibliothèque UCL"

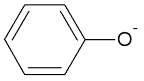
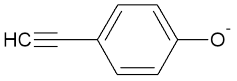
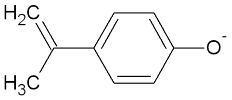
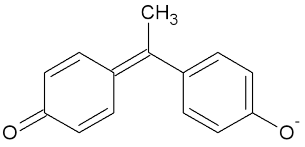
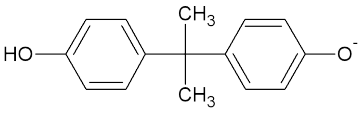
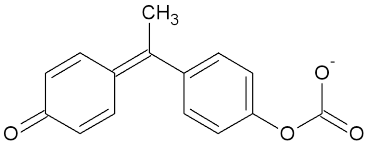
Fragment	Mass [u]	Structure
C_4H^-	49.01	
C_5^-	60.00	
$C_6H_5^-$	77.04	
$C_6H_5O^-$	93.03	
$C_8H_5O^-$	117.03	
$C_9H_9O^-$	133.07	
$C_{14}H_{11}O_2^-$	211.08	
$C_{15}H_{15}O_2^-$	227.11	
$C_{15}H_{11}O_4^-$	255.07	

Table A.2: *Characteristic fragments of PC in the negative polarity*

Copy for "Bibliothèque UCL"

In the positive polarity, the characteristic ions of polycarbonate are in generally similar to those of polystyrene [240].

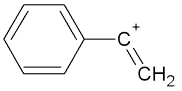
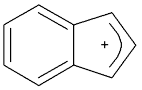
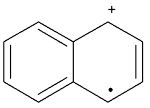
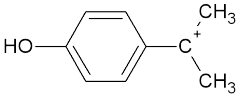
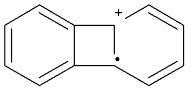
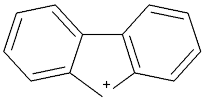
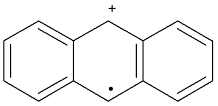
Fragment	Mass [u]	Structure
$C_4H_3^+$	51.02	
$C_5H_3^+$	63.02	
$C_6H_5^+$	77.04	
$C_7H_7^+$	91.06	cyclic
$C_8H_7^+$	103.06	
$C_9H_7^+$	115.06	
$C_{10}H_8^+$	128.06	
$C_9H_{11}O^+$	135.08	
$C_{12}H_8^+$	152.06	
$C_{13}H_9^+$	165.07	
$C_{14}H_{10}^+$	178.08	
$C_{14}H_{11}O^+$	195.08	

Table A.3: *Characteristic fragments of polycarbonate in the positive polarity*

Copy for "Bibliothèque UCL"

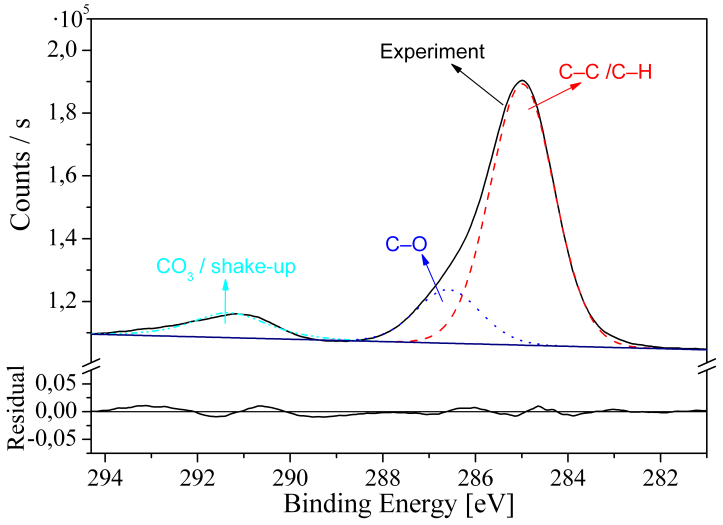


Figure A.3: *Contributions of the C1s XPS peak of a pristine PC sample.*

	PC	
Contribution	theo	exp
C−C / C−H	81	75
C−O	13	16
C=O / O-C-O	0	0
O−C=O	0	0
CO_3 / $\pi \rightarrow \pi^*$	6	9
max. deviation		±1

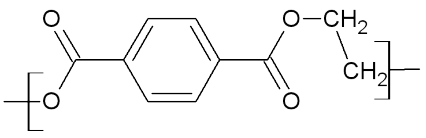
Table A.4: *Theoretical and experimental percentage of the different C1s XPS peak contribution of a pristine PC sample.*

Copy for "Bibliothèque UCL"

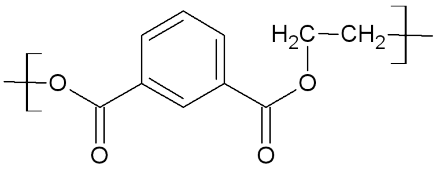
A.2.2 Polyethylene terephthalate - isophthalate

Polyethylene terephthalate is a thermoplastic polymer resin of the polyester family. Depending on its thickness, PET can be semi-rigid to rigid. It is very lightweight and impact-resistant. It is naturally colorless with a high transparency. Because of its high mechanical strength, PET film is often used in tape applications, beverage, food and other liquid containers. Aluminuzed biaxially oriented PET film have a reduced permeability, which is useful in flexible food packaging and thermal insulation. Non-oriented PET sheet can be thermoformed to make packaging trays withstanding both freezing and oven baking temperatures.

A common PET modifier is isophthalic acid, replacing some of the 1,4-(para-) linked terephthalate units. The 1,2-(ortho-) or 1,3-(meta-) linkage produces an angle in the chain, which lowers the polymer's melting point and also disturbs crystallinity.



(a) *Molecular structure of PET*



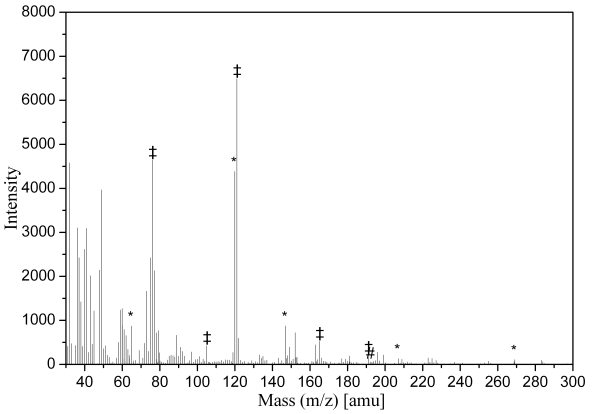
(b) *Molecular structure of PET-I*

Molecular formula	$C_{10}H_8O_4$
Monoisotopic Mass	192.02 u
Melting Temperature	260 °C
Glass transition temperature	75 °C
Refracting index	$1.575 + 0.052i$
Density	$1.37 \frac{g}{cm^3}$
Surface free energy	$45 \frac{mJ}{m^2}$

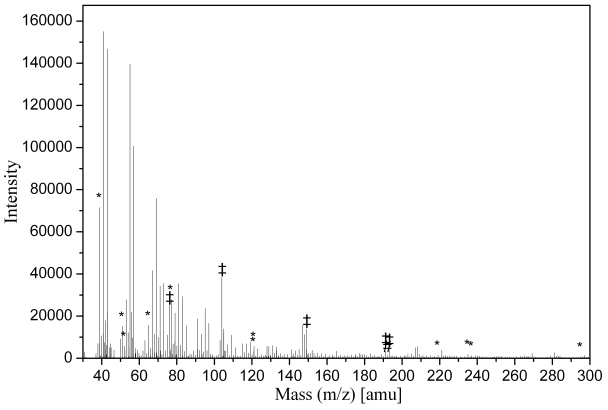
(c) *Properties of polyethylene terephthalate*

Figure A.4: *Molecular structure of a) polyethylene terephthalate (PET) and b) polyethylene isophthalate (PET-I).*

Copy for "Bibliothèque UCL"



(a) *negative polarity*



(b) *positive polarity*

Figure A.5: *Spectra of poly(etylene terephthalate) isophthalate in the negative and positive polarities. The peaks mark by a * indicates characteristic peaks found in the literature. # indicates the position of the monomer. ‡ indicates the position of the characteristic peaks which are evaluated in this work.*

Copy for "Bibliothèque UCL"

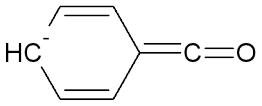
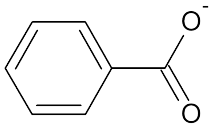
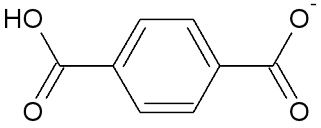
Fragment	Mass [u]	Structure
$C_6H_4^-$	76.03	
$C_7H_5O^-$	105.02	
$C_7H_5O_2^-$	121.02	
$C_8H_5O_4^-$	165.00	
$C_{10}H_7O_4^-$	191.02	$[\mathbb{M}-\mathrm{H}]^-$

Table A.5: *Characteristic fragments of poly(etylene terephthalate) in the negative polarity*

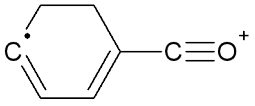
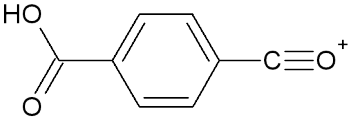
Fragment	Mass [u]	Structure
$C_4H_4^+$	51.03	
$C_6H_4^+$	76.03	
$C_7H_4O^+$	104.02	
$C_8H_5O_3^+$	149.01	
$C_{10}H_7O_4^+$	191.02	$[\mathbb{M}-\mathrm{H}]^+$
$C_{10}H_9O_4^+$	193.03	$[\mathbb{M}+\mathrm{H}]^+$

Table A.6: *Characteristic fragments of poly(etylene terephthalate) in the positive polarity*

Copy for "Bibliothèque UCL"

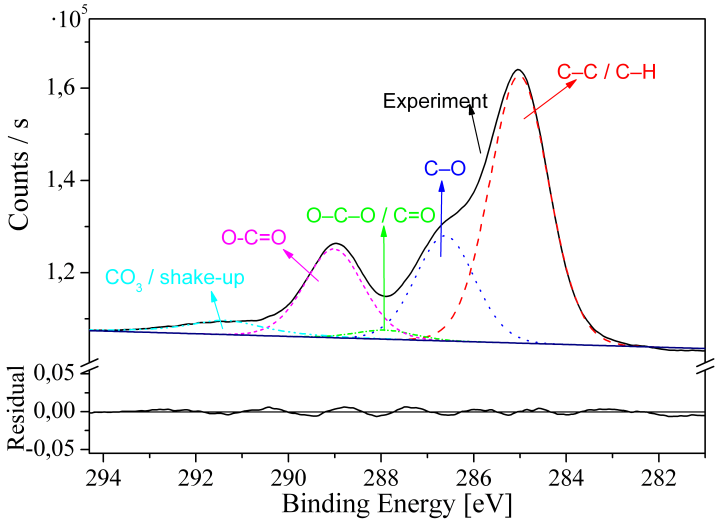


Figure A.6: *Contributions of the C1s XPS peak of a pristine PET-I sample.*

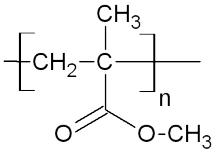
	PET-I	
Contribution	theo	exp
C−C / C−H	60	55
C−O	20	21
C=O / O-C-O	0	2
O−C=O	20	19
CO_3 / $\pi \rightarrow \pi^*$	0	3
max. deviation		±3

Table A.7: *Theoretical and experimental percentage of the different C1s XPS peak contribution of a pristine PET-I sample.*

Copy for "Bibliothèque UCL"

A.2.3 Poly (methyl methacrylate)

Poly(methyl methacrylate) (PMMA) is a transparent thermoplastic. Chemically, it is the synthetic polymer of methyl methacrylate. PMMA is often used as a light or shatter-resistant alternative to glass. It is an economical alternative to polycarbonate (PC) when extreme strength is not necessary. It has an excellent environmental stability and is therefore often the material of choice for outdoor applications.



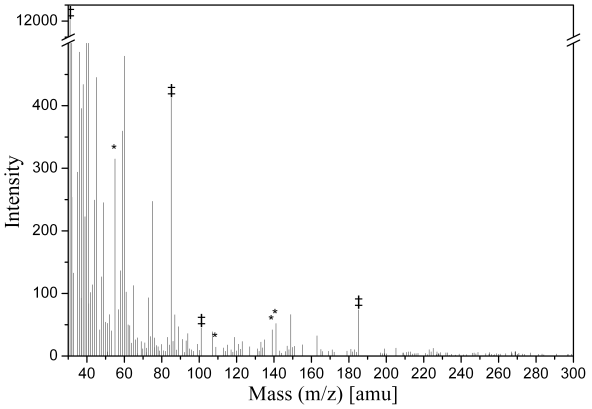
(a) *Molecular structure*

Molecular formula	$C_5H_8O_2$
Monoisotopic Mass	100.05 u
Melting Temperature	160 °C
Glass transition temperature	105 °C
Refracting index	1.486
Density	1.18 $\frac{g}{cm^3}$
Surface free energy	41 $\frac{mJ}{m^2}$

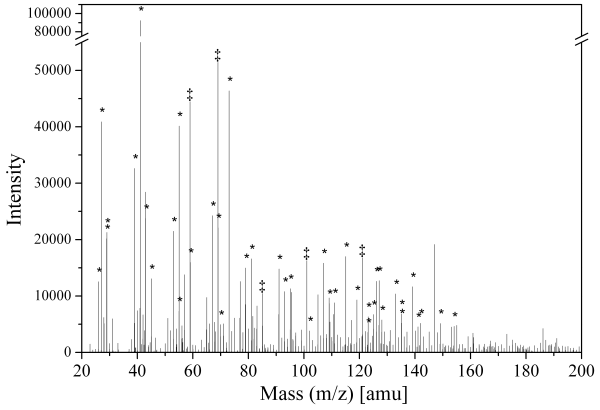
(b) *Properties of poly(methyl methacrylate)*

Figure A.7: *Molecular structure and properties of PMMA*

Copy for "Bibliothèque UCL"



(a) *negative polarity*



(b) *positive polarity*

Figure A.8: *Spectra of PMMA in the negative and positive polarities. The peaks mark by a * indicates characteristic peaks found in the literature. # indicates the position of the monomer. ‡ indicates the position of the characteristic peaks which are evaluated in this work.*

Copy for "Bibliothèque UCL"

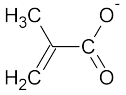
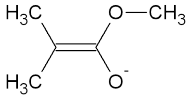
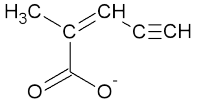
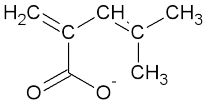
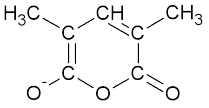
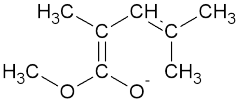
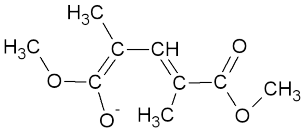
Fragment	Mass [u]	Structure
CH_3O^-	31.02	
$C_3H_3O^-$	55.02	
$C_4H_5O_2^-$	85.03	
$C_5H_9O_2^-$	101.06	
$C_6H_5O_2^-$	109.03	
$C_7H_9O_2^-$	125.06	
$C_7H_7O_3^-$	139.04	
$C_8H_{13}O_2^-$	141.09	
$C_9H_{13}O_4^-$	185.09	

Table A.8: *Characteristic fragments of PMMA in the negative polarity*

Copy for "Bibliothèque UCL"

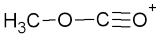
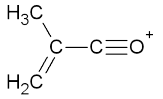
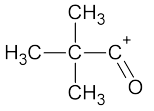
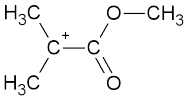
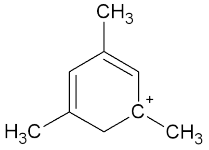
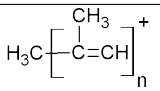
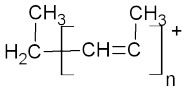
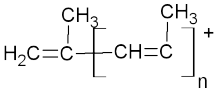
Fragment	Mass [u]	Structure
CH_3^+	15.02	
$C_2H_3O_2^+$	59.01	
$C_4H_5O^+$	69.03	
$C_5H_9O^+$	85.07	
$C_5H_9O_2^+$	101.06	
$C_9H_{13}^+$	121.10	
$CH_3-(C_3H_4)_n^+$	$15.02 + n \cdot 40.03$	
$C_2H_5-(C_3H_4)_n^+$	$29.04 + n \cdot 40.03$	
$C_3H_5-(C_3H_4)_n^+$	$41.04 + n \cdot 40.03$	

Table A.9: *Characteristic fragments of PMMA in the positive polarity*

Copy for "Bibliothèque UCL"

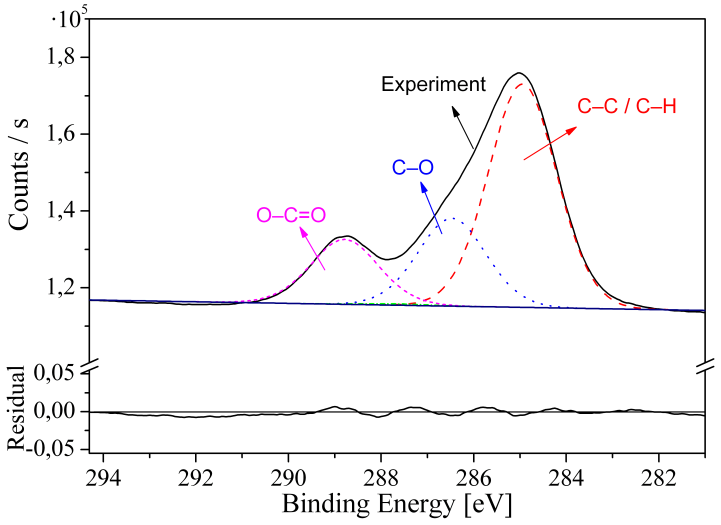


Figure A.9: *Contributions of the C1s XPS peak of a pristine PMMA sample.*

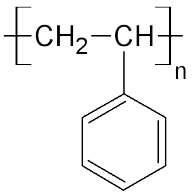
	PMMA	
Contribution	theo	exp
C−C / C−H	60	66
C−O	20	17
C=O / O-C-O	0	4
O−C=O	20	12
CO_3 / $\pi \rightarrow \pi^*$	0	1
max. deviation		±1

Table A.10: *Theoretical and experimental percentage of the different C1s XPS peak contribution of a pristine PMMA sample.*

Copy for "Bibliothèque UCL"

A.2.4 Polystyrene

Polystyrene, made from the aromatic monomer styrene, belongs to a group of thermoplastic substance. Pure solid polystyrene is a colorless (transparent), hard plastic with limited flexibility. Polystyrene is used in disposable cutlery, plastic models, CD/DVD cases, packing materials and insulation.



(a) *Molecular structure*

Molecular formula	C_8H_8
Monoisotopic Mass	104.06 u
Melting Temperature	240 °C
Glass transition temperature	95 °C
Refracting index	1.586
Density	1.06 $\frac{g}{cm^3}$
Surface free energy	41 $\frac{mJ}{m^2}$

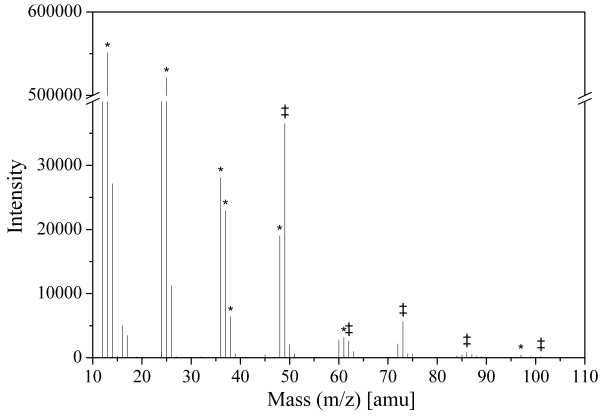
(b) *Properties of polystyrene*

Figure A.10: *Molecular structure and properties of polystyrene*

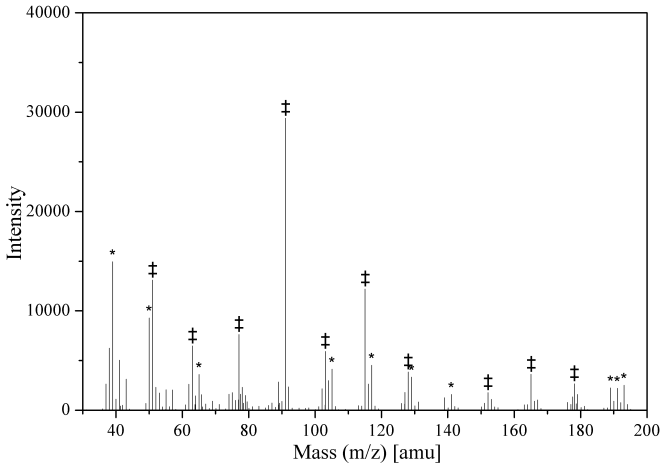
Fragment	Mass [u]
C_3H^-	37.01
C_4H^-	49.01
$C_5H_2^-$	62.02
C_6H^-	73.01

Table A.11: *Characteristic fragments of polystyrene in the negative polarity*

Copy for "Bibliothèque UCL"



(a) *negative polarity*



(b) *positive polarity*

Figure A.11: *Spectra of polysytrene in the negative and positive polarities. The peaks mark by a * indicates characteristic peaks found in the literature. # indicates the position of the monomer. ‡ indicates the position of the characteristic peaks which are evaluated in this work.*

Copy for "Bibliothèque UCL"

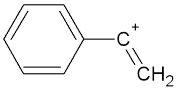
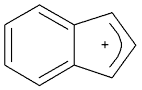
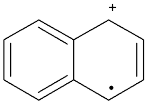
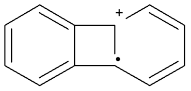
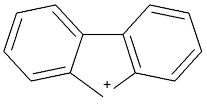
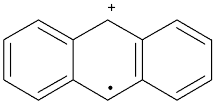
Fragment	Mass [u]	Structure
$C_4H_3^+$	51.02	
$C_5H_3^+$	63.02	
$C_6H_5^+$	77.04	
$C_7H_7^+$	91.06	cyclic
$C_8H_7^+$	103.06	
$C_9H_7^+$	115.06	
$C_{10}H_8^+$	128.06	
$C_{12}H_8^+$	152.06	
$C_{13}H_9^+$	165.07	
$C_{14}H_{10}^+$	178.08	

Table A.12: *Characteristic fragments of polystyrene in the positive polarity*

Copy for "Bibliothèque UCL"

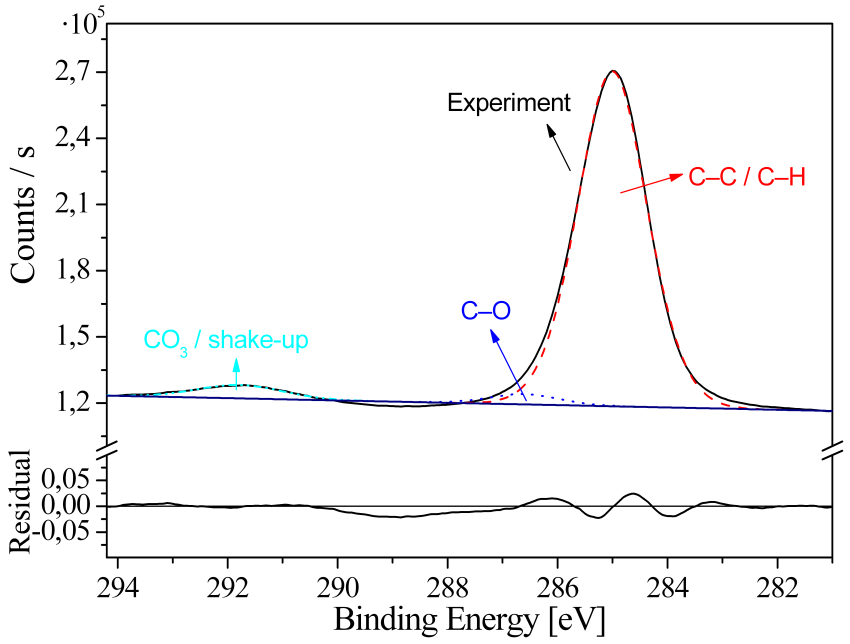


Figure A.12: *Contributions of the C1s XPS peak of a pristine PS sample.*

	PS	
Contribution	theo	exp
C−C / C−H	100	93
C−O	0	3
C=O / O-C-O	0	0
O−C=O	0	0
CO_3 / $\pi \rightarrow \pi^*$	0	4
max. deviation		±4

Table A.13: *Theoretical and experimental percentage of the different C1s XPS peak contribution of a pristine PS sample.*

Copy for "Bibliothèque UCL"